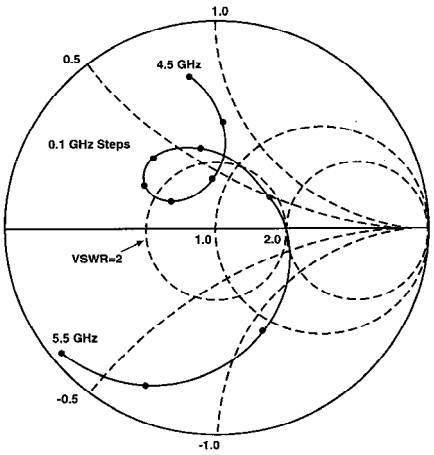

Applied Computational Electromagnetics Society Journal

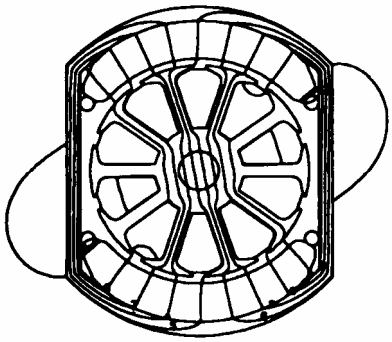

Editor-in-Chief
Atef Z. Elsherbeni

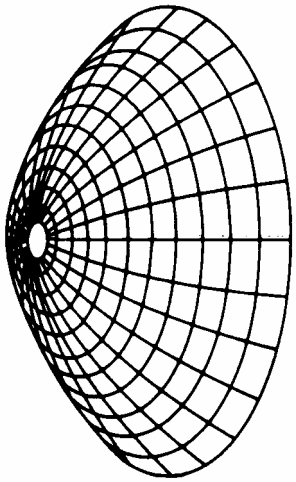

August 2009
Vol. 24 No. 4
ISSN 1054-4887

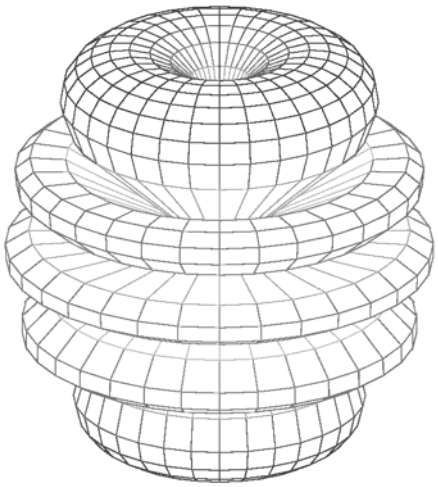

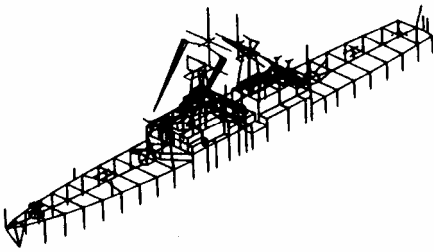

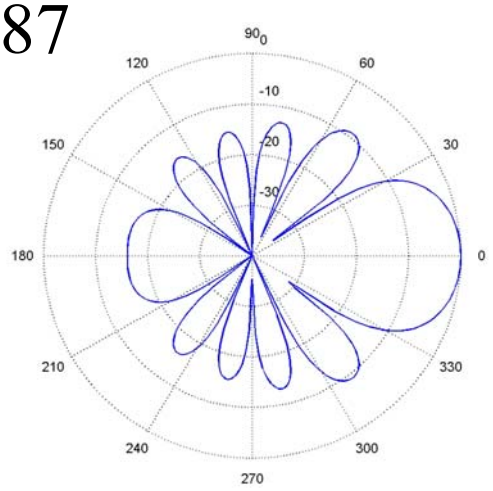

GENERAL PURPOSE AND SCOPE: The Applied Computational Electromagnetics Society ***(ACES)*** Journal hereinafter known as the ***ACES Journal*** is devoted to the exchange of information in computational electromagnetics, to the advancement of the state-of-the art, and the promotion of related technical activities. A primary objective of the information exchange is the elimination of the need to "re-invent the wheel" to solve a previously-solved computational problem in electrical engineering, physics, or related fields of study. The technical activities promoted by this publication include code validation, performance analysis, and input/output standardization; code or technique optimization and error minimization; innovations in solution technique or in data input/output; identification of new applications for electromagnetics modeling codes and techniques; integration of computational electromagnetics techniques with new computer architectures; and correlation of computational parameters with physical mechanisms.

SUBMISSIONS: The ***ACES Journal*** welcomes original, previously unpublished papers, relating to applied computational electromagnetics. Typical papers will represent the computational electromagnetics aspects of research in electrical engineering, physics, or related disciplines. However, papers which represent research in applied computational electromagnetics itself are equally acceptable.

Manuscripts are to be submitted through the upload system of ***ACES*** web site http://aces.ee.olemiss.edu See "Information for Authors" on inside of back cover and at ***ACES*** web site. For additional information contact the Editor-in-Chief:

Dr. Atef Elsherbeni
Department of Electrical Engineering
The University of Mississippi
University, MS 386377 USA
Phone: 662-915-5382 Fax: 662-915-7231
Email: atef@olemis.edu

SUBSCRIPTIONS: All members of the Applied Computational Electromagnetics Society who have paid their subscription fees are entitled to receive the ***ACES Journal*** with a minimum of three issues per calendar year and are entitled to download any published journal article available at http://aces.ee.olemiss.edu.

Back issues, when available, are $15 each. Subscriptions to ***ACES*** is through the web site. Orders for back issues of the ***ACES Journal*** and changes of addresses should be sent directly to ***ACES***:

Dr. Allen W. Glisson
302 Anderson Hall
Dept. of Electrical Engineering
Fax: 662-915-7231
Email: aglisson@olemiss.edu

Allow four week's advance notice for change of address. Claims for missing issues will not be honored because of insufficient notice or address change or loss in mail unless the Executive Officer is notified within 60 days for USA and Canadian subscribers or 90 days for subscribers in other countries, from the last day of the month of publication. For information regarding reprints of individual papers or other materials, see "Information for Authors".

LIABILITY. Neither ***ACES***, nor the ***ACES Journal*** editors, are responsible for any consequence of misinformation or claims, express or implied, in any published material in an ***ACES Journal*** issue. This also applies to advertising, for which only camera-ready copies are accepted. Authors are responsible for information contained in their papers. If any material submitted for publication includes material which has already been published elsewhere, it is the author's responsibility to obtain written permission to reproduce such material.

APPLIED COMPUTATIONAL ELECTROMAGNETICS SOCIETY JOURNAL

Editor-in-Chief
Atef Z. Elsherbeni

August 2009
Vol. 24 No. 4
ISSN 1054-4887

The ACES Journal is abstracted in INSPEC, in Engineering Index, DTIC, Science Citation Index Expanded, the Research Alert, and to Current Contents/Engineering, Computing & Technology.

The first, fourth, and sixth illustrations on the front cover have been obtained from the Department of Electrical Engineering at the University of Mississippi.

The third and fifth illustrations on the front cover have been obtained from Lawrence Livermore National Laboratory.

The second illustration on the front cover has been obtained from FLUX2D software, CEDRAT S.S. France, MAGSOFT Corporation, New York.

THE APPLIED COMPUTATIONAL ELECTROMAGNETICS SOCIETY

JOURNAL

Vol. 24 No. 4 August 2009

TABLE OF CONTENTS

A Closed-Form Sensitivity Analysis of Transmission Lines

G. Antonini, L. De Camillis, and F. Ruscitti

Dipartimento di Ingegneria Elettrica e dell'Informazione
Università degli Studi dell'Aquila
Monteluco di Roio, 67040, L'Aquila, Italy
antonini@ing.univaq.it

Abstract – A new approach for frequency-domain sensitivity analysis of transmission lines is presented. The propagation problem for the voltage sensitivity is considered and solved in terms of the closed-form Green's function of the 1-D wave propagation problem. This leads to a closed-form solution for the voltage sensitivity. The accuracy of the proposed method is verified by comparison with the perturbation approach.

Keywords: Transmission lines, interconnects, sensitivity analysis, Green's function.

I. INTRODUCTION

With the rapid increase in operating speeds, density, and complexity of modern electronics, the effects of interconnects such as delay, ringing and distortion have become a dominant factor. As the rise-times in nowadays interconnects may be few tens of picoseconds, distributed lossy transmission line models must be used assuming the quasi-TEM mode as the dominant one [1, 2].

At the design stage, it may be useful to compute not only the response of the line to a given excitation, but also its sensitivity with respect to a physical or geometrical parameter. From this perspective, it is frequently required that designers make the proper trade-off, often between conflicting design requirements using optimization techniques, to obtain the best possible performance [3].

Sensitivity analysis has been widely used in control and circuit theory [4, 5]. An extensive research work has been done over the recent years in the implementation of sensitivity analysis techniques with full-wave electromagnetic solvers for high frequency problems [6–14].

The knowledge of response derivatives is also crucial for macro-modeling purposes [15]. In fact, recent advancements in macro-modeling techniques have demonstrated that the use of response derivatives is effective to speed-up the generation of macromodels of linear systems while preserving the accuracy [16–18].

Although the application of full-wave techniques to compute transmission lines sensitivity is surely feasible, efficient use of computing resources is always to be preferred and, when possible, analytical solutions are to be considered. In this paper we present a new approach to frequency-domain sensitivity of transmission lines which is based on the use of the Green's function of the 1-D wave propagation problem. Telegrapher's equations are modified inorder to incorporate port currents as external sources to the system. In [19] it has been shown that such a technique allows to treat the Telegrapher's equation as a Sturm-Liouville problem for the voltage which can be directly written in terms of the Green's function of the 1-D wave propagation [20]. Voltage and current sensitivities satisfy the same Sturm-Liouville problem as voltages and currents but with a different forcing term. Hence, the same Green's function can be adopted. The knowledge of the closed-form Green's function for the transmission line problem permits to compute the voltage sensitivity analytically, thus avoiding any numerical processing and pawns the way to an accurate and efficient sensitivity analysis. The proposed methodology is well suited to be extended to the computation of higher-order sensitivities.

The paper is organized as follows. In Section II the formulation is presented leading to the computation of the voltage sensitivity in terms of the closed-form Green's function. Section III presents the computation of derivatives and voltage sensitivities in a closed-form. Two numerical examples are described in Section IV confirming the capability of the proposed approach to provide a fast and reliable method to sensitivity of transmission lines. The conclusions are drawn in Section V.

II. SENSITIVITY FORMULATION

Let us consider the transmission line illustrated in Fig. 1.

The physics of transmission lines under the quasi-TEM hypothesis is captured by the Telegrapher's equations [1],

$$\frac{\partial}{\partial z}v(z,t) = -R\ i(z,t) - L\ \frac{\partial}{\partial t}i(z,t) \tag{1a}$$

$$\frac{\partial}{\partial z}i(z,t) = -G\ v(z,t) - C\ \frac{\partial}{\partial t}v(z,t) + i_S(z,t), \tag{1b}$$

where $R \in \Re$, $L \in \Re$, $C \in \Re$ and $G \in \Re$ are the per-unit-length (p.u.l.) parameters of the transmission line, $v(z,t) \in \Re$ and $i(z,t) \in \Re$ represent the voltage and current as a function of position z and time t, and $i_S(z,t)$ describe a distributed current source along the line. Differentiating (1a) and (1b) with respect to a

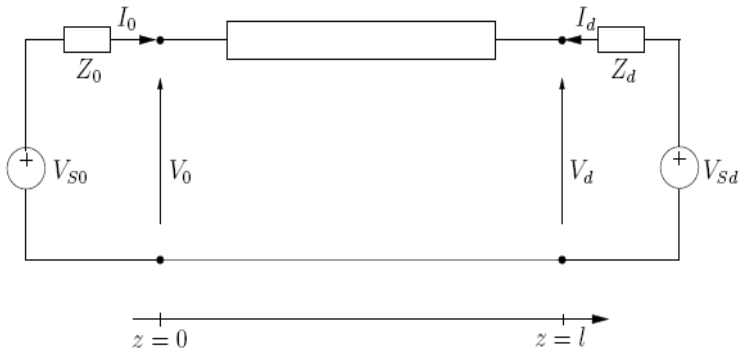

Fig. 1. Transmission line with linear terminations.

parameter λ (where λ represents any electrical or physical parameter of interest of the transmission line) yields the following equations,

$$\frac{\partial}{\partial z}\hat{v}(z,t) = -R\,\hat{i}(z,t) - L\,\frac{\partial}{\partial t}\hat{i}(z,t) - \left(\frac{\partial R}{\partial \lambda}\,i(z,t) + \frac{\partial L}{\partial \lambda}\frac{\partial}{\partial t}i(z,t)\right) \tag{2a}$$

$$\frac{\partial}{\partial z}\hat{i}(z,t) = -G\,\hat{v}(z,t) - C\,\frac{\partial}{\partial t}\hat{v}(z,t) - \left(\frac{\partial G}{\partial \lambda}\,v(z,t) + \frac{\partial C}{\partial \lambda}\frac{\partial}{\partial t}v(z,t)\right) + \frac{\partial}{\partial \lambda}i_S(z,t), \tag{2b}$$

where the sensitivity variables in equations (2a) and (2b) are defined as,

$$\hat{v}(z,t) = \frac{\partial}{\partial \lambda}v(z,t) \qquad \hat{i}(z,t) = \frac{\partial}{\partial \lambda}i(z,t). \tag{3}$$

Transforming equations (1a), (1b), (2a) and (2b) in the Laplace domain, we obtain,

$$\frac{\partial}{\partial z}V(z,s) = -Z_s(s)I(z,s) \tag{4a}$$

$$\frac{\partial}{\partial z}I(z,s) = -Y_p(s)V(z,s) + I_S(z,s), \tag{4b}$$

$$\frac{\partial}{\partial z}\widehat{V}(z,s) = -Z_s(s)\widehat{I}(z,s) - \frac{\partial Z_s(s)}{\partial \lambda}I(z,s), \tag{4c}$$

$$\frac{\partial}{\partial z}\widehat{I}(z,s) = -Y_p(s)\widehat{V}(z,s) - \frac{\partial Y_p(s)}{\partial \lambda}V(z,s) + \frac{\partial}{\partial \lambda}I_S(z,s), \tag{4d}$$

where the series impedance $Z_s(s)$ and the parallel admittance $Y_p(s)$ of the line are defined as,

$$Z_s(s) = R + sL \tag{5a}$$

$$Y_p(s) = G + sC. \tag{5b}$$

Differentiating equation (4c) with respect to z we obtain,

$$\frac{\partial^2}{\partial z^2}\widehat{V}(z,s) = -Z_s(s)\frac{\partial}{\partial z}\widehat{I}(z,s) - \frac{\partial Z_s(s)}{\partial \lambda}\frac{\partial}{\partial z}I(z,s). \tag{6}$$

If we substitute equations (4b) and (4d) in equation (6), we can write,

$$\frac{\partial^2}{\partial z^2}\widehat{V}(z,s) - \gamma^2(s)\,\widehat{V}(z,s) = \frac{\partial \gamma^2}{\partial \lambda}V(z,s) - Z_s(s)\frac{\partial I_S(z,s)}{\partial \lambda} - \frac{\partial Z_s(s)}{\partial \lambda}I_S(z,s) \tag{7}$$

where

$$\gamma^2 = Z_s(s)Y_p(s)$$
$$\frac{\partial(\gamma^2)}{\partial \lambda} = \left(Z_s(s)\frac{\partial Y_p(s)}{\partial \lambda} + Y_p(s)\frac{\partial Z_s(s)}{\partial \lambda}\right). \tag{8}$$

In the following, the current sources $I_S(z,s)$ are assumed to be located only in correspondence of the terminations, yielding,

$$I_S(z,s) = I_0(z,s)\delta(z) + I_l(z,s)\delta(z-l) \tag{9}$$

where $\delta(z)$ represents the Dirac delta function.

Equation (7) represents a Helmholtz equation whose formal solution can be obtained by using the Green's function approach. The computation of the forcing term in equation (7) requires the evaluation of the derivative of the p.u.l. parameters with respect to λ, the port currents I_S and the voltage distribution $V(z,s)$. The latter expression can be obtained through the standard transmission line technique while the expression of the derivative of I_S is to be computed.

The transmission line can be represented as a multiport system with port voltages and currents at $z=0$ and $z=l$ related by,

$$\begin{bmatrix} V_0 \\ V_l \end{bmatrix} = \begin{bmatrix} Z_{11} & Z_{12} \\ Z_{21} & Z_{22} \end{bmatrix}\begin{bmatrix} I_0 \\ I_l \end{bmatrix} \tag{10}$$

where V_0 and V_l are the voltage at the port $z=0$ and $z=l$. Furthermore, the termination conditions at the port $z=0$ and $z=d$, as shown in Fig. 1, read,

$$\begin{bmatrix} V_0 \\ V_l \end{bmatrix} = \begin{bmatrix} V_{S0} \\ V_{Sd} \end{bmatrix} - \begin{bmatrix} Z_0 & 0 \\ 0 & Z_l \end{bmatrix}\begin{bmatrix} I_0 \\ I_l \end{bmatrix} \tag{11}$$

Combining equations (10) and (11) we obtain,

$$\begin{bmatrix} I_0 \\ I_l \end{bmatrix} = \left(\begin{bmatrix} Z_0 & 0 \\ 0 & Z_l \end{bmatrix} + \begin{bmatrix} Z_{11} & Z_{12} \\ Z_{21} & Z_{22} \end{bmatrix} \right)^{-1} \begin{bmatrix} V_{S0} \\ V_{Sd} \end{bmatrix} \tag{12}$$

The evaluation of the forcing term equation (7) requires computing the port current sensitivities,

$$\frac{\partial}{\partial \lambda} \begin{bmatrix} I_0 \\ I_l \end{bmatrix} = \frac{\partial}{\partial \lambda} \left(\begin{bmatrix} Z_0 & 0 \\ 0 & Z_l \end{bmatrix} + \begin{bmatrix} Z_{11} & Z_{12} \\ Z_{21} & Z_{22} \end{bmatrix} \right)^{-1} \begin{bmatrix} V_{S0} \\ V_{Sd} \end{bmatrix} \tag{13}$$

where voltage sources are assumed not depending on the parameter λ. Although it can be obtained by first computing the inverse of the global impedance matrix and then evaluating the derivative, an elegant way to do that is to separate the derivative from the matrix inverse. It can be done observing that,

$$\boldsymbol{A}(\lambda)\boldsymbol{A}^{-1}(\lambda) = \boldsymbol{I}.$$

Hence, by the chain rule,

$$\frac{d\boldsymbol{A}(\lambda)}{d\lambda}\boldsymbol{A}^{-1}(\lambda) + \boldsymbol{A}(\lambda)\frac{d\boldsymbol{A}^{-1}(\lambda)}{d\lambda} = \boldsymbol{0}$$

we obtain

$$\frac{d\boldsymbol{A}^{-1}(\lambda)}{d\lambda} = -\boldsymbol{A}^{-1}(\lambda)\frac{d\boldsymbol{A}(\lambda)}{d\lambda}\boldsymbol{A}^{-1}(\lambda).$$

This identity allows to calculate the current sensitivity equation (12) as follows,

$$\frac{\partial}{\partial \lambda} \begin{bmatrix} I_0 \\ I_l \end{bmatrix} = -\left(\begin{bmatrix} Z_0 & 0 \\ 0 & Z_l \end{bmatrix} + \begin{bmatrix} Z_{11} & Z_{12} \\ Z_{21} & Z_{22} \end{bmatrix} \right)^{-1} \frac{\partial}{\partial \lambda} \left(\begin{bmatrix} Z_0 & 0 \\ 0 & Z_l \end{bmatrix} + \begin{bmatrix} Z_{11} & Z_{12} \\ Z_{21} & Z_{22} \end{bmatrix} \right) \left(\begin{bmatrix} Z_0 & 0 \\ 0 & Z_l \end{bmatrix} + \begin{bmatrix} Z_{11} & Z_{12} \\ Z_{21} & Z_{22} \end{bmatrix} \right)^{-1} \begin{bmatrix} V_{S0} \\ V_{Sd} \end{bmatrix}. \tag{14}$$

Equation (14) can be simplified since Z_0 and Z_l are not depending from λ,

$$\frac{\partial}{\partial \lambda} \begin{bmatrix} I_0 \\ I_l \end{bmatrix} = -\left(\begin{bmatrix} Z_0 & 0 \\ 0 & Z_l \end{bmatrix} + \begin{bmatrix} Z_{11} & Z_{12} \\ Z_{21} & Z_{22} \end{bmatrix} \right)^{-1} \frac{\partial}{\partial \lambda} \begin{bmatrix} Z_{11} & Z_{12} \\ Z_{21} & Z_{22} \end{bmatrix} \left(\begin{bmatrix} Z_0 & 0 \\ 0 & Z_l \end{bmatrix} + \begin{bmatrix} Z_{11} & Z_{12} \\ Z_{21} & Z_{22} \end{bmatrix} \right)^{-1} \begin{bmatrix} V_{S0} \\ V_{Sd} \end{bmatrix}. \tag{15}$$

Again, although the derivative of the impedance matrix $[Z]$ can be computed relying on the standard transmission line theory [1], a different approach can be adopted which is based on the Green's function method [20] and pawns the way to the extension of the proposed method to time-domain.

Assuming boundary condition of the Neumann type, having incorporated port currents into sources $I_S(z,s)$, a two-conductor transmission line is characterized by the following closed-form Green's function [20],

$$G(z,z',s) = -\frac{\cosh[\gamma(s)(l-z_>)]\cosh[\gamma(s)z_<]}{\gamma(s)\sinh[\gamma(s)l]} \tag{16}$$

where $z_>$ and $z_<$ indicate the greater and lesser of the pair (z,z'), respectively, and γ is defined as,

$$\gamma = \sqrt{Z_s Y_p}. \tag{17}$$

It can be proved that the impedance matrix $[Z]$ can be expressed in terms of the Green's function as,

$$[Z] = \begin{bmatrix} G(0,0,s)(-Z_s(s)) & G(0,l,s)(-Z_s(s)) \\ G(l,0,s)(-Z_s(s)) & G(l,l,s)(-Z_s(s)) \end{bmatrix}. \tag{18}$$

Next, differentiating equation (18) with respect to λ, we obtain the derivative of the Z matrix. The result is shown at the top of the next page in equation (19).

The voltage distribution $V(z,s)$ in equation (7) can also be computed through the use of the Green's function as a function of the port currents,

$$V(z,s) = \begin{bmatrix} G(z,0,s)(-Z_s(s)) & G(z,l,s)(-Z_s(s)) \end{bmatrix} \begin{bmatrix} I_0 \\ I_l \end{bmatrix} \tag{20}$$

The differential problem equation (7) can be regarded as a Sturm-Liouville problem for the voltage sensitivity $\widehat{V}(z,s)$ satisfying the same boundary conditions of Neumann type as the voltage $V(z,s)$. Indeed, the following identities hold,

$$\left.\frac{\partial}{\partial z}\widehat{V}(z,s)\right|_{z=0} = \left.\frac{\partial}{\partial z}\frac{\partial}{\partial \lambda}V(z,s)\right|_{z=0} = \left.\frac{\partial}{\partial \lambda}\frac{\partial}{\partial z}V(z,s)\right|_{z=0} = 0 \tag{21a}$$

$$\left.\frac{\partial}{\partial z}\widehat{V}(z,s)\right|_{z=d} = \left.\frac{\partial}{\partial z}\frac{\partial}{\partial \lambda}V(z,s)\right|_{z=d} = \left.\frac{\partial}{\partial \lambda}\frac{\partial}{\partial z}V(z,s)\right|_{z=d} = 0, \tag{21b}$$

where the order of derivatives has been exchanged according to Schwarz's theorem being the partial derivatives continuous. Hence, it can be claimed that the Green's function for the voltage sensitivity is the same as for the voltage along the line. Hence, the voltage sensitivity can be computed as convolution between the Green's function and the forcing term $f(z')$,

$$\widehat{V}(z,s) = \int_0^l G(z,z')f(z')\mathrm{d}z' \tag{22}$$

where

$$f(z') = \frac{\partial(\gamma^2)}{\partial \lambda}V(z',s) - Z_s(s)\frac{\partial I_S(z',s)}{\partial \lambda} - \frac{\partial Z_s(s)}{\partial \lambda}I_S(z',s). \tag{23}$$

$$\frac{\mathrm{d}}{\mathrm{d}\lambda}[Z] = \begin{bmatrix} \frac{\mathrm{d}}{\mathrm{d}\lambda}\left[G(0,0,s)\right](-Z_s(s)) + G(0,0,s)\frac{\mathrm{d}}{\mathrm{d}\lambda}\left[(-Z_s(s))\right] & \frac{\mathrm{d}}{\mathrm{d}\lambda}\left[G(0,l,s)\right](-Z_s(s)) + G(0,l,s)\frac{\mathrm{d}}{\mathrm{d}\lambda}\left[(-Z_s(s))\right] \\ \frac{\mathrm{d}}{\mathrm{d}\lambda}\left[G(l,0,s)\right](-Z_s(s)) + G(l,0,s)\frac{\mathrm{d}}{\mathrm{d}\lambda}\left[(-Z_s(s))\right] & \frac{\mathrm{d}}{\mathrm{d}\lambda}\left[G(l,l,s)\right](-Z_s(s)) + G(l,l,s)\frac{\mathrm{d}}{\mathrm{d}\lambda}\left[(-Z_s(s))\right] \end{bmatrix} \tag{19}$$

III. COMPUTATION OF DERIVATIVES

Using equations (18) and (19), we are able to compute the $[Z]$ matrix and its derivative $\frac{\mathrm{d}}{\mathrm{d}\lambda}[Z]$ required for the calculation of equation (15). For this purpose, we can compute the derivative of Green's function analytically,

$$\begin{aligned} \frac{\mathrm{d}}{\mathrm{d}\lambda}\left[G(0,0,s)\right] &= \tfrac{\mathrm{d}}{\mathrm{d}\lambda}\left[G(l,l,s)\right] && (24a)\\ &= \frac{\mathrm{d}\gamma/\mathrm{d}\lambda}{\gamma^2\sinh^2(\gamma l)} \quad [l\gamma + \sinh(\gamma l)\cosh(\gamma l)] \\ \frac{\mathrm{d}}{\mathrm{d}\lambda}\left[G(0,l,s)\right] &= \tfrac{\mathrm{d}}{\mathrm{d}\lambda}\left[G(l,0,s)\right] && (24b)\\ &= \frac{\mathrm{d}\gamma/\mathrm{d}\lambda}{\gamma^2\sinh^2(\gamma l)} \quad [\sinh(\gamma l) + l\gamma\cosh(\gamma l)]\,. \end{aligned}$$

The function to be integrated in (22) reads,

$$F(z,z',s) = G(z,z',s)\tfrac{\partial(\gamma^2)}{\partial\lambda}V(z',s) - G(z,z',s)\left[-Z_s(s)\tfrac{\partial I_S(z',s)}{\partial\lambda} - \tfrac{\partial Z_s(s)}{\partial\lambda}I_S(z',s)\right] \tag{25}$$

The computation of equation (25) can be split in two terms $F(z,z',s) = F_1(z,z',s) + F_2(z,z',s)$, where $V(z',s)$ is given by equation (20),

$$\begin{aligned} F_1(z,z',s) &= \frac{\partial(\gamma^2)}{\partial\lambda}I_0(-Z_s(s))\cdot G(z,z',s)\cdot G(z',0,s) \\ &\quad + \frac{\partial(\gamma^2)}{\partial\lambda}I_l(-Z_s(s))\cdot G(z,z',s)\cdot G(z',l,s) && (26a)\\ F_2(z,z',s) &= \left[-Z_s(s)\frac{\partial I_0}{\partial\lambda}\delta(z') - Z_s(s)\frac{\partial I_l}{\partial\lambda}\delta(z'-l)\right. \\ &\quad \left. - \frac{\partial Z_s(s)}{\partial\lambda}I_0\delta(z') - \frac{\partial Z_s(s)}{\partial\lambda}I_l\delta(z'-l)\right]\cdot G(z,z',s), && (26b) \end{aligned}$$

where z is the abscissa wherein we compute the sensitivity and z' is the integration variable. Hence, the calculation of the integral of $F_1(z,z',s)$ depends on the products,

$$\begin{aligned} G(z,z') &\cdot G(z',0) && (27a)\\ G(z,z') &\cdot G(z',l) && (27b) \end{aligned}$$

Being interested to the voltage sensitivity at abscissa $z=0$ and $z=l$, it is useful exploiting the dependence of equation (27) on the z' coordinate, yielding,

$$\begin{aligned} G(0,z')\cdot G(z',0) &= K\cdot\left[\cosh(2\gamma l)\cosh(2\gamma z')\right. \\ &\quad \left. - \sinh(2\gamma l)\sinh(2\gamma z') + 1\right] && (28a)\\ G(0,z')\cdot G(z',l) &= K\cdot\left[\cosh(\gamma l) + \cosh(\gamma l)\cosh(2\gamma z')\right. \\ &\quad \left. - \sinh(2\gamma z')\sinh(\gamma l)\right], && (28b)\\ G(l,z')\cdot G(z',0) &= K\cdot\left[\cosh(\gamma l) + \cosh(\gamma l)\cosh(2\gamma z')\right. \\ &\quad \left. - \sinh(2\gamma z')\sinh(\gamma l)\right], && (28c)\\ G(l,z')\cdot G(z',l) &= K\cdot\left[1 + \cosh(2\gamma z')\right], && (28d) \end{aligned}$$

where

$$K = \frac{1}{2\gamma^2\sinh^2(\gamma l)}. \tag{29}$$

The integration of equations (28a) to (28d) is straightforward. Equations (30a) to (30d) show the definite integrals,

$$\begin{aligned} \int_0^l G(0,z')\cdot G(z',0)\mathrm{d}z' &= K\cdot\left[\frac{1}{2\gamma}\sinh(2\gamma z')\cosh(2\gamma l) - \right. \\ &\quad \left. - \frac{1}{2\gamma}\cosh(2\gamma z')\sinh(2\gamma l) + z'\right]\Big|_0^l && (30a) \end{aligned}$$

$$\begin{aligned} \int G(0,z')\cdot G(z',l)\mathrm{d}z' &= K\cdot\left[\cosh(\gamma l)\cdot z' + \right. \\ &\quad \left. + \frac{1}{2\gamma}\sinh(2\gamma z')\cosh(\gamma l) - \frac{1}{2\gamma}\cosh(2\gamma z')\sinh(\gamma l)\right]\Big|_0^l, && (30b) \end{aligned}$$

$$\begin{aligned} \int G(l,z')\cdot G(z',0)\mathrm{d}z' &= K\cdot\left[\cosh(\gamma l)\cdot z' + \right. \\ &\quad \left. + \frac{1}{2\gamma}\sinh(2\gamma z')\cosh(\gamma l) - \frac{1}{2\gamma}\cosh(2\gamma z')\sinh(\gamma l)\right]\Big|_0^l, && (30c) \end{aligned}$$

$$\int G(l,z')\cdot G(z',l)\mathrm{d}z' = K\cdot\left[z' + \frac{1}{2\gamma}\sinh(2\gamma z')\right]\Big|_0^l. \tag{30d}$$

The second term $F_2(z,z',s)$ in equation (26b) is finally considered.

Its contribution to the overall voltage sensitivity, taking the delta Dirac function sampling property into account [21], is given by,

$$\begin{aligned} \int_0^l F_2(z,z',s)dx' &= -Z_s(s)\frac{\partial I_0}{\partial\lambda}G(z,0,s) - Z_s(s)\frac{\partial I_l}{\partial\lambda}G(z,l,s) \\ &\quad - \frac{\partial Z_s(s)}{\partial\lambda}I_0G(z,0,s) - \frac{\partial Z_s(s)}{\partial\lambda}I_lG(z,l,s). \end{aligned} \tag{31}$$

Finally, the voltage sensitivity with respect to parameter λ at abscissa $z=0$ and $z=l$ can be computed as,

$$\begin{aligned} \widehat{V}(0,s) &= \int_0^l\left(F_1(0,z',s) + F_2(0,z',s)\right)\mathrm{d}z' && (32a)\\ \widehat{V}(l,s) &= \int_0^l\left(F_1(l,z',s) + F_2(l,z',s)\right)\mathrm{d}z'. && (32b) \end{aligned}$$

Space limitations do not permit the description of the time-domain analysis here but it can be easily obtained working with linear loads from the inverse fast Fourier transform (IFFT).

A. Higher-order sensitivities

The voltage sensitivities of equation (32) correspond to first-order sensitivities of port voltages with respect to parameter λ. The evaluation of higher-order sensitivities can be performed using the same approach outlined in Section II. In fact, the governing equation for the k-order voltage sensitivity is,

$$\frac{\partial^2}{\partial z^2}\widehat{V}_k(z,s) - \gamma^2(s)\ \widehat{V}_k(z,s) = k\frac{\partial \gamma^2}{\partial \lambda}\widehat{V}_{k-1}(z,s) + \frac{\partial^k \gamma^2}{\partial \lambda^k}V(z,s) - \frac{\partial^k}{\partial \lambda^k}\left(Z_s(s)I_S(z,s)\right). \quad (33)$$

The Sturm-Liouville problem for the k-order voltage sensitivity $\widehat{V}_k(z,s)$ admits the same Green's function as the voltage distribution $V(z,s)$ and, as a consequence, it can be computed as,

$$\widehat{V}_k(z,s) = \int_0^l G(z,z')f_k(z')\mathrm{d}z' \quad (34)$$

where

$$f_k(z') = k\frac{\partial \gamma^2}{\partial \lambda}\widehat{V}_{k-1}(z',s) + \frac{\partial^k \gamma^2}{\partial \lambda^k}V(z',s) - \frac{\partial^k}{\partial \lambda^k}\left(Z_s(s)I_S(z',s)\right). \quad (35)$$

Each term of the forcing term (35) can be analytically computed as well as the integrand function in equation (34) and its integral, leading to a closed-form k-order voltage sensitivity.

IV. NUMERICAL RESULTS

In this section we present two examples of transmission lines whose voltage sensitivity with respect to geometrical parameters are computed by using the proposed methodology. For the sake of comparison, the voltage sensitivity is also computed by the perturbative approach by giving a small perturbation $\Delta\lambda$ to the parameter λ and computing the sensitivity as,

$$\widehat{V}^p(z,s) = \frac{V(z,s,\lambda+\Delta\lambda) - V(z,s,\lambda)}{\Delta\lambda}. \quad (36)$$

A. Two-conductor transmission line

Let us consider a couple of conductors of radius $r_0 = 2$ mm and length $l = 0.1$ m, at a distance $d = 1$ cm, in the free space (permittivity $\varepsilon_0 = 8.854$ pF/m and permeability $\mu_0 = 0.4\pi$ mH/m). The p.u.l. parameters of the line are [1],

$$R = \frac{\rho}{\pi r_0^2} \qquad G = 0$$
$$L = \frac{\mu_0}{2\pi}\ln\frac{2d}{r_0} \qquad C = \frac{2\pi\varepsilon_0}{\ln\frac{2d}{r_0}}. \quad (37)$$

The voltage sensitivity is computed with respect to the distance between the conductors $\lambda = d$. First we can compute the series impedance Z_s and the parallel admittance Y_p and their derivatives with respect to sensitivity parameter d,

$$Z_s(d,s) = R + sL \quad (38a)$$
$$Y_p(d,s) = G + sC, \quad (38b)$$
$$\frac{\partial}{\partial d}Z_s(d,s) = s\cdot\frac{\mu_0}{2\pi}\frac{1}{d}, \quad (38c)$$
$$\frac{\partial}{\partial d}Y_p(d,s) = s\cdot\left(-\frac{2\pi\varepsilon_0}{d\ \ln^2\left[\frac{2d}{r_0}\right]}\right). \quad (38d)$$

The circuit is excited by a voltage pulse V_s with 800 ps width and 500-ps rise and fall times, whose magnitude spectrum is shown in Fig. 2. The frequency range of analysis is $0-5$ GHz.

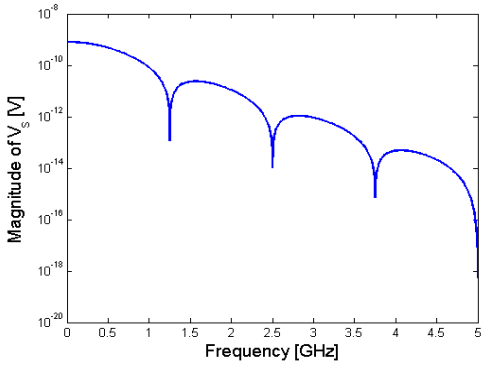

Fig. 2. Magnitude spectrum of the voltage source (example IV-A).

In Figs. 3 and 4 it is shown the magnitude and phase spectra of the voltage sensitivity at $z = 0$ and $z = l$ as computed by using equations (32a) and (32b) and compared with the perturbative approach.

No noticeable difference can be observed between the proposed and perturbative approach.

B. Microstrip

As a second example we consider a microstrip transmission line. It can be characterized by geometrical and physical parameters such as width of the strip W, height of the dielectric substrate H, strip thickness T, permeability and dielectric constants. The p.u.l. capacitance in free space is given by [22],

$$C_a = \begin{cases} \varepsilon_0\left[\frac{W_e}{H} + 1.393 + 0.667\cdot \ln\left(\frac{W_e}{H} + 1.444\right)\right] & W/H > 1 \\ \dfrac{2\pi\varepsilon_0}{\ln\left(\frac{8H}{W_e} + \frac{W_e}{4H}\right)} & W/H \le 1 \end{cases} \quad (39)$$

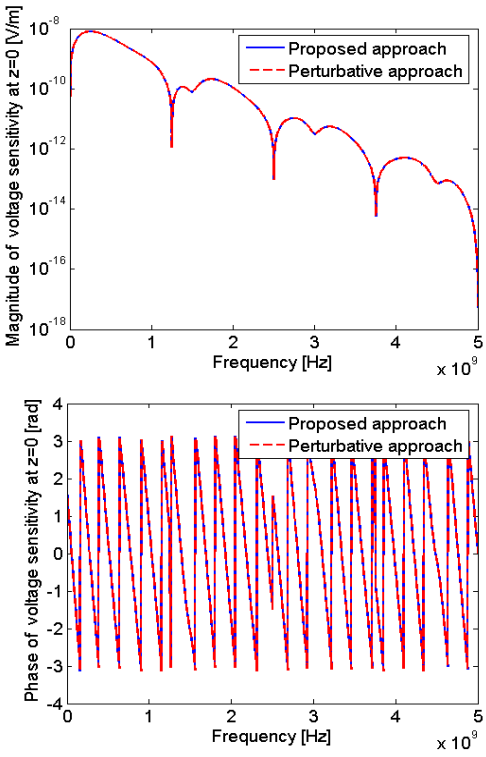

Fig. 3. Magnitude and phase spectra of voltage sensitivity at $z = 0$ (example IV-A).

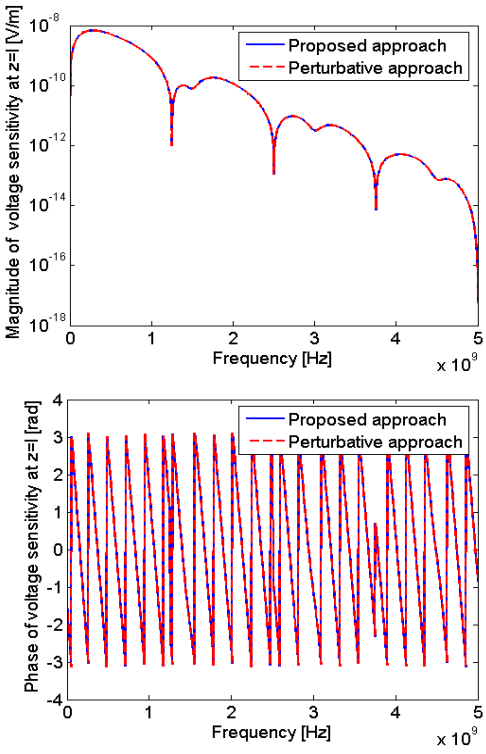

Fig. 4. Magnitude and phase spectra of voltage sensitivity at $z = l$ (example IV-A).

where the effect of the finite thickness can be included using effective width W_e instead of W [22],

$$W_e = \begin{cases} W + 0.398T\left(1 + \ln\dfrac{2\pi}{T}\right) & W/H > \dfrac{1}{2\pi} \\ W + 0.398T\left(1 + \ln\dfrac{4\pi W}{T}\right) & W/H \leq \dfrac{1}{2\pi} \end{cases} \tag{40}$$

The effective dielectric constant, ε_{eff}, for a microstrip line with an isotropic substrate is given by [22],

$$\varepsilon_{eff} = \frac{\varepsilon_r + 1}{2} + \frac{\varepsilon_r - 1}{2}\left(1 + \frac{12H}{W_e}\right)^{-\frac{1}{2}} + F(\varepsilon_r, H) - 0.217(\varepsilon_r - 1)\frac{T}{\sqrt{W_e H}} \tag{41}$$

where

$$F(\varepsilon_r, H) = \begin{cases} 0 & W/H > 1 \\ 0.02(\varepsilon_r - 1)\left(1 - \dfrac{W_e}{H}\right)^2 & W/H \leq 1 \end{cases} \tag{42}$$

The p.u.l capacitance and inductance, assuming an homogeneous medium, is given by [22],

$$C = C_a \varepsilon_{eff} \tag{43a}$$

$$L = \frac{\mu_0 \varepsilon_0 \varepsilon_{eff}}{C} = \frac{\mu_0 \varepsilon_0}{C_a}. \tag{43b}$$

In order to obtain the voltage sensitivity, the derivatives of equations (43a) and (43b) are needed. In the following both the voltage sensitivity with respect the width of the strip W as well as the height of the dielectric substrate H are computed. The derivatives read,

$$\frac{\mathrm{d}C}{\mathrm{d}W} = \frac{\mathrm{d}C_a}{\mathrm{d}W}\varepsilon_{eff} + C_a\frac{\mathrm{d}\varepsilon_{eff}}{\mathrm{d}W} \tag{44a}$$

$$\frac{\mathrm{d}L}{\mathrm{d}W} = -\frac{\varepsilon_0\mu_0}{C_a^2}\frac{\mathrm{d}C_a}{\mathrm{d}W}, \tag{44b}$$

$$\frac{\mathrm{d}C}{\mathrm{d}H} = \frac{\mathrm{d}C_a}{\mathrm{d}H}\varepsilon_{eff} + C_a\frac{\mathrm{d}\varepsilon_{eff}}{\mathrm{d}H}, \tag{44c}$$

$$\frac{\mathrm{d}L}{\mathrm{d}H} = -\frac{\varepsilon_0\mu_0}{C_a^2}\frac{\mathrm{d}C_a}{\mathrm{d}H}, \tag{44d}$$

where

$$\frac{dC_a}{dW} = \begin{cases} \dfrac{\varepsilon_0 W_e'}{H}\left[1 + 0.667\dfrac{1}{W_e/H + 1.444}\right] & W/H > 1 \\ -\dfrac{2\pi\varepsilon_0\left(-\dfrac{8W_e' H}{W_e^2} + \dfrac{W_e'}{4H}\right)}{\ln^2\left(\dfrac{8H}{W_e} + \dfrac{W_e}{4H}\right)\cdot\left(\dfrac{8H}{W_e} + \dfrac{W_e}{4H}\right)} & W/H \leq 1 \end{cases} \tag{45}$$

$$\frac{dC_a}{dH} = \begin{cases} -\varepsilon_0\dfrac{W_e}{H^2}\left[1 + 0.667\dfrac{1}{W_e/H + 1.444}\right] & W/H > 1 \\ -\dfrac{2\pi\varepsilon_0\left(\dfrac{8}{W_e} - \dfrac{W_e}{4H^2}\right)}{\ln^2\left(\dfrac{8H}{W_e} + \dfrac{W_e}{4H}\right)\cdot\left(\dfrac{8H}{W_e} + \dfrac{W_e}{4H}\right)} & W/H \leq 1 \end{cases} \tag{46}$$

$$\frac{\mathrm{d}\varepsilon_{eff}}{\mathrm{d}W} = \frac{\varepsilon_r - 1}{2}\frac{6HW_e^{'}}{W_e^2}\left(1+\frac{12H}{W_e}\right)^{-\frac{3}{2}} + \frac{\mathrm{d}F(\varepsilon_r,H)}{\mathrm{d}W} + \\ +0.217(\varepsilon_r-1)\frac{HTW_e^{'}}{2}(W_eH)^{-\frac{3}{2}}, \quad (47)$$

$$\frac{\mathrm{d}\varepsilon_{eff}}{\mathrm{d}H} = -\frac{\varepsilon_r - 1}{2}\frac{6}{W_e}\left(1+\frac{12H}{W_e}\right)^{-\frac{3}{2}} + \frac{\mathrm{d}F(\varepsilon_r,H)}{\mathrm{d}H} + \\ +0.217(\varepsilon_r-1)\frac{W_eT}{2}(W_eH)^{-\frac{3}{2}}, \quad (48)$$

$$\frac{\mathrm{d}W_e}{\mathrm{d}W} = W_e^{'} = \begin{cases} 1 & W/H > \dfrac{1}{2\pi} \\ 1+0.398\dfrac{T}{W} & W/H \le \dfrac{1}{2\pi} \end{cases} \quad (49)$$

$$\frac{\mathrm{d}F(\varepsilon_r,H)}{\mathrm{d}W} = \begin{cases} 0 & W/H > 1 \\ 0.02(\varepsilon_r-1)\dfrac{2W_e^{'}}{H}\left(\dfrac{W_e}{H}-1\right) & W/H \le 1 \end{cases} \quad (50)$$

$$\frac{\mathrm{d}F(\varepsilon_r,H)}{\mathrm{d}H} = \begin{cases} 0 & W/H > 1 \\ 0.02(\varepsilon_r-1)\dfrac{2W_e}{H^2}\left(1-\dfrac{W_e}{H}\right) & W/H \le 1 \end{cases} \quad (51)$$

where $W_e^{'}$ stands for the derivative of W_e with respect to W, since it does not depend on H.

As a numerical test, a microstrip line has been considered with length $l = 5$ cm, width of the strip $W = 2$ mm, height of the dielectric substrate $H = 1$ mm and strip thickness $T = 0.5$mm. The relative permittivity of the substrate is $\varepsilon_r = 3$.

The voltage sensitivity has been computed using equations (32a) and (32b), considering as parameter λ the width of the strip W and the height of the dielectric substrate H. The circuit input is the same of the previous example (Fig. 2) and the frequency range of analysis is $0-5$ GHz. The magnitude and phase spectra of the voltage sensitivity with respect to W are shown in Figs. 5 and 6, while those of the voltage sensitivity with respect to H are shown in Figs. 7 and 8.

As before, a very good agreement is achieved between the proposed and the perturbative approach. For the sake of comparison the sensitivities have also been computed numerically. The computation has been performed on a machine equipped with AMD Athlon 64 processor. It took about 10 s to be completed by using the proposed technique and 73 s computing the sensitivities numerically, for 3751 frequency samples, leading to a speed-up of 7.3.

V. CONCLUSIONS

In this paper we have proposed a new approach to analyze frequency-domain sensitivity of transmission lines. It is based on the closed-form Green's function of the 1-D wave propagation problem. Relying on the knowledge of the Green's function for the transmission line problem, a closed-form solution for the voltage sensitivity with respect to either physical or geometrical parameters is readily computed. The proposed technique is well suited to be extended to the computation of higher-order

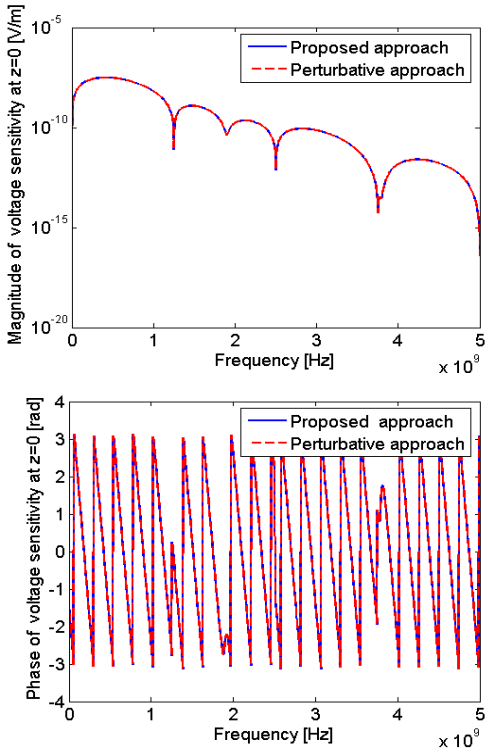

Fig. 5. Magnitude and phase of voltage sensitivity with respect to W at $z = 0$ (example IV-B).

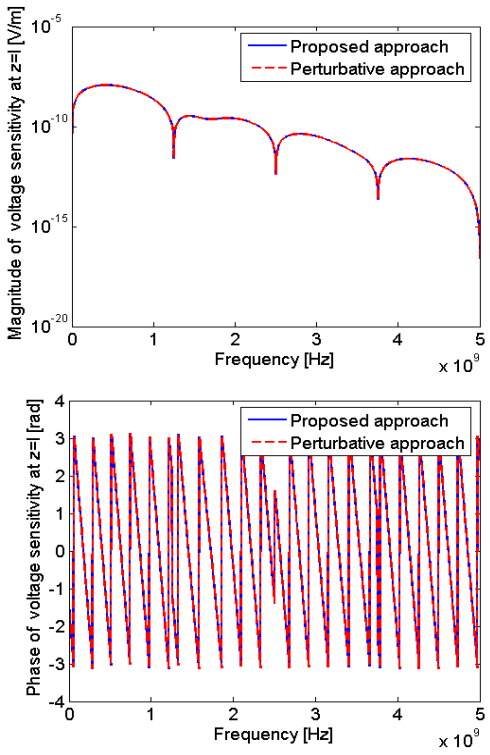

Fig. 6. Magnitude and phase of the voltage sensitivity with respect to W at $z = l$ (example IV-B).

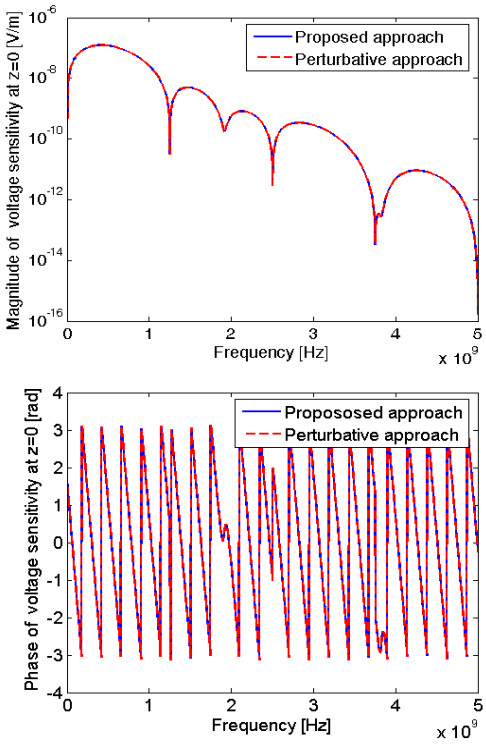

Fig. 7. Magnitude and phase spectra of voltage sensitivity with respect to H at $z = 0$ (example IV-B).

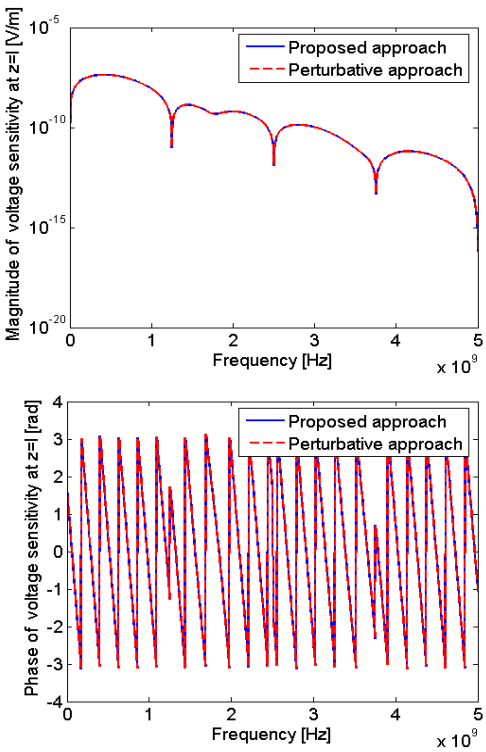

Fig. 8. Magnitude and phase spectra of voltage sensitivity with respect to H at $z = l$ (example IV-B).

sensitivity. Its implementation is straightforward and does not require any numerical processing. Two examples were presented showing the accuracy of the method compared to the perturbation technique.

REFERENCES

[1] C. R. Paul, *Analysis of Multiconductor Transmission Lines*, 2nd ed. New York, NY: John Wiley & Sons, 2008.

[2] R. Achar and M. Nakhla, "Simulation of high-speed interconnects," *Proceedings of the IEEE*, vol. 89, no. 5, pp. 693–728, May 2001.

[3] Q. Zhang, S. Lum, and M. Nakhla, "Minimization of delay and crosstalk in high-speed VLSI interconnects," *IEEE Transactions on Microwave Theory and Techniques*, vol. 40, pp. 1555–1563, 1992.

[4] L. J. Lions, *Optimal Control of Systems Governed by Partial Diffeential Equations*, S. K. Mitter, Ed., 1971.

[5] S. W. Director and R. A. Rohrer, "The generalized adjoint network and network sensitivities," *IEEE Transactions on Circuits and Systems*, vol. 16, pp. 318–323, Aug. 1969.

[6] Y. S. Chung, C. C. Cheon, I. H. Park, and S. Y. Hahn, "Optimal design method for microwave device using time domain method and design sensitivity analysis-Part II: FDTD case," *IEEE Transactions on Magnetics*, vol. 37, pp. 3255–3259, Sep. 2001.

[7] J. P. Webb, "Design sensitivity for scattering-matrix calculation with tetrahedral egde elements," *IEEE Transactions on Magnetics*, vol. 36, pp. 1043–1046, Jul. 2000.

[8] ——, "Design sensitivity using high-order tetrahedral vector elements," *IEEE Transactions on Magnetics*, vol. 37, pp. 3600–3603, Sep. 2001.

[9] ——, "Design sensitivity of frequency response in 3-D finite-element analysis of microwave devices," *IEEE Transactions on Magnetics*, vol. 35, pp. 1109–1112, Mar. 2002.

[10] N. K. Nikolova, J. W. Bandler, and M. H. Bakr, "Adjoint techniques for sensitivity analysis in high frequency structure CAD," *IEEE Transactions on Microwave Theory and Techniques*, vol. 52, no. 1, pp. 403–419, Jan. 2004.

[11] N. K. Nikolova and M. H. Bakr, "An adjoint variable method for time-domain transmission-line modeling with fixed structured grids," *IEEE Transactions on Microwave Theory and Techniques*, vol. 52, no. 2, pp. 554–559, Feb. 2004.

[12] E. A. Soliman, M. H. Bakr, and N. N. Nikolova, "An adjoint variable method for sensitivity calculations of multiport devices," *IEEE Transactions on Microwave Theory and Techniques*, vol. 52, no. 2, pp. 589–599, Feb. 2004.

[13] S. Ali, N. N. Nikolova, and M. H. Bakr, "Sensitivity analysis with full-wave electromagnetic solvers based on structured grids," *IEEE Transactions on Magnetics*, vol. 40, no. 3, pp. 1521–1530, May 2004.

[14] N. K. Nikolova, J. Zhu, D. Li, M. H. Bakr, and J. W. Bandler, "Sensitivity analysis of network parameters with electromagnetic frequency-domain simulators," *IEEE Transactions on Microwave Theory and Techniques*, vol. 54, no. 2, pp. 670–681, Feb. 2006.

[15] D. Deschrijver, B. Haegeman, and T. Dhaene, "Orthonormal vector fitting: a robust macromodeling tool for rational approximation of frequency domain responses," vol. 30, no. 2, pp. 216–225, May 2007.

[16] T. Dhaene and D. Deschrijver, "Generalised vector fitting algorithm for macromodeling of passive electronic components," *Electronics Lett.*, vol. 41, no. 6, pp. 299–300, Mar. 2005.

[17] P. Liu, Z.-F. Li, and G.-B. Han, "Application of asymptotic waveform evaluation to eigenmode expansion method for analysis of simultaneous switching noise in printed circuit boards (PCBs)," *IEEE Transactions on Electromagnetic Compatibility*, vol. 48, no. 3, pp. 485–492, Aug. 2006.

[18] J. Ureel and D. De Zutter, "A new method for obtaining the shape sensitivities of planar microstrip structures by a full-wave analysis," *IEEE Transactions on Microwave Theory and Techniques*, vol. 44, no. 2, pp. 249–260, Feb. 1996.

[19] G. Antonini, "A dyadic Green's function based method for the transient analysis of lossy and dispersive multiconductor transmission lines," *IEEE Transactions on Microwave Theory and Techniques*, vol. 56, no. 4, pp. 880–895, Apr. 2008.

[20] G. W. Hanson and A. B. Yakovlev, *Operator Theory for Electromagnetics*. Springer, 2002.

[21] J. V. Bladel, *Singular Electromagnetic Fields and Sources*. Oxford, Clarendon Press, 1991.

[22] F. Güneş, N. T. Tokan, and F. Gürgen, "Support vector design of the microstrip lines," *International Journal of RF and Microwave Computer-Aided Engineering*, pp. 326–336, 2007.

Giulio Antonini (M'94, SM'05) received his Laurea degree (summa cum laude) in Electrical Engineering in 1994 from the Università degli Studi dell'Aquila and the Ph.D. degree in Electrical Engineering in 1998 from University of Rome "La Sapienza". Since 1998 he has been with the *UAq EMC Laboratory*, Department of Electrical Engineering of the University of L'Aquila where he is currently Associate Professor. His research interests focus on EMC analysis, numerical modeling and in the field of signal integrity for high-speed digital systems. He has authored or co-authored more than 170 technical papers and 2 book chapters. Furthermore, he has given keynote lectures and chaired several special sessions at international conferences. He has been the recipient of the IEEE Transactions on Electromagnetic Compatibility Best Paper Award in 1997, the CST University Publication Award in 2004, the IBM Shared University Research Award in 2004, 2005 and 2006, the IET-SMT Best Paper Award in 2008. In 2006 he has received a Technical Achievement Award from the IEEE EMC Society "for innovative contributions to computational electromagnetic on the Partial Element Equivalent Circuit (PEEC) technique for EMC applications". He holds one European Patent.

Prof. Antonini is vice-chairman of the dell'IEEE EMC Italy Chapter, he is member of the TC-9 committee of the IEEE EMC Society and vice-chairman of the TC-10 Committee of the same IEEE Society. He serves as member of the Editorial Board of IET Science, Measurements and Technology. He serves as reviewer in a number of international journals.

Luca De Camillis Luca De Camillis was born in Teramo, Italy, in September 1982. He received the Laurea degree in Computer Science Engineering from the University of L'Aquila in 2007. He is currently a research scientist at the ACE Laboratory of the University of Washington, Seattle. His research interests are in the field of macromodeling technique and sensitivity applied to the high speed digital boards.

Fabrizio Ruscitti was born in L'Aquila, Italy in 1982. He received the Laurea degree in Electronic Engineering from the University of L'Aquila in 2008. He is currently a research scientist at the EMC Laboratory of the University of L'Aquila.

Relationship Between the Path Loss Exponent and the Room Absorption for Line-of-Sight Communication

[1] C. W. Trueman, [1, 2] D. Davis, and [2] B. Segal

[1] Department of Electrical and Computer Engineering, Concordia University, Montreal, Canada
trueman@ece.concordia.ca, megadon_emc@yahoo.com

[2] McGill University and SMBD Jewish General Hospital, Montreal, Canada
b_segal@sympatico.ca

Abstract – In indoor propagation, the log-distance path loss model represents the received power as declining with distance from the transmitter according to $1/r^n$, where r is the straight-line distance from the transmitter to the receiver. Previously, the value of the path loss exponent n has been derived from measured received signal strengths at a specific site. In this paper, the value of n is estimated from the geometry of the room and the electrical properties of the walls. Using the Sabine model, these determine the room absorption and hence the received power as a function of distance from the transmitter. Then, a least-square-error curve fit of the log-distance path loss model to the Sabine model determines the value of n. The electric field strength in a typical rectangular room is compared using ray tracing, the Sabine model, and the path loss model. Then the value of the path loss exponent is presented as a function of the power absorption coefficient of the walls, floor and ceiling of the room, for a typical ceiling height. Evaluating n from analytic information rather than from measurement enhances the usefulness of the path loss model in simulations of the coverage of antennas for the design of wireless local area network installations at specific sites.

I. INTRODUTION

In indoor propagation, communication must be established between a transmitter and a receiver located inside a building [1-3]. For a fixed transmitter position and a roaming receiver, the signal strength of the transmitter must be sufficiently large; the delay spread of the multipath components sufficiently small; and the interference from other transmitters operating on the same frequency sufficiently small. Designing the location of access-point antennas for a wireless local area network would benefit from a simple method for an approximate assessment of the field strength of each antenna throughout the whole floor plan.

The "log-distance path loss model" [1, 3, 4, 5] represents the received power in an indoor environment as declining with distance according to,

$$P(r) = \frac{P_0}{r^n} \tag{1}$$

where n is the "path loss exponent" [6] or "slope index" [4], r is the distance between the transmitter and the receiver, and P_O is the received power at a one-meter distance. The value of n depends on the construction of the walls of the room and on other factors. The path loss model is applied to both line-of-sight (LOS) and non-line-of-sight (NLOS) scenarios. If the ray from the source to the observer passes through a wall, the power can be reduced by a "wall attenuation factor", which is often approximated as a fixed number of dB independent of the incidence angle or polarization. This model is empirical, with the value of n determined from measured received powers. Values of the path loss exponent n are cited from the literature for various environments in [1]. Values of n from 1.6 to 2.1 for factory environments were given in [5], where there was a LOS path from the transmitter to the receiver. Where the LOS path is obstructed by partitions or by furnishings, values of n greater than two were used, and the field strength decreased more quickly with distance r than it would in free space. Some authors use free-space propagation ($n = 2$) closer to the antenna than a "break point" distance, and the log-distance path loss model for larger distances [6]. The break point distance depends on the size of the first Fresnel zone [4, 5] compared to the position of obstacles in the room that obstruct the direct path from the transmitter to the observer. The log-distance path loss model is site specific in that the power associated with a ray passing through a wall is reduced by a wall attenuation factor, but otherwise the floor plan information is not used.

Site-specific predictions of the electric field strength throughout a floor plan are often made using ray tracing [4,7]. Ray paths are identified joining the transmitter to the location of the receiver, accounting for specular reflection from walls, and transmission through walls. The "vector sum method" [2] adds the field strengths of the rays accounting for phase and vector direction. The rapid variations of this "local" field strength as the position of the observer changes are called "fast fading". To assess coverage, it is sufficient to estimate the local mean power, obtained by averaging the received power along a path of length 5 to 40 wavelengths [3]. Averaging removes the rapid variations of fast fading and leaves the slow changes due to attenuation with distance and shadowing, called "slow fading". Evaluating the fast fading at closely-spaced points followed by explicit averaging is computationally expensive. However, the local mean power can be estimated by ray tracing by the "power sum method" [3], which combines the field strengths of the rays on an energy basis. Since the local mean power varies slowly with position, much more widely spaced points can be used, and so the computation is much faster.

The Sabine method is less well known, and is based on Sabine's method in acoustics extended to electromagnetics. The Sabine method characterizes the room by its "room absorption", which is calculated from the angle-averaged power absorption coefficient of each surface of the room [8] and the area of the surface. "Live" rooms with low power absorption use Sabine's formula for the room absorption, but when the absorption is high the room is said to be "dead" and Eyring's formula is used [9,10]. To predict the decline in the received field strength as a function of distance from the source, the field is split into the "direct" field strength, which is the field of the source in free space, and the "indirect" field strength or "multipath" field strength, which is the contribution of the room [11, 12]. The local mean power is obtained by adding the power in the direct field and in the indirect field. The calculation of the local mean power by the Sabine method is simple enough to be done with pencil and paper. The Sabine method is readily extended to complex floor plans [11] and because it is computationally inexpensive, it is useful for assessing the field strength of many sources transmitting at various locations throughout a complex floor plan.

To the authors' knowledge, the value of the path loss exponent n has not been explicitly related to the geometry of the room and to the construction of the walls. This paper will derive the value of n in rooms where there is a LOS path between the transmitter and the receiver. The value of n will be determined from the geometry of the room and the average power absorption coefficients of the various room surfaces. The room properties will determine the Sabine room absorption, which in turn will be used to find the local mean power as a function of distance from the transmitter. Then least squares approximation will be used to curve-fit the log-distance path loss model to the local mean strength, to determine the value of n. The method will be illustrated for a small rectangular room. Electric field strengths using the log-distance path loss model will be compared with fields found by ray tracing using the "power sum method", and using the Sabine method. Then the value of n will be graphed for a square room as a function of the power absorption coefficient of the walls for various room areas from small to large.

II. THE SABINE METHOD

The Sabine method [12] divides the electric field strength into the direct field E_d, which is the field of the transmitter in free space, the and the multi-path field, E_m, which is the net field strength due to rays which reflect and re-reflect from the surfaces of the room. The power received by an antenna of effective area equal to unity and operating into a matched load is,

$$P_s(r) = \frac{1}{\eta}\left(E_d^2(r) + E_m^2\right) \quad \text{watts,} \tag{2}$$

where η is the intrinsic impedance of space and r is the separation distance. Assuming that there is an unobstructed path between the transmitter and the receiver, that is, that the first Fresnel zone is clear of furnishing and clutter [4, 13], the direct field is given by,

$$E_d(r) = \sqrt{\frac{\eta D P_t}{4\pi r^2}} \quad \text{volts/meter} \tag{3}$$

where D is the directive gain of the transmitter, and P_t is the transmitted power. The Sabine method gives the local mean value of the multipath field as [12],

$$\widetilde{E}_m = \sqrt{\frac{4\eta P_t}{A_{in}}} \quad \text{volts/meter} \tag{4}$$

where the tilde indicates the local area average. The "indirect" room absorption [12] is,

$$A_{in} = \frac{A S_T}{S_T - A} \tag{5}$$

where S_T is the total area of the surfaces of the room, and where the room is characterized by the Sabine room absorption, given by,

$$A = \sum_{k=1}^{N} S_k \widetilde{\alpha}_k \ . \tag{6}$$

The room has N surfaces, the area of the k^{th} surface is S_k, and $\widetilde{\alpha}_k$ is the angle- and polarization-averaged power absorption coefficient [8, 12]. If the walls of the room are modelled as uniform layered structures, the power absorption coefficient is readily evaluated. If the surfaces of the room are highly absorbing, then the room might be classified as "dead" or in the "non-reverberated regime" in the terminology used in [10], and the Eyring formula can be used to calculate the room absorption according to,

$$A_E = S_T \ln\left(\frac{1}{1-\alpha}\right) \tag{7}$$

where $\alpha = A/S_T$. The Eyring indirect absorption is given by,

$$A_{E,in} = \frac{S_T}{1-\alpha}\ln\left(\frac{1}{1-\alpha}\right). \tag{8}$$

Thus the Sabine model consists of either using equations (5) or (8) to calculate the indirect room absorption, then equation (4) for the multipath field strength, which is by definition constant throughout the room, and equation (3) for the direct field, which varies with distance from the transmitter. Then equation (2) is used to find the received power. Note that functional form of the decline in received power with distance is contained in the direct field term and is different from that of the log-distance path loss model of equation (1).

III. EVALUATING THE PATH LOSS EXPONENT

The Sabine model relates the decline in field strength with distance from the transmitter to the geometry of the room, to the room construction, and to the electrical properties of the room surfaces thorough the average power absorption coefficients. Consider a path running radially away from the transmitter from distance r_a to distance r_b. The value of the path loss exponent will be found by minimizing the mean square error in decibels between the path loss model (1) and the Sabine model (2). The square of the mean square error is given by,

$$e^2 = \frac{1}{r_b - r_a}\int_{r_a}^{r_b}\left(\ln\left(\frac{P_0}{r^n}\right) - \ln\left(P_s(r)\right)\right)^2 dr\,. \tag{9}$$

To minimize the error, choose n such that $\frac{\partial}{\partial n}\left(e^2\right) = 0$ to obtain,

$$n = \frac{1}{\int_{r_a}^{r_b}\ln^2(r)dr}\begin{bmatrix}\ln(P_0)\int_{r_a}^{r_b}\ln(r)dr \\ -\int_{r_a}^{r_b}\ln(r)\ln(P_s(r))dr\end{bmatrix}. \tag{10}$$

Equation (10) is readily evaluated as follows. Parameter P_0 is the power at r=1 m from the antenna in free space and using equation (3), $P_0 = DP_t/(4\pi)$ W. The integrals in equation (10) can be approximated with the rectangular rule. Thus choose a set of evenly-spaced distances $\{r_k : k = 1,...,N\}$ over the interval r_a to r_b with $\Delta = (r_b - r_a)/(N-1)$ and use equation (2) to compute the received power at each distance $\{P_{sk} = P_s(r_k)\}$. Then,

$$n \approx \frac{1}{\Delta\sum_k \ln^2(r_k)}\begin{bmatrix}\ln(P_0)\Delta\sum_k \ln(r_k) \\ -\Delta\sum_k \ln(r_k)\ln(P_{Sk})\end{bmatrix}. \tag{11}$$

Equation (11) is readily evaluated with a short computer program. Note that the received powers $\{P_{sk} = P_s(r_k)\}$ could also be computed from ray-tracing field strengths using the "power sum method".

In the Sabine model, the received power of equation (2) is always greater than that of the transmitter in free space, because it is enhanced by the multipath field given by equation (4). Hence, the value of the path loss exponent computed with equation (11) will always be less than two. As the average power absorption coefficient α approaches unity, the room absorption approaches the surface area of the room, $A \to S_T$, and the indirect absorption becomes large, $A_{in} \to \infty$. Then the multipath field $\widetilde{E}_m$ becomes small, and the signal strength approaches that of free space, from above. The value of n given by equation (11) approaches the free space value of two.

IV. FIELD STRENGTH IN A RECTANGULAR ROOM

This section compares the field strength found using the log-distance path loss model (1) with the field strength from the Sabine model and from the ray-tracing model. The value of the path loss exponent n is obtained using equation (11).

Figure 1 is a plan of a rectangular room, 6.83 m wide by 8.68 m deep, with a ceiling height of $h = 3.75$ m. The transmitter was a vertical, half-wave dipole radiating 100 mW at 2388 MHz, with directivity $D = 1.64$, centered

1.03 m above the floor. The receiver was moved along the path shown in the figure, starting at r_a=1 m from the antenna and ending at r_b = 4.8 m away, and was 1.07 m above the floor. The walls of the rectangular room were modelled as layered structures with 1.5 cm of concrete (ε_r=5.37, σ=149.5 mS/m), 0.8 cm of brick (ε_r=4.38, σ=18.5 mS/m), a center air layer 7.8 cm thick, and symmetric layers of brick and concrete. The angle- and polarization-averaged power absorption coefficient at 2388 MHz was $\tilde{\alpha} = 0.65$. The floor and ceiling were modelled as concrete slabs of thickness 30 cm, and average power absorption coefficient of 0.79. One wall of the room had a row of metal lockers, 3.48 m from the path, as shown in Fig. 1, with a power absorption coefficient of zero. In the ray-tracing simulation, ray paths with up to 32 reflections were calculated. Field strengths were measured in this room, and [12] reports reasonable agreement with the Sabine model using equation (5) and with the ray-tracing model.

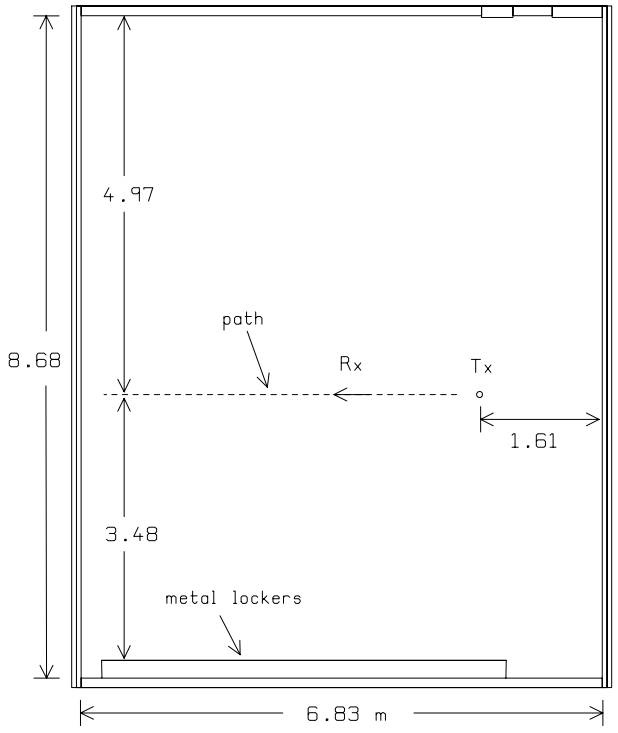

Fig. 1. Plan of the rectangular room.

To use the Sabine model, the area of the room surfaces was calculated to be $S_T = 239$ m^2, and the Sabine room absorption was $A = 166$ m^2, hence the average power absorption coefficient for the room was $\alpha = A/S_T = 0.69$. This was high enough that the room might classified as "dead", in which case the Eyring model for the absorption might be used. The Eyring value for the room absorption was $A_E = 284$ m^2. The Sabine indirect absorption of equation (5) was $A_{in} = 543$ m^2, and the Eyring indirect absorption of equation (8) was $A_{E,in} = 903$ m^2. These values were used with equation (3) to calculate the multipath field strength, which was smaller by a factor of about 0.78 when the Eyring model was used.

Figure 2 shows the electric field strength as a function of separation distance from the transmitter along the path shown in Fig. 1. The ray-tracing method was used to find the local mean field strength (solid curve) by the "power sum method" [3]. The Sabine approximation (dashed curve with crosses) using the Sabine room absorption agreed closely with the ray-tracing curve. When the Eyring room absorption was used (long-dashed curve) the field strength was too small in comparison to the ray-tracing value. Thus, although the room might be classified as "dead", the Sabine absorption led to better agreement with the ray tracing model than did the Eyring absorption.

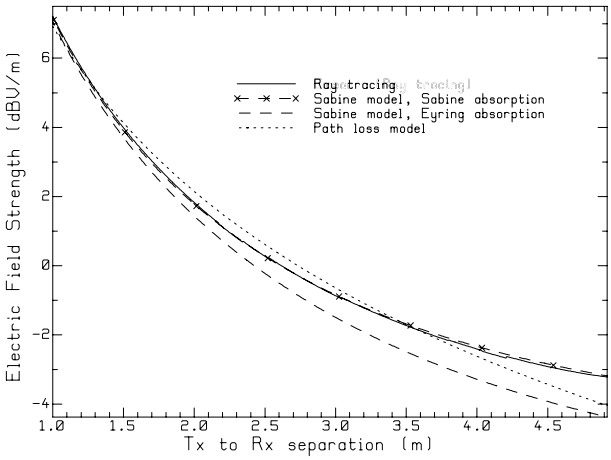

Fig. 2. Electric field strength as a function of distance from the antenna in the rectangular room.

The path loss exponent of $n = 1.58$ was found by evaluating equation (11) using received powers along the path computed with equation (2) using the Sabine absorption. The electric field strength associated with the path loss model is given by,

$$E(r) = \frac{E_0}{r^{n/2}}, \tag{12}$$

where $E_0 = \sqrt{\eta D P_t/(4\pi)}$ is the field strength at one-meter distance from the transmitter. Figure 2 compares the field strength from the path loss model (dotted curve), from ray tracing (solid curve), and from the Sabine method (dashed curve with crosses). Choosing n with equation (11) leads to a best-fit approximation of the

Sabine model by the path loss model. The field strength of the path loss model was too large between 1 and 3.5 m distance, but the error is small. Towards the end of the path, the field strength of the path loss model decreased too quickly with distance, with a 0.8 dB error at the end of the path.

Figure 2 showed that the Sabine absorption led to a better approximation of the ray-tracing mean value than did the Eyring absorption, so in the following the Sabine absorption will be used to demonstrate the dependence of the path loss exponent on the power absorption coefficient of the room surfaces and the room geometry.

V. PATH LOSS EXPONENT IN A TYPICAL ROOM

Figure 3 shows the variation of the path loss exponent n with the floor area of a square room and with the average power absorption coefficient of the room surfaces, for a square room of ceiling height h=2.75 m. The room had side length w, floor area $S_F = w^2$, and surface area $S_T = 2w^2 + 4wh$. The average power absorption coefficient of the surfaces of the room was α, the Sabine absorption was $A = \alpha S_T$ and the indirect absorption was $A_{in} = \alpha S_T / (1-\alpha)$. To evaluate n, a vertical dipole of directivity $D = 1.64$, radiating P_t watts, was used. The received power was calculated on a path starting at distance $r_a = 1$ m from the dipole and ending at distance $r_b = \sqrt{2}w - 1$ m. Given the value for the average power absorption coefficient α, equation (2) was used to compute a set of received power values at intervals of $\Delta = 1$ cm from r_a to r_b, and then equation (11) was used to compute the path loss exponent. The calculation was repeated as the power absorption coefficient α varied from 0.01 to 0.99, and as floor area varied from $S_F = 10$ m^2 (e.g., an office) to $S_F = 400$ m^2 (e.g. a large auditorium).

These calculations show that at a given absorption, the path loss exponent increases with room size. Thus for absorption $\alpha = 0.5$, an office of area 10 m^2 would have a path loss exponent of $n = 0.69$, a mid-sized room of area 50 m^2 would have $n = 1.13$, and an open-plan office of area 200 m^2 would have $n = 1.32$. For small rooms and low power absorption coefficients, the multipath field strength of equation (4) dominated the direct field over most of the area of the room, and the received power of equation (2) was almost constant with distance. Thus it was not possible to calculate a path loss exponent. For example, for an office of area 10 m^2 with power absorption coefficient less than 0.3, no path loss exponent could be evaluated. For a power absorption coefficient greater than 0.3, the path loss exponent increased rapidly with absorption. As the room got larger, the minimum absorption for which a path loss exponent could be found decreased. Thus for a room of floor area 50 m^2, the path loss exponent increased from zero starting at absorption $\alpha = 0.1$. For all rooms, as the power absorption coefficient approached unity, corresponding to perfectly-absorbing or "free space" walls, the path loss exponent approached $n = 2$, corresponding to free space propagation.

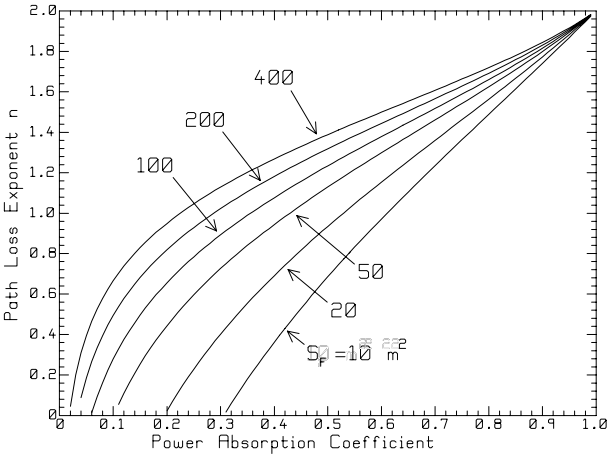

Fig. 3. Path loss exponent as a function of power absorption coefficient and floor area in a square room.

The rectangular room of Fig. 1 had surface area $S_T = 239$ m^2 and average power absorption coefficient α =0.69. Using Fig. 3, the value of n is between 1.5 and 1.55, which is close to the value of 1.58 found above for the rectangular room. Note that the ceiling height of the rectangular room was 3.75 m, considerably higher than the ceiling height of 2.75 m used to draw Fig. 3.

Table 4.6 in [5] gave values of $n = 1.6$ and 1.8 for a metal-working factory and a paper/cereals factory respectively, both with a LOS path. However, no floor area or ceiling height was given, nor an indication of the wall construction. Assuming a power absorption coefficient of $\alpha = 0.7$, typical of many wall constructions, Fig. 3 shows that for a 200 m^2 area, $n = 1.57$; for 400 m^2, $n = 1.61$, these values being not greatly different from those in [5]. A larger floor area would lead to a larger value of n.

VI. CONCLUSION

The log-distance path loss model (1) is often used to approximate the received power as a function of distance from a transmitter, using values of the path loss exponent n based on measurements in an indoor environment when there is a line-of-sight path from the transmitter to the receiver. This paper showed how to derive the value

of n from the geometry of the room, and from the electrical properties and construction of the walls, floor and ceiling.

Figure 2 demonstrated that in a mid-sized rectangular room, field strengths from the Sabine model and from a ray-tracing model agreed closely. The value of n was derived from the Sabine field strengths, and then the field strength of the path loss model were close to the Sabine values.

Figure 3 showed the behavior of the path loss exponent as a function of the floor area of a square room and of the power absorption coefficient of the walls. For very low absorption, the path loss model was not useful. For higher absorption, the path loss exponent increased rapidly and approached $n = 2$ as the absorption coefficient of the walls approached unity, making the walls perfectly absorbing. Figure 3 can be used to estimate the path loss exponent and hence the received power when there is an unobstructed LOS path in an indoor environment, from a knowledge of the wall materials and construction of the room dimensions, and should be useful in the design wireless local area networks.

ACKNOWLEDGEMENT

The authors gratefully acknowledge the support of PROMPT, Nortel, Bell Canada, FQRNT, and the National Science and Engineering Research Council of Canada.

REFERENCES

[1] H. Hashemi, "The indoor propagation channel," *Proc. IEEE*, vol. 81, no. 7, pp. 943-968, July 1993.

[2] R. A. Valenzuela, O. Landron, and D. L. Jacobs, "Estimating local mean signal strength of indoor multipath propagation," *IEEE Trans. on Vehicular Technology*, vol. 46, no. 1, pp. 203- 212, Feb. 1997.

[3] R. A. Valenzuela, O. Landron, and D. L. Jacobs, "Estimating local mean signal strength of indoor multipath propagation," *IEEE Trans. on Veh. Tech* , vol. 46, no. 1, pp. 203-212, Feb. 1997.

[4] H. Bertoni, W. Honcharenko, L. R. Maciel, and H. H. Xia, "UHF propagation prediction for wireless personal communications," *Proc. IEEE*, vol. 82, no. 9, pp. 1333-1359, Sept. 1994.

[5] T. S. Rappaport, *Wireless Communications Principles and Practice,* 2nd edition. New Jersey: Prentice Hall PRT, 2002.

[6] K. W. Cheung, J. H. M. Sau, and R. D. Murch, "A new empirical model for indoor propagation prediction," *IEEE Trans. on Veh. Tech.,* vol. 47, no. 3, pp. 996-1001, Aug. 1998.

[7] D. Lee, M. J. Neve, and K. W. Sowerby, "The impact of structural shielding on the performance of wireless systems in a single floor office building," *IEEE Trans. on Wireless Comm.,* vol. 6, no. 5, pp. 1787-1795, May 2007.

[8] D. A. Hill, "A reflection coefficient derivation for the Q of a reverberation chamber," *IEEE Trans. on EMC,* vol. 38, no. 4, pp. 591-592, Nov. 1992.

[9] C. L. Holloway, D. A. Hill, J. M. Ladbury, and G. Koepke, "Requirements for an effective reverberation chamber: loaded or unloaded," *IEEE Trans. on EMC* , vol. 48, no. 1, pp. 187-194, Feb. 2006.

[10] C. L. Holloway, M. G. Cotton, and P. McKenna, "A model for predicting the power delay profile characteristics in a room," *IEEE Trans. on Veh. Tech.,* vol. 48, no. 4, pp. 1110-1120, July 1999.

[11] C. W. Trueman, S. S. Muhlen, D. Davis, and B. Segal, "Field strength estimation in indoor propagation by the Sabine method," in *Proceedings of the 24th Annual Review of Progress in Applied Computational Electromagnetics.* Niagara Falls, Ontario, Canada: ACES 2008, pp. 876-881.

[12] C. W. Trueman, D. Davis, B. Segal, and W. Muneer, "Validation of fast site-specific mean-value models for indoor propagation," to be published in the Applied Computational Electromagnetics Society Journal, April 2009.

[13] J. B. Andersen, J. O. Nielsen, G. F. Pedersen, G. Bauch, and M. Herdin, "Room electromagnetics," *IEEE Ant. and Prop. Mag*. vol. 49, no. 2, pp. 27-33, April 2007.

Christopher W. Trueman received his Ph.D. from McGill University in 1979. He has applied the methods of computational electromagnetics to problems such as aircraft antenna performance, antenna-to-antenna coupling and EMC on aircraft, aircraft and ship radar cross-section at HF frequencies, suppression of scattering of the signal of a commercial radio station from power lines, dielectric resonators, unconditionally-stable formulations for the finite-difference time-domain method, and the fields of portable radios such as cellular phones held against the head. Recently, his research has investigated the radar cross-section of ships at VHF frequencies, composite materials for aircraft, indoor propagation, and EMC issues between portable radios and medical equipment. Dr. Trueman is currently the Associate Dean for Academic Affairs in the Faculty of Engineering and Computer Science at Concordia University.

Donald P. Davis received the B.Eng in electrical engineering degree from Concordia University in 1991, the MaSc. degree in electrical engineering from Concordia University in 1994 and the PhD. Degree in electrical engineering from McGill University 2004. Since 1995 he has been a sessional instructor teaching both graduate and undergraduate engineering courses at Concordia University. In 2006 he joined the Jewish General Hospital of Montreal as a post-doctoral researcher studying electromagnetic compatibility of medical equipment due to the presence of wireless communication systems. His research interests include indoor radio wave propagation measurement and modeling, electromagnetic interference estimation and safe implementation of wireless communication systems within clinical environments.

Bernard Segal is a highly-inter-disciplinary Research Engineer (Electrical Engineering, with a Master's in Electrical (Biomedical) Engineering and a PhD in Neurophysiology, all from McGill University). He is an Associate Professor in the Ear-Nose-Throat (ENT) Department of McGill University, with appointments in Biomedical Engineering and in Physiology. He is the Director of Research in ENT at McGill, and at the SMBD-Jewish General Hospital. He is the Director of Graduate Studies in ENT at McGill. He has contributed to many medical-EMC standards, EMC-healthcare policies, and EMC-healthcare recommendations. He has organized over thirty national and international conferences, workshops and teaching sessions on EMC in Healthcare. His current research is directed towards clarifying the nature of electromagnetic-interference risk in hospitals, towards minimising this risk, and towards evaluating how to best use wireless informatics in health care safely.

Optimum Cell Size for High Order Singular Basis Functions At Geometric Corners

[1]M. M. Bibby, [1]A. F. Peterson, and [2]C. M. Coldwell

[1]School of ECE, Georgia Institute of Technology, Atlanta, GA 30332,
mbibby@ece.gatech.edu, peterson@ece.gatech.edu

[2]Red Hat Inc., 10 Technology Park Drive, Westford, MA 01886,
coldwell@frank.harvard.edu

Abstract – Both low-order and high-order singular basis functions have been previously proposed for modeling edge singularities in the current and charge densities at geometric corners in electromagnetic integral equation formulations. This paper attempts to identify an optimum dimension for the cells adjacent to corners, as a function of the polynomial degree of the representation used away from the corner cells. The residual error obtained via the solution of an over-determined system of equations is used to judge the relative accuracy of various approaches.

Keywords: boundary element method, corner singularity, edge condition, high order basis functions, method of moments, over-determined systems, residual error, singular basis functions.

I. INTRODUCTION

For several decades, most numerical procedures for solving the integral equations for electromagnetic field problems have been based on low-order methods, where the representation of the primary unknown is in terms of constant or linear polynomials, and the convergence rates are often no faster than $O(h^2)$, where h is the characteristic cell dimension associated with the numerical model. Higher order methods have been shown to provide a better trade-off between high accuracy and improved computational efficiency than low-order methods. However, many practical structures contain corners or edges, where the charge density or current density may exhibit a singularity. In the absence of an explicit attempt to incorporate the actual singularity into the representation for the unknown quantity, the accuracy improvements offered by high order basis functions are negated. A number of authors have proposed singular basis functions [1-5], including the possibility of incorporating multiple singular terms to provide high order behavior [6-7].

Reference [7] proposed a methodology for high order modeling of edge singularities in two-dimensional problems. In cells not adjacent to corners or edges, a complete polynomial representation was employed up to order q, or degree q–1. In cells adjacent to corners, this representation was augmented with approximately $(q+1)/2$ additional, singular terms. The singular terms were obtained from the asymptotic series for the current density near the tip of the appropriate infinite wedge [8]. However, the work reported in reference [7] only considered the case where the cells adjacent to the corners were of the same dimension as the other cells used throughout the model.

In the following, the investigation of [7] is extended to consider the relative cell size of the corner cells, in an attempt to optimize the overall computational efficiency. The number of additional singular terms used in the corner cells and the corner cell dimension are permitted to vary, while local and global error levels are monitored. Results show that the accuracy in the corner cells improves as additional singular terms are included, and as the corner cell dimension is reduced. However, if the corner cell dimension is made too small, the accuracy degrades in the cell adjacent to the corner cell. Until this limit is reached, an optimum balance between the error in the corner cells and the non-corner cells is achieved when the number of singular terms is approximately equal to q and the corner cell size is roughly twice that of the non-corner cells.

II. SINGULAR BASIS FUNCTIONS FOR CORNER CELLS

A solution for the surface current density on an infinite wedge is developed in [8]. Based on those results, a general asymptotic expression for the current density as a function of ρ on the face of the wedge, near the tip ($\rho = 0$), can be written for the transverse magnetic (TM)-to-z case as,

$$J_z : \sum_{m=0}^{\infty}\sum_{n=1}^{\infty} c_{mn}\rho^{2m+\upsilon_n-1} \tag{1}$$

where a cylindrical coordinate system (ρ, ϕ, z) is employed in equation (1),

$$\upsilon_n = \frac{n\pi}{(2\pi - \alpha)}, \quad n = 1,\ 2,\ 3,\ \ldots \tag{2}$$

A similar expression for the transverse electric (TE)-to-*z* case is,

$$J_\rho : \sum_{m=0}^{\infty}\sum_{n=0}^{\infty} d_{mn}\rho^{2m+\upsilon_n} \tag{3}$$

where υ_n is defined as,

$$\upsilon_n = \frac{n\pi}{(2\pi - \alpha)}, \quad n = 0,\ 1,\ 2,\ \ldots \tag{4}$$

Reference [7] proposed a hierarchical family of basis functions for use in cells adjacent to geometric corners. For cells that are not adjacent to a corner of the contour, a Legendre expansion of order q is employed. In the corner cells, the same representation is augmented by including some number of terms with non-integer exponents from equation (1) or equation (3).

As an illustration, consider the representation used in the cell adjacent to a 90 degree corner. The exponents arising from the expansion in equation (1) can be arranged in a sequence,

$$\left\{-\frac{1}{3},\ \frac{1}{3},\ 1,\ \frac{5}{3},\ \frac{7}{3},\ 3,\ \frac{11}{3},\ \ldots\right\}$$

Table 1 illustrates the specific exponents that would be included in an "order q" representation for two different approaches. In the first, $[(q+1)/2]$ singular terms are included in the expansion, where the square brackets denote the greatest integer. In the second approach, q singular terms are incorporated. In either case orthogonal hierarchical basis functions are constructed from the set of exponents in Table 1, using a Gram-Schmidt procedure as described in [7]. For the case of $q = 3$, and $N_{sing} = [(q+1)/2]$, the representation at a 90° corner involves 5 basis functions, constructed from terms of the form,

$$\left\{u^{-1/3},\ 1,\ u^{1/3},\ u,\ u^2\right\}$$

As another example, the expansion functions for a 60° corner were previously given in [7].

While [7] concluded that approximately $(q+1)/2$ singular terms were required in corner cells to produce higher order behavior and accuracy comparable to that in non-corner cells, that conclusion was limited to the case where the corner cells were the same size as the non-corner cells. In the present investigation, the optimum number of singular terms is considered as the corner cell dimensions are varied relative to the non-corner cells.

Table 1. Exponents used in the representation for TM current density in the case of a 90 degree angle, as a function of the order q and the parameter N_{sing}.

q	Regular exponents	Singular exponents when $N_{sing} = [(q+1)/2]$	Singular exponents when $N_{sing} = q$
1	0	–1/3	–1/3
2	0, 1	–1/3	–1/3, 1/3
3	0, 1, 2	–1/3, 1/3	–1/3, 1/3, 5/3
4	0, 1, 2, 3	–1/3, 1/3	–1/3, 1/3, 5/3, 7/3

III. DEFINITIONS

A specific representation of the surface current density will involve some number of unknown coefficients that must be determined. We refer to that as the number of *degrees of freedom* (DoF) in the expansion. As indicated above, non-corner cells will employ an expansion of order q, meaning q degrees of freedom per cell. Corner cells will employ N_{sing} additional terms, for a total of $(q + N_{sing})$ degrees of freedom per cell. Our expansions do not straddle adjacent cells or impose cell-to-cell continuity.

Numerical results will be obtained using the electric-field integral equation (EFIE) and the magnetic field integral equation (MFIE). These equations and the method of moments numerical solution procedure are described in [9]. For the present investigation, a weighted point-matching procedure is used to enforce the integral equations. The procedure uses an over-determined system of equations obtained by employing twice as many testing points within each cell ($m = 2$) as there are unknowns to be determined in that cell. Thus, a cell with q expansion functions produces mq equations. The equations are obtained at nodes of a Gauss-Legendre quadrature rule and weighted by the square root of quadrature weights, and the resulting numerical solution minimizes the integrated square error of the residual on the scatterer surface [10-11]. The primary motivation for the use of an over-determined system is that, as a byproduct of the least-square solution algorithm, we obtain the local residual error at each test point. The residual error associated with the integral equation is used to assess the relative accuracy of each numerical result.

The residual error is scaled by the excitation to produce the normalized residual error (*NRE*). For instance, the *NRE* is expressed for the TM-to-*z* EFIE on a perfectly conducting scatterer as,

$$NRE = \frac{\sqrt{\int \left|E_z^{inc} - E_z^s\right|^2 dt}}{\sqrt{\int \left|E_z^{inc}\right|^2 dt}} \cong \frac{\sqrt{\sum_{i=1}^{N_{tp}} w_i \left|E_z^{inc}(t_i) - E_z^s(t_i)\right|^2}}{\sqrt{\sum_{i=1}^{N_{tp}} w_i \left|E_z^{inc}(t_i)\right|^2}} \tag{5}$$

where $\{t_i\}$ and $\{w_i\}$ denote Gauss-Legendre quadrature nodes and weights. N_{tp} is the total number of points included in the measure. To provide a local error estimate, equation (5) is computed for each cell with N_{tp} equal to the number of test points within that cell. The number of test points in a corner cell is usually different from the number of test points in cells not adjacent to a corner. To obtain a global error estimate, equation (5) is computed for the entire problem domain with $N_{tp} = m(\text{DoF})$. For the other integral equations considered, equation (5) is modified in an obvious way to implement the appropriate residual.

The rate at which the global *NRE* decreases as a function of cell size or number of unknowns can be used to judge the extent to which high order behavior is exhibited by the results. Consider two results, the first yielding NRE_1 with N_1 unknowns, and the second exhibiting NRE_2 with N_2 unknowns. The incremental slope of the associated error curve may be obtained from successive results using [12],

$$Slope_q = \frac{\log_{10}(NRE_2) - \log_{10}(NRE_1)}{\log_{10}(N_2) - \log_{10}(N_1)} \qquad (6)$$

where the subscript serves as a reminder that the principal expansions are of order q. For smooth scatterers, values of equation (6) often approximate integers as N increases.

The *edge cell size ratio* (ECSR) will be used to denote the ratio of the dimension of the corner cells to that of the non-corner cells. In the following, all non-corner cells will be maintained at a common dimension, while all corner cells are scaled from that dimension by the factor ECSR.

IV. RESULTS FOR ECSR = 1

In a previous work by the authors with high order representations [12], circular cylinders were considered since they offer exact analytical solutions. To establish a baseline for reference, Figs. 1(a) and 1(b) show the global *NRE* and $Slope_q$ versus the degrees of freedom for a circular cylinder of 12 λ circumference, where λ is the wavelength. These plots illustrate uniform *h*-refinement (shrinking all the cells in unison for a fixed degree representation). These data were obtained from a solution of the MFIE for the TM polarization, using Legendre polynomial representations for the current density, and models employing equal-sized curved cells.

The data in Fig. 1 clearly exhibit higher order behavior, and the $Slope_q$ values approximate integers as the discretizations are refined. A general goal of higher-order representations for problems with edges or corners is to achieve similar behavior. Figures 2(a) and 2(b) show plots of the global *NRE* and $Slope_q$ versus the degrees of freedom for a cylinder of triangular cross section shape, and a total periphery of 12 λ.

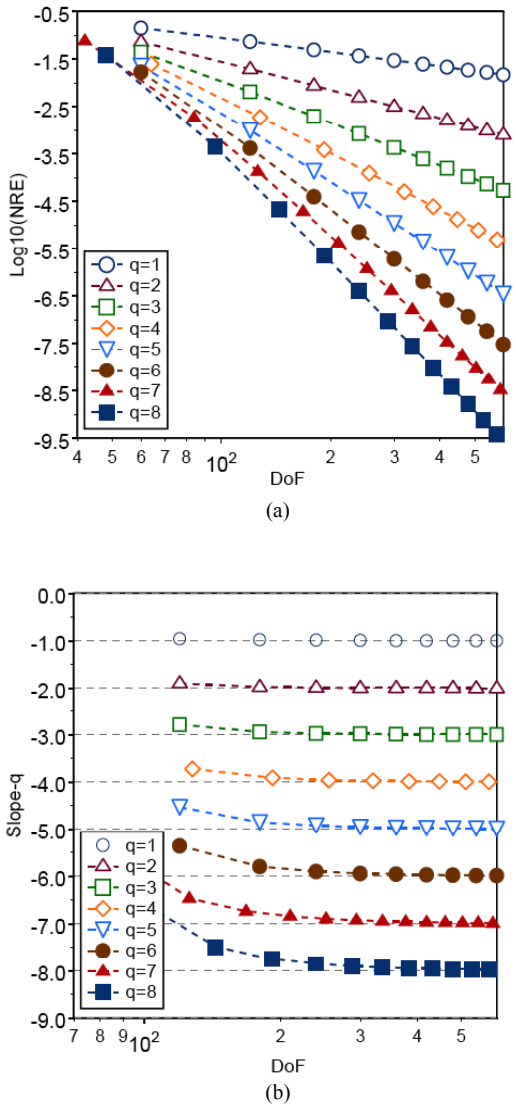

Fig. 1. (a) Global *NRE* values and (b) $Slope_q$ values for the TM MFIE solutions for a circular cylinder of 12 λ circumference, when illuminated by a uniform plane. wave. Uniform cell sizes were used with a Legendre polynomial representation of order q.

Results in Fig. 2 were obtained from the TM MFIE. Corner cells have the same dimension as non-corner cells (ECSR = 1). In this situation, Legendre polynomial representations of order q are used in non-corner cells, while corner cells employ an additional $N_{sing}=[(q + 1)/2]$ singular terms, where the square bracket denotes greatest integer. As the number of degrees of freedom increases, the *NRE* curves in Fig. 2(a) level off, and the global results do not appear to produce high order convergence. This is reflected in the $Slope_q$ curves in Fig. 2(b).

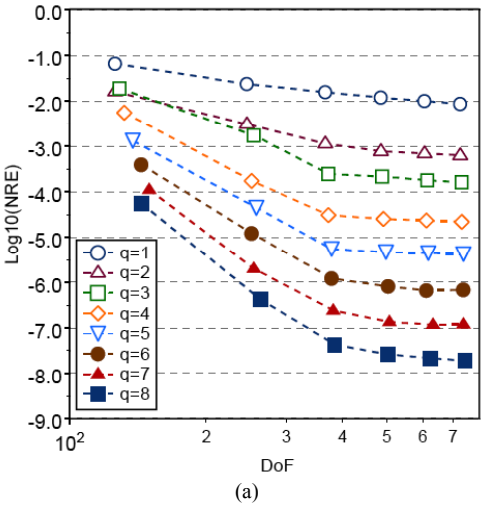

(a)

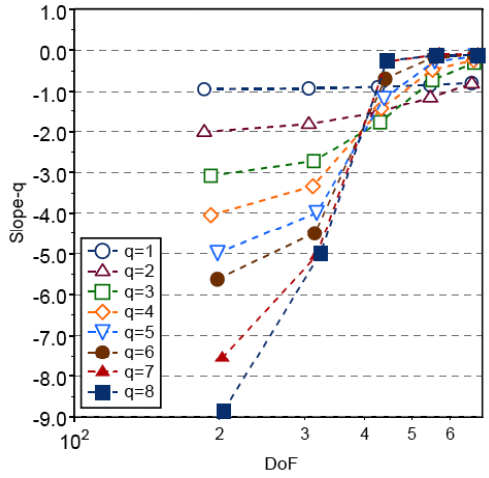

(b)

Fig. 2. (a) Global *NRE* values and (b) $Slope_q$ values for the TM MFIE solutions for a triangular cylinder of 12 wavelength perimeter. The solutions were obtained using ECSR = 1 and $N_{sing} = [(q + 1)/2]$.

An analysis of the local error in the triangular cylinder example shows that as uniform *h*-refinement is applied and the cell sizes are reduced, the error in the corner cells steadily drops. However, the error within the cell next to the corner cell actually begins to grow as that cell gets closer to the corner, and that neighboring cell error dominates the global error measure.

One possible remedy to this situation is to modify the expansion in additional cells near a corner, to better represent the more rapid variation in current density in that region. An alternative remedy is to increase the dimension of the corner cells, relative to the other cells, as suggested by a previous study [6]. This possibility will be investigated in the following.

V. OPTIMUM CORNER CELL DIMENSION

A systematic parameter study was carried out, with the goal of determining the *ECSR* values that minimize the global *NRE*, as a function of q and N_{sing}. The non-corner cell dimensions were fixed at $w_{nc} = q/10\ \lambda$, with the corner cells defined by $w_c = ECSR\ w_{nc}$. Thus, as the order q increases, the cell dimensions increase to maintain a similar number of unknowns. This study considered TM scattering from triangular cylinders, square cylinders, and infinite strips, over a range of sizes. The MFIE was used for the triangular and square cylinders, while the EFIE was used for strips.

Figure 3 shows a plot typical of those generated throughout this investigation. In Fig. 3, the *ECSR* that minimizes the global *NRE* is plotted as a function of q and N_{sing} for the triangular cylinder with perimeter 12 λ. The *ECSR* value is observed to be a rather strong function of both parameters. However, a further study of Fig. 3 yields the observation that the *NRE*-minimizing *ECSR* value for a choice of $N_{sing} = q$ is always near $ECSR = 2$. This observation suggests that the combination of $ECSR = 2$ and $N_{sing} = q$ will generally produce a more accurate result than other values of *ECSR*.

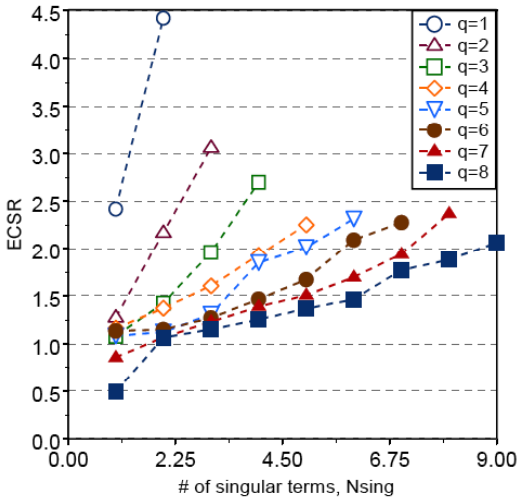

Fig. 3. The ECSR value that minimizes the global *NRE*, as a function of q and N_{sing}. The TM MFIE solutions involve a triangular cylinder of 12 λ perimeter. The non-corner cell size is $w_{nc} = q/10\ \lambda$; the corner cells have dimension $w_c = ECSR\ w_{nc}$.

Figures 4(a) and 4(b) show plots of the global *NRE* and $Slope_q$ versus the degrees of freedom for the same triangular cylinder, obtained from the TM MFIE for $ECSR = 2$ and $N_{sing} = q$. These are improved as compared with Fig. 2, although they still do not offer the ideal behavior of the circular cylinder illustrated by Fig. 1 as *h*-refinement pushes the cell dimensions smaller.

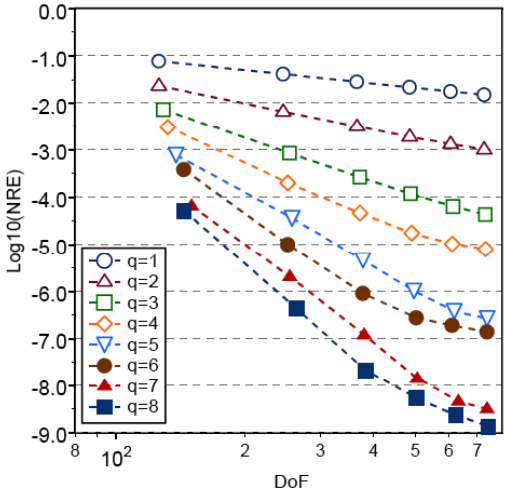

(a)

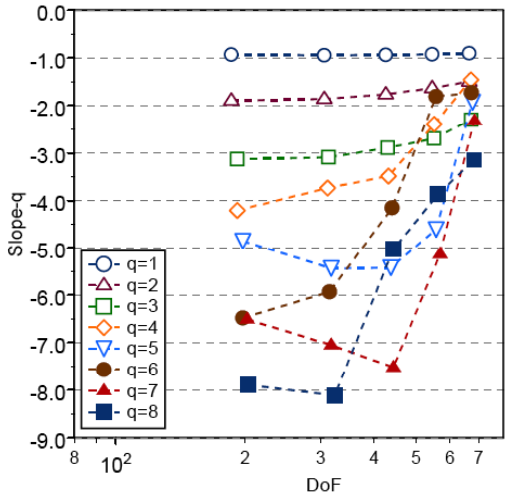

(b)

Fig. 4. (a) Global *NRE* values and (b) $Slope_q$ values for the TM MFIE solutions for a triangular cylinder of 12 wavelength perimeter. The solutions were obtained using ECSR = 2 and $N_{sing} = q$.

Additional parameter studies were carried out, allowing both the non-corner cell dimensions and the ECSR value to vary. One result of that study is shown in Fig. 5, which shows the corner cell dimension that minimizes the global *NRE* versus the non-corner cell dimension, for various values of q with $N_{sing} = q$, for the triangular cylinder used in Figs. 2 and 4. These data indicate that while *ECSR* = 2 is nearly optimal over a wide range of cell sizes, the optimum *ECSR* value generally increases as the cells become small. The data in Fig. 5 are closely tracked by the simple formula,

$$w_c \cong 0.0364 + 1.6723\, w_{nc} + 0.0096q\,. \qquad (7)$$

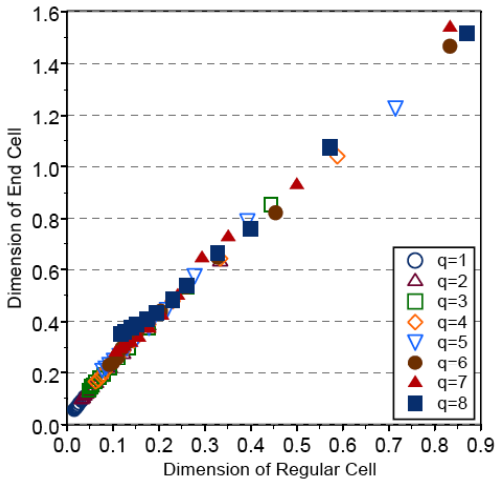

Fig. 5. The corner cell dimension that minimizes the global *NRE* for the TM MFIE solutions for a triangular cylinder of 12 wavelength perimeter. The solutions were obtained using $N_{sing} = q$.

Figures 6(a) and 6(b) show plots of the global *NRE* and $Slope_q$ values versus the degrees of freedom for the triangular cylinder, for $N_{sing} = q$, with each individual result adjusted for the optimum value of *ECSR* corresponding to the results in Fig. 5 (identical results are obtained using the formula in equation (7)). These curves illustrate a much better approximation to the ideal behavior of the circular cylinder, at least for $q \leq 4$. Of course, the identification of the optimal *ECSR* in this manner is not practical for non-canonical targets, and a formula such as equation (7) will vary somewhat from target to target. However, Fig. 6 suggests that a suitable corner cell dimension does exist. Furthermore, it is likely that in the not-too-distant future, some form of adaptive refinement algorithm (perhaps initiated with *ECSR* = 2 and incorporating singular basis functions) should be able to approximate the ideal behavior presented in Fig. 1.

Table 2 summarizes the TM results for several scatterer geometries, including square cylinders and strips, with a range of sizes. Over this range of parameters, it appears that *ECSR* = 2 is a good compromise for q in the range $2 \leq q \leq 8$ and $N_{sing} = q$. Additional studies were carried out for the TE polarization, and lead to similar conclusions as to the optimal *ECSR* value. As an illustration, Figs. 7(a) and 7(b) show plots of the global *NRE* and $Slope_q$ values versus the degrees of freedom for a TE MFIE analysis of the equilateral triangular cylinder with 12 λ perimeter, for $N_{sing} = q$ and *ECSR* = 2.

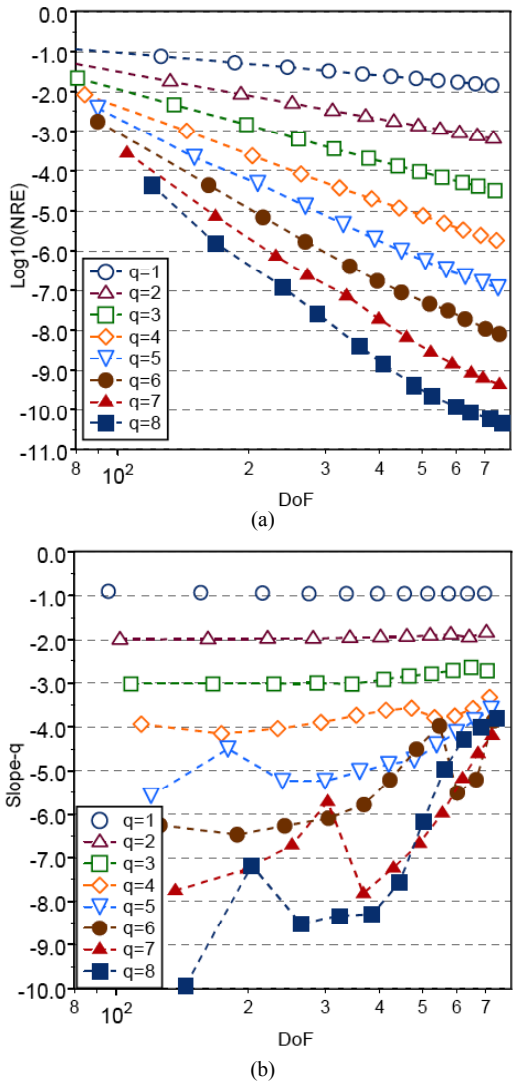

Fig. 6. (a) Global *NRE* values and (b) $Slope_q$ values for the TM MFIE solutions for a triangular cylinder of 12 wavelength perimeter. The solutions were obtained using optimal ECSR values and $N_{sing} = q$.

Table 2. ECSR that provides the minimum NRE, for models with non-corner cell size = $q/10$ wavelengths, $N_{sing}=q$, and the TM polarization.

	Side = 4 wavelengths			Side = 8 wavelengths			Side = 12 wavelengths		
q	Strip	Triangle	Square	Strip	Triangle	Square	Strip	Triangle	Square
1	1.19	2.42	2.59	1.19	2.44	2.15	1.18	2.49	2.03
2	1.74	2.17	1.85	1.67	2.12	1.77	1.64	2.12	1.73
3	1.84	1.96	1.91	1.77	2.02	1.84	1.73	2.03	1.81
4	1.92	1.93	2.03	1.77	1.97	1.93	1.72	1.97	1.89
5	2.00	2.01	2.19	1.87	2.08	2.06	1.81	1.97	2.03
6	2.03	2.09	2.36	1.82	1.77	2.12	1.79	2.01	2.04
7	2.19	1.94	2.67	1.90	1.88	2.20	1.87	1.90	2.12
8	2.27	1.88	2.04	1.97	1.98	2.38	1.90	1.91	2.23

Figures 2, 4, 6, and 7 all involve the triangular cylinder. In these plots, for a constant number of degrees of freedom, as q increases the cell dimensions also increase. Despite the larger cell sizes, the *NRE* is substantially reduced for each increase in q. These curves clearly show the improved accuracy possible with high order basis functions, even for problems that contain an edge singularity.

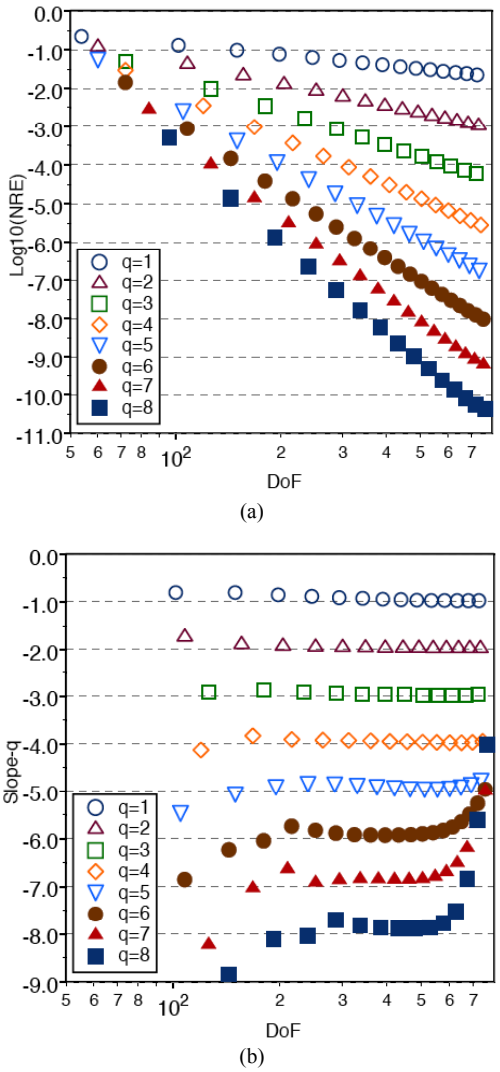

Fig. 7. (a) Global *NRE* values and (b) $Slope_q$ values for the TE MFIE solutions for a triangular cylinder of 12 wavelength perimeter. The solutions were obtained using ECSR = 2 and $N_{sing} = q$.

VI. CONCLUSIONS

This investigation has shown that the local accuracy of the singular representation used in a corner cell is a function of both the number of singular terms employed in that representation, and the corner cell dimension. If uniform *h*-refinement is carried too far in an attempt to

improve accuracy, the global error will tend to be dominated by the error in cells near (but not immediately adjacent to) the corners, unless the corner cells are not reduced in size to the same extent as the non-corner cells. The parameter studies carried out in this investigation suggest that a fairly optimal combination employs corner cells that are twice the dimension of the non-corner cells (*ECSR* = 2), with an expansion in corner cells that contains a number of singular terms equal to the number of regular terms incorporated within the non-corner cell basis function definition ($N_{sing} = q$). These guidelines should provide a good initial starting point for an electromagnetic analysis of structures containing edges.

REFERENCES

[1] D. R. Wilton and S. Govind, "Incorporation of edge conditions in moment method solutions," *IEEE Trans. Antennas Propagat.*, vol. AP-25, pp. 845-850, 1977.

[2] J. H. Richmond, "On the edge mode in the theory of TM scattering by a strip or strip grating," *IEEE Trans. Antennas Propagat.,* vol. AP-28, pp. 883-887, November 1980.

[3] T. Andersson, "Moment method calculations on apertures using singular basis functions," *IEEE Trans. Antennas Propagat.,* vol. 41, pp. 1709-1716, December 1993.

[4] W. J. Brown and D. R. Wilton, "Singular basis functions and curvilinear triangles in the solution of the electric field integral equation," *IEEE Trans. Antennas Propagat.,* vol. 47, pp. 347-353, February 1999.

[5] R. D. Graglia and G. Lombardi, "Singular higher order complete vector bases for finite methods," *IEEE Trans. Antennas Propagat.*, vol. 52, pp. 1672-1685, July 2004.

[6] D.-K. Sun, L. Vardapetyan, and Z. Cendes, "Two-dimensional curl-conforming singular elements for FEM solutions of dielectric waveguiding structures," *IEEE Trans. Microwave Theory Tech.*, vol. 53, pp. 984-992, March 2005.

[7] M. M. Bibby, A. F. Peterson, and C. M. Coldwell, "High order representations for singular currents at corners," *IEEE Trans. Antennas Propagat.*, vol. 56, pp. 2277-2287, August 2008.

[8] R. F. Harrington, *Time Harmonic Electromagnetic Fields*. New York: McGraw-Hill, 1961, pp. 238-242.

[9] A. F. Peterson, S. L. Ray, and R. Mittra. *Computational Methods for Electromagnetics*. New York: IEEE Press, 1998.

[10] K. J. Bunch and R. W. Grow, "The boundary residual method for three-dimensional homogeneous field problems with boundaries of arbitrary geometries," *International Journal of Infrared and Millimeter Waves*, vol. 10, pp. 1007-1032, 1989.

[11] K. J. Bunch and R. W. Grow, "On the convergence of the method of moments, the boundary residual method, and the point-matching method with a rigorously convergent formulation of the point matching method," *Applied Computational Electromagnetics Society (ACES) J.*, vol. 8, pp. 188-202, 1993.

[12] M. M. Bibby and A. F. Peterson, "On the use of over-determined systems in the adaptive numerical solution of integral equations," *IEEE Trans. Antennas Propagat.,* vol. 53, pp. 2267-2273, July 2005.

Malcolm M. Bibby received the B.Eng. and Ph.D. degrees in Electrical Engineering from the University of Liverpool, in 1962 and 1965, respectively, and an MBA from the University of Chicago. He is currently an Adjunct Professor in ECE at Georgia Tech. He has been interested in the numerical aspects associated with antenna design for the last twenty-five years.

Andrew F. Peterson received the B.S., M.S., and Ph.D. degrees in Electrical Engineering from the University of Illinois, Urbana-Champaign in 1982, 1983, and 1986 respectively. Since 1989, he has been a member of the faculty of the School of Electrical and Computer Engineering at the Georgia Institute of Technology, where he is now Professor and Associate Chair for Faculty Development.

Charles M. Coldwell received an A.B. in Mathematics and Ph.D. in Physics from Harvard University, Cambridge, MA, in 1992 and 2002, respectively. He is currently a Senior Software Engineer with Red Hat Inc., Westford, MA, where he specializes in the storage subsystems of the Linux kernel.

Improved Version of the Second-Order Mur Absorbing Boundary Condition Based on a Nonstandard Finite Difference Model

J. B. Cole and D. Zhu

University of Tsukuba, Japan
cole@is.tsukuba.ac.jp

Abstract **–** It is often necessary to terminate the computational domain of an FDTD calculation with an absorbing boundary condition (ABC). The Perfectly Matched Layer (PML) is an excellent ABC, but it is complicated and costly. Typically at least 8 layers are needed to give satisfactory absorption. Thus in a 100^3 domain less than 84^3 or 59% of the grid points are usable. The second-order Mur ABC requires just 2 layers, but its absorption is inadequate for many problems. In this paper we introduce an improved version of the second-order Mur ABC based on a nonstandard finite difference (NSFD) model which has the same low computational cost but with much better absorption on a coarse grid.

Keywords: Absorbing Boundary Condition, ABC, Mur ABC, Nonstandard Finite Difference, FDTD.

I. INTRODUCTION

Unless the computational domain boundary is periodic or the fields vanish on it, an absorbing boundary condition (ABC) is needed for finite difference time domain (FDTD) calculations. An ideal ABC absorbs fields incident at all angles without reflection, and thus mimics an infinite computational domain. Except in one dimension, there is no perfect ABC. In general, the better the ABC, the more complicated and computationally costly it is. The second-order Mur ABC [1] is simple and economical, but it performs poorly at incidence angles greater than about 30° from the boundary normal. The PML [2] can, in principle, absorb fields at high incidence angles with arbitrarily low reflection, but it is complicated and costly to implement. Using a nonstandard (NS) finite difference model of the Engquist-Majda [3] one-way wave equations we derive an improved version of the Mur ABC that delivers much better absorption for the same computational cost.

II. ENGQUIST-MAJDA ONE-WAY WAVE EQUATIONS

The two-dimensional wave equation can be expressed in the form,

$$\left(\partial_t^2 - v^2\partial_x^2 - v^2\partial_y^2\right)\psi(\boldsymbol{x},t) = 0 \tag{1.1}$$

where $\boldsymbol{x} = (x, y)$ Defining $P = \sqrt{\partial_t^2 - v^2\partial_y^2}$, equation (1.1) can be factored into,

$$\left(P + v\partial_x\right)\left(P - v\partial_x\right)\psi(\boldsymbol{x},t) = 0 \tag{1.2}$$

to yield the Engquist-Majda (EM) one-way wave equations,

$$\left(P \pm v\partial_x\right)\psi(\boldsymbol{x},t) = 0\,. \tag{1.3}$$

General solutions of equation (1.3) are $\varphi_\pm(\boldsymbol{x},t) = f(\hat{\boldsymbol{k}}\bullet\boldsymbol{x} \mp vt)$, where $\hat{\boldsymbol{k}} = (\cos\theta, \sin\theta)$ and f an arbitrary function, θ is the angle $\hat{\boldsymbol{k}}$ makes with the x-axis. $P \pm v\partial_x$ absorbs waves moving in the $\pm x$-directions, respectively. On the domain $(0 \le x \le a)\times(0 \le y \le b)$, solving $\left(P \mp v\partial_x\right)\psi = 0$ at $x = 0, a$, respectively gives an ABC on the x-axis. A y-axis ABC can be similarly derived.

Since P is ill-defined, we must express it in a more suitable form. Writing $P^2 = \partial_t^2\left(1 - v^2\partial_y^2/\partial_t^2\right)$, expanding $\sqrt{P^2}$ in a Taylor series, and retaining the first two terms gives $P \cong \partial_t - \frac{1}{2}v^2\partial_y^2/\partial_t$. Inserting into equation (1.3) and multiplying by ∂_t, yields the second-order EM one-way wave equations along the x-axis,

$$\left(\partial_t^2 \pm v\partial_x\partial_t - \frac{1}{2}v^2\partial_y^2\right)\psi(\boldsymbol{x},t) = 0\,. \tag{1.4}$$

Defining $W_\pm$ to be the differential operator in equation (1.4), the annihilation error $\varepsilon_{\mathrm{EM}} = W_\pm\varphi_\pm/\varphi_\pm$ is

$$\varepsilon_{\mathrm{EM}} = v^2\frac{f''(\hat{\boldsymbol{k}}\bullet\boldsymbol{x} \mp vt)}{f(\hat{\boldsymbol{k}}\bullet\boldsymbol{x} \mp vt)}\times \left(1 - \cos\theta - \frac{1}{2}\sin^2(\theta)\right)\cdot \tag{1.5}$$

II. SECOND-ORDER MUR ABSORBING BOUNDARY

We now construct a difference equation model of equation (1.4). Taking $\Delta x = \Delta y = h$, we discretize x, y, and t in the form $x = 0, h, \cdots N_x h$, $y = 0, h, \cdots N_y h$, $t = 0, \Delta t, 2\Delta t, \cdots$. Defining the difference operators d_x, d_t', and d_x^2 by $d_x f(x) = f(x+h/2) - f(x-h/2)$, $d_t' f(t) = f(t+\Delta t) - f(t-\Delta t)$, $d_x^2 f(x) = f(x+h) + f(x-h) - 2f(x)$, finite difference expressions for the derivatives are $f'(x) \cong d_x f(x)/h$, $f'(t) \cong d_t' f(t)/2\Delta t$, and $f''(x) \cong d_x^2 f(x)/h^2$. Substituting into (1.4) yields,

$$\left(d_t^2 \pm \frac{1}{2}\frac{v\Delta t}{h} d_x d_t' - \frac{1}{2}\frac{v^2\Delta t^2}{h^2} d_y^2 \right) \psi(\mathbf{x}, t) = 0 . \quad (2.1)$$

To simplify the notation, denote the x-coordinate of the computational boundary by b, where $b = 0$ on the left, and $b = N_x h$ on the right. Let i be the x-coordinate one grid spacing inside the boundary, thus $i = b \pm h$, on the left and right respectively. The midpoint between b and i is $m = (b+i)/2$. Finally write $\psi(x, y, t) = \psi_{x,y}^t$ and $\psi(x, y, t \pm \Delta t) = \psi_{x,y}^{t\pm1}$. Evaluating (2.1) at $x = m$ using $\psi_{m,y}^t \cong \left(\psi_{b,y}^t + \psi_{i,y}^t\right)/2$, with the abbreviation $v\Delta t/h = \overline{v}$, we obtain,

$$d_t^2 \left(\psi_{b,y}^t + \psi_{i,y}^t\right) + \overline{v}\left[\left(\psi_{b,y}^{t+1} - \psi_{i,y}^{t+1}\right) - \left(\psi_{b,y}^{t-1} - \psi_{i,y}^{t-1}\right)\right] - \frac{1}{2}\overline{v}^2 d_y^2 \left(\psi_{b,y}^t + \psi_{i,y}^t\right) = 0 . \quad (2.2)$$

Henceforth, we call equation (2.2) the standard finite-difference (SFD) model of the EM equation (1.4). Equation (2.2) holds on both the left and right boundaries because $\left(\psi_{b,y}^{t\pm1} - \psi_{i,y}^{t\pm1}\right)$ has opposite signs on opposite sides. Expanding $d_t^2 \psi_{b,y}^t$ and solving for $\psi_{b,y}^{t+1}$, yields the second-order Mur ABC [4] the time-marching algorithm,

$$\psi_{b,y}^{t+1} = \psi_{b,y}^t + \left(\psi_{i,y}^t - \psi_{i,y}^{t-1}\right) + \left(\frac{1-\overline{v}}{1+\overline{v}}\right)\left[\left(\psi_{b,y}^t - \psi_{b,y}^{t-1}\right) - \left(\psi_{i,y}^{t+1} - \psi_{i,y}^t\right)\right] + \frac{1}{2}\left(\frac{\overline{v}^2}{1+\overline{v}}\right) d_y^2 \left(\psi_{b,y}^t + \psi_{i,y}^{t-1}\right) . \quad (2.3)$$

A similar expression for the $\pm y$ directions can be derived. Henceforth we call equation (2.3) the S (standard)-Mur ABC.

Let us now evaluate how well the S-Mur ABC annihilates an infinite plane wave, $\psi_\pm = e^{i(\mathbf{k}\cdot\mathbf{x} \mp \omega t)}$, with propagation vector $\mathbf{k} = k\hat{\mathbf{k}} = \left(k_x, k_y\right)$ and angular frequency $\omega = vk$. Defining the left side of equation (2.2) as $M_{\mathrm{SFD}}\psi$, where M_{SFD} is a difference operator, the annihilation error is $\varepsilon_{\mathrm{SFD}} = M_{\mathrm{SFD}}\psi_\pm / \psi_\pm$. Writing $\tilde{\varepsilon}_{\mathrm{SFD}} = \varepsilon_{\mathrm{SFD}} / 8\sin^2\left(\overline{\omega}/2\right)$, where $\omega\Delta t = \overline{\omega}$, $kh = \overline{k}$, $k_{x,y}h = \overline{k}_{x,y}$, and using the identities,

$$\psi_{b,y}^t + \psi_{i,y}^t = 2\cos\left(k_x h/2\right)\psi_{m,y}^t \quad (2.4a)$$

$$\psi_{b,y}^t - \psi_{i,y}^t = 2i\sin\left(k_x h/2\right)\psi_{m,y}^t , \quad (2.4b)$$

$$d_y^2 \psi_{x,y}^t / \psi_{x,y}^t = -4\sin^2\left(k_y h/2\right) , \quad (2.4c)$$

we find

$$\tilde{\varepsilon}_{\mathrm{SFD}}(\theta) = -\cos\left(\overline{k}_x/2\right) + \overline{v}\frac{\sin\left(\overline{k}_x/2\right)}{\tan\left(\overline{\omega}/2\right)} + \frac{1}{2}\overline{v}^2 \frac{\sin^2\left(\overline{k}_y/2\right)}{\sin^2\left(\overline{\omega}/2\right)}\cos\left(\overline{k}_x/2\right) . \quad (2.5)$$

Comparing $\varepsilon_{\mathrm{SFD}}$ with $\varepsilon_{\mathrm{EM}}$, we see that the SFD model equation (2.1) is a poor approximation to the EM equation (1.4). We now seek a better one.

III. NONSTANDARD FINITE DIFFERENCE VERSION

The SFD model of the EM equations is not the only one possible. The quantities $\overline{v}$ and $\overline{v}^2$ in equation (2.2) can be regarded as independent free parameters (u_1 and u_2^2, respectively) that can be chosen to optimize the ABC. Defining M_{NSFD} by ,

$$M_{\mathrm{NSFD}}\psi = d_t^2 \left(\psi_{b,y}^t + \psi_{i,y}^t\right) + u_1\left[\left(\psi_{b,y}^{t+1} - \psi_{i,y}^{t+1}\right) - \left(\psi_{b,y}^{t-1} - \psi_{i,y}^{t-1}\right)\right] - \frac{1}{2}u_2^2 d_y^2 \left(\psi_{b,y}^t + \psi_{i,y}^t\right) \quad (3.1)$$

we obtain a family of difference models of the EM equations, parameterized by u_1 and u_2^2,

$$M_{\mathrm{NSFD}}\psi = 0 . \quad (3.2)$$

This is an example of a nonstandard finite-difference (NSFD) model [4]. The SFD model is just the special case $u_1 = \overline{v}$, $u_2^2 = \overline{v}^2$. Let us now minimize

$\varepsilon_{\text{NSFD}} = M_{\text{NSFD}}\psi_{\pm}/\psi_{\pm}$ with respect to u_1 and u_2^2.

Writing $\tilde{\varepsilon}_{\text{NSFD}} = \varepsilon_{\text{NSFD}}/8\sin^2(\bar{\omega}/2)$, $u_1 = w_1\tan(\bar{\omega}/2)$, $u_2^2 = w_2^2\sin^2(\bar{\omega}/2)$, and making the replacements $\bar{v} \to u_1$, and $\bar{v}^2 \to u_2^2$ in equation (2.5) we obtain,

$$\tilde{\varepsilon}_{\text{NSFD}}(\theta) = -\cos(\bar{k}_x/2) + w_1\sin(\bar{k}_x/2) + \frac{1}{2}w_2^2\sin^2(\bar{k}_y/2)\cos(\bar{k}_x/2). \tag{3.3}$$

First let us require that $\tilde{\varepsilon}_{\text{NSFD}}(0) = 0$. This gives,

$$w_1 = \cot(\bar{k}/2). \tag{3.4}$$

Next inserting equation (3.4) into equation (3.3) we obtain,

$$\tilde{\varepsilon}_{\text{NSFD}}(\theta) = \delta_0(\theta) + \frac{1}{2}w_2^2\delta_2(\theta) \tag{3.5}$$

where

$$\delta_0(\theta) = -\cos(\bar{k}_x/2) + \cos(\bar{k}/2)\sin(\bar{k}_x/2), \tag{3.6a}$$

$$\delta_2(\theta) = \sin^2(\bar{k}_y/2)\cos(\bar{k}_x/2). \tag{3.6b}$$

Now requiring that $\tilde{\varepsilon}_{\text{NSFD}}(\theta_2) = 0$ yields,

$$w_2^2(\theta_2) = \frac{-2\delta_0(\theta_2)}{\delta_0(\theta_2)}. \tag{3.7}$$

The larger θ_2 the greater the absorption at high incidence angles, but the greater the reflection at intermediate angles, $0 < \theta < \theta_2$. We have examined various choices of θ_2, and conclude that the best overall choice is $\theta_2 = 45^\circ$. When radiation is incident over a wide range of large angles, however, $\theta_2 = 60^\circ$ is a reasonable compromise. We could also require that $\tilde{\varepsilon}_{\text{NSFD}}(\theta_0) = 0$ ($\theta_0 \neq 0$) and $\tilde{\varepsilon}_{\text{NSFD}}(\theta_2) = 0$ ($\theta_2 \neq \theta_0$), and simultaneously solve for w_1 and w_2^2. This choice is suitable for special applications where most of the radiation in incident on the boundary over a particular angular band. Henceforth, unless otherwise specified we take $\theta_2 = 45^\circ$.

Putting equations (3.4) and (3.7) into the expressions for u_1 and u_2^2 we have,

$$u_1 = \frac{\tan(\omega\Delta t/2)}{\tan(kh/2)} \tag{3.8a}$$

$$u_2^2(\theta_2) = -2\sin^2(\omega\Delta t/2)\frac{\delta_0(\theta_2)}{\delta_2(\theta_2)}. \tag{3.8b}$$

Inserting the simple substitutions $\bar{v} \to u_1$ and $\bar{v}^2 \to u_2^2$ into the S-Mur ABC (2.3) with the now yields the NS (nonstandard)-Mur ABC,

$$\psi_{b,y}^{t+1} = \psi_{b,y}^{t} + \left(\psi_{i,y}^{t} - \psi_{i,y}^{t-1}\right) + \left(\frac{1-u_1}{1+u_1}\right)\left[\left(\psi_{b,y}^{t} - \psi_{b,y}^{t-1}\right) - \left(\psi_{i,y}^{t+1} - \psi_{i,y}^{t}\right)\right] + \frac{1}{2}\left(\frac{u_2^2}{1+u_1}\right)d_y^2\left(\psi_{b,y}^{t} + \psi_{i,y}^{t-1}\right). \tag{3.9}$$

IV. NUMERICAL STABILITY

Consider a two-step FD algorithm of the form,

$$\psi(t+\Delta t) = a\psi(t-\Delta t) + 2b\psi(t) \tag{4.1}$$

where *a* and *b* are constants. Taking $t = \tau\Delta t$, $\tau = 0,1,2,\cdots$ and writing $\psi(t) = \psi^{\tau}$, equation (4.1) becomes,

$$\psi^{\tau+1} = a\psi^{\tau-1} + 2b\psi^{\tau}. \tag{4.2}$$

Postulating a solution to equation (4.2) of the form $\psi^{\tau} = \eta^{\tau}$, yields the equation $\eta^2 - 2b\eta - a = 0$, which has the solutions,

$$\eta_{\pm} = b \pm \sqrt{b^2 + a}. \tag{4.3}$$

The general solution of equation (4.2) is therefore,

$$\psi^{\tau} = \alpha_{+}\eta_{+}^{\tau} + \alpha_{-}\eta_{-}^{\tau} \tag{4.4}$$

where the constants $\alpha_{\pm}$ are determined by the initial values $\psi(0)$ and $\psi(\Delta t)$. Since the fields on the boundary cannot rise exponentially with time, we require that,

$$|\eta_{\pm}| \leq 1. \tag{4.5}$$

Condition (4.5) is a form of the CFL (Courant, Friedrich, Levy) [5] stability condition.

Suppose that $|\eta_+| \le 1$ and $|\eta_-| > 1$. If $\alpha_- = 0$ in equation (4.4) it might seem that $\lim_{\tau\to\infty} \psi^\tau$ is finite. In principle it is, but after a large number of iterations (N), computer round-off error gives rise to a small η_- component, and $\psi^N = a_+\eta_+^N + \delta\eta_-$. Thus ψ diverges with further iteration.

Let us now analyze the numerical stability of the NSFD model (3.2). Assuming an infinite plane wave, the spatial derivatives and averages can be expressed using equation (2.4). Equation (3.2) becomes,

$$c_x\left(\psi_{m.y}^{t+1} + \psi_{m.y}^{t-1} - 2\psi_{m.y}^{t}\right) + iu_1 s_x\left(\psi_{m.y}^{t+1} - \psi_{m.y}^{t-1}\right) + 2c_x s_y^2 u_2^2 \psi_{m.y}^{t} = 0, \tag{4.6}$$

where $s_x = \sin(k_x h/2)$, $c_x = \cos(k_x h/2)$, $s_y = \sin(k_y h/2)$. Writing $\alpha = c_x + iu_1 s_x$, and $\beta = 1 - s_y^2 u_2^2$, we can cast equation (4.6) into the form of equation (4.2) with $a = -\alpha^*/\alpha$ and $b = \beta c_x/\alpha$ in equation (4.2). The solution of equation (4.6) is thus,

$$\eta_\pm = \frac{1}{\alpha}\left[\beta c_x \pm \sqrt{\beta^2 c_x^2 - |\alpha|^2}\right]. \tag{4.7}$$

If $\beta^2 c_x^2 \le |\alpha|^2$ equation (4.7) becomes,

$$\eta_\pm = \frac{1}{\alpha}\left[\beta c_x \pm i\sqrt{|\alpha|^2 - \beta^2 c_x^2}\right] \tag{4.8}$$

whence $|\eta_\pm|^2 = 1$. On the other hand if $\beta^2 c_x^2 > |\alpha|^2$, it can be shown that either $|\eta_+| > 1$ or $|\eta_-| > 1$. The CFL condition is thus $\beta^2 c_x^2 \le |\alpha|^2$, which can be rewritten as,

$$\frac{\left(1 - s_y^2 u_2^2\right)^2}{1 + u_1^2\left(s_x^2/c_x^2\right)} \le 1. \tag{4.9}$$

Because the denominator is ≥ 1 and $s_y^2 \le 1$, equation (4.9) reduces to,

$$u_2^2(\theta_2) \le 2. \tag{4.10}$$

For the S-Mur ABC, $u_2^2 = (v\Delta t/h)^2$ and equation (4.9) gives the stability condition $v\Delta t/h \le \sqrt{2}$. For the NS-Mur ABC, putting equation (3.8) into equation (4.9) and using $\omega = kv \Rightarrow \bar{\omega} = \bar{v}\bar{k}$, the stability condition becomes,

$$-\sin^2\left(\bar{v}\bar{k}/2\right) \le \frac{\delta_2(\theta_2)}{\delta_0(\theta_2)}. \tag{4.11}$$

Since the maximum spacing between the grid points is $h\sqrt{2}$, the Nyquist sampling condition requires that we choose $\lambda/h > 2\sqrt{2} \Rightarrow 0 < \bar{k} < \pi/\sqrt{2}$. We now seek the maximum value, c, of $\bar{v} = v\Delta t/h$ such that equation (4.11) is satisfied. Numerically solving equation (4.11) gives $c = 1.31$ for $\theta_2 = 45^\circ$, and $c = 1.22$ $\theta_2 = 60^\circ$. The NS-Mur stability condition can now be expressed in the form,

$$\frac{v\Delta t}{h} \le c(\theta_2). \tag{4.12}$$

These stability constraints are looser than that of the FDTD algorithm used to compute the fields in the interior of the computational domain. In the standard (S) FDTD (Yee) algorithm, the CFL stability condition is $v\Delta t/h \le \sqrt{2}/2 \cong 0.70$, but the nonstandard (NS) FDTD algorithm [6,7] is stable for $v\Delta t/h \le 0.84$ in two dimensions. We used the NS-FDTD algorithm to calculate the electromagnetic fields in the interior of the computational domain in the results shown below.

The above analysis applies to an infinite plane wave impinging at arbitrary angle on an infinite computational boundary. A difficulty common to all ABCs is the indeterminacy of the corner points. At the corners the stability analysis is extremely difficult so it is best verified numerically. We have found that computing the ABC at the corner points with either the left-right (x-axis) ABC or the top-bottom (y-axis) ABC yields excellent stability. Some authors take the average of the left-right and top-bottom ABCs. While the resultant ABC is stable, it does not increase the absorption.

V. IMPLEMENTATION

The implementation of the ABC depends upon the details of the FDTD algorithm used to compute the electromagnetic fields, such as the placement of the electromagnetic fields on the numerical grid. For example, if the magnetic field ($\boldsymbol{H}$) is updated first in the TE mode ($H_x = H_y = E_z = 0$) with periodic FD operators, the ABC need be applied only to H_z because the electric field ($\boldsymbol{E}$) depends only on H_z. If d_x is periodic on $x = 0, h, \cdots N_x h$, then $d_x f(N_x h) = f(0) - f(N_x h - h)$, and $d_x f(0) = f(h) - f(N_x h)$.

VI. COMPARISONS AND PERFORMANCE TESTS

To test the effectiveness of our ABC we used a modification of the test described in [2] (equation (6.46), p. 258) and [8]. Expressing equation (6.46) of [2] in the space domain we have,

$$p_0(x)=\frac{1}{32}\Big[10-15\cos\left(\tfrac{1}{3}k_p x\right)+6\left(\tfrac{2}{3}k_p x\right)-\cos k_p x\Big]. \tag{6.1}$$

We center the pulse at $x=0$ by defining,

$$p(x)=p_0\left(x-\tfrac{3}{2}\lambda_p\right) \tag{6.2}$$

where $\lambda_p=2\pi/k_p$, equation (6.2) defines a smooth pulse of half-width λ_p. To suppress periodicity we add the condition $p(x)=0$ for $|x|>\lambda_p$. In [2] $\lambda_p=40h/3$, but we take $\lambda_p=2\lambda$, and use (6.2) to construct a square incident pulse envelope for a signal of wavenumber $k=2\pi/\lambda$ as depicted in Fig. 1.

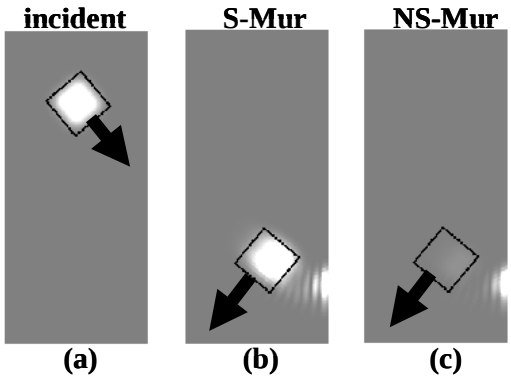

Fig. 1. (a) Incident pulse (50° from normal) reflects from the right boundary where (b) the S-Mur ABC or (c) the NS-Mur ABC is enforced.

Figure 1 depicts a typical calculation. Using the NS-FDTD algorithm, the input pulse (Fig. 1(a)) is propagated onto the right boundary, where either the S-Mur ABC (Fig. 1(b)), or the NS-Mur ABC (Fig. 1(c)) is enforced ($\theta_2=45^\circ$). Incident intensity I_0, is the mean intensity of the incident pulse within the box (outlined in black, Fig. 1(a)). The reflected pulse is propagated away from the boundary, and the reflected intensity (I_r), mean intensity within the box, is recorded. The intensity reflection coefficient is $r=I_r/I_0$. Note that the reflected pulse is not exactly centered within the box. Box position is computed under the assumption that the angle of reflection equals the angle of incidence, and that pulse group velocity equals phase velocity.

We also investigated the total energy absorption, by comparing total incident energy (E_0) with total reflected energy (E_r). Total energy is the local intensity summed over all grid points in the computational domain interior. The total energy reflection coefficient is $\rho=E_r/E_0$. Before reflection, the energy is concentrated about the pulse center, but afterwards some of the energy remains near the boundary and propagates along it (lower right of Figs. 1(a) and (b)). Thus r and ρ are somewhat different. For $\theta_2=45^\circ$ in equation (3.7) for the NS-Mur ABC, the difference is very small, but for $\theta_2=60^\circ$, ρ is much greater than r. For this reason we take $\theta_2=45^\circ$. In all that follows "NS-Mur ABC" means $\theta_2=45^\circ$.

Figures 2 and 3 show plots of the intensity reflection coefficient (r) as a function of incidence angle (θ) for the S-Mur, and NS-Mur ABCs. In Fig. 4 ρ is similarly plotted.

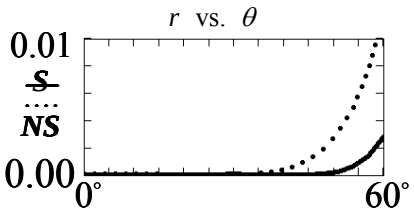

Fig. 2. Intensity reflection coefficient (r) vs. incidence angle (θ) for the S-Mur ABC (S), and NS-Mur_ABC (NS); $\lambda/h=8,\ v\Delta t/h=0.84$.

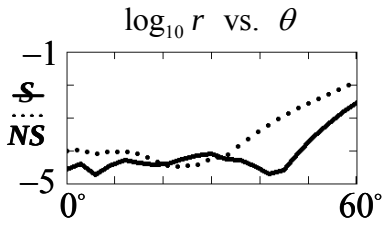

Fig. 3. Same data as Fig. 2, $\log_{10} r$ versus θ.

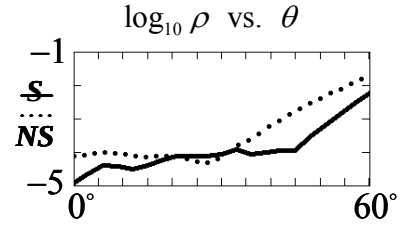

Fig. 4. Total energy reflection coefficient (ρ) vs. incidence angle (θ) for the S-Mur ABC (S), and NS-Mur_ABC (NS), $\lambda/h=8,\ v\Delta t/h=0.84$.

The NS-Mur ABC has the lowest values of both r and ρ over the range $0 \le \theta \le 45^\circ$, except in the narrow band $25^\circ \le \theta \le 30^\circ$, where the S-Mur ABC is slightly lower. For $\theta > 30^\circ$, S-ABC reflection rises rapidly and is always much higher than NS-ABC reflection.

We investigated the "global" energy absorption due to a pulsed point source centered in a $\lambda \times \lambda$ computational domain. Using equation (6.1) in the time domain ($k_p \to \omega_p = 2\omega_0$) to modulate a source of angular frequency ω_0, we plot the signal decay as a function of time step in Fig. 5.

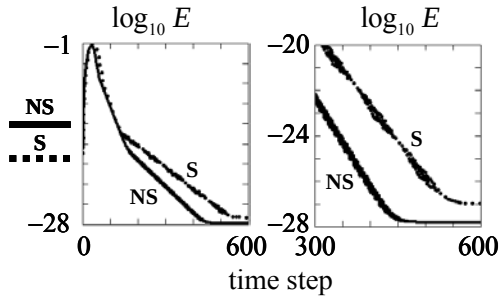

Fig. 5. Total energy (veritcal) vs. time step for the S-Mur ABC (S), and NS-Mur_ABC (NS); $\lambda/h = 8$. Right figure shows magnified scale.

As Fig. 5 shows, not only is the global energy absorption higher for the NS-Mur ABC, but also the signal decays more quickly. This faster decay is probably because the signal requires fewer "bounces" off the boundary to be absorbed.

Since the NS-Mur ABC is optimized to absorb a particular angular frequency, ω_0, it is interesting to investigate in greater detail how well it absorbs pulses. Fig. 6 depicts a normally incident pulse, and its S-Mur ABC and NS-Mur ABC intensity reflections.

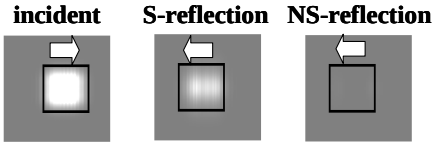

Fig. 6. Normally Incident and reflected pulses with the S-Mur and NS-Mur ABCs.

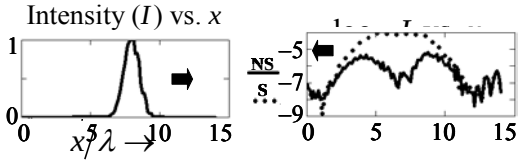

Fig. 7. Intensity profile of pulses in Fig. 6. Left: incident pulse; right: reflected pulses.

Where the pulse rises and falls $\omega \ne \omega_0$ frequency components are large but the NS-Mur ABC reflected intensity is still less than 10^{-1} that of the S-Mur ABC. In pulse center the NS-Mur ABC reflected intensity is less than 10^{-3} that the S-Mur ABC, as shown in Fig. 7.

To compute propagation in a photonic crystal consisting of vacuum holes in a dielectric substrate of refractive index n_s, we set $v\Delta t/h = c_0 = 0.84$ in the vacuum, and take $v\Delta t/h = c_0/n_s$ in the substrate. The total energy reflection (ρ) using both the S-Mur and NS-Mur ABC is little affected by the value of $v\Delta t/h$ but the intensity reflection (r) decreases somewhat for $\theta > 55^\circ$. This is, however, probably due to pulse spreading. We also examined the sensitivity of r and ρ to the value of λ/h, but found little effect.

VII. SUMMARY AND CONCLUSIONS

The NSFD version of the second-order Mur ABC is obtained with the simple replacements $\overline{v} \to u_1$, and $\overline{v}^2 \to u_2^2$. We found that the best ABC for general use is the choice $\theta_2 = 45^\circ$ in equation (3.7). Existing computer codes can be easily modified to give much better absorption for the same computational cost. Although the NS-Mur ABC is optimized for monochromatic radiation, it also absorbs moderately broad pulses effectively. The data of Figs. 2 to 5 are taken with bandwidth $\Delta\omega_0 \sim \omega_0/4$ about the central frequency, ω_0. The performance of the S-Mur ABC is also frequency dependent, and its performance deteriorates as λ/h decreases. On the other hand the NS-Mur ABC is optimized to grid spacing, and does well on a coarse grid. As Figs. 2-5 show, both the S-Mur ABC and NS-Mur ABC give low reflection up to incidence angles (θ) of about 30°, but the NS-Mur ABC is much better than the S-Mur ABC for $\theta > 30^\circ$.

The NS-Mur ABC is still fundamentally a second-order ABC. For wide-band absorption at high incidence angles a more sophisticated ABC, such as PML, must be used with its concomitant complexity and high computational cost.

This work greatly expands the utility of the simple, low-cost second-order Mur ABC. The foregoing developments have been extended to three dimensions. In three dimensions where there are line corners and point corners, special care must be taken to correctly join the Mur ABC with the FDTD algorithm.

REFERENCES

[1] G. Mur, "Absorbing boundary conditions for the finite-difference approximation of the time domain electromagnetic field equations," *IEEE Transactions on Electromagnetic Compatibility*, vol. 23, pp. 377-382, 1981.

[2] A. Taflove and S. C. Hagness, "Computational electrodynamics: the finite-difference time-domain method. norwood," *Artech House, Inc., Norwood, MA,* 2000.

[3] B. Engquist and A. Majda, "Absorbing boundary conditions for the numerical simulation of waves," *Mathematics of Computation,* vol. 31, pp. 629-651, 1977.

[4] R. E. Mickens, "Nonstandard finite difference models of differential equations," *World Scientific, Singapore*, 1994.

[5] S. K. Godunov, "Difference Schemes," North-Holland, Amsterdam, 1987.

[6] J. B. Cole, "High accuracy Yee algorithm based on nonstandard finite differences: new developments and verifications", *IEEE Trans. Antennas and Propagation,* vol. 50, no. 9, pp. 1185-1191, Sept. 2002.

[7] J. B. Cole, "High accuracy nonstandard finite-difference time-domain algorithms for computational electromagnetics: applications to optics and photonics," Chapter 4, pp. 89-109 in *Advances in the Applications of Nonstandard Finite Difference Schemes*, R. E. Mickens, ed., Scientific, Singapore, 2005.

[8] T. G. Moore, J. G. Blaschak, A. Taflove, and G. A. Kriegsmann, "Theory and application of radiation boundary operators," *IEEE Trans. Antennas and Propagation*, vol. 36, pp. 1797-1812, 1988.

Comparative Study of Three Wave Propagation Software Programs for the Modeling of Coupled Maxwell and Boltzmann Equations at THz Frequency

[1]B. Tissafi, [1]F. Aniel, [2]L. Pichon, [2]B. Essakhi, [3]C. Guiffaut, and [4]S. Lepaul

[1]IEF – UMR 8622 CNRS, Département N.A.E.L., Université Paris Sud,
Bât 220, 91405 Orsay, France
[2]LGEP – UMR 8507 CNRS, SUPELEC, Université Paris-Sud, Université Pierre et Marie Curie
Plateau de Moulon, 91192 Gif-sur-Yvette cedex, France
[3]XLIM – UMR 6172 CNRS, Département O.S.A., Faculté des Sciences et Techniques,
123 avenue Albert Thomas, 87060 Limoges, France
[4]EDF R&D – Département O.S.I.R.I.S., 1 avenue du Général De Gaulle, BP 408, 92141
Clamart, France

Abstract – The modeling of optoelectronic devices operating at THz frequency requires self consistently solving the Maxwell equations and the Boltzmann transport equation. In this article, it is the numerical method for solving Maxwell's equations that is debated in the frame of its ability to be combined with transport equations. For this purpose, three software programs mainly devoted to the simulation of 3D electromagnetic equations in time-domain (one based on a 3D finite element method and two on 3D FDTD methods) are first presented and compared. The structure used for the modeling comparison is a coplanar waveguide structure. Results provided by the three solvers are compared according to two factors of merit. Then, the coupling of Maxwell and Boltzmann equations in the FDTD frame is briefly presented and the difficulties to use other methods are explained, showing that the variable-mesh FDTD method is most suitable for such a coupling.

I. INTRODUCTION

The behavior of a THz optoelectronic device such as a photoconductive switch excited by a fs laser pulse is controlled by the coupling between two physical phenomena: the photo-generated carrier transport and the electromagnetic propagation. The modeling of electromagnetic propagation requires to solve Maxwell's equations (the all set of equations) while for the transport of carriers supposed to be classical it is necessary to solve the Boltzmann Transport Equation (BTE). During these last few years, we developed at the Institut d'Electronique Fondamentale (IEF) a software (MAXTRA3D) to solve the whole equation system (Maxwell equations and carrier transport equations) [1]. The software is based on a 3D Finite-Difference Time-Domain (FDTD) method with a variable step mesh allowing a realistic structure design for an accurate description of photo-generated carriers and of their transport mechanisms.

The very first question one asked at the beginning of this work consisted in finding the appropriate numerical approach to solve both electromagnetic and transport equations self consistently. The finite element methods seemed to be the best suited ones. But the modeling of electromagnetic propagation was an autonomous field of study with its dedicated methods and no method could be drawn aside a priori. The 3D electromagnetic problems in time domain can be solved by various numerical methods: FDTD [2], Transmission Line Matrix (TLM) [3], Finite Integrated Technique (FIT) [4], Finite Element Method (FEM) [5], Finite Volume (FV) [6] and Discontinuous Galerkin Methods (DGM) [7]. Among all of these methods, this article focuses on one variational method, the finite element method (FEM) and on one differential method, the FDTD method. This choice has been mainly motivated by two factors. First, FDTD is an explicit method with the capability to perform 3D realistic propagation simulation. Secondly, FEM is a powerful method for carrier transport simulation with complex geometries. Taking into account all this considerations, the best suited method for solving Maxwell equations but also for combining these equations with transport equations can be identified.

Previous works have been already done concerning hybrid full wave models. The review article by Grondin et al [3] provides a good overview of the work done in this area prior to 1999. More recently, some articles provide last development in these Topics ([9-11]). The authors present a Full Band hybrid model based on a Monte Carlo resolution of the BTE. In the most recent articles, the authors used a non uniform mesh to simulate an InGaAs HEMT (High Electron Mobility Transistor). But some progresses need also to be done to provide a

totally self consistent Maxwell and Boltzmann solver with a non uniform meshing. Moreover some critical mechanisms such as the quantum confinement of electrons in the HEMT channel and therefore the 2D transport of electrons are not taken into account yet in these hybrid models. The topic is difficult and many works have still to be done in next future.

The article is divided into three main parts. After this introduction, three software programs mainly devoted to the simulation of 3D electromagnetic equations in time-domain are presented in the first section. A short overview of these numerical tools is provided to the readers. These tools can solve a large variety of electromagnetic phenomena but we insist here on their specificity and on their main application domain. The first software FEM from LGEP [12] is based on a finite element method and the second software TEMSI-FD from XLIM [13] is based on a 3D FDTD method with constant mesh step. To finish this section, the propagation part of the last software MAXTRA3D is introduced and a briefly overview of its application domains is given. In the second section, the results provided by the different software on a basic structure (coplanar waveguide) are compared in order to exhibit their abilities to solve accurately the propagation phenomena. The third section shows some results of coupling Maxwell and Boltzmann equations within FDTD frame with MAXTRA3D applied to a Photoconductive Switch (PS) device.

II. SOFTWARE PRESENTATION (MAXTRA3D, TEMSI-FD, FEM)

A. FDTD Method

Both TEMSI-FD and MAXTRA3D software are based on FDTD method. This numerical method allows the solution of the set of Maxwell equations in a rigorous manner. The FDTD (finite difference time domain) technique developed by K.S. Yee [2] discretizes the two Maxwell curl equations directly in time and spatial domains, and put them into iterative forms. The physical geometry is divided into small (mostly rectangular or cubical) cells. Both time and spatial partial derivatives are handled with finite central difference approximation and the solution is obtained with a leapfrog scheme in iterative form. The characteristics of the medium are defined by three parameters that are permittivity, conductivity and permeability. Three electric and three magnetic field components are calculated at different locations of each cell [14]. Beside the spatial differences in field components, there is also a half time step difference between electric and magnetic field components, which is called as leapfrog computation. The numerical stability of the common FDTD scheme is ensured by respecting the relationship between the time and the spatial steps known as CFL (Courant-Friedrichs-Levy) stability criterion [2]. Besides, when using non regular mesh FDTD, it is important to reduce the numerical dispersion by choosing an appropriate value for the greatest spatial increment. It must be smaller than λ /10, where λ is the wavelength in the medium corresponding to the highest frequency of operation (≈1 THz). This numerical method owes its success to the power and simplicity that it provides. Furthermore, it is possible to achieve the response in a chosen frequency band in one calculation by using a pulse excitation. This cannot be achieved with a frequency domain method. On the other hand the Cartesian grid conforms badly to the real geometry, thus introducing so called stair stepping errors. Besides, one disadvantage of FDTD is that, in common with most other techniques, the problem size and the thinness of the mesh will dictate the computation time. The fineness of the grid is determined by the dimensions of the smallest feature to be modeled, and so codes that offer a variation in the mesh size over the structure would have an advantage. Also, the entire object, including most of the near field, must be covered.

TEMSI-FD is a numerical code based on 3D FDTD analysis that uses a uniform mesh. It has been developed at XLIM institute to simulate wide variety of wave-matter interaction problems. It has been coded with Fortran 90 language and is suited for vector processors (like Nec-SX8) and SMP architectures (Symmetric MultiProcessing) by development of OPEN-MP parallelism. Hence billion cells can be solved efficiently from eight Nec-SX8 processors of the CNRS/IDRIS (French intensive computing center). To truncate the computational domains for open-region wave propagation problems, TEMSI-FD use the Convolution Perfect Matched Layers (CPML) that offers a number of advantages. Specifically, the application of the CPML is completely independent of the host medium. Secondly, it is shown that the CPML is highly absorption of evanescent. TEMSI-FD has already been used to simulate various technologies: ground penetrating radars [15], Wifi transmission systems [16]. More generally, the software is devoted to EMC studies [17].

MAXTRA3D is 3D FDTD code using non-uniform mesh. It is developed by IEF laboratory in order to couple the Maxwell and the transport equations to model optoelectronic devices at terahertz frequency. For a question of simplicity, the same method (an integrated approach) was chosen for both propagation and transport equations. The transport property of the carriers is simulated within the frame of a 3D Drift-Diffusion approach or of a 3D Hydrodynamic model. Both models are solved using the FDTD numeric scheme as for the Maxwell equations. These transport models provide the local current density which constitutes the source term in Maxwell equations. All the data required for the transport model namely momentum and energy relaxation times, or effective mass versus average carrier energy are

calculated using a Monte-Carlo solver. When coupling a Monte-Carlo solver of the BTE with a FDTD base solver of Maxwell equations, we did observe a large variance of current density in the Monte Carlo code due to the strong variation of carrier concentration from cells below the optical pulse to the others. So the numerically determinist codes (Drift Diffusion and Hydrodynamic) were preferred instead of a stochastic solvers for the transport equation.

The current version of MAXTRA3D is numerically stable as a result of rewording of both material passages and current interfaces and calculating transport equations on whole transport region without imposing a fixed conductivity. The solver actually runs in a Dual-Core AMD Opteron with 16 GB Ram that allows the reduction of computation time as well as modular and optimal programming. The formulation used to truncate FDTD lattice in MAXTRA3D is the uniaxial anisotropic PML (UPML) introduced by S. D. Gedney [18]. This formulation has the advantage of keeping Maxwell's equations in their familiar form without the need of Berenger's field splitting. MAXTRA3D has been designed to simulate compact optoelectronic structures (Photoconductive switches). But the main goal of the software is to investigate the optoelectronic devices in conjunction with his propagation environment when operating in THz frequency.

B. Finite Element Method in Time Domain

A 3D finite element method for numerically solving the vector wave equation in time domain has been developed (FEM software) in the Laboratoire de Génie Electrique de Paris. The method uses Whitney's edge element on tetrahedral for the electric field interpolation. The time derivates are discretized by the Newmark Method, which allows an unconditionally stable scheme with second order accuracy. The finite-element time-domain method proposed by L. Pichon is mainly devoted to EMC studies [12] or antenna analysis [19]. Let's focus on the edge element approximation. The electromagnetic analysis is achieved by a finite element time domain approach. In the time domain, the electromagnetic problem is described with the double curl's equation. The studied domain is discretized with tetrahedral elements and the electric vector is written in terms of first order tetrahedral edge elements. The finite-element time-domain method provides increased geometrical flexibility by making elements conform to complex features. Furthermore, finite elements lead to irregular meshes and take easily inhomogeneous materials. The edge element method [20] can be considered as one of the most important methods developed 15 years after the FDTD method. The edge elements used in FEM preserve the energy and guarantee the continuity of the tangential field component across the interelement boundaries. The studied region in which the fields are computed must be bounded. In FEM a Silver-Müller absorbing condition (first order) was chosen because it was easy to implement and allowed us to obtain a satisfactory results [21].

The variational formulation of the electromagnetic problem described with the double curl's equation leads to an ordinary differential equation (ODE equation). In order to solve this equation step-by-step in time, the time derivates must be approximated by finite difference. We use the Newmark method. This standard approach (consistent method) leads to a high computational cost, since a matrix inversion is needed at each time step. So, there is a strong motivation to use mass-lumping technique [22] to deal with transient Maxwell's equations. In this approach, an explicit scheme is obtained allowing an important decrease in memory CPU time since no matrix inversion is required [23].

The next section is devoted to a comparison of Gaussian shape electric pulse propagation in a coplanar waveguide with MAXTRA3D, FEM and TEMSI-FD. The size of the structure has been chosen quite small because in FEM a matrix has to be invert at each time step.

III. MODELINGS

A. The Structure Selected for the Comparison

The modeled structure is a coplanar waveguide (CPW) with infinite ground planes. The length of the guide is 100µm, a width of the central band S and of the lateral ground planes is 10µm and the spacing between the central band and the ground planes W is 6µm.

The CPW is excited with two voltages placed in the ground plane surface. The electric fields of excitation are symmetrical with respect to the plane (xz), and each is placed between the central band and one of the ground planes (Fig. 1). The excitation is a Gaussian pulse with a Full Width at Half Maximum of 100 fs and maximum amplitude of 0.6 V. The next section describes the simulation environment for the different software namely the mesh and boundary condition parameters.

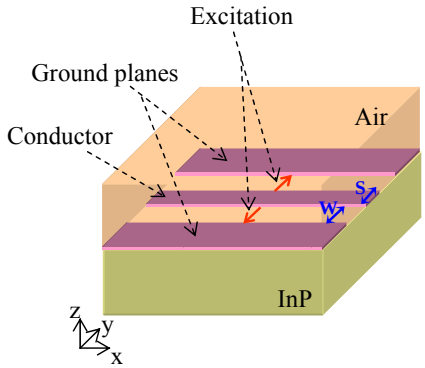

Fig. 1. CPW modeled structure.

B. Modeling Environment

Three different designs are used to mesh the CPW reference structure (Figs. 2 to 4). The first one is used by both TEMSI-FD and MAXTRA3D and it is the 1µm regular grid structure. The mesh dimensions are 100 × 62 × 100 respectively following x, y and z directions. The second one is used by MAXTRA3D and it is the variable orthogonal mesh scheme with 1 µm as the smallest mesh size and 40 × 24 × 40 mesh dimensions. The last one is used by the FEM and it is the tetrahedral finite element scheme with 1 µm as the smallest mesh size and 37128 elements (6947 nodes and 45542 edges). The time step estimated for TEMSI-FD and MAXTRA3D (with uniform or variable grid) is 1.88732fs with 2119 iterations. And for FEM, the time step is equal to 20 fs. The simulation duration chosen for all the simulations is 4 ps.

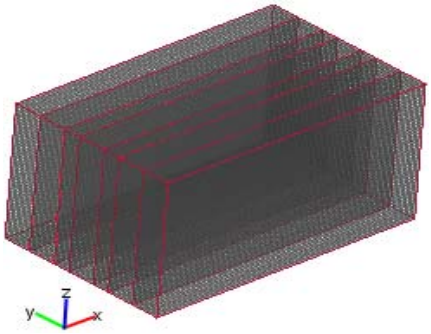

Fig. 2. Uniform mesh scheme (TEMSI-FD and MAXTRA3D).

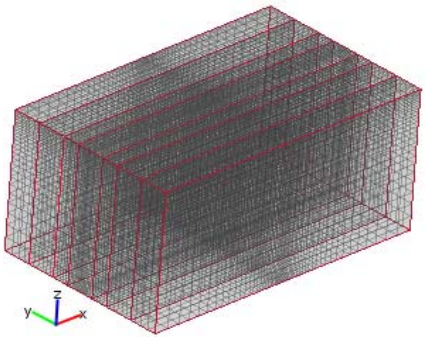

Fig. 3. Variable orthogonal mesh scheme (MAXTRA3D).

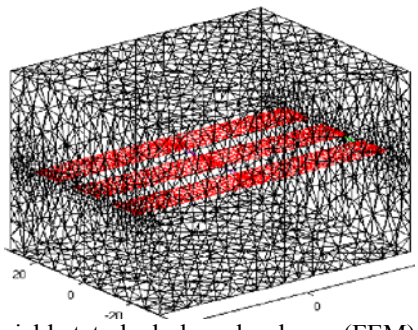

Fig. 4. Variable tetrahedral mesh scheme (FEM).

In open-region electromagnetic simulations, the computational domain has to be truncated by absorbing boundary conditions (ABC) to model the infinite space. In TEMSI-FD software, the ABC applied are Convolutional PML (CPML) conditions. In MAXTRA3D, the ABC adopted are PML and MUR conditions. And in the FEM software, the ABC are Silver-Müller conditions.

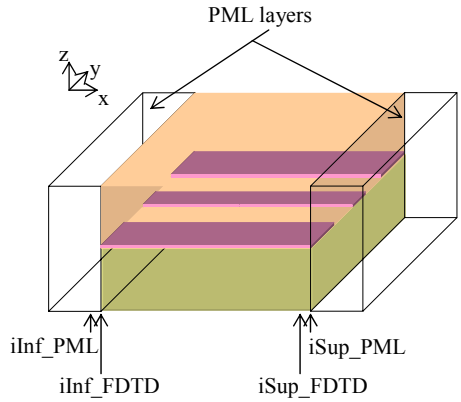

Fig. 5. PML layers added along the propagation direction.

The simulation results presented in the following section are carried out with TEMSI-FD, FEM and MAXTRA3D using the variable-mesh configuration for this last one (with MUR conditions at the first time and UPML conditions at the second time (Fig. 5)). All the FDTD simulations are running on a Dual-Core AMD Opteron with 16 GB RAM.

C. Results and Comparison

The results of calculations coming from the three software programs are obviously close but they also exhibit some differences. In order to identify those differences, we have selected two factors of merit: the amplitude error and the runtime. It is believed that the results provided by TEMSI-FD are most accurate since they are using a constant mesh (fewer numerical errors) and the most successful boundary conditions (CPML). Fig. 6 shows TEMSI-FD results of the wave propagation at three different distances from the excitation source (4 µm, 20 µm and 48 µm). One notes that the return to the equilibrium state (0 Volt) is free of any numerical oscillations contrary to the solution of Maxtra3D with MUR conditions (Fig. 7). In Fig. 8, one compares the results of the propagation at 20 µm from the excitation source for FEM, MAXTRA3D with MUR conditions and TEMSI-FD. One can notice that the result of Maxtra3D with MUR conditions have the same shape before 1 ps than TEMSI-FD result with an amplitude error of 0.015 V. However, the electric pulse shape calculated with MAXTRA3D seems to be like the one calculated with FEM. In fact, there are some oscillations before the return

to the equilibrium state. In order to point up the influence of the MAXTRA3D ABC on the simulation results, we display in Fig. 9 the same results than those in Fig. 8 but we substitute MAXTRA3D result that use MUR conditions with the one using UPML conditions. We can see a right correlation between MAXTRA3D and TEMSI-FD results. table 1 shows the differences between the results of TEMSI-FD, FEM and the two configuration of MAXTRA3D (with MUR or UPML) through two factors of merit. The first factor that is the amplitude error allows us to see that the deviation between the reference results of TEMSI-FD and the other software results increases when the ABC used are MUR conditions and can reach 13% close the edge of the structure. While the deviation is significantly smaller when using UPML conditions because it takes low value around 1%. This result is not original. PML conditions are known to provide far better result than MUR conditions. In addition, the runtime that is the second factor of merit indicates that using non uniform mesh for the FDTD method reduces the runtime and divides it by three (with UPML conditions) and even by four (with MUR conditions).

Table 1. The comparison of software results by using two factors of merit: the amplitude percent error at three different distances from the excitation source and the total runtime.

Software	Amplitude Percent Error			Total Runtime
	At 4 µm	At 20 µm	At 48 µm	
FEM	7.88 %	13.2 %	15.8 %	7mn10s
MAXTRA3D -MUR-	1.98 %	3.84 %	13.29 %	1mn13s
MAXTRA3D -UPML-	1.73 %	1.85 %	1.52 %	1mn45s
TEMSI-FD	Reference results			4mn52s

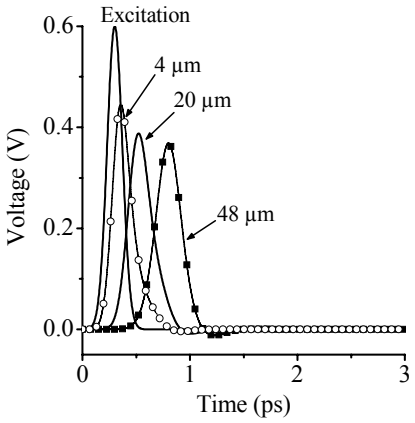

Fig. 6. Terahertz wave propagation along the CPW solved by TEMSI-FD software.

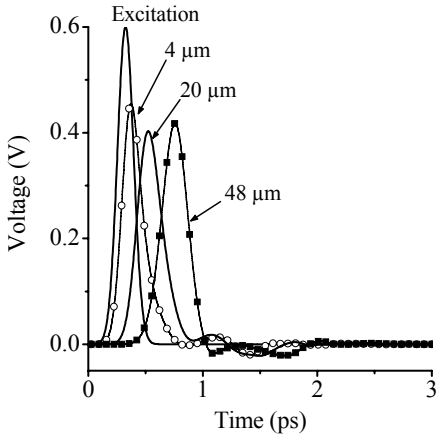

Fig. 7. Terahertz wave propagation along the CPW solved by MAXTRA3D software with MUR conditions.

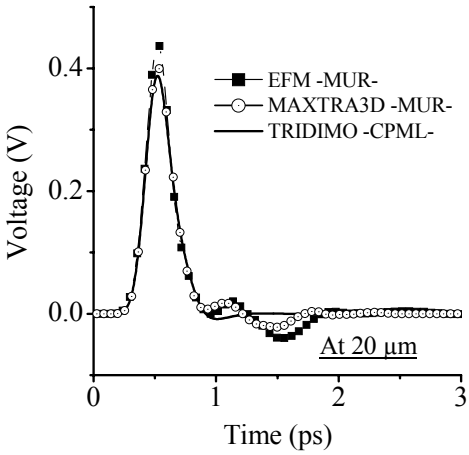

Fig. 8. The comparison of the electric pulse at 20 µm from the excitation source for the different simulators: FEM, MAXTRA3D with MUR conditions and TEMSI-FD.

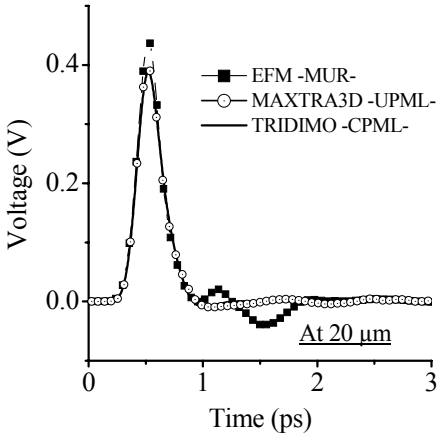

Fig. 9. The comparison of the electric pulse at 20 µm from the excitation source for the different simulators: FEM, MAXTRA3D with UPML conditions and TEMSI-FD.

IV. DISCUSSION

The comparison of TEMSI-FD, MAXTRA3D and FEM has been performed on a coplanar waveguide, in order to compare the three software programs only for their ability to simulate the wave propagation. TEMSI-FD, MAXTRA3D and the FEM software provide qualitatively and quantitatively almost the same results for the coplanar waveguide. The main difference is concentrated on the runtime. This is a key issue for the coupling of Maxwell equations with transport equations. MAXTRA3D has been developed for this purpose. This last paragraph is devoted to a very short discussion on the difficulties to identify a method that could be used to solve both the propagation and the transport (an integrated method). The previous results are good materials for the discussion. The FEM method has the longest runtime relatively to the FDTD method. The major weakness of finite element in time-domain comes from the presence of the mass matrix in front of the time derivative. At each time step in the Newmark scheme it is necessary to solve the linear system. The use of gradient conjugate leads to an algorithm with an O(n2) complexity if the number of unknowns is n. So the difference in runtime between the explicit FDTD method and the implicit FEM method will rapidly increase. Some authors have proposed to use a mass lumping technique [23] in order to get quasi-explicit method in time-domain like FDTD method. But even with a quasi-explicit scheme FEM methods require to manipulate matrix. The size of the matrix for the system Maxwell-Boltzmann exceeds 2 GB RAM. In the first and the second sections, the FDTD method with non uniform grid thanks to its runtime performances and its mesh fle1xibility has been identified as a good candidate for solving Maxwell equations.

These performances have been exploited to solve self consistently the Maxwell equations with Drift-Diffusion (DD) approach in a Coplanar Photoconductive Switch (PS) [1]. This coupling have already been investigated by some research teams ([3, 4, 24, 25]) but the defined spatial increment was great for the transport model because of the disproportion between the active layer size where the carrier transport happens and the environment skirting it. Here, THz voltage response of PS is briefly presented to illustrate this coupling with variable-mesh FDTD method. The details of the coupling will not be discussed here because it is not the main purpose of the present article. For more details about the coupling involving the Drift-Diffusion model one can refer to [1].

The simulated PS is described in fig. 10.a. The structure is a 2 µm broad gap in the center conductor of the waveguide. The active layer (gap) is a 0.3 µm depth In0.53Ga0.47As thin film. The CPW is the same structure as described previously at section 1 with a 76 µm depth InP substrate. A 2.5 V bias is applied between the Ohmic contacts located in CPW central strip.

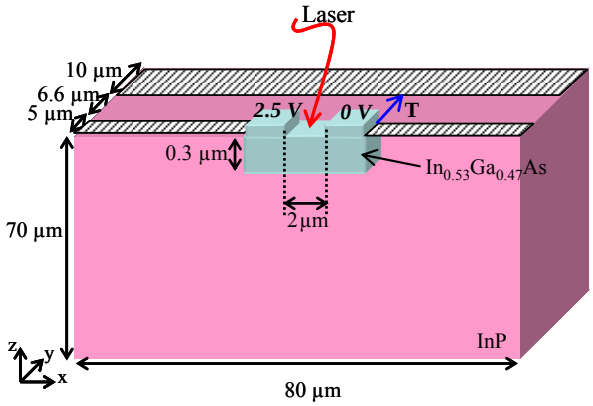

(a) Cross-section of the photoconductive switch

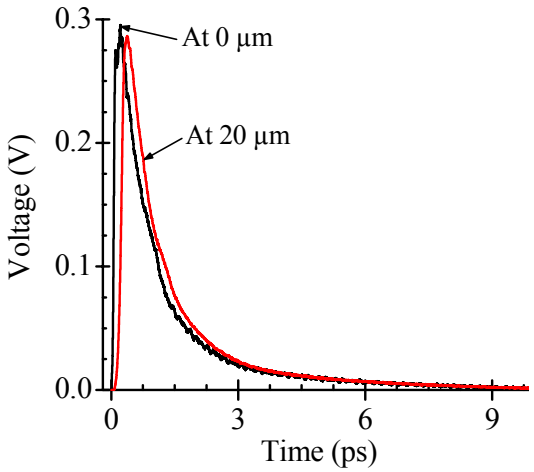

(b) Output voltage wave at 0 µm and 20 µm at the edge of the gap with MAXTRA_DD.

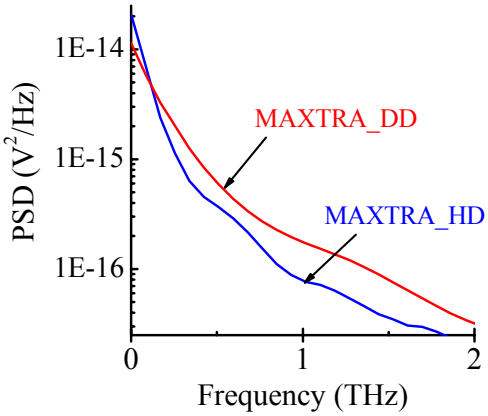

(c) Output power spectral density at 20 µm calculated with MAXTRA_DD and with MAXTRA_HD model

Fig. 10. Photoconductive switch and the terahertz response.

The gap is excited by a 30 fs Gaussian shape laser pulse at 1550 nm. It is necessary to couple the electromagnetic propagation to the photo-generated carrier transports because the shape of the THz pulse is mainly controlled by the mixing of the two physics. The voltage pulse presented in Fig. 10(a) is obtained following the integration path ($\vec{T}$) drawn in the same figure between the central metallization and the ground planes. The propagation of this voltage pulse is illustrated in Fig. 10(b) and it results from the drift-diffusion & full-wave (MAXTRA_DD) coupling [1]. At the edge of the gap (0 V), the generated electric pulse rises tanks to the conduction current and falls down when the number of individual and very local conduction current source decreases in each layer. This pulse propagates along the guide (the pulse at 20 µm from the gap is presented in Fig. 10(b) with time-lag and its peak widening represents a multimode propagating in the waveguide.

The Fig. 10(c) shows the comparison of the power spectral density (PSD) propagating calculated with MAXTRA_DD and MAXTRA_HD (the hydrodynamic & full-wave code) in the coplanar waveguide at 20µm from the edge of the gap. In the Hydrodynamic modeling, the inertial effect modeled through the momentum and energy relaxation times involves a smaller frequency extension of the PSD if one compares with Drift-Diffusion modeling. The maximum amplitude and the time shape of the voltage pulse modeled by the two simulators are slightly different.

On the other hand, the FDTD method has already been compared to mixed methods (FDTD-FVM [26] and FDTD-FEM [27]). To improve the accuracy of the PS active layer modeling, some mixed approaches should be investigated. But the difficulties linked to the use of other methods (TLM, FEM, FV, FIT, DGM) with transport model is far to be simple. The main advantage of these methods in MAXTRA3D is linked to transport equations and consequently the mesh refinement. However, care should be taken at execution runtime.

V. CONCLUSION

In this article, it has been demonstrated that the variable-mesh FDTD code (Maxtra3D) is one of the most powerful technique because of its ability to combine physics required different size of meshes. When focusing on the modeling of electromagnetic problem, the results for the comparison of 3D variable-mesh FDTD method showed close agreement with those obtained both by the 3D finite element method and the 3D constant step mesh FDTD method. Moreover, Maxtra3D enables to reduce the memory storage and the computational time without degrading results. Consequently FDTD scheme is tractable to perform a coupling between electromagnetism and carrier transport physics with a much reduced step meshing when necessary. For instance, in the active layer of a PS the mesh is forty times smaller than in the peripheral access waveguide. The variable-mesh FDTD method could be used for a large number of structures requiring a meshing both at the nanometer scale and at the micrometer scale. It could be interesting to investigate in the future new mixing numerical methods for the improvement of the coupling of physics.

The present work has been supported by national funding ANR-07-BLAN-0318.

REFERENCES

[1] M. Sirbu, S. Lepaul, and F. Aniel, "Coupling 3D Maxwell and Boltzmann equations for analyzing a terahertz photoconductive switch," *IEEE Trans. on Microwave Theory and Techniques*, vol. 53. no. 9, pp. 2991-2998, 2005.

[2] K. S. Yee, "Numerical solution of initial boundary value problems involving Maxwell's equations in isotropic media," *IEEE Trans. on Antennas and Propagation*, AP-14, pp. 302-307, 1966.

[3] P. B. Johns and R. L. Beurle, "Numerical solution of 2-dimensional scattering problems using a transmission line matrix," *Proc. IEE,* vol. 118, no. 9, pp. 1203-1208, 1971.

[4] T. Weiland, "A discretization method for the solution of Maxwell's equations for six-component fields," *Electron Comm.*, 31, 3, pp. 116-120, 1977.

[5] J. C. Nédélec, "Mixed finite elements in R3," *Numer. Math.*, vol. 35, pp. 315-341, 1980.

[6] M. Remaki, "A new finite volume scheme for solving Maxwell's system," *COMPEL*, 19:913-931, 2000.

[7] J. Hesthaven and T. Warburton, "Discontinuous Galerkin methods for time-domain Maxwell's equations: an introduction," *ACES Newletter*, vol. 19, pp. 10-29, 2004.

[8] R. O. Grondin, S. M. El-Ghazaly, and S. Goodnick, "A review of global modeling of charge transport in semiconductors and full-wave electromagnetics," *IEEE Trans. on Microwave Theory and Techniques*, vol. 47, no. 6, pp. 817-829, 1999.

[9] J. S. Ayubi-Moak, S. M. Goodnick, S. J. Aboud, M. Saraniti, and S. El-Ghazaly, "Coupling Maxwell's equations to full band particle-based simulators," *Journal of Computational Electronics*, vol. 2, pp. 183-190, 2003.

[10] J. S. Ayubi-Moak, S. M. Goodnick, and M. Saraniti, "Global modeling of high frequency devices," *Journal of Computational Electronics*, vol. 5, pp. 415-418, 2006.

[11] J. S. Ayubi-Moak, R. Akis, D. K. Ferry, S. M. Goodnick, N. Farralli, and M. Saraniti, "Towards the global modeling of InGaAs-based pseudomorphic

HEMTs," *Journal of Computational Electronics*, DOI 10.1007/s10825-008-0207-5, 2008.

[12] S. Benhassine, L. Pichon, and W. Tabbara, "An efficient finite-element time-domain method for the analysis of the coupling between wave and shielded enclosure," *IEEE Trans. on Magnetics*, vol. 38, no. 2, pp. 709-712, 2002.

[13] Ch. Guiffaut and A. Reineix, "Improvement of FDTD codes for EMC applications," *PIERS*, 2004 – 28-31 March 204- Pise - Italie – Session 41.

[14] A. Taflove and S. C. Hagness, *Computational electrodynamics the finite-difference time-domain method*. 3rd ed., London, UK: Artech House, Chapter 2, pp. 44-60, 2005.

[15] J. J. Berthelier, S. Bonaimé, V. Ciarletti, R. Clairquin, F. Dolon, A. Le Gall, D. Nevejans, R. Ney, and A. Reinex, "Initial results of the NETLANDER imaging ground penetrating radar operated on the Antarctic ice shelf," *Geophysical research letters*, 32, L22305, 10.1029/2005GL024203

[16] S. Reynaud, Y. Cocheril, A. Reineix, C. Guiffaut, and R. Vauzelle "A hybrid FDTD/UTD radiowave propagation modeling : Application to indoor channel simulations," *Microwave and Optical Technology Letters*, vol. 49, no. 6, pp. 1312-1320, 2007.

[17] A. Reineix, C. Guiffaut, F. Torres, B. Pecqueux, J. Ch. Joly, and P. Hoffmann, "VULCAIM : A Methodology Project for the Study of the Printed Circuit Boards Vulnerability," 2ème EMC – *IEEE Symposium on embedded EMC*, Session 3 "EMC Methodology" – 3C, Rouen, France – September 2005.

[18] J. A. Roden and S. D. Gedney, "Convolution PML (CPML): an efficient FDTD implementation of the CFS-PML for arbitrary media," *Microwave and Optical Technology Letters*, vol. 27, no. 5, pp. 334-338, December 2000.

[19] B. Essakhi, G. Akoun, and L. Pichon, "A global time domain circuit simulation of a microwave rectenna," *International Journal of Numerical Modeling Electronic Networks*, devices and fields, vol. 20, pp. 3-15, 2006.

[20] J. P. Webb, "Edge elements and what they can do for you," *IEEE Trans. on Magnetics*, vol. 25, no. 2, pp. 1460-1465, 1993.

[21] W. P. Carpes, L. Pichon, and A. Razek, "A finite element method for the numerical modeling of bounded and unbounded electromagnetic problems in the time domain," *International Journal of Numerical Modeling*, vol. 13, pp. 527-540, 2000.

[22] S. Cohen and P. Monk, "Gauss point mass lumping schemes for Maxwell's equations," *Numer. Meth. Part. Diff. Equns.*, vol. 14, pp. 63-68, 1998.

[23] S. Benhassine, W. P. Carpes, and L. Pichon, "Comparison of Mass Lumping Techniques for solving the 3D Maxwell's equations in the time domain," *IEEE Trans. on Magnetics*, vol. 36, no. 4, pp. 1548-1552, 2000.

[24] S. El-Ghazaly, R. P. Joshi, and R. O. Grondin, "Electromagnetic and transport considerations in subpicosecond photoconductive modeling," IEEE *Trans. on Microwave Theory and Techniques*, vol. 38, no. 5, pp. 629-637, 1990.

[25] M. A. Alsunaidi, S. M. S. Imtiaz, and S. El-Ghazaly, "Electromagnetic wave effects on microwave transistors using a full-wave time-domain model," *IEEE Trans. on Microwave Theory and Techniques*, vol. 44, no. 6, pp. 799-808, 1996.

[26] F. Edelvik and G. Ledfelt, "A comparison of time-domain hybrid solvers for complex scattering problems," *International Journal of Numerical Modeling: Electronic Networks*, Devices and Fields, vol. 15, pp. 475-487, 2002.

[27] S. Selleri, J. Y. Dauvignac, G. Pelosi, and Ch. Pichot, "Comparison between FDTD and hybrid FDTD-FETD applied to scattering and antenna problems," *Microwave and Optical Technology Letters*, vol. 18, no. 4, pp. 247-250, 1998.

Bouchra Tissafi was born in 1982 in Rabat, Morocco. She obtained the Dip. Eng. in electronics and telecommunications From Ecole Mohammadia d'Ingénieurs (EMI), Rabat, in 2004 and the M.S. degree in development of scientific instruments, optics and detection from the University of Rouen, France, in 2005. She is currently working toward the Ph.D. degree in physics at the University of Fundamental Electronics, Paris Sud University, Orsay, France. Her research interests are the interaction of electromagnetic field and carrier transport in the ultrafast optoelectronic devices.

Frédéric Aniel received the Ph-D degree from University Paris Sud, Orsay (UPS) in 1994. He worked on device development at France-Telecom CNET in 1995. He is currently Professor at UPS and heads research team at Institut D'electronique Fondamentale (IEF) on the analysis of physical phenomena in very high frequency devices up to THz range. His research activities are mainly on heterojunction devices based on III-V or SiGe materials. The emphasis is on device high frequency and optical characterizations both at 300K and at low temperatures supported by physical and electrical modeling.

Lionel Pichon was born in Romorantin, France, in 1961. He obtained the Dip. Eng. from Ecole Supérieure d'Ingénieurs en Electronique et Electrotechnique (ESIEE) in 1984. In 1985 he joined the Laboratoire de Génie Electrique de Paris LGEP associated to CNRS, SUPELEC, University of Paris-Sud, University of Pierre et Marie Curie where he earned a PhD in 1989. He is now Chargé de Recherche at the CNRS. His research interests include computational electromagnetics in microwaves, and electromagnetic compatibility.

Brahim Essakhi was born in Rabat, in 1974. He obtained a Master's in Applied Mathematics from Ecole Normale Supérieure (ENS) in Cachan (France) in 2001. In 2002 he joined the Laboratoire de Génie Electrique de Paris (LGEP) associated to CNRS, SUPELEC, University of Paris-Sud and University of Pierre et Marie Curie where he earned a PhD in 2005. His main scientific interests are numerical methods, wave propagation modeling, and electromagnetic compatibility.

Christophe Guiffaut was born on March 14, 1973 in Chateaubriant, France. He received the Ph.D. degree from the University of Rennes, France, in 2000. He joined The CNRS research center in 2002 and he integrated the same year the XLIM laboratory at the University of Limoges. He is currently working on the development of numerical modeling in electromagnetism.

Sébastien B. P. Lepaul received the M.S. and Ph.D. degrees in numerical and nonlinear analysis from the University of Paris VI, Paris, France, in 1993 and 1996 respectively. From 1996 to 1998, he was staff member of the University of Southampton, Southampton, U.K. He is currently a Research Engineer with Research and Development, Electricité de France (EDF), France, where he is on a team that deals with numerical analysis and models for electromagnetic field and solid mechanism simulations. Since 2004, he has been with the French National Center for Scientific Research (CNRS), Institute of Fundamental Electronics (IEF), Orsay, France, where he is currently the Associated Director of Research (DRA). He is also involved with the coupling of Maxwell's and Boltzmann's equations for optoelectronic applications.

Plane Wave Scattering by Two Dielectric Coated Conducting Strips

H. A. Ragheb and E. Hassan

Department of Electrical Engineering,
King Fahd University of Petroleum and Minerals
Dhahran, Saudi Arabia
hragheb@kfupm.edu.sa , ehassan@kfupm.edu.sa

Abstract — A plane electromagnetic wave scattered by two dielectric coated conducting strips is addressed here. Two methods of solutions are introduced. The first is based on solving the Helmholtz wave equation in terms of elliptical coordinates. As a result a Fourier series of radial and angular Mathieu functions of unknown coefficients in each region is obtained. The unknown coefficients can be obtained by enforcing the boundary conditions. The application of the boundary condition requires the use of the addition theorem of Mathieu function. The second method is based on an asymptotic approximate technique introduced by Karp and Russek for solving scattering by wide slit. Numerical examples are calculated using both methods and they are compared with each other. Excellent agreement between both cases is found.

Keywords — scattering by cylinders, coated strips, multiple scattering.

I. INTRODUCTION

Scattering from conducting strip and strip grating were the subject of many investigations [1-3]. Also the scattering of an electromagnetic wave from a single strip coated with a dielectric was addressed [4]. The multiple scattering of a plane electromagnetic wave by two strips of parallel edges was also presented in [5]. Recently, the scattering by two dielectric elliptic cylinders [6] and by metamaterial coated elliptic cylinders [7] has been addressed. The scattering of electromagnetic waves by coated strips has not been addressed yet. Therefore this paper presents two methods for solving the scattering of an electromagnetic plane wave by two dielectric coated conducting strips. This geometry can be used to simulate a dielectric coated conducting plane when the strips are close to each other. It could also have an application of diffraction by slit of dielectric coated conducting slits.

II. FORMULATION OF THE PROBLEM

Figure 1 shows two dielectric coated conducting strips of infinite length with their axes parallel to the z axis and widths $2d_1$ and $2d_2$, respectively. The dielectric coating have permittivities ε_1 and ε_2, and focal length is equal to the conducting strip width. The outer surface of the dielectric coating of the first strip has semi-major axis a_1 and semi-minor axis b_1, while a_2 and b_2 are, respectively denoting semi-major and semi-minor axes of the outer surface of the second strip coating. The center of the first coated strip is located at $x = c$ while the center of the second is located at $x = -c$ with respect to the global coordinates (x, y, z). The coated strips are inclined with respect to the x-axis by angle β_1 and β_2, respectively. In addition to the global coordinate system, two coordinate systems (x_1, y_1, z_1) and (x_2, y_2, z_2) are defined at the strip centers such that the plane of the first strip lies in the $x_1 - z_1$ plane while that of the second strip lies in the $x_2 - z_2$ plane.

A plane wave, with $e^{-j\omega t}$ time dependence, is incident with an angle φ_o with respect to the x-axis of the global coordinate system and polarized in z-direction, i.e.,

$$E_z^i = e^{-jk_o(x\cos\varphi_o + y\sin\varphi_o)} \tag{1}$$

where k_o is the wave number in free space. The incident wave can also be expressed in terms of the local coordinates at the coated strip centers. Upon doing the transformation and expanding it in terms of the elliptic wave function, one obtains,

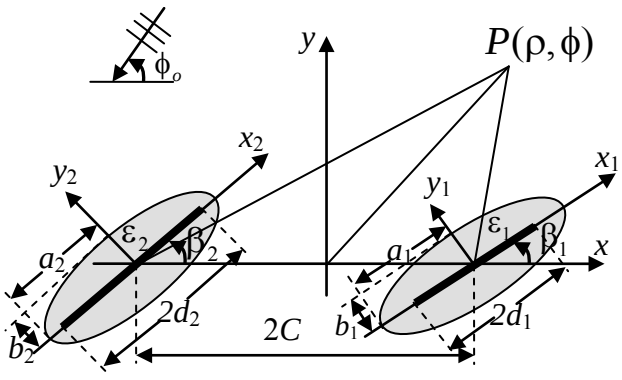

Fig. 1. Geometry of the problem.

$$E^{i}_{z_1} = \sqrt{8\pi}\, e^{-jkc\cos\varphi_o} \sum_{m=0}^{\infty} j^{-m} \left[\frac{1}{N^{(e)}_m(h_1)} Je_m(h_1,\zeta_1) S_m(h_1,\eta_1) S_m(h_1,\cos\varphi_{01}) + \frac{1}{N^{(o)}_m(h_1)} Jo_m(h_1,\zeta_1) S_m(h_1,\eta_1) S_m(h_1,\cos\varphi_{01}) \right] \quad (2)$$

and

$$E^{i}_{z_2} = \sqrt{8\pi}\, e^{jkc\cos\varphi_o} \sum_{m=0}^{\infty} j^{-m} \left[\frac{1}{N^{(e)}_m(h_2)} Je_m(h_2,\zeta_2) Se_m(h_2,\eta_2) Se_m(h_2,\cos\varphi_0) + \frac{1}{N^{(o)}_m(h_2)} Jo_m(h_2,\zeta_2) So_m(h_2,\eta_2) So_m(h_2,\cos\varphi_{02}) \right] \quad (3)$$

where

$$\varphi_{01} = \varphi_o - \beta_1 \quad \text{and} \quad \varphi_{02} = \varphi_o - \beta_2 \quad (4)$$

while $Je_m(h,\zeta)$ and $Jo_m(h,\zeta)$ are respectively even and odd modified Mathieu functions of the first kind and order m. Also, $Se_m(h,\eta)$ and $So_m(h,\eta)$ are respectively even and odd angular Mathieu functions of order m. $N^{(e)}_m(h)$ and $N^{(o)}_m(h)$ are even and odd normalized functions, respectively. The Mathieu functions arguments $h_i = k_o d_i$, $\zeta_i = \cosh u_i$ and $\eta_i = \cos v_i$ $(i = 1 \text{ or } 2)$ where u_i and v_i are elliptical cylindrical coordinates defined by,

$$\begin{aligned} x_i &= d_i \cosh u_i \cos v_i \\ y_i &= d_i \sinh u_i \sin v_i \\ z &= z_i \end{aligned} \quad (5)$$

The scattered electric field from the coated strips can be expressed in terms of the local coordinates at the center of each coated strip. Region (I) is inside the dielectric coating and region (II) is outside the dielectric coating. Scattered field from the first strip in region (I) is given by,

$$E^{(I)}_{z_1} = \sqrt{8\pi} \sum_{m=0}^{\infty} A^{(1)}_m \left\{ Je_m(H_1,\zeta_1) - \frac{Je_m(H_1,1)}{Ne_m(H_1,1)} Ne_m(H_1,\zeta_1) \right\} Se_m(H_1,\eta_1) \quad (6)$$

where $Ne_m(h,\zeta)$ is the even modified Mathieu function of the second kind and order m, $H_1 = k_1 d_1$ and $k_1 = k_o\sqrt{\mu_{r_1}\varepsilon_{r_1}}$, $A^{(1)}_m$ are unknown coefficients to be calculated from the boundary conditions. The boundary condition of the vanishing the tangential component of the electric field on the conducting strip surface was satisfied in equation (6).

Similarly, the scattered field from the second strip inside its dielectric is,

$$E^{(I)}_{z_2} = \sqrt{8\pi} \sum_{m=0}^{\infty} A^{(2)}_m \left\{ Je_m(H_2,\zeta_2) - \frac{Je_m(H_2,1)}{Ne_m(H_2,1)} Ne_m(H_2,\zeta_2) \right\} Se_m(H_2,\eta_2) \quad . (7)$$

The scattered field in region (II) from the first and the second strips are given by,

$$E^{(II)}_{z_1} = \sqrt{8\pi} \sum_{m=0}^{\infty} B^{(1)}_m\, He^{(1)}_m(h_1,\zeta_1) Se_m(h_1,\eta_1) \quad (8)$$

and

$$E^{(II)}_{z_2} = \sqrt{8\pi} \sum_{m=0}^{\infty} B^{(2)}_m\, He^{(1)}_m(h_2,\zeta_2) Se_m(h_2,\eta_2) \quad (9)$$

where

$$He^{(1)}_m(h,\zeta) = Je_m(h,\zeta) + j\, Ne_m(h,\zeta) .$$

In addition $B^{(1)}_m$ and $B^{(2)}_m$ are unknown coefficients to be calculated from the boundary conditions of homogenous tangential components of electric and magnetic fields at the surface of the dielectric coatings, i.e,

$$E^{inc}_{Z_1} + E^{(II)}_{z_1} + E^{(II)}_{z_2} = E^{(I)}_{z_1} \text{ on dielectric coating (I)} \quad (10)$$

$$E^{inc}_{Z_2} + E^{(II)}_{z_1} + E^{(II)}_{z_2} = E^{(I)}_{z_2} \text{ on dielectric coating (II),} \quad (11)$$

$$H^{inc}_{v_1} + H^{(II)}_{v_1} + H^{(II)}_{v_2} = H^{(I)}_{v_1} \text{ on dielectric coating (I),} \quad (12)$$

$$H^{inc}_{v_2} + H^{(II)}_{v_1} + H^{(II)}_{v_2} = H^{(I)}_{v_2} \text{ on dielectric coating (II).} \quad (13)$$

In order to apply the above boundary conditions, one has to transfer the electric and magnetic field expressions from one coordinate system to the other. This can be done using the addition theorem of the Mathieu functions, namely

- From coated strip (2) to coated strip (1),

$$He_m(a_2,\zeta_2)\,Se_m(a_2,\eta_2)=\sum_{q=0}^{\infty}Ke_{q,m}Je_q(a_1,\zeta_1)\,Se_q(a_1,\eta_1)+\sum_{q=1}^{\infty}We_{q,m}Jo_q(a_1,\zeta_1)\,So_q(a_1,\eta_1) \tag{14}$$

- From coated strip (1) to coated strip (2),

$$He_m(a_1,\zeta_1)\,Se_m(a_1,\eta_1)=\sum_{q=0}^{\infty}Ge_{q,m}\,Je_q(a_2,\zeta_2)\,Se_q(a_2,\eta_2)+\sum_{q=0}^{\infty}Fe_{q,m}Jo_q(a_2,\zeta_2)\,So_q(a_2,\eta_2) \tag{15}$$

where

$$Ke_{q,m}=\frac{\pi(j)^{q-m}}{N_q^{(e)}(a_1)}\sum_{s=0}^{\infty}\sum_{p=0}^{\infty}(-j)^{s-p}\,De_p^q(a_1)\,De_s^m(a_2)\,Be_{s,p} \tag{16}$$

$$We_{q,m}=\frac{\pi(j)^{q-m}}{N_q^{(o)}(a_1)}\sum_{s=0}^{\infty}\sum_{p=0}^{\infty}(-j)^{s-p}\,De_p^q(a_1)\;Do_s^m(a_2)\;Be_{s,p}, \tag{17}$$

$$Ge_{q,m}=\frac{\pi(j)^{q-m}}{N_q^{(e)}(a_2)}\sum_{s=0}^{\infty}\sum_{p=0}^{\infty}(-j)^{p-s}\,De_p^q(a_2)\;De_s^m(a_1)\;Ue_{s,p}, \tag{18}$$

$$Fe_{q,m}=\frac{\pi(j)^{q-m}}{N_q^{(o)}(a_2)}\sum_{s=0}^{\infty}\sum_{p=0}^{\infty}(-j)^{p-s}\,De_p^q(a_2)\;Do_s^m(a_1)\;Ue_{s,p}, \tag{19}$$

and

$$Be_{s,p}=H_{p-s}^{(1)}(kc)\;\cos(p\beta_1-s\beta_2)+(-1)^s H_{p+s}^{(1)}(kc)\;\cos(p\beta_1+s\beta_2), \tag{20}$$

$$Ue_{s,p}=H_{p-s}^{(1)}(kc)\cos(p\beta_2-s\beta_1)+(-1)^s H_{p+s}^{(1)}(kc)\cos(p\beta_2+s\beta_1). \tag{21}$$

Applying the boundary condition (11) one obtains,

$$\begin{aligned}&\sqrt{8\pi}\;e^{-jkc\cos\phi_o}\sum_{m=0}^{\infty}j^{-m}\Bigg[\frac{1}{N_m^{(e)}(h_1)}Je_m(h_1,\zeta_{10})\,Se_m(h_1,\eta_1)\,Se_m(h_1,\cos\phi_{o1})+\frac{1}{N_m^{(o)}(h_1)}Jo_m(h_1,\zeta_{10})\,So_m(h_1,\eta_1)\,So_m(h_1,\cos\phi_{o1})\Bigg]+\\&\sqrt{8\pi}\sum_{m=0}^{\infty}B_m^{(1)}\;He_m^{(1)}(h_1,\zeta_{10})\,Se_m(h_1,\eta_1)+\\&\sqrt{8\pi}\sum_{m=0}^{\infty}B_m^{(2)}\Bigg\{\sum_{q=0}^{\infty}Ke_{q,m}\,Je_q(h_1,\zeta_{10})Se_q(h_1,\eta_1)+\sum_{q=1}^{\infty}We_{q,m}Jo_q(h_1,\zeta_{10})\,So_q(h_1,\eta_1)\Bigg\}\\&=\sqrt{8\pi}\sum_{m=0}^{\infty}A_m^{(1)}\;\Bigg\{\;Je_m(H_1,\zeta_{10})-\frac{Je_m(H_1,1)}{Ne_m(H_1,1)}\,Ne_m(H_1,\zeta_{10})\;\Bigg\}Se_m(H_1,\eta_1).\end{aligned} \tag{22}$$

Multiplying both sides of equation (22) by $Se_l(H_1,\eta_1)$ and integrating over ν_1 from 0 to 2π, one obtains,

$$\begin{aligned}&e^{-jkc\cos\phi_o}\sum_{n=0}^{\infty}j^{-n}\frac{1}{N_n^{(e)}(h_1)}Je_n(h_1,\zeta_{10})\,Se_n(h_1,\cos\phi_{o1})M_{n,m}(h_1,H_1)+\sum_{n=0}^{\infty}B_n^{(1)}\;He_n^{(1)}(h_1,\zeta_{10})\,M_{n,m}(h_1,H_1)+\\&\sum_{n=0}^{\infty}B_n^{(2)}\;\sum_{q=0}^{\infty}Ke_{q,n}Je_q(h_1,\zeta_{10})\,M_{q,m}(h_1,H_1)\\&=A_m^{(1)}\;\Bigg\{\;Je_m(H_1,\zeta_{10})-\frac{Je_m(H_1,1)}{Ne_m(H_1,1)}\,Ne_m(H_1,\zeta_{10})\;\Bigg\}N_m^{(e)}(H_1)\end{aligned} \tag{23}$$

where

$$M_{n,m}(h_1,H_1)=\int_0^{2\pi}Se_n(h_1,\eta_1)\,Se_m(H_1,\eta_1)\,d\nu_1. \tag{24}$$

Applying boundary condition (12), one gets,

$$\sqrt{8\pi}\, e^{jkc\cos\phi_o}\sum_{m=0}^{\infty} j^{-m}\left[\frac{1}{N_m^{(e)}(h_2)}\, Je_m(h_2,\zeta_{20})\right.$$
$$Se_m(h_2,\eta_2)\, Se_m(h_2,\cos\phi_{o2}) + \frac{1}{N_m^{(o)}(h_2)}$$
$$\left. Jo_m(h_2,\zeta_{20})\, So_m(h_2,\eta_2)\, So_m(h_2,\cos\phi_{o2})\right]$$
$$+\sqrt{8\pi}\sum_{m=0}^{\infty} B_m^{(2)}\; He_m^{(1)}(h_2,\zeta_{20})\, Se_m(h_2,\eta_2) +$$
$$\sqrt{8\pi}\sum_{m=0}^{\infty} B_m^{(1)}\left\{\sum_{q=0}^{\infty} Ge_{q,m}\, Je_q(h_2,\zeta_{20})\, Se_q(h_2,\eta_2)\right.$$
$$\left.+\sum_{q=1}^{\infty} Fe_{q,m}\, Jo_q(h_{20},\zeta_2)\, So_q(h_2,\eta_2)\right\} =$$
$$\sqrt{8\pi}\sum_{m=0}^{\infty} A_m^{(2)}\left\{Je_m(H_2,\zeta_{20}) - \frac{Je_m(H_2,1)}{Ne_m(H_2,1)}\right.$$
$$\left. Ne_m(H_2,\zeta_{20})\right\} Se_m(H_2,\eta_2). \tag{24}$$

Multiplying both sides of equation (25) by $Se_l(h_2,\eta_2)$ and integrating over v_1 from 0 to 2π, one obtains,

$$e^{jkc\cos\phi_o}\sum_{n=0}^{\infty} j^{-n}\,\frac{1}{N_n^{(e)}(h_2)}\, Je_n(h_2,\zeta_{20})$$
$$Se_n(h_2,\cos\phi_{o2}) M_{n,m}(h_2,H_2)$$
$$+\sum_{n=0}^{\infty} B_n^{(2)}\; He_n^{(1)}(h_2,\zeta_{20})\, M_{n,m}(h_2,H_2) +$$
$$\sum_{n=0}^{\infty} B_n^{(1)}\sum_{q=0}^{\infty} Ge_{q,n}\, Je_q(h_2,\zeta_{20})\, M_{q,m}(h_2,H_2) \tag{25}$$
$$= A_m^{(2)}\left\{Je_m(H_2,\zeta_{20}) - \frac{Je_m(H_2,1)}{Ne_m(H_2,1)}\right.$$
$$\left. Ne_m(H_2,\zeta_{20})\right\} N_m^{(e)}(H_2)$$

where

$$M_{n,m}(h_2,H_2) = \int_0^{2\pi} Se_n(h_2,\eta_2)\; Se_m(H_2,\eta_2)\, dv_2. \tag{27}$$

The magnetic field component H_v is given by,

$$H_v = \frac{-jk}{\omega\mu d\sqrt{\zeta^2-\eta^2}}\,\frac{\partial E_z}{\partial u}. \tag{28}$$

Employing equation (28) and applying boundary condition (14) lead to,

$$\sqrt{8\pi}\, e^{-jkc\cos\phi_o}\sum_{m=0}^{\infty} j^{-m}\left[\frac{1}{N_m^{(e)}(h_1)}\, Je'_m(h_1,\zeta_{10})\right.$$
$$Se_m(h_1,\eta_1)\, Se_m(h_1,\cos\phi_{o1}) + \frac{1}{N_m^{(o)}(h_1)}$$
$$\left. Jo'_m(h_1,\zeta_{10}) So_m(h_1,\eta_1)\, So_m(h_1,\cos\phi_{o1})\right]$$
$$+\sqrt{8\pi}\sum_{m=0}^{\infty} B_m^{(1)}\; He_m^{(1)}{}'(h_1,\zeta_{10})\, Se_m(h_1,\eta_1) +$$
$$\sqrt{8\pi}\sum_{m=0}^{\infty} B_m^{(2)}\left\{\sum_{q=0}^{\infty} Ke_{q,m}\, Je'_q(h_1,\zeta_{10})\, Se_q(h_1,\eta_1)\right.$$
$$\left.+\sum_{q=1}^{\infty} We_{q,m} Jo'_q(h_1,\zeta_{10}) So_q(h_1,\eta_1)\right\}$$
$$= \sqrt{\frac{8\pi\varepsilon_{r1}}{\mu_{r1}}}\sum_{m=0}^{\infty} A_m^{(1)}\left\{Je'_m(H_1,\zeta_{10}) - \frac{Je_m(H_1,1)}{Ne_m(H_1,1)}\right.$$
$$\left. Ne'_m(H_1,\zeta_{10})\right\} Se_m(H_1,\eta_1). \tag{29}$$

Again multiplying both sides of equation (29) by $Se_l(h_1,\eta_1)$ and integrating over v_1 from 0 to 2π, one obtains,

$$e^{-jkc\cos\phi_o}\sum_{n=0}^{\infty} j^{-n}\,\frac{1}{N_n^{(e)}(h_1)}\, Je'_n(h_1,\zeta_{10})$$
$$Se_n(h_1,\cos\phi_{o1}) M_{n,m}(h_1,H_1)$$
$$+\sum_{n=0}^{\infty} B_n^{(1)}\; He_n^{(1)}{}'(h_1,\zeta_{10})\, M_{n,m}(h_1,H_1) +$$
$$\sum_{n=0}^{\infty} B_n^{(2)}\sum_{q=0}^{\infty} Ke_{q,n} Je'_q(h_1,\zeta_{10})\, M_{q,m}(h_1,H_1) \tag{30}$$
$$= \sqrt{\varepsilon_r}\, A_m^{(1)}\left\{Je'_m(H_1,\zeta_{10}) - \frac{Je_m(H_1,1)}{Ne_m(H_1,1)}\right.$$
$$\left. Ne'_m(H_1,\zeta_{10})\right\} N_m^{(e)}(H_1) \quad .$$

Similarly applying boundary condition (15), and employing the orthogonally of the Mathieu functions, results in,

$$
\begin{aligned}
& e^{jkc\cos\phi_o}\sum_{n=0}^{\infty} j^{-n}\frac{1}{N_n^{(e)}(h_2)}Je_n'(h_2,\zeta_{20})\\
& Se_n(h_2,\cos\phi_{o2})M_{n,m}(h_2,H_2)\\
& +\sum_{n=0}^{\infty}B_n^{(2)}\ He_n^{(1)}{}'(h_2,\zeta_{20})\,M_{n,m}(h_2,H_2)+\\
& \sum_{n=0}^{\infty}B_n^{(1)}\sum_{q=0}^{\infty}Ge_{q,n}Je_q'(h_2,\zeta_{20})\,M_{q,m}(h_2,H_2)\\
& =\sqrt{\varepsilon_r}A_m^{(2)}\left\{Je_m'(H_2,\zeta_{20})-\frac{Je_m(H_2,1)}{Ne_m(H_2,1)}\right.\\
& \left.Ne_m'(H_2,\zeta_{20})\right\}N_m^{(e)}(H_2).
\end{aligned}
\tag{31}
$$

From equations (23) and (30), one can obtain,

$$
\begin{aligned}
& -e^{-jkc\cos\phi_o}\sum_{n=0}^{\infty}j^{-n}\frac{1}{N_n^{(e)}(h_1)}Se_n(h_1,\cos\phi_{o1})\\
& M_{n,m}(h_1,H_1)\left[\frac{Je_n(h_1,\zeta_{10})}{X_m(H_1)}-\frac{Je_n'(h_1,\zeta_{10})}{X_m'(H_1)}\right]\\
& =\sum_{n=0}^{\infty}B_n^{(1)}\ M_{n,m}(h_1,H_1)\left[\frac{He_n^{(1)}(h_1,\zeta_{10})}{X_m(H_1)}\right.\\
& \left.-\frac{He_n^{(1)}{}'(h_1,\zeta_{10})}{X_m'(H_1)}\right]+\sum_{n=0}^{\infty}B_n^{(2)}\sum_{q=0}^{\infty}Ke_{q,n}M_{q,m}(h_1,H_1)\\
& \left[\frac{Je_q(h_1,\zeta_{10})}{X_m(H_1)}-\frac{Je_q'(h_1,\zeta_{10})}{X_m'(H_1)}\right]
\end{aligned}
\tag{32}
$$

where

$$
\begin{aligned}
X_m(H_1)=&\left\{Je_m(H_1,\zeta_{10})-\frac{Je_m(H_1,1)}{Ne_m(H_1,1)}\right.\\
&\left.Ne_m(H_1,\zeta_{10})\right\}N_m^{(e)}(H_1),
\end{aligned}
\tag{33}
$$

$$
\begin{aligned}
X_m'(H_1)=\sqrt{\varepsilon_r}&\left\{Je_m'(H_1,\zeta_{10})-\frac{Je_m(H_1,1)}{Ne_m(H_1,1)}\right.\\
&\left.Ne_m'(H_1,\zeta_{10})\right\}N_m^{(e)}(H_1).
\end{aligned}
\tag{34}
$$

From equations (26) and (31) one can find out that,

$$
\begin{aligned}
& -e^{jkc\cos\phi_o}\sum_{n=0}^{\infty}j^{-n}\frac{1}{N_n^{(e)}(h_2)}Se_n(h_2,\cos\phi_{o2})\\
& M_{n,m}(h_2,H_2)\left[\frac{Je_n(h_2,\zeta_{20})}{X_m(H_2)}-\frac{Je_n'(h_2,\zeta_{20})}{X_m'(H_2)}\right]=\\
& \sum_{n=0}^{\infty}B_n^{(1)}\sum_{q=0}^{\infty}Ke_{q,n}\ M_{q,m}(h_2,H_2)\left[\frac{Je_q(h_2,\zeta_{20})}{X_m(H_2)}\right.\\
& \left.-\frac{Je_q'(h_2,\zeta_{20})}{X_m'(H_2)}\right]+\sum_{n=0}^{\infty}B_n^{(2)}\ M_{n,m}(h_2,H_2)\\
& \left[\frac{He_n^{(1)}(h_2,\zeta_{20})}{X_m(H_2)}-\frac{He_n^{(1)}{}'(h_2,\zeta_{20})}{X_m'(H_2)}\right]
\end{aligned}
\tag{35}
$$

where

$$
\begin{aligned}
X_m(H_2)=&\left\{Je_m(H_2,\zeta_{20})-\frac{Je_m(H_2,1)}{Ne_m(H_2,1)}\right.\\
&\left.Ne_m(H_2,\zeta_{20})\right\}N_m^{(e)}(H_2),
\end{aligned}
\tag{36}
$$

$$
\begin{aligned}
X_m'(H_2)=\sqrt{\varepsilon_r}&\left\{Je_m'(H_2,\zeta_{20})-\frac{Je_m(H_2,1)}{Ne_m(H_2,1)}\right.\\
&\left.Ne_m'(H_2,\zeta_{20})\right\}N_m^{(e)}(H_2).
\end{aligned}
\tag{37}
$$

Equations (32) and (35) can be written in a matrix form,

$$
\begin{bmatrix} C_{m,n}^{(11)} & C_{m,n}^{(12)} \\ C_{m,n}^{(21)} & C_{m,n}^{(22)} \end{bmatrix}\begin{bmatrix} B_n^{(1)} \\ B_n^{(2)} \end{bmatrix}=\begin{bmatrix} Z_m^{(1)} \\ Z_m^{(2)} \end{bmatrix}
\tag{38}
$$

where

$$
\begin{aligned}
Z_m^{(1)}=&-e^{-jkc\cos\phi_o}\sum_{n=0}^{\infty}j^{-n}\frac{1}{N_n^{(e)}(h_1)}\\
&Se_n(h_1,\cos\phi_{o1})M_{n,m}(h_1,H_1)\left[\frac{Je_n(h_1,\zeta_{10})}{X_m(H_1)}\right.\\
&\left.-\frac{Je_n'(h_1,\zeta_{10})}{X_m'(H_1)}\right],
\end{aligned}
\tag{39}
$$

$$
\begin{aligned}
C_{m,n}^{(11)}=&M_{n,m}(h_1,H_1)\left[\frac{He_n^{(1)}(h_1,\zeta_{10})}{X_m(H_1)}\right.\\
&\left.-\frac{He_n^{(1)}{}'(h_1,\zeta_{10})}{X_m'(H_1)}\right],
\end{aligned}
\tag{40}
$$

$$C_{m,n}^{(12)} = \sum_{q=0}^{\infty} Ke_{q,n}\ M_{q,m}(h_1, H_1) \left[\frac{Je_q(h_1,\zeta_{10})}{X_m(H_1)} - \frac{Je_q(h_1,\zeta_{10})}{X'_m(H_1)} \right], \quad (41)$$

$$Z_m^{(2)} = -e^{jkc\cos\phi_o} \sum_{n=0}^{\infty} j^{-n} \frac{1}{N_n^{(e)}(h_2)} Se_n(h_2, \cos\phi_{o2}) M_{n,m}(h_2, H_2) \left[\frac{Je_n(h_2,\zeta_{20})}{X_m(H_2)} - \frac{Je'_n(h_2,\zeta_{20})}{X'_m(H_2)} \right], \quad (42)$$

$$C_{m,n}^{(21)} = \sum_{q=0}^{\infty} Ge_{q,n} M_{q,m}(h_2, H_2) \left[\frac{Je_q(h_2,\zeta_{20})}{X_m(H_2)} - \frac{Je'_q(h_2,\zeta_{20})}{X'_m(H_2)} \right], \quad (43)$$

$$C_{m,n}^{(22)} = M_{n,m}(h_2, H_2) \left[\frac{He_n^{(1)}(h_2,\zeta_{20})}{X_m(H_2)} - \frac{He_n^{(1)}{}'(h_2,\zeta_{20})}{X'_m(H_2)} \right]. \quad (44)$$

Once we calculate the unknown coefficients the total scattered field can be calculated from,

$$E_z^{(s)} = \sqrt{8\pi} \left\{ \sum_{m=0}^{\infty} B_m^{(1)}\ He_m^{(1)}(h_1,\zeta_1)\ Se_m(h_1,\eta_1) + \sum_{m=0}^{\infty} B_m^{(2)}\ He_m^{(1)}(h_2,\zeta_2) Se_m(h_2,\eta_2) \right\}. \quad (45)$$

The far field can be evaluated using the asymptotic expansion of $He_m^{(1)}(h,\zeta)$ which is given by,

$$He_m^{(1)}(h,\zeta) = \frac{1}{\sqrt{h\zeta}} e^{j(h\zeta-(2m+1/4)\pi)} \quad . \quad (46)$$

If $h\zeta$ is very large it can be represented in terms of circular cylindrical coordinates, where $h_1\zeta_1 = k_o\rho_1$ and $h_2\zeta_2 = k_o\rho_2$. In this case the total scattered field is given by,

$$E_Z^{(s)} = \sqrt{\frac{2}{\pi k_o \rho}}\ \ e^{jk_o\rho}\ P(\varphi) \quad (47)$$

$$E_{total}^{s} = E_{z_1}^{(II)} + E_{z_2}^{(II)} = c(k\rho)\, P(\varphi),$$

$$c(k\rho) = \sqrt{2/\pi k\rho}\ \ e^{jk\rho}\, e^{-j\pi/4} \quad , \quad (48)$$

$$P(\phi) = 2\pi \sum_{m=0}^{\infty} (-j)^m \{ B_m^{(1)} Se_m(h_1, \cos(\phi-\beta_1)) e^{-jkc\cos\phi} + B_m^{(2)} Se_m(h_2, \cos(\phi-\beta_2)) e^{jkc\cos\phi} \}. \quad (49)$$

The echo width is,

$$W(\phi) = \frac{4}{k} |\ P(\phi)\ |^2 \ . \quad (50)$$

III. APPROXIMATE SOLUTION

The approximate solution is based on a technique that was established by Karp and Russek [8]. Such a technique considers the scattered field from each coated strip as a sum of scattered field from that coated strip due to a plane wave incident plus the scattered field due to a line source of unknown intensity located at the center of the other coated strip. The factious line source accounts in an approximate sense for the multiple scattering between the two coated strips. In order to apply this technique one needs to obtain the far scattered field from one coated strip due to both a plane wave incident and a line source. In such a case, consider a plane wave given by equation (1), is incident on a coated strip located at x_i and $y = 0$, the coated strip is inclined by an angle β_i on the x-axis. The conducting strip has a width $2d_i$ and the coating dielectric constant is ε_i. The scattered field in the region outside the coated cylinder can be written as,

$$E_z^{(s)} = \sqrt{8\pi} \sum_{n=0}^{\infty} A_n^{(i)} He_n^{(1)}(h_i,\zeta_i) Se_n(h_i,\eta_i) \quad (51)$$

while the electric field inside the coating is,

$$E_z^{(I)} = \sqrt{8\pi} \sum_{n=0}^{\infty} B_n^{(i)} \left\{ Je_n(H_i,\zeta_i) - \frac{Je_n(H_i,1)}{Ne_n(H_i,1)} Ne_n(H_i,\zeta_i) \right\} Se_n(H_i,\eta_i). \quad (52)$$

Matching the boundary condition gives,

$$\sqrt{8\pi}\, e^{-jkx_i\cos\phi_o}\sum_{n=0}^{\infty} j^{-n}\Bigg[\frac{1}{N_n^{(e)}(h_i)}Je_n(h_i,\zeta_{0i})\, Se_n(h_i,\eta_i)\, Se_n(h_i,\cos\phi_{0i})+\frac{1}{N_n^{(o)}(h_i)}Jo_n(h_i,\zeta_{0i})\, So_n(h_i,\eta_i)\, So_n(h_i,\cos\phi_{0i})\Bigg] \quad (53)$$

$$+\sqrt{8\pi}\sum_{n=0}^{\infty}A_n^{(i)}He_n^{(1)}(h_i,\zeta_{0i})\, Se_n(h_i,\eta_i) = \sqrt{8\pi}\sum_{n=0}^{\infty}B_n^{(i)}\Bigg\{ Je_n(H_i,\zeta_{0i})-\frac{Je_n(H_i,1)}{Ne_n(H_i,1)}Ne_n(H_i,\zeta_{0i})\Bigg\}Se_n(H_i,\eta_i).$$

Multiplying both sides of equation (53) by $Se_m(H_1,\eta_i)$ and integrating over ν_i from 0 to 2π, one obtains,

$$e^{-jkx_i\cos\phi_o}\sum_{n=0}^{\infty} j^{-n}\Bigg\{\frac{1}{N_n^{(e)}(h_i)}Je_n(h_i,\zeta_{0i})\, Se_n(h_i,\cos\phi_{0i})M_{n,m}(h_i,H_i)\Bigg\} + \sum_{n=0}^{\infty}A_n^{(i)}He_n^{(1)}(h_i,\zeta_{0i})\, M_{n,m}(h_i,H_i) = B_m^{(i)}\Bigg\{Je_m(H_i,\zeta_{0i})-\frac{Je_m(H_i,1)}{Ne_m(H_i,1)}Ne_m(H_i,\zeta_{0i})\Bigg\}N_m^{(e)}(H_1). \quad (54)$$

Similarly matching the boundary condition corresponding to H_v, one can get,

$$e^{-jkx_i\cos\phi_o}\sum_{n=0}^{\infty} j^{-n}\Bigg\{\frac{1}{N_n^{(e)}(h_i)}Je_n'(h_i,\zeta_{0i})\, Se_n(h_i,\cos\phi_{0i})M_{n,m}(h_i,H_i)+\sum_{n=0}^{\infty}A_n^{(i)}He_n^{(1)}{}'(h_i,\zeta_{0i})M_{n,m}(h_i,H_i)=\sqrt{\varepsilon_{r_i}}B_m^{(i)} \quad (55)$$

$$\Big\{Je_m'(H_i,\zeta_{0i})-\frac{Je_m(H_i,1)}{Ne_m(H_i,1)}Ne_m'(H_i,\zeta_{0i})\Big\}N_m^{(e)}(H_1).$$

From equations (54) and (55), one obtains,

$$\sum_{n=0}^{\infty}A_n^{(i)}\Bigg\{\frac{He_n^{(1)}(h_i,\zeta_{0i})}{X_m(H_i)}-\frac{He_n'^{(1)}(h_i,\zeta_{0i})}{X_m'(H_i)}\Bigg\} M_{n,m}(h_i,H_i) = -e^{-jkx_i\cos\phi_o}\sum_{n=0}^{\infty}j^{-n}\frac{1}{N_n^{(e)}(h_i)} \Bigg\{\frac{Je_n(h_i,\zeta_{0i})}{X_m(H_i)}-\frac{Je_n'(h_i,\zeta_{0i})}{X_m'(H_i)}\Bigg\} Se_n(h_i,\cos\phi_{0i})M_{n,m}(h_i,H_i) \quad (56)$$

where

$$X_m(H_i)=\Bigg\{Je_m(H_i,\zeta_{0i})-\frac{Je_m(H_i,1)}{Ne_m(H_i,1)}Ne_m(H_i,\zeta_{0i})\Bigg\}N_m^{(e)}(H_i),$$

$$X_m'(H_i)=\sqrt{\varepsilon_r}\Big\{\Big\}\Bigg\{Je_m'(H_i,\zeta_{0i})-\frac{Je_m(H_i,1)}{Ne_m(H_i,1)}Ne_m'(H_i,\zeta_{0i})\Bigg\}N_m^{(e)}(H_i).$$

Equation (56) can be written a matrix form as,

$$[F_{m,n}][A_m]=[Y_m] \quad (57)$$

where

$$F_{m,n}=\Bigg\{\frac{He_n^{(1)}(h_i,\zeta_{0i})}{X_m(H_i)}-\frac{He_n'^{(1)}(h_i,\zeta_{0i})}{X_m'(H_i)}\Bigg\}M_{n,m}(h_i,H_i), \quad (58)$$

$$Y_m=-e^{-jkx_i\cos\phi_o}\sum_{n=0}^{\infty}j^{-n}\frac{1}{N_n^{(e)}(h_i)}\Bigg\{\frac{Je_n(h_i,\zeta_{0i})}{X_m(H_i)}-\frac{Je_n'(h_i,\zeta_{0i})}{X_m'(H_i)}\Bigg\}Se_n(h_i,\cos\phi_{0i})M_{n,m}(h_i,H_i). \quad (59)$$

Once the coefficients are calculated the scattered electric field in the outer region is given by equation (51). Since $He_m^{(1)}(h,\zeta)=\frac{1}{\sqrt{h\zeta}}e^{j(h\zeta-(2m+1/4)\pi)}$ and for large $h\zeta$ it can be represented in terms of circular cylindrical coordinates, where $h_i\zeta_i=k_o\rho_i$. In this case the total scattered field is given by,

$$E_z^{(s)} = \sqrt{8\pi}\,\frac{e^{jk_i\rho_o}}{\sqrt{k_o\rho_i}}\sum_{n=0}^{\infty}(-j)^n A_n^{(i)} Se_n(h_i,\eta_i) = c(k_o\rho_i)\,f(h_i,x_i,\phi_i,\phi_{0i}) \tag{60}$$

where

$$f(h_i,x_i,\phi_i,\phi_{0i}) = 2\pi\sum_{m=0}^{\infty}(-j)^m A_m^{(i)} Se_m(h_i,\cos\phi_i). \tag{61}$$

Line source excitation

Consider a line source placed at $(x_{0k},0)$ with respect to the coordinates at the center of strip 1 ($i=1$) or at the center of strip 2 ($i=2$), then the *z*-component of the electric field due to such a line source can be expressed as,

$$E_z^{inc} = 4\left[\sum_{m=0}^{\infty}\frac{Se_m(h_i,\eta_{0k})}{N_m^{(e)}(h_i)}\;Se_m(h_1,\eta_i)\begin{cases}Je_m(h_i,\zeta_{0k})He_m^{(1)}(h_i,\zeta_i) & u>u_{0k}\\ Je_m(h_i,\zeta_i)He_m^{(1)}(h_i,\zeta_{0k}) & u<u_{0k}\end{cases} + \frac{So_m(h_i,\eta_{0k})}{N_m^{(o)}(h_i)}\;So_m(h_i,\eta_i)\begin{cases}Jo_m(h_i,\zeta_{0k})Ho_m^{(1)}(h_i,\zeta_i) & u>u_{0k}\\ Jo_m(h_i,\zeta_i)Ho_m^{(1)}(h_i,\zeta_{0k}) & u<u_{0k}\end{cases}\right] \tag{62}$$

where *k* takes the values 1 or 2.

$$\zeta_{0k} = \left[\frac{1}{2}\left(\frac{s_{0k}^2}{d_i^2}+1\right) + \left(\frac{1}{4}\left(\frac{s_{0k}^2}{d_i^2}+1\right)^2 - \frac{x_{0k}'^2}{d_i^2}\right)^{1/2}\right]^{1/2}, \tag{63}$$

$$\eta_{0k} = \frac{x_{0k}'}{\zeta_{0k}d_i}, \tag{64}$$

$$s_{0k} = \left((x_i-x_{0k})^2+(y_i-y_{0k})^2\right)^{1/2}, \tag{65}$$

$$\psi_{0k} = \tan^{-1}\left[\frac{y_{0k}-y_i}{x_{0k}-x_i}\right]-\beta_i, \tag{66}$$

$$x_{0k}' = s_{0k}\cos\psi_{0k} \quad y_{0k}' = s_{0k}\sin\psi_{0k}. \tag{67}$$

The scattered field in the region outside the coated cylinder can be written as,

$$E_z^{(s)} = 4\sum_{n=0}^{\infty}C_n^{(i)}He_n^{(1)}(h_i,\zeta_i)\;Se_n(h_i,\eta_i). \tag{68}$$

While the electric field inside the coating is given by,

$$E_z^{(I)} = 4\sum_{n=0}^{\infty}D_n^{(i)}\left\{\;Je_n(H_i,\zeta_i) - \frac{Je_n(H_i,1)}{Ne_n(H_i,1)}Ne_n(H_i,\zeta_i)\right\}Se_n(H_i,\eta_i). \tag{69}$$

Matching the boundary condition gives,

$$\begin{aligned}&\sum_{n=0}^{\infty}\frac{Se_n(h_i,\eta_{0k})}{N_n^{(e)}(h_i)}\;Se_n(h_1,\eta_i)Je_n(h_i,\zeta_{0i})\\ &\quad He_n^{(1)}(h_i,\zeta_{0k}) + \frac{So_n(h_i,\eta_{0k})}{N_n^{(o)}(h_i)}\\ &\quad So_n(h_i,\eta_i)Jo_n(h_i,\zeta_{0i})Ho_n^{(1)}(h_i,\zeta_{0k})\\ &\quad + \sum_{n=0}^{\infty}C_n^{(i)}He_n^{(1)}(h_i,\zeta_{0i})\;Se_n(h_i,\eta_i)\\ &\quad = \sum_{n=0}^{\infty}D_n^{(i)}\left\{\;Je_n(H_i,\zeta_{0i}) - \frac{Je_n(H_i,1)}{Ne_n(H_i,1)}\right.\\ &\quad \left.Ne_n(H_i,\zeta_{0i})\;\right\}Se_n(H_i,\eta_i).\end{aligned} \tag{70}$$

Multiplying both sides of equation (70) by $Se_m(H_1,\eta_i)$ and integrating over ν_i from 0 to 2π, one obtains,

$$\begin{aligned}&\sum_{n=0}^{\infty}\frac{He_n^{(1)}(h_i,\zeta_{0k})}{N_n^{(e)}(h_i)}Je_n(h_i,\zeta_{0i})\;Se_n(h_i,\eta_{0k})\\ &\quad M_{n,m}(h_i,H_i) + \sum_{n=0}^{\infty}C_n^{(i)}\;He_n^{(1)}(h_i,\zeta_{0i})\\ &\quad M_{n,m}(h_i,H_i) = D_m^{(i)}\left\{Je_m(H_i,\zeta_{0i})\right.\\ &\quad \left.-\frac{Je_m(H_i,1)}{Ne_m(H_i,1)}Ne_m(H_i,\zeta_{0i})\;\right\}N_m^{(e)}(H_1).\end{aligned} \tag{71}$$

Similarly matching the boundary condition corresponding to H_v, one can get,

$$\sum_{n=0}^{\infty}\frac{He_n^{(1)}(h_i,\zeta_{0k})}{N_n^{(e)}(h_i)}Je_n'(h_i,\zeta_{0i})\,Se_n(h_i,\eta_{0k})$$
$$M_{n,m}(h_i,H_i)+\sum_{n=0}^{\infty}C_n^{(i)}He_n'^{(1)}(h_i,\zeta_{0i})$$
$$M_{n,m}(h_i,H_i)=D_m^{(i)}\Big\{\;Je_m'(H_i,\zeta_{0i})-$$
$$\frac{Je_m(H_i,1)}{Ne_m(H_i,1)}Ne_m'(H_i,\zeta_{0i})\Big\}N_m^{(e)}(H_1). \tag{72}$$

Solving equations (71) and (72), one gets,

$$\sum_{n=0}^{\infty}C_n^{(i)}\left\{\frac{He_n^{(1)}(h_i,\zeta_{0i})}{X_m(H_i)}-\frac{He_n'^{(1)}(h_i,\zeta_{0i})}{X_m'(H_i)}\right\}$$
$$M_{n,m}(h_i,H_i)=-\sum_{n=0}^{\infty}\frac{He_n^{(1)}(h_i,\zeta_{0k})}{N_n^{(e)}(h_i)} \tag{73}$$
$$\left\{\frac{Je_n(h_i,\zeta_{0i})}{X_m(H_i)}-\frac{Je_n'(h_i,\zeta_{0i})}{X_m'(H_i)}\right\}$$
$$Se_n(h_i,\eta_{0k})M_{n,m}(h_i,H_i).$$

Equation (73) can be written in a matrix form similar to equation (57), where,

$$Y_m=-\sum_{n=0}^{\infty}\frac{He_n^{(1)}(h_i,\zeta_{0k})}{N_n^{(e)}(h_i)}$$
$$\left\{\frac{Je_n(h_i,\zeta_{0i})}{X_m(H_i)}-\frac{Je_n'(h_i,\zeta_{0i})}{X_m'(H_i)}\right\} \tag{74}$$
$$Se_n(h_i,\eta_{0k})M_{n,m}(h_i,H_i).$$

Once the coefficients are calculated the scattered electric field in the outer region is given by equation (51).

$$E_z^{(s)}=\sqrt{8\pi}\,\frac{e^{jk_i\rho_i}}{\sqrt{k_o\rho_i}}\sum_{n=0}^{\infty}(-j)^nC_n^{(i)}Se_n(h_i,\eta_i) \tag{75}$$
$$=c(k_o\rho_i)g(h_i,\phi_i,\zeta_{ok},\eta_{ok}),$$

where

$$g(h_i,\phi_i,\zeta_{0k},\eta_{0k})=\sqrt{8\pi}\sum_{m=0}^{\infty}(-j)^mC_m^{(i)} \tag{76}$$
$$Se_m(h_i,\cos\phi_i).$$

Now consider the problem of the two strips shown in Fig. 1. Assuming a fictitious line source C_1 at the center of the first strip and another line source C_2 at the center of the second strip the far scattered field from the first strip is given by,

$$E_1^s=c(k_o\rho_1)\big[f(h_1,x_1,\phi_1,\phi_{01})$$
$$+C_2g(h_1,\phi_1,\zeta_{01},\eta_{01})\big]. \tag{77}$$

Similarly, the far scattered field due to the second strip is given by,

$$E_2^s=c(k_o\rho_2)\big[f(h_2,x_2,\phi_2,\phi_{02})$$
$$+C_1g(h_2,\phi_2,\zeta_{02},\eta_{02})\big]. \tag{78}$$

The partial scattered field from the first strip due to the scattered field from the second strip can be determined by considering the scattered field from the second strip as the intensity of a line source at $\phi_2=-\beta_2$ times the well-known response [8], i.e.,

$$E_{12}^s=c(k_o\rho_1)\big[f(h_2,x_2,-\beta_2,\phi_{02})$$
$$+C_1g(h_2,-\beta_2,\zeta_{01},\eta_{01})\big]g(h_1,\phi_1,\zeta_{02},\eta_{02}). \tag{79}$$

On the other hand this partial scattered field is given by,

$$E_{12}^s=C_2\;c(k_o\rho_1)\,g(h_1,\phi_1,\zeta_{02},\eta_{02})\;. \tag{80}$$

Using equivalence between equations (79) and (80), one obtains,

$$f(h_2,x_2,-\beta_2,\phi_{02})$$
$$+C_1g(h_2,-\beta_2,\zeta_{01},\eta_{01})=C_2. \tag{81}$$

In a similar way one can obtain,

$$f(h_1,x_1,\pi-\beta_1,\phi_{01})+C_2$$
$$g(h_1,\pi-\beta_1,\zeta_{02},\eta_{02})=C_1. \tag{82}$$

Solving equations (81) and (82), one can get,

$$C_1=\frac{Nu_1}{Du_1} \tag{83}$$

where

$$Nu_1=f(h_1,x_1,\pi-\beta_1,\phi_{01})+$$
$$f(h_2,x_2,-\beta_2,\phi_{02})g(h_1,\pi-\beta_1,\zeta_{02},\eta_{02})$$
$$Du_1=1-g(h_1,\pi-\beta_1,\zeta_{02},\eta_{02})$$
$$g(h_2,-\beta_2,\zeta_{01},\eta_{01})$$
$$C_2=\frac{Nu_2}{Du_2}. \tag{84}$$

where

$$Nu_2 = f(h_2, x_2, -\beta_2, \phi_{02}) + f(h_1, x_1, \pi - \beta_1, \phi_{01}) g(h_2, -\beta_2, \zeta_{01}, \eta_{01})$$

$$Du_2 = 1 - g(h_1, \pi - \beta_1, \zeta_{02}, \eta_{02}) \, g(h_2, -\beta_2, \zeta_{01}, \eta_{01}).$$

Once C_1 and C_2 are known, one can determine the z-component of the total scattered field from the two strips, i. e.,

$$E_z^s = c(k_o \rho) P(\phi) \tag{85}$$

$$p(\phi) = e^{-jk_o c \cos\phi} \left[f(h_1, x_1, \phi - \beta_1, \phi_{01}) + C_2 g(h_1, \phi - \beta_1, \zeta_{02}, \eta_{02}) \right] + e^{jk_o c \cos\phi} \left[f(h_2, x_2, \phi - \beta_2, \phi_{02}) + C_1 g(h_2, \phi - \beta_2, \zeta_{01}, \eta_{01}) \right] \tag{86}$$

The plane wave scattering properties of a two-dimensional body of infinite length are conveniently described in terms of the echo width equation (50).

IV. RESULTS AND DISCUSSION

In the following results the first method is implemented in all calculations, however every presented result is checked using the approximate method and a good agreement is found. Also in all figures the case of no dielectric coating $\varepsilon_r = 1$ is introduced in order to illustrate the effect of the dielectric coating on the scattering echo width. The first case is of a plane wave normally incident on two dielectric coating conducting strips with $\beta_1 = \beta_2 = 0^o$. As can be seen from Fig. 2 the forward and backscattering echo widths are increasing with thin coating of dielectric and decreases as the dielectric coating increases.

For the second case same coated strips are considered except in the angles $\beta_1 = \beta_2 = 90^o$ is the only change. The scattering echo width was calculated again for different thickness which shows that it is increasing in forward and backward directions for thin dielectric and decreasing for thick one. The third example has different geometrical parameter as shown in Fig. 4. The angle of incidence was taken as $\phi_o = 60^o$. Again this example illustrates the effect of the coating thickness in the back and forward scattering echo width. As one can see from Fig. 4, the scattering echo width is increasing for thin dielectric layer and decreases as it gets thick. The forth example shows the echo width pattern for angles $\beta_1 = 45^o$ and $\beta_2 = -45^o$ while $\phi_o = 90^o$.

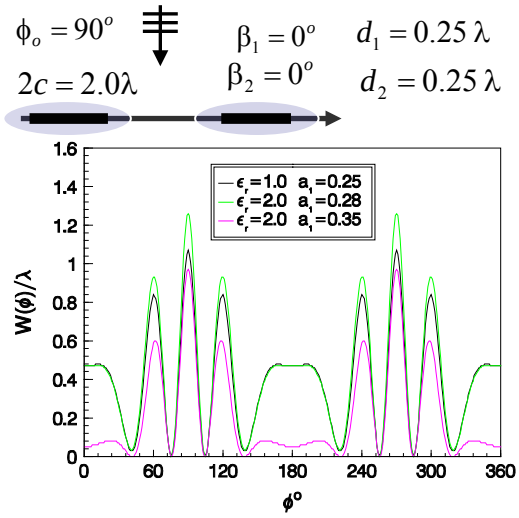

Fig. 2. Echo width pattern for different coating thickness.

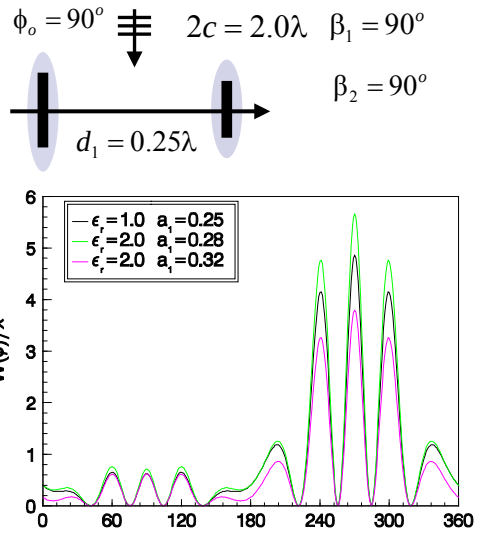

Fig. 3. Echo width pattern for different coating thickness.

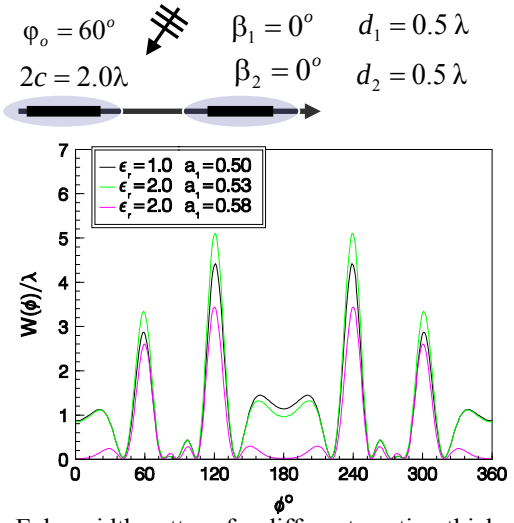

Fig. 4. Echo width pattern for different coating thickness.

As shown in Fig. 5 that same behavior can be concluded for this case. The fifth case is similar to the forth except that $\beta_1 = \beta_2 = 45^o$. Figure 6 illustrates the echo width pattern for fifth example, where the thin dielectric coating produces higher forward and backward echo width while the thick one produces less echo width values. In the sixth case different geometrical parameters were considered where larger strips are considered and $\beta_1 = 0^o$, $\beta_2 = 90^o$ while $\phi_o = 60^o$.The echo width pattern corresponding to this case is plotted in Fig. 7.

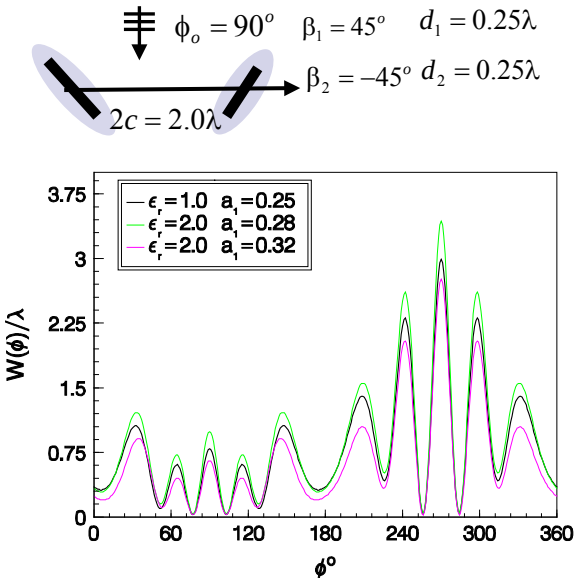

Fig. 5. Echo width pattern for different coating thickness.

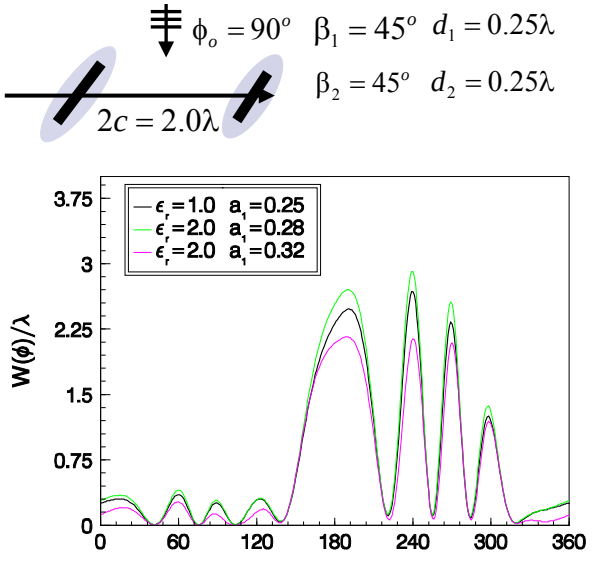

Fig. 6. Echo width pattern for different coating thickness.

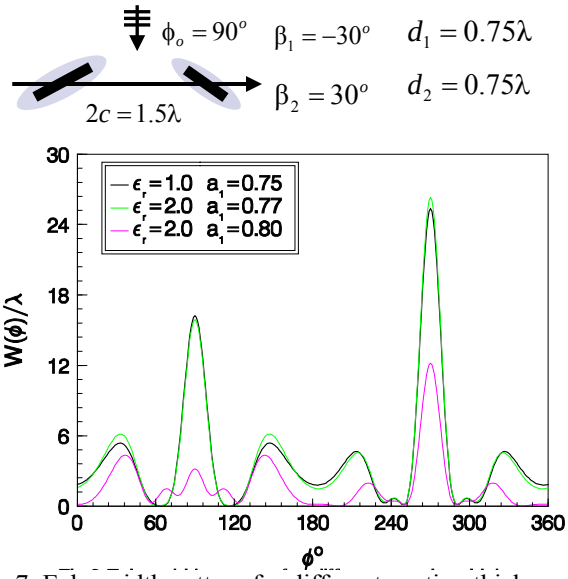

Fig. 7. Echo width pattern for different coating thickness.

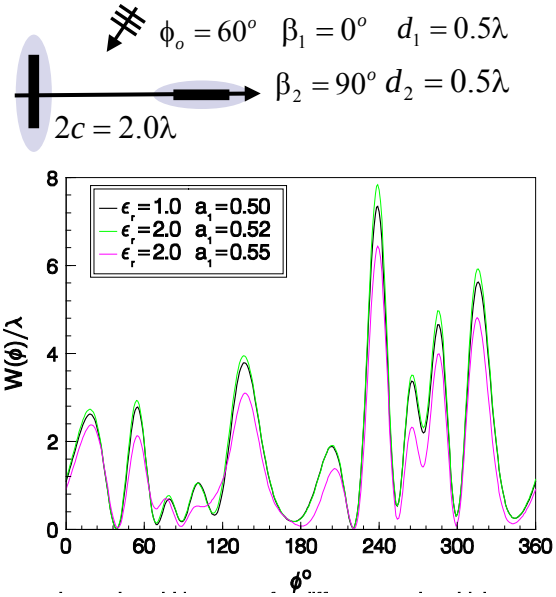

Fig. 8. Echo width pattern for different coating thickness.

Again the same behavior is noticed as previous cases. In the seventh example a relatively large strips are considered and the separation between them is also decreased relative to previous cases. Again the echo width pattern showed a very slight increase for very thin coating and then it gets lower as the coating thickness increases. In the last example new parameters were introduced in order to show the effect of the dielectric permittivity on the scattering echo width. As one can see in Fig. 9, echo width pattern is decreasing with increasing the dielectric permittivity.

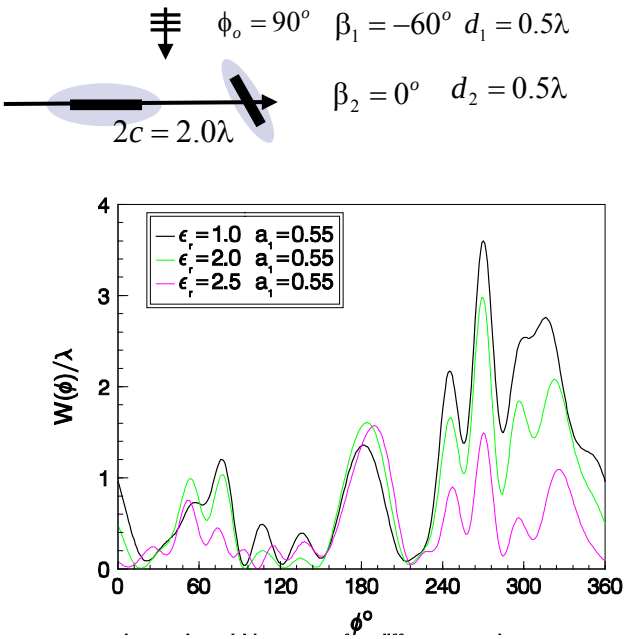

Fig. 9. Echo width pattern for different coating permittivity.

V. CONCLUSIONS

Scattering of an electromagnetic wave by two dielectric coated conducing strips is achieved to study the effect of the coating on the echo width. It is found that very thin dielectric coating increases the scattering echo width in forward and back directions, and as the thickness increases the forward and backscattered echo width decreases. It is also found that for a constant thickness the scattering echo width pattern decreases with the increasing of dielectric permittivity of the coating.

ACKNOWLEDGEMENT

The authors wish to thank *King Fahd University of Petroleum and Minerals* for providing all the facilities required to perform this research.

REFERENCE

[1] J. J. Bowman, T. Senior, and P. Uslenghi, *Electromagnetic and Acoustic Scattering by Simple Shapes.* Amsterdam: North-Holland Publishing Company, 1969.

[2] P. M. Morse and P. J. Rubensten, "The diffraction of waves by ribbons and by slits," *Physics Review*, vol. 54, pp. 895-898, 1938.

[3] R. I. Primich, "Some electromagnetic transmission and reflection properties of a strip grating," *I. R. E. Trans. on Antennas and Propagation*, vol. 5, pp. 176-182, 1957.

[4] R. Holland and V. Cable, "Mathieu function and their applications to scattering by a coated strip," *IEEE on Electromagnetic Compatibility*, vol. 34, pp. 9-16, Feb. 1992.

[5] H. A. Ragheb and M. Hamid, "Scattering by two conducting strips with parallel edges," *Canadian J. of Phys,* vol. 66, pp. 376-383, 1987.

[6] A. Sebak, "Electromagnetic scattering by two elliptic cylinders," *IEEE antyennasa and Propag.*, vol. 42, no. 11, pp. 1521-1527, 1994.

[7] B. N. Khatir and A. Sebak, "Transverse electric wave scattering by parallel metamaterial coated elliptic cylinders," *EMTS 2007 - International URSI Commission B - Electromagnetic Theory Symposium, Ottawa, ON, Canada*, July 26-28, 2007.

[8] S. N. Karp and A. Russek, "Scattering by s wide slit," *J. of Applied Physics*, vol. 27, pp. 886-889, 1952.

Hassan Ragheb was born in Port-Said, Egypt, in 1953. He received the B. Sc. Degree in Electrical Engineering from Cairo University, Egypt, in 1977 and the M. Sc. and Ph. D. degrees in Electrical Engineering from the University of Manitoba, Winnipeg, Canada, in 1984 and 1987, respectively. From 1987 to 1989, he was a research assistant in the Department of Electrical Engineering, University of Manitoba. In 1989, he joined the Department of Electrical Engineering at the King Fahd University of Petroleum and Minerals, where he is now as Associate Professor of Electrical Engineering. His research interests include electromagnetic scattering by multiple and coated objects, microstrip antennas, phased arrays, slot and open ended waveguide antennas.

Essam E. Hassan, Obtained his B.Sc. from Alexandria University, Egypt on 1970, and his M.Sc. and Ph.D. from the university of Manitoba in 1974 and 1978 respectively. Dr. Hassan worked with Northern Telecom Canada in the digital switching division from 1977 to 1979. Since then he joined the electrical engineering department at King Fahd University of Petroleum and Minerals at Dhahran, Saudi Arabia where he is now a Professor in the EE dept. Dr. Hassan's research interest is primarily in the microwave filters and devices, electromagnetic field and anomalous propagation. He is an author or coauthor of over 50 papers in this field or closely related fields.

Evaluating the Radar Cross Section of Maritime Radar Reflectors Using Computational Electromagnetics

R. L. Haupt, S. E. Haupt, and D. Aten

The Pennsylvania State University, Applied Research Laboratory
P. O. Box 30, State College, PA 16804-0030

Abstract – This paper presents results from calculating the radar cross section (RCS) of two maritime radar reflectors using the method of moments. The Echomaster 152, although smaller in size, produces a higher maximum RCS than the Echomax 230 that includes three layers of corner reflectors. The Echomaster 152 also has deeper nulls in the RCS pattern, which means it is less detectable at those angles.

Keywords: Radar cross section, radar reflectors, ground plane, ocean, method of moments.

I. INTRODUCTION

Pleasure and commercial boats in the crowded harbors and bays of the United States use a horizontally polarized maritime X-band radar operating at 9.41 GHz. Large boats are easy to see with these radars, but smaller non-metallic hulls, like those of a sailboat, have a low radar cross section (RCS) and are difficult to detect. The RCS is particularly low from the fore and the aft, making them even more difficult to detect in those directions. Placing the reflectors at a high point on the boat, like the top of a sail boom, increase the detection range of the low RCS boats [1].

In order to be effective, the RCS of the radar reflector must be larger than the RCS of the boat. Also, the reflector/boat RCS should be large enough in all directions in order for other boats to detect it in time to avoid a collision. Several commercial reflectors claim to increase the RCS of sailboats. Two of the more popular reflectors are the Echomax 230 [2] and the Echomaster 152 [3]. Both reflectors make use of simple corner reflectors arranged to provide a high azimuthal RCS.

The impact of these reflectors has been analyzed and measured in free space [4]. Unfortunately, these RCS results do not consider the ocean, which has a tremendous effect upon the RCS of the reflector. This paper presents RCS results from modeling several types of reflectors with and without a salt water ground plane using the method of moments. The presence of a calm ocean greatly enhances the RCS of both reflectors in all azimuthal directions. The Echomaster 152 has a higher RCS at most angles than the Echomax 230, but the Echomax 230 has a higher minimum RCS than the Echomaster 152.

II. RADAR REFLECTOR MODELS

The goal of this effort was to evaluate and compare the RCS of two popular commercial radar reflectors in both free space and over an ocean ground plane. In addition, these RCS results are compared to the RCS of a cylinder and sphere. All the reflectors are assumed to be perfectly conducting. Figure 1 shows the four reflectors drawn at the correct relative sizes. For the calculations, each reflector is centered on the coordinate system with ϕ measuring azimuth angle and θ measuring elevation angle. The ocean is assumed to be in the x-y plane, so the orientation of the reflectors in Fig. 1 corresponds to how they would be deployed.

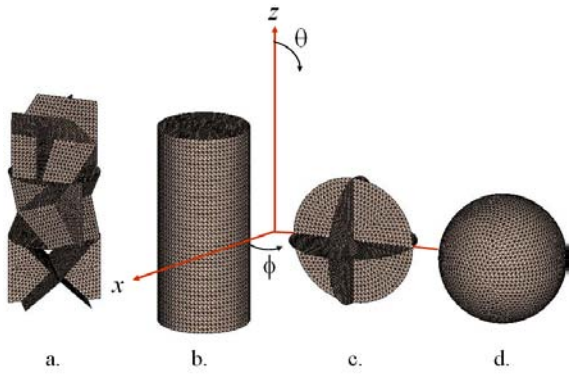

Fig. 1. FEKO CAD models of the reflectors: (a) Echomax 230, (b) cylinder, (c) Echomaster 152, and (d) sphere.

The Echomax 230 (Fig. 1(a)) consists of a stack of three aluminum quad-trihedral reflectors inside a cylindrical shell (Fig. 1(b)). Figure 2 is a photograph of the aluminum reflector outside of its plastic shell (laying on its side) Echomax 230. The Echomax 230 reflector is h=496 mm high and has a radius of r=153 mm [2]. A model of one layer of the Echomax 230 with dimensions appears in Fig. 3. Each layer displays a 30^o twist in order to create a more omni-directional RCS in the azimuth plane.

The second commercial reflector to be modeled is the Echomaster 152, whose geometry is shown in Fig. 1(c). It consists of three intersecting, orthogonal 305 mm diameter aluminum disks [3]. The sphere (Fig. 1(d)) has a radius of r=153 mm**.** It does not come with a cover.

Fig. 2. Photograph of the Echomax 230 reflector and its plastic cylindrical cover.

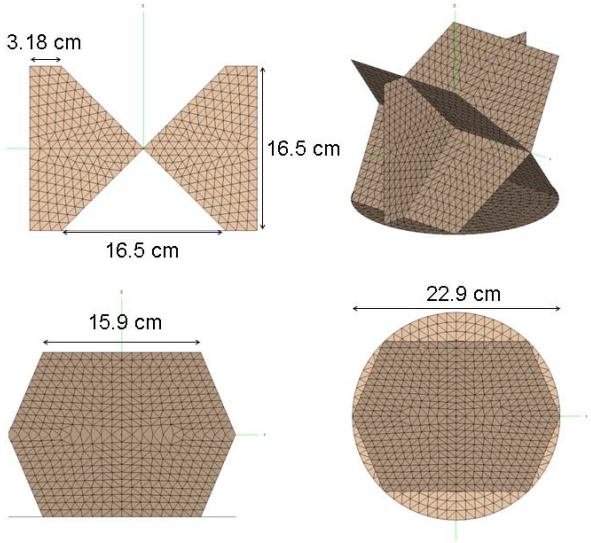

Fig. 3. Dimensions of one layer of the Echomax 230.

Two canonical RCS reflector shapes are also included in this study: cylinder and sphere. The cylinder in Fig. 1(b) has the same height and radius as the Echomax 230, and the sphere in Fig. 1(d) has the same radius as the Echomaster 152. The RCS of these reflectors is well known analytically, so they serve as a check for the method of moment's calculation of the RCS as well as having the desired omni-directional RCS pattern in the azimuth plane. The simple physical optics formulas [5] predict that the peak RCS of the cylinder, σ_{cyl}, is,

$$\sigma_{cyl} = \frac{2\pi r h^2}{\lambda} = 7.5 \text{ dBsm} \quad (1)$$

and of the sphere, σ_{cyl}, is,

$$\sigma_{sph} = \pi r^2 = -11.4 \text{ dBsm} . \quad (2)$$

This data is used to check the computational results for accuracy.

III. COMPUTED RCS OF THE RADAR REFLECTORS

Most pleasure boats on crowded waterways use maritime radar. X-band maritime radars operate with horizontal polarization (ϕ – polarized) at 9.41 GHz with a wavelength of $\lambda = 3.19$ cm. This type of radar is commonly used by pleasure and commercial boats when near land. Boats far from land also have much larger and more powerful S-band radar. Only the X-band frequency will be considered here.

The RCS of these four reflectors are computed using the method of moments program, FEKO [6]. All reflectors have the same size triangular mesh with a maximum triangle side of $\lambda/5$. This triangle size resulted in the computed peak RCS of the cylinder and sphere matching the values in equations (1) and (2). Increasing the size of the maximum triangle side resulted in RCS values that did not match equations (1) and (2).

Each reflector is modeled in free space and in the presence of an infinite ocean ground plane. The free space RCS is calculated over $60^o \le \theta \le 90^o$ and $0^o \le \phi \le 90^o$. The range of elevation angles accounts for the difference in height between a radar on the larger boat and the reflector on the smaller boat and some motion of the boats. In addition, the RCS of the reflectors is calculated over an infinite ground plane having a permittivity of $\varepsilon_r = 55 + j31$ with a loss tangent of $\tan\delta = 0.56$. This ground plane corresponds to a calm ocean at a temperature of 14° C and a salinity of 33 parts per thousand [7].

The first RCS calculations are done with the cylinder and sphere test cases. Figure 4 displays the computed results for the cylinder and the sphere. The ground plane significantly enhances both the RCS of the cylinder and of the sphere. As θ approaches 90^o, the RCS with the ground plane is about 6 dB higher than the free space RCS.

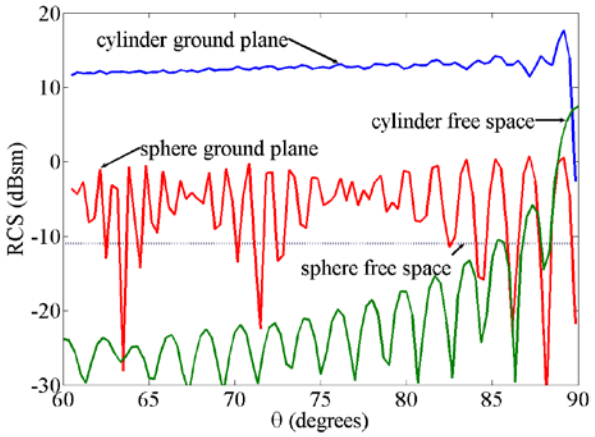

Fig. 4. RCS of a cylinder and sphere in free space and above a ground plane.

Figures 5 through 8 plot the RCS over the azimuth and elevation angles of interest for the Echomax 230 and the Echomaster 152 reflectors. Each reflector is shown both in free space (Figs. 5 and 7) and at 5 m above an ocean ground plane (Figs. 6 and 8). Echomax specifies that the maximum RCS of their Echomax 230 radar reflector is 24 m^2 or 13.8 dBsm. The maximum computed result is 13.4 dBsm, so the computations appear to be accurate. The Echomaster 152 appears to give a larger RCS over a greater angular extent than the Echomax 230. It also appears to have the deepest nulls over the greatest area. Its maximum free space RCS is 17.2 dBsm which is close to that of a disk with r=153 mm (18.2 dBsm). The ocean ground plane boosts the maximum RCS of both free space models by about 8 dB and also produces much broader maxima.

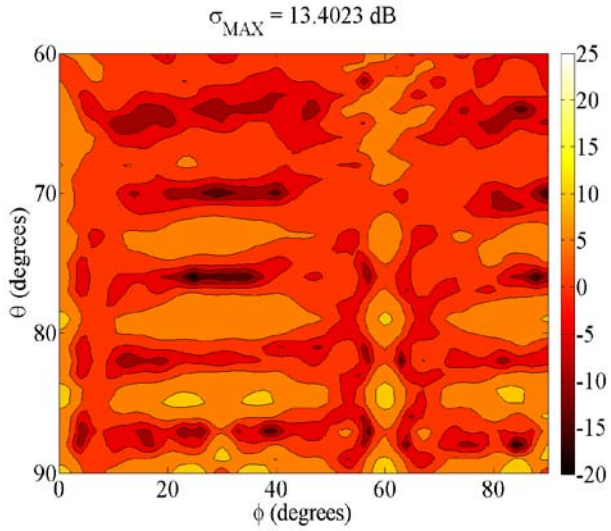

Fig. 5. RCS of Echomax 230 in free space.

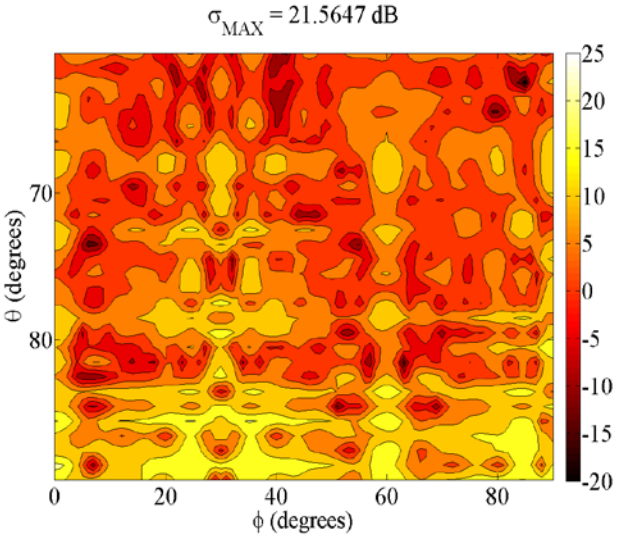

Fig. 6. RCS of Echomax 230 when placed 5m above an ocean ground plane.

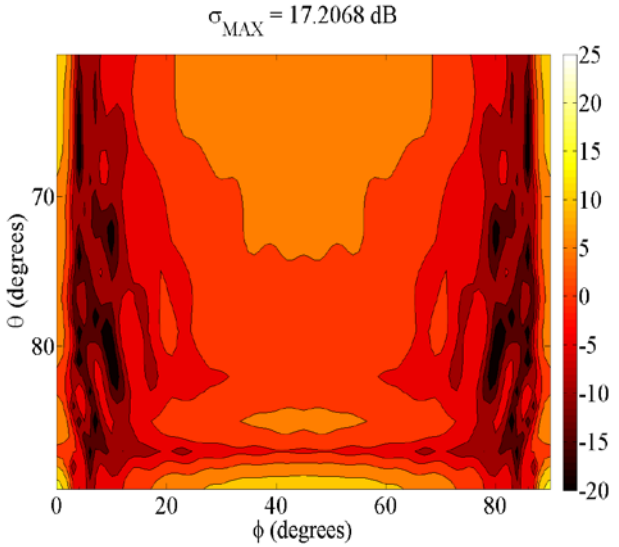

Fig. 7. RCS of Echomaster 152 in free space.

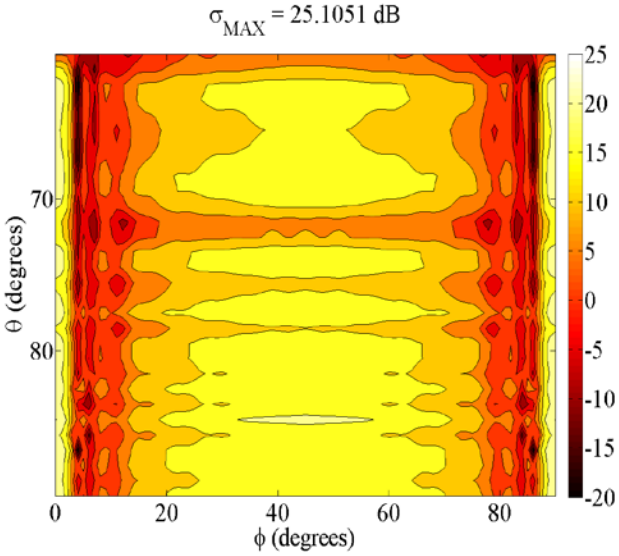

Fig. 8. RCS of Echomaster 152 when placed 5m above an ocean ground plane.

Figure 9 shows a plot of the free space RCS patterns for the two reflectors at $\theta = 90^o$. The Echomax 230 RCS has a lower maximum RCS, but does not have the broad nulls of the Echomaster 152. Inserting the ocean ground plane increases the overall RCS of both reflectors but maintains a similar shape as indicated in Fig. 10. This advantage is due to the stacked design that provides reflection from at least one of the corner reflectors at each angle of incidence. The elevation angles do not extend to $\theta = 90^o$ because the ground plane is assumed to be infinite in extent.

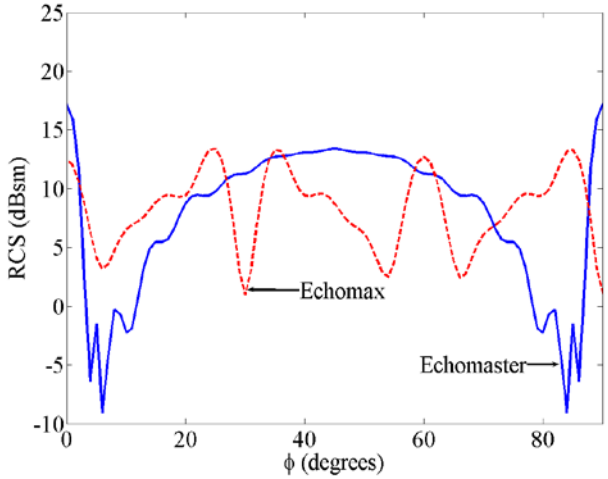

Fig. 9. RCS of Echomax 230 and Echomaster 152 in free space at $\theta = 90^{o}$.

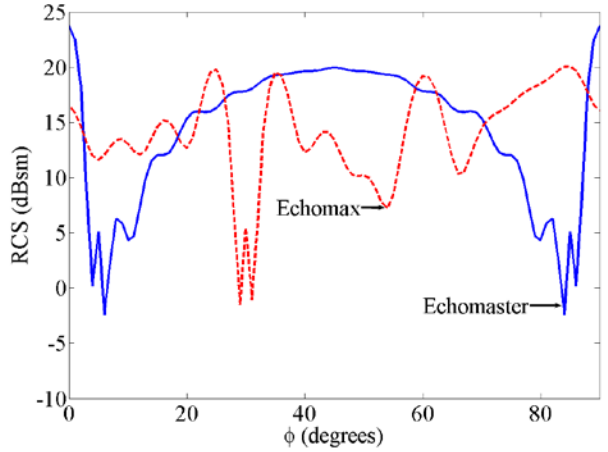

Fig. 10. RCS of Echomax 230 and Echomaster 152 above an ocean ground plane at $\theta = 89.5^{o}$.

IV. CONCLUSIONS

The results of this modeling study indicate that both the spherical Echomaster 152 comprised of three intersection orthogonal disks and the Echomax 230, which stacks three layers of corner reflectors, are likely to enhance the RCS of a small sailboat. Although the Echomaster 152 boasts a higher maximum RCS, it also displays the deepest nulls over a larger extent of azimuth angles. Including a ground plane representing the ocean in the calculations increases the average and maximum RCS for both models. The variability of the RCS patterns in both the azimuth and elevation angles suggests that the RCS highly depends on sea state, which causes the boat to pitch, roll, and yaw. Typically, the best RCS occurs when the sea is calm (RCS with ground plane), and the worst RCS occurs with waves (free space RCS).

REFERENCES

[1] P. G. Gallman, *Radar Reflectors for Cruising Sailboats*, Canada: Ulyssian Publications, 2005.
[2] Echomax Radar Reflectors, www.echomax.co.uk /Echomax_Products.htm, 2008.
[3] Davis Instrument Echomaster 152, (www.davisnet.com /marine/products/list_marine.asp?grp=m21-4), 2008.
[4] S. Luke, "Performance investigation of marine radar reflectors on the market," Report QINETIQ/D&TS/SEA/CR0704527 /2.0.
[5] E. F. Knot, J. F. Shaeffer, and M. T. Tuley, *Radar Cross Section*, Dedham, MA: Artech House, Inc., 1999.
[6] FEKO Suite 5.1, EM Software and Systems (www.feko.info), 2005.
[7] T. Meissner and F. J. Wentz, "The complex dielectric constant of pure and sea water from microwave satellite observations," *IEEE Trans. Geoscience and Remote Sensing*, vol. 42, no. 9, pp. 1836-1849, Sep. 2004.

Randy L. Haupt is an IEEE and an ACES Fellow and is Dept. Head of Computational Electromagnetics and Senior Scientist at the Penn State Applied Research Lab. He has a Ph.D. in Electrical Engineering from the University of Michigan, MS in Electrical Engineering from Northeastern University, MS in Engineering Management from Western New England College, and BS in Electrical Engineering from the USAF Academy. He was Professor and Department Head of Electrical and Computer Engineering at Utah State University from 1999-2003. He was a Professor of Electrical Engineering at the USAF Academy and Professor and Chair of Electrical Engineering at the University of Nevada Reno. In 1997, he retired as a Lt. Col. in the USAF. Dr. Haupt was a project engineer for the OTH-B radar and a research antenna engineer for Rome Air Development Center.

Sue Ellen Haupt is Head of the Department of Atmospheric and Oceanic Physics at the Applied Research Laboratory of The Pennsylvania State University and Associate Professor of Meteorology. She earned her Ph.D. in Atmospheric Science from the University of Michigan, M.S. in Mechanical Engineering from Worcester Polytechnic Institute, and B.S. in Meteorology from Penn State. In addition to PSU, she has worked at New England Electric System, the National Center for Atmospheric Research, University of Colorado/Boulder, University of Nevada, Reno, and Utah State University. Dr. Haupt chairs the Committee on Artificial Intelligence Applications to Environmental Science of the American Meteorological Society, has co-authored *Practical Genetic Algorithms*, is primary editor for *Applications of Artificial Intelligence Methods in the Environmental Sciences*, and has authored over 150 book chapters, journal articles, conference papers, and technical reports.

Daniel Aten is a Research and Developer Engineer 2 at the Penn State Applied Research Laboratory. He has a BS in Electrical Engineering from Penn State University and his MSEE also from Penn State. He worked as an intern at Lockheed-Martin Corp. and his interests are in antennas, electromagnetic measurements, signal processing, and wireless systems.

The Impact of Vertical Structures on Ship Radar Cross Section in the High Frequency Range

[1]R. C. Solomon, [2]H. Leong, [3]C. W. Trueman, and [1]Y. M. M Antar

[1]Department of Electrical and Computer Engineering, Royal Military College of Canada, Kingston, Ontario, Canada
[2]Defence R&D Canada – Ottawa, Canada
[3]Concordia University, Montreal, Quebec, Canada

Abstract **–** The monostatic and bistatic Radar Cross Section (RCS) of various complex ship targets are numerically simulated in the High Frequency range of 3-20 MHz. The process by which these complex ship models are built and simulated using the FEKO code is described. Validation of the simulated RCS against full-scale measurements is described. Details are added to the ship model and the changes in the bistatic RCS are explored. Bistatic data from the simulations are used to assess the performance of a pair of surface-wave radar stations operated in a bistatic mode. The results of these findings will be of importance to future RCS simulation work using numerical modelling.

I. INTRODUCTION

High Frequency Surface Wave Radar (HFSWR) operates in the High Frequency (HF) band between 3 and 30 MHz. Capitalizing on the conducting properties of the ocean, the radar's vertically-polarized surface wave propagates well beyond the visible horizon, by following the curvature of the earth. HFSWR is increasingly seen as an attractive, cost-effective means in providing near-real time monitoring for Beyond-the-Line-Of-Sight (BLOS) surveillance applications over large areas of sea surface [1].

Bistatic HFSWR potentially offers better coverage than a monostatic system as the ionospheric clutter may appear farther away in the bistatic configuration [2]. The reduction of any Electromagnetic Interference (EMI) to other HF users is an important factor in the densely-populated HF frequency band. There is the potential to reduce the EMI susceptibility when utilizing the spectrally-efficient Frequency Modulated Continuous Wave (FMCW) method of transmission. This mode of transmission can only be supported through a sufficient separation between the transmitter and receiver, which represents a bistatic configuration. The performance of bistatic HFSWR for coastal surveillance is currently being investigated. As part of this investigation, it is desired to estimate the Radar Cross Sections (RCS) of certain Targets of Interest (TOI). This paper describes some of the ship models that were built for simulation in the 3-20 MHz range, and describes the behavior of the bistatic RCS as topside detail is added.

Very little has been published in the open literature with regard to ship RCS. As a rough approximation, the monostatic, free-space RCS of vessels is often given by the empirical formula [3],

$$\sigma = 52 f^{1/2} D^{3/2} \quad (1)$$

where σ is the RCS in square meters, D is the full-load displacement of the vessel in kilotons and f is the radar frequency in Megahertz. This relationship was based on measurements of various ships at low grazing angles in the X, S and L bands, of bow and both port and starboard quarter aspects, to produce the median RCS of those aspects. It was later used as a rough approximation for the HF range [4], where the ratio of the target dimensions to the wavelength signifies that the RCS values fall in the Rayleigh or resonance (Mie) regions [5]. As was proven in [6], the rough estimate of equation (1) does not account for vertical resonators such as ship masts, cranes and antennas, which can significantly impact RCS values. These structures are especially important in HFSWR scattering and they often are aligned with the vertically-polarized electric field vector used in HFSWR.

The monostatic RCS of ship targets in the HF band has already been researched and observed, in [5, 6], through the use of numerical techniques, which is an effective means of exploring the behavior of scattering from complex targets such as ships. The work in [5] highlighted the potential impact on monostatic RCS of vertical wires on a complex target, when they are of resonant lengths at the operating frequency. It showed that components up to the third order of resonance can have a significant influence on the monostatic RCS. The present work reports the bistatic RCS of similar complex targets illuminated by an HFSWR.

This research uses models that have been built with CAD FEKO [7], which computes ship RCS using the Method Of Moments (MOM) [8]. The *Bonn Express* (~36000 ton) of Fig. 1 and the *Teleost* (~2400 ton) of Fig.

2 were used as sample complex targets. As described in the following, models of these ships with increasing levels of detail were built and analyzed with the FEKO program. Monostatic RCS predictions from the models were validated by comparing with the measured RCS of these ships, available from an actual HFSWR. The models were then used to explore the behavior of the bistatic RCS, and the influence of vertical, conductive components of the vessel such as antennas, crane wires, and masts on the RCS.

Fig. 1. The Cargo Vessel *Bonn Express.*

Fig. 2. The CCGS *Teleost.*

II. MODELING PROCEDURE

When modeling Rayleigh-region targets, such as a ship much smaller in size than the wavelength in the HF band, a simple representation can be applied and few details are required. Indeed, equation (1) uses no detail at all except for the ship's displacement. However, as size of the ship approaches the resonance region, details such as vertical, conductive components can have a strong influence on the RCS returns and should be included in the model. This work uses detailed wire-grid models of the ship targets and solves them with the FEKO program.

All the models were composed of Perfect Electric Conductor (PEC) material and designed using reference information, which included actual ship's drawings, when available, to accurately represent the target's geometry. Meshing was applied such that edges and segment lengths were approximately $\lambda/10$ long at the highest tested frequency. For instance testing was conducted such that the 3-20 MHz range was separated into three sub-ranges, 3-10 MHz, 10-15 MHz and 15-20 MHz. Therefore meshing was set in accordance with 10, 15 and 20 MHz respectively. The number of unknowns that FEKO used for meshing is much larger at 20MHz than at 15 or 10 MHz, so a substantial saving in simulation time is achieved by using sub-ranges. The wire radius was set to be approximately equal to the segment length divided by 2π [5]. Models were attached to an infinite PEC ground plane to simulate a flat, conductive ocean surface. This feature was used as a method of accounting for the scattering influences from the targets image and any potential coupling. Vertically polarized, low grazing angle, incident plane waves were utilized to find the 360^{o} XY-plane scattering returns at 2^{o} intervals. All the simulations described were conducted at 1 MHz intervals from 3 to 20 MHz. The solutions used MOM with Combined Field Integral Equations (CFIE), instead of Electric Field Integral Equations (EFIE), to avoid potential internal body resonance impacts on the collected data [9].

Simulation models to be solved with the FEKO program were built for the freighter *Bonn Express*, shown in Fig. 1, and the Canadian Coast Guard Ship (CCGS) *Teleost* in Fig. 2. These targets were of primary interest because a set of measured RCS data was available from an actual Surface Wave Radar [6]. This set of measured data was used to validate the models.

Various different models were built for each ship that included increasing amounts of topside detail. The RCS from the simulations was then compared to the measured RCS, as described below. The agreement showed that the simulation models predicted monostatic RCS values that corresponded well to the measured data and so validated the models. The same simulation models were then used to study the bistatic RCS of these ships.

The *Teleost* was used to explore the monostatic-to-bistatic RCS returns relations, as detailed ships drawing were available to allow a realistic simulation model to be built. Figures 3(a), (b), and (c) show the basic, intermediate, and most detailed models used to represent the *Teleost* in this work.

III. VALIDATION RESULTS

All three of the *Teleost* models predicted monostatic RCS values that compared extremely well to the measured, full-scale RCS. There was generally a difference of no more than a single decibel when compared individually at each tested aspect and a difference of about 0.7 dB on average [10]. When the

results were summarized, the detailed model of Figure 3c had only a slight advantage over the simpler models. For instance the measured RCS for stern incidence was 40.5 dBsm. The basic, intermediate and detailed models resulted in 41.76 dBsm, 40.70 and 40.49 dBsm respectively.

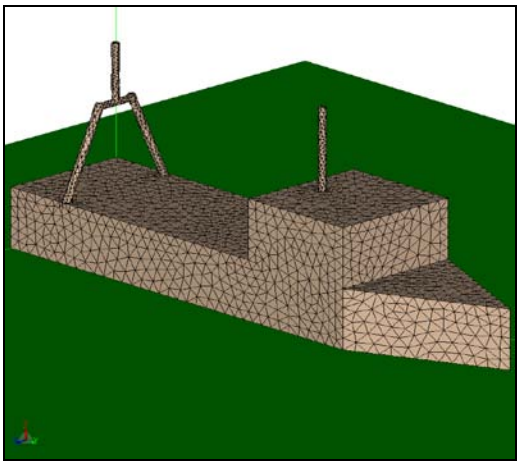

Fig. 3(a). The Basic *Teleost* Model.

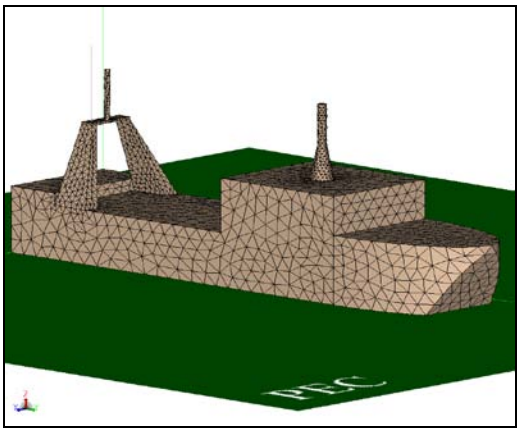

Fig. 3(b). The Intermediate *Teleost* Model.

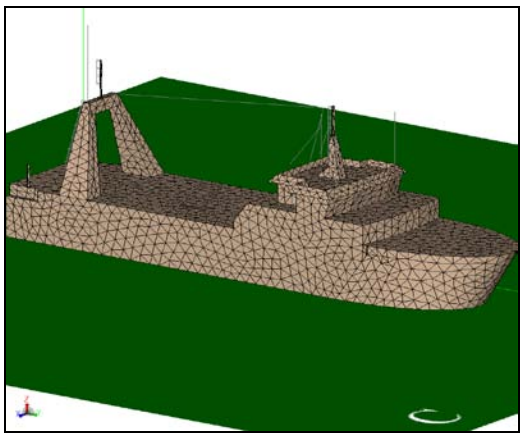

Fig. 3(c). The Detailed *Teleost* Model.

Figure 4 shows one of the *Bonn Express* models, which was comparable in the level of detail to the basic *Teleost* model. The simulated monostatic RCS of the *Bonn Express* models did not compare as well to the measurements as found in the *Teleost* models, but the results were still considered to be acceptable. The different models varied showing an average difference of 1-2 dB, with an even higher variation found when comparing individual aspects. As more detail was added to the models, the more significant was the variance in the RCS returns. Indeed the best *Bonn Express* results came from the simplest model used with the addition of forward and after masts, as seen in Fig. 4. It was found that without the addition of these masts there was an average difference of 11.65 dB when compared to the measured data and a maximum difference of 19.28 dB when compared around a testing aspect of 130-135^{o}. When the model was modified to include the masts the values improved dramatically to an average difference of 3.53 dB and a maximum difference of 5.41 dB. The presence of vertical scattering points on the ship models could be observed using POST FEKO, by looking for high concentration of currents formed on current on edges and vertical masts. The relatively good agreement of all these results to those of experimental data gave us the confidence that the models provided a sound basis to explore bistatic RCS behaviour.

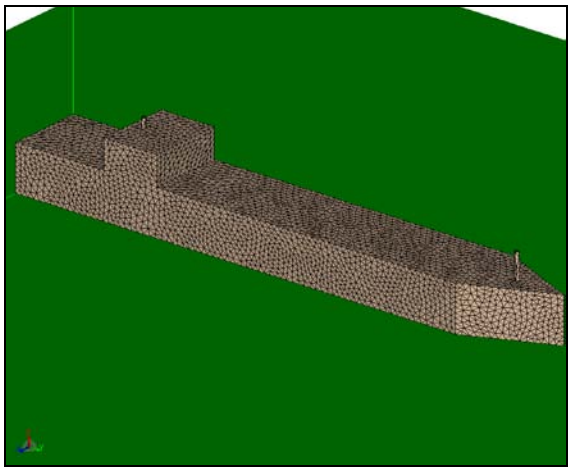

Fig. 4. Bonn Express with added masts.

Since no measured bistatic RCS values were available, to test the validity of the ship models constructed for analysis with the FEKO code, similar models were built to be solved with the NEC program [11]. Like FEKO, NEC uses a moment-method solution to find the currents on the wires of the ship model, but the details of the formulation are very different, and so an agreement of the simulations with NEC and FEKO is a good measure of validity. The bistatic RCS was compared for incidence on the stern and on the bow, and for broadside incidence of the plane wave, and in each

case the bistatic RCS was calculated at 30° intervals. NEC and FEKO were in good agreement for the bistatic calculation, with a maximum deviation of 0.22 dB in the values and an average difference of 0.19 dB. This was better than the agreement between the methods for the monostatic case. The simulation models were then used to study the bistatic RCS using the FEKO code.

IV. BISTATIC RCS

This section examines the bistatic RCS of the *Teleost* models of various complexity. All three of the *Teleost* models gave similar monostatic RCS values for each of the different tested aspects. The basic *Teleost* model, Fig. 3(a), being symmetrical, produced the same RCS results for both the starboard and port broadside aspects. Very few actual ships share this design feature. The intermediate and detailed *Teleost* models of Fig. 3(b) and 3(c) respectively are unsymmetrical, giving rise to different monostatic RCS from the port and starboard sides, which is similar to the behaviour of the measured RCS values. The intermediate and detailed *Teleost* models provided the unique scattering detail for these complex targets that could be used to establish the target's orientation by matching the returns to the experimental RCS data.

The bistatic returns from the three *Teleost* models differ in the location and size of maxima and nulls as the bistatic angle varies. This was noted to occur at every frequency throughout the 3 - 20 MHz test range. For example, Fig. 5 shows the bistatic RCS of all three *Teleost* models for starboard broadside incidence at 18 MHz. Nulls at 90 degrees and 240 degrees differ by as much as 20 dB. Some peaks, such as those noted at 75 and 290 degrees, show deviations as large as 8 dB, which is not as much difference as in the nulls. Slight changes of a couple of degrees in the angle of the peaks and nulls were noted as well. At other frequencies, generally the monostatic returns were comparable for the three models for bow, stern and broadside incidence, whereas the bistatic returns showed strong variations in the size of nulls and peaks and small changes in the angles of these features.

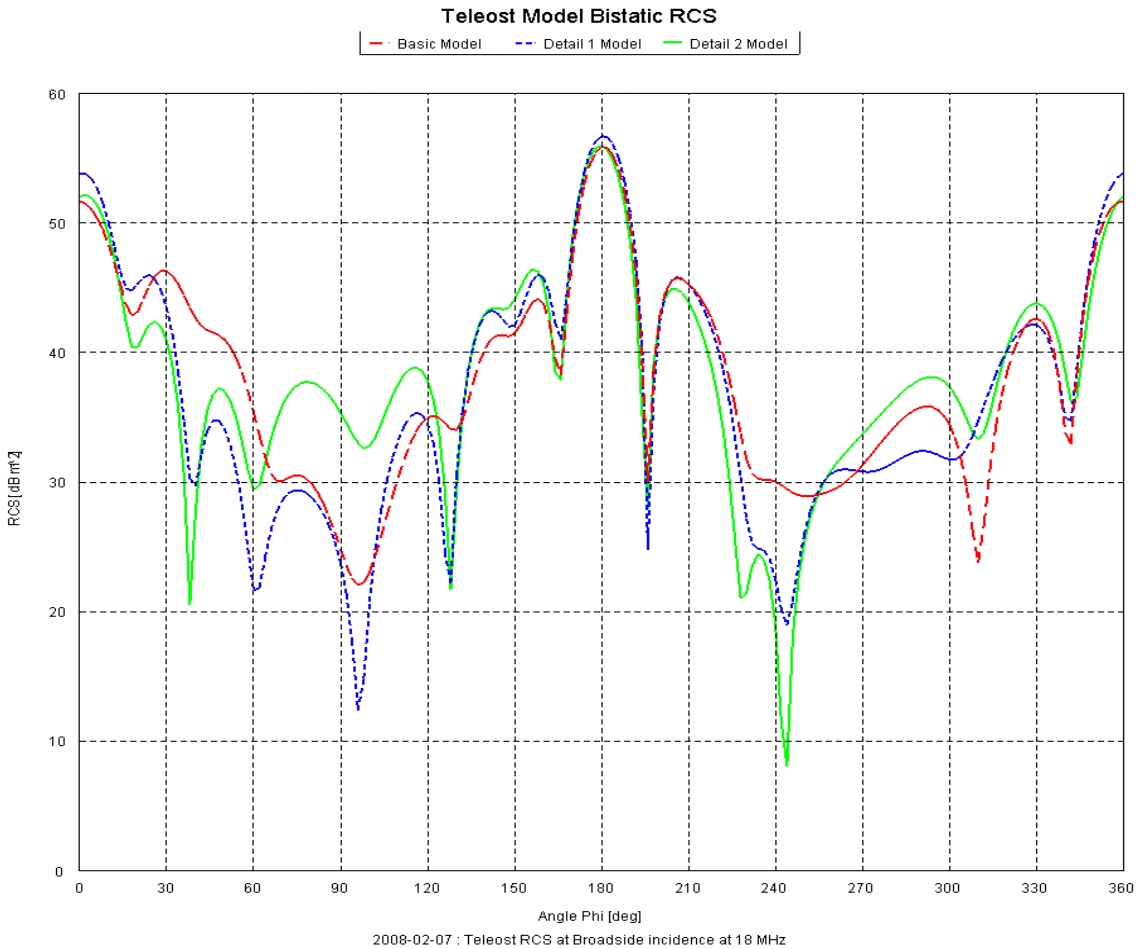

Fig. 5. Teleost models bistatic results.

The nature of the bistatic RCS fluctuations suggests that multiple receivers in for this type of HFSWR would be optimal. This arrangement would provide consistent coverage, as the different receivers would monitor different bistatic angles to offset when any one antenna was experiencing a null. This configuration has potential for classification and even identification purposes as well.

V. CURRENTS ON THE SHIP MODELS

Some features of the RCS of a ship model can be directly related to the currents flowing on the surfaces of the ship, and on the masts and other topside features. The FEKO code can be used to examine the surface currents, shown for the *Bonn Express* model at 18 MHz for bow incidence in Fig. 6. The 236m *Bonn Express* is 14 wavelengths long at 18 MHz, and when the vessel is many wavelengths long, currents tend to concentrate on vertical edges. The masts on the bow of the ship and on the top of the deckhouse also carried strong RF currents, which was typical of all the ship targets tested. As an observation of this trait Fig. 7 shows the current on the *Teleost's* mast, located on top of the deckhouse, illuminated at starboard broadside incidence at 3 MHz.

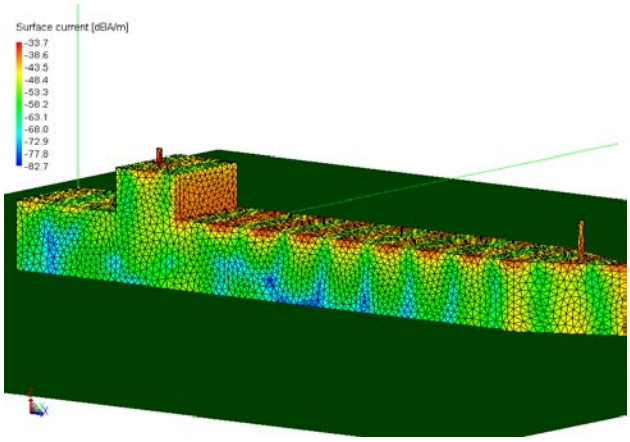

Fig. 6. Bonn Express with vertical scatters along the vertical edges, masts and sides.

Each of these concentrations forms a vertical scattering point on the ship. Interference of the fields scattered from the various edges and masts is what influences the nulls and peaks of the bistatic RCS pattern. Vertical edges are longer in terms of the wavelength with increasing frequency and gain in importance. The bistatic angles of the nulls in the scattering pattern changes with frequency and angle of incidence of the plane wave and characterize the ship. These unique RCS signatures from a sample of different aspects suggest a strong potential for applications such as vessel classification or even identification.

In many situations, such as that in Fig. 6, the plane wave induces large currents on the ship, which are seen across the horizontal portion of the deck and edges. It is important to note that these horizontal "deck" currents do not radiate a vertical component and are quickly attenuated by the ocean. They do not contribute to the peaks-and-nulls in the bistatic RCS that would be observed by receivers in the horizontal plane.

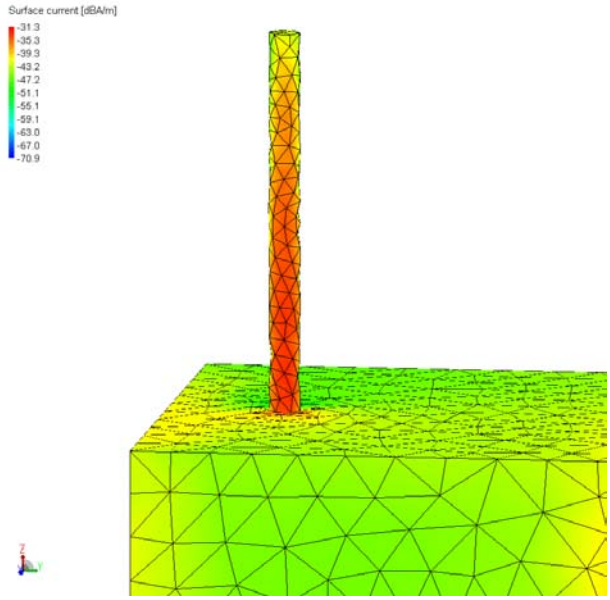

Fig. 7. Current concentration along modeled masts and vertical edges of the *Teleost* basic model.

V. CONCLUSION

The close agreement of the simulation results to the available measured data for monostatic RCS suggest that the MOM numerical technique implemented in the FEKO code is quite accurate for the computation of the RCS of ships in an HFSWR environment.

The scattering results found through this work were consistent with that in [5, 6]; however, it was also observed that the inclusion of potential resonators, such as masts, antennas and thin metal structures with a vertical component, were even more important factors in the overall bistatic RCS than that of the monostatic case. This is understandable, particularly when the mast or other structure approaches a resonant length. Such features had a greater impact on the number, position, intensity and sharpness of nulls in the bistatic RCS patterns than for monostatic RCS patterns, even for non-resonant wavelengths. These findings suggest that bistatic HFSWR configurations could be used to better accomplish such goals as target classification and potentially identification.

REFERENCES

[1] L. Pederson and D. E. Barrick, "HF surface-wave radar- revisiting a solution for EEZ ship surveillance," *EEZ International,* pp. 35-37, Spring 2004.

[2] H. Leong, "The potential of bistatic HF surface wave radar system for the surveillance of water-entry area along coastline," *IEEE Radar 2006*, Verona, NY, April 24-27, 2006.

[3] M. I. Skolnik, "An empirical formula for the radar cross section of ships at Grazing incidence," *IEEE Trans.*,vol AES-10, p 292, March 1974.

[4] A. M Ponsford, "Surveillance of the 200 nautical mile exclusive economic zone (EEZ) using high frequency surface wave radar," *Canadian Journal of Remote Sensing*, vol. 27, no. 4, August 2001.

[5] C. W. Trueman and S. J. Kubina, "The radar cross-section of aircraft, ships and missiles at HF frequencies," *TN-EMC-92-06 Final Report*, September 1992.

[6] H. Leong and H. Wilson, "An estimation and verification of vessel radar cross sections for high-frequency surface-wave radar," *IEEE Antennas and Propagation Magazine*, vol. 48, no. 2, April 2006.

[7] FEKO (online) EM Software and Solutions. www.feko.info/feko-product-info/technical.org, Access date: 8 Feb. 2008.

[8] D. B. Davdison, *Computational Electromagnetics for RF and Microwave Engineering*, Cambridge University press, 2005.

[9] F. X. Canning, "Protecting EFIE-Based Scattering Computations from Effects of Interior Resonances," *IEEE Antennas and Propagation Magazine,* vol. 39, no. 11, November 1991.

[10] R. Solomon, "An investigation in high frequency range bistatic radar cross section values of complex targets," *Royal Military College of Canada Master's Thesis*, April 2008.

[11] NEC Unofficial Site. Trevor Marshall. http://www.nec2.org/ Access date: 3 Jul. 2008.

Design of Wideband Planar Absorbers using Composite Materials

[1]E. A. Hashish, [1]S. M. Eid, and [2]S. F. Mahmoud

[1]Department of Electronics and Communication, Faculty of Engineering, Cairo University, Egypt
essamhh@ieee.org

[2] Electrical Engineering Department, Kuwait University, P.O. Box 5969, Safat 13060, Kuwait
Samirfm2000@yahoo.com

Abstract – Design of planar microwave absorbers usually incorporates the use of either magnetic or electric lossy materials. In this study, chiral materials are included in the design process of these absorbers. The genetic algorithm is used to obtain suitable solutions satisfying the design requirements. Wideband absorbers are designed using different configurations and presented in this paper. It is shown that the inclusion of chiral materials in the design process leads to more efficient absorbers.

Keywords: Electromagnetic absorbers, chiral materials, composite materials.

I. INTRODUCTION

Wideband microwave absorbers are of great interest for their important applications. These applications include radar cross section reduction of a wide range of objects, suppression of unwanted radiation and development of anechoic chambers [1-3]. Different designs of such absorbers are presented for various configurations including single layer [4-8], two layers [9-12] and multilayer absorbers [3, 13-16]. The design techniques of these absorbers are based on graphical methods [4, 7], local optimization methods [13], global optimization methods [3, 14, and 15] and analytical methods [9-11]. All of the above designs utilize layers of absorber materials which are of simple lossy electric or lossy magnetic types.

In this paper, chiral materials are used in the design process in addition to the above materials to construct the absorber. Design of wideband absorbers with different layer configurations is performed with the aid of the genetic algorithm as a global optimization technique. Better performance is expected when chiral materials are included in the design procedure of these absorbers, by virtue of the extra degree of freedom provided by the chirality parameter.

II. FORMULATION OF THE PROBLEM

Consider a planar absorber that is composed of N layers of lossy materials backed by a perfectly conducting surface as shown in Fig. 1. Each layer is defined by its complex permittivity ε_n, complex permeability μ_n, thickness d_n, in addition to chiral admittance ξ_n where $1 \le n \le N$. The time variation of the electromagnetic fields is assumed sinusoidal with the factor $e^{j\omega t}$. The electromagnetic fields inside any layer is controlled by the equations [16],

$$\underline{D}_n = \varepsilon_n \underline{E}_n - j\,\xi_n \underline{B}_n \tag{1}$$

$$\underline{B}_n = \mu_n (\underline{H}_n + j\,\xi_n \underline{E}), \tag{2}$$

where ε_n, μ_n are the usual electric permittivity and magnetic permeability, and ξ_n is the chiral admittance.

Let a uniform plane wave be normally incident to the absorber interface with the air.

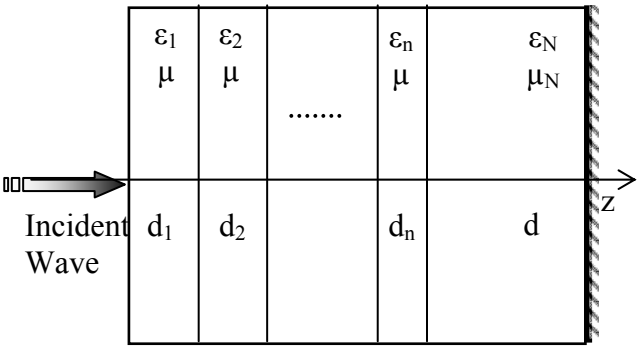

Fig. 1. N-layer planar absorber.

Because of the chirality, there are two normal propagating modes in each layer; one is having right circular polarization (RCP) with $\exp(-jk_n^+ z)$ propagation factor and the other left circular polarization (LCP) with $\exp(-jk_n^- z)$ propagation factor where [17,18],

$$k_n^{\pm} = \sqrt{\omega^2 \mu_n \varepsilon_n + \omega^2 \mu_n^2 \xi_n^2} \pm \omega \mu_n \xi_n \tag{3}$$

writing ξ_n in the form,

$$\xi_n = \sqrt{\frac{\varepsilon_0}{\mu_0}}\,\chi_n \tag{4}$$

where χ_n is a dimensionless chirality factor, we re-express $k_n^{\pm}$ as,

$$k_n^{\pm} = k_n\left[\sqrt{1+\left(\frac{\eta_n}{\eta_0}\right)^2\chi_n^2} \pm \frac{\eta_n}{\eta_0}\chi_n\right] \tag{5}$$

where

$$k_n = \omega\sqrt{\mu_n\,\varepsilon_n} \tag{6}$$

and

$$\eta_n = \sqrt{(\mu_n/\varepsilon_n)}\ , \tag{7}$$

with η_0 is the free space wave impedance.

It can be shown that the reflection coefficient Γ of a circularly polarized plane wave, which is normally incident on the absorber, is given by,

$$\Gamma = \frac{z_1-\eta_0}{z_1+\eta_0} \tag{8}$$

where,

$$z_n = \zeta_n\,\frac{\zeta_n\tanh(\gamma_n d_n)+z_{n+1}}{\zeta_n+z_{n+1}\tanh(\gamma_n d_n)}, \tag{9}$$

with

$$\zeta_n = \frac{\eta_n}{\sqrt{1+(\eta_n/\eta_0)^2\chi^2}}\ , \tag{10}$$

$$z_N = \zeta_n\tanh(\gamma_n d_n), \tag{11}$$

and

$$\gamma_n = j\,\frac{\left(k_n^{+}+k_n^{-}\right)}{2} = jk_n\,, \tag{12}$$

where γ_n is the average propagation constant of the forward and backward plane waves in the chiral medium, which have opposite circular polarization. We note here that equation (8) applies to either an RCP or LCP incident wave. Hence it is also valid for a linearly polarized incident wave. On the other hand, the case when $\chi_n = 0$ represents either an ordinary lossy electric or lossy magnetic material, with no chirality.

It is worth noting that in the design process of chiral absorbers, only magnetic materials are considered as chiral materials while electric materials are still non-chiral. In other words, the chirality is imposed on magnetic materials only and this is quite sufficient to achieve good performance for the designed absorbers. Moreover, all the materials that are used to construct the absorbers are assumed to be dispersive. This dispersion is imposed such that the complex relative permittivity of the electric layers and the complex relative permeability of the magnetic layers are inversely proportional to square root of the operating frequency. In such case, the electric and magnetic parameters of these layers ε_n and μ_n are expressed as,

$$\begin{aligned}\varepsilon_n &= \varepsilon_0\,\varepsilon_{rn}\,(1-\tan\delta_{en})\sqrt{f\ /f_0}\\ \mu_n &= \mu_0\end{aligned} \tag{13}$$

for the electric layers, and,

$$\begin{aligned}\varepsilon_n &= 10\varepsilon_0\\ \mu_n &= \mu\,\mu_{rn}\,(1-\tan\delta_{mn})\sqrt{f\ /f_0}\end{aligned} \tag{14}$$

for the magnetic layers. This frequency dependence is satisfied by most materials.

The depth of each layer d_n is normalized with respect to the wavelength of the wave inside this layer.

III. APPLICATION OF THE GENETIC ALGORITHM

A conventional genetic algorithm is built to solve the optimization problem, whose objective is to minimize the total reflected power from the layered structure, over a wide frequency range. We choose to maximize the total power transmitted to the absorber and at the same time minimize the maximum power reflected over the frequency band. A set of constraints is used to impose limitations or specifications on the system parameters. The variables (genes) in the fitness function are the intrinsic electric and magnetic parameters, the chirality factor as well as the thickness of the layers.

The genetic algorithm is applied for 100 design experiments in each layer configuration of chiral and non chiral absorbers with 6000 iterations in each experiment. In each design experiment, the fitness criterion is examined over a normalized frequency range from 0.1 to 9.0 with five samples in the range. Of course, larger number of samples within the range can be considered; however, this would cost more computational time without guarantee of much better results. The fitness criterion is defined as,

$$\begin{aligned}fitness = \frac{1}{2}Q\left\{\sum_{i=1}^{N_s}(1-\left|\Gamma_i^2\right|)\ \right\}\\ +(1-Q)\left\{1-\left|\Gamma_{\max}^2\right|\right\}\end{aligned} \tag{15}$$

where Q is a factor ranging from 0 to 1 and it is set to 0.5 in these experiments, N_s , is the number of applied samples through the frequency range, Γ_i is the reflection

coefficient at any sampling frequency, Γ_{max} is the maximum reflection coefficient amplitude among the samples.

IV. RESULTS

The best four designs in the above experiments are chosen for each layer configuration of the absorber based on the fitness criterion equation (15). The parameters of these designs are given in Tables 1 to 3 for two, three and four layer chiral absorber models. Examination of the fitness criteria in these leads to the conclusion that the absorber performance improves with the increased number of layers. The frequency responses of these chiral absorbers are presented in Figs. 2 to 4. The best design of each layer configuration exhibits reflection level below than -20 dB all over the frequency range. This level decreases obviously as the number of layers increases. The frequency response of the best four design experiments of the five layer nonchiral absorber is shown in Fig. 5. It is clear that the frequency response of these designs has much lower performance than those of the chiral absorbers.

Table 1. Design parameters for a two layer chiral absorber.

	Layer No.	Type	ε_{rn}, $\tan(\delta_n/2)$	μ_{rn}, $\tan(\delta_n/2)$	d_n/λ_n	Chirality
Design 1 Fitness = 99.518%	1	mag.	10.0, 0.0	7.48, .75	099	.779
	2	mag.	10.0, 0.0	29.8, .797	076	.556
Design 2 Fitness = 99.332%	1	mag.	10.0, 0.0	5.86, .75	.099	.691
	2	mag.	10.0, 0.0	35.1, .797	.075	.622
Design 3 Fitness = 99.328%	1	mag.	10.0, 0.0	10.08, .65	.08	.772
	2	mag.	10.0, 0.0	25.0, .80	.09	.694
Design 4 Fitness = 99.202%	1	mag.	10.0, 0.0	20.36, .737	.07	.783
	2	mag.	10.0, 0.0	36.1, .787	.06	.516

A comparison between the chiral and nonchiral absorbers according to the best fitness criterion is given in Fig. 6 for each layer configuration. This comparison shows clearly that the chiral absorbers have much better performance than the nonchiral one. Even, it is evident that the fitness criterion of the two layer chiral absorber is better than the five layer nonchiral one. The conclusion is that less number of chiral layers is needed to achieve a prescribed reflection level over a wide frequency bandwidth.

Table 2. Design parameters for a three layer chiral absorber.

	Layer No.	Type	ε_{rn}, $\tan(\delta_n/2)$	μ_{rn}, $\tan(\delta_n/2)$	d_n/λ_n	Chirality
Design 1 Fitness = 99.842%	1	mag.	10.0, 0.0	18.04 .7148	.05311	.746
	2	elec.	9.353, .065	1.0, 0.0	.03647	.000
	3	mag.	10.0, 0.0	26.76, .792	.09839	.541
Design 2 Fitness = 99.814%	1	mag.	10.0, 0.0	18.46, .552	.08656	.78
	2	elec.	3.93, .629	1.0, 0.0	.04328	.00
	3	mag	10.0, 0.0	36.53, .796	.08245	.36
Design 3 Fitness = 99.808%	1	mag	10.0, 0.0	22.62, .790	.02281	.78
	2	elec.	9.41, .713	1.0, 0.0	.01375	.00
	3	mag	10.0, 0.0	38.3, .799	.09689	.44
Design 4 Fitness = 99.75%	1	mag	10.0, 0.0	23.7, .769	.03856	.80
	2	elec.	8.89, .054	1.0, 0.0	.02695	.00
	3	mag	10.0, 0.0	36.6, .798	.08868	.62

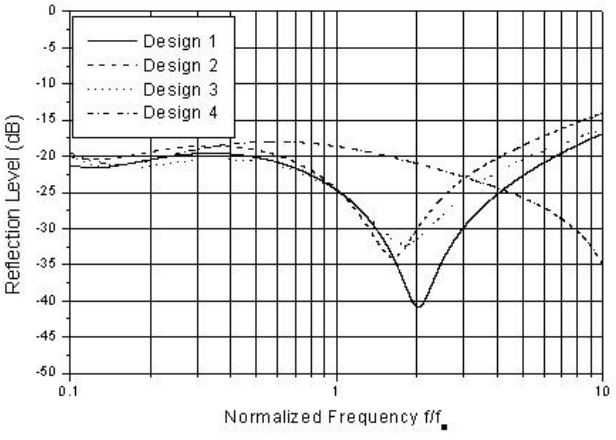

Fig. 2. Power reflection level for a two-layer chiral model.

Table 3. Design parameters for a four layer chiral absorber.

	Layer No.	Type	ε_{rn}, tan (δ_n/2)	μ_{rn}, tan (δ_n/2)	d_n/λ_n	Chirality
Design 1 Fitness = 99.97%	1	elec.	3.43, .448	1.0, 0.0	.001	.00
	2	mag.	10.0, 0.0	14.39, .781	.04	.80
	3	elec.	7.50, .198	1.0, 0.0	.044	.00
	4	mag.	10.0, 0.0	26.16, .793	.097	.45
Design 2 Fitness = 99.99 %	1	mag.	10.0, 0.0	8.50, .707	.055	.70
	2	elec.	3.21, .422	1.0, 0.0	.056	.00
	3	mag.	10.0, 0.0	37.2, .66	.022	.49
	4	mag	10.0, 0.0	32.4, .793	.092	.64
Design 3 Fitness = 99.872%	1	mag.	10.0, 0.0	24.0, .666	.054	.77
	2	elec.	6.15, .387	1.0, 0.0	.025	.00
	3	mag.	10.0, 0.0	30.1, .795	.036	.58
	4	Mag	10.0, 0.0	39.79, .791	.089	.79
Design 4 Fitness = 99.864%	1	Mag	10.0, 0.0	30.40, .486	.089	.77
	2	Mag	10.0, 0.0	25.68, .746	.068	.77
	3	elec.	7.15, .519	1.0, 0.0	.097	.00
	4	Mag	10.0, 0.0	27.59, .784	.098	.49

To simply explain why chiral absorbers surpass the non chiral ones, refer to the layer intrinsic impedance parameter in equation (10).

When the layer is magnetic with high loss, such that $|\mu/\mu_0|\chi^2 >> |\varepsilon/\varepsilon_0|$, then $\zeta \approx \eta_0/\chi$. So a highly lossy magnetic layer with chirality parameter χ =1, is a good match to air! (over a wide band) [19]. Of course χ=1 is too much chirality, so it is hard to manufacture. But this shows that adding one or more layers to the one magnetic layer should lead to a practical absorber. This should explain why few numbers of chiral layers could make a wide-band good absorber.

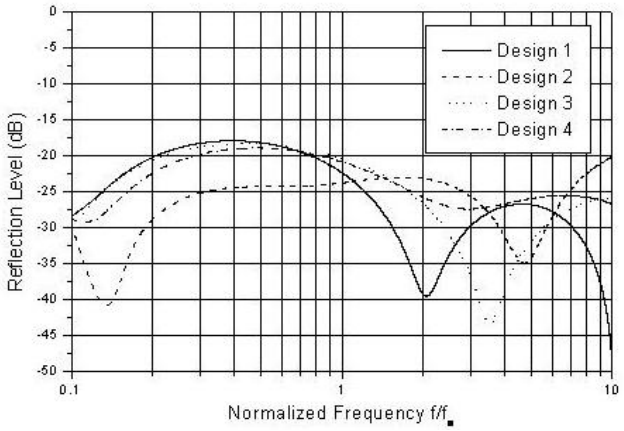

Fig. 3. Power reflection level for a three-layer chiral model.

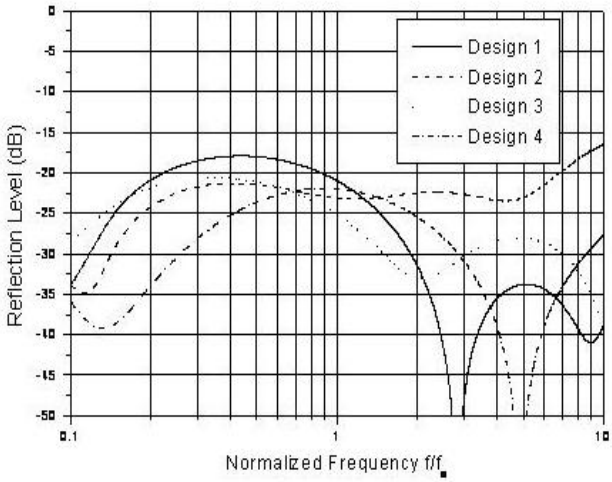

Fig. 4. Power reflection level for a four-layer chiral model.

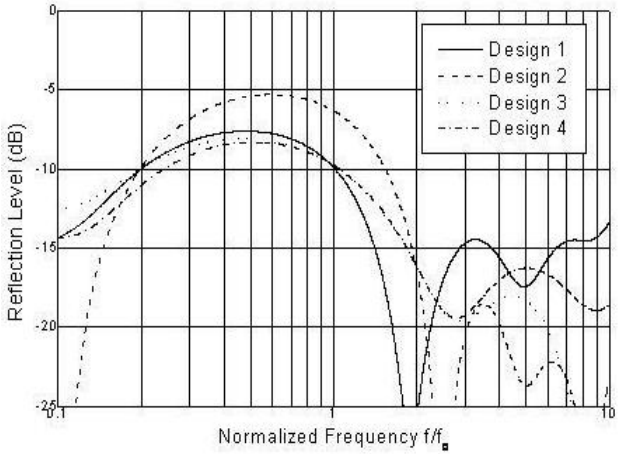

Fig. 5. Power reflection level for a five-layer non-chiral model.

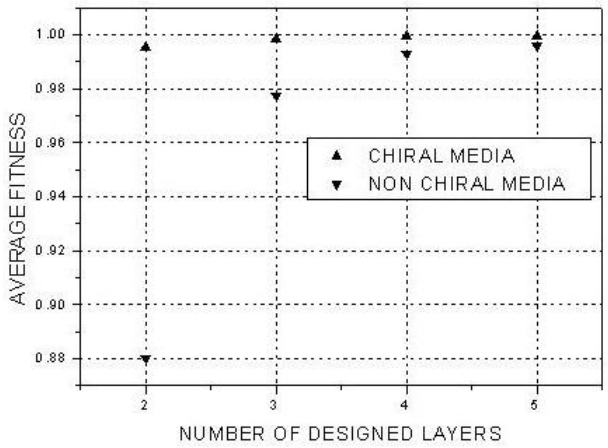

Fig. 6. Maximum fittness versus number of Layers for chiral and non-chiral media.

V. CONCLUSION

In this paper, the analysis of chiral planar absorber is presented. The genetic algorithm is applied to obtain the best four designs over 100 design experiments for each layer configuration of chiral and non-chiral absorbers. Inspection of the fitness criterion of these experiments indicates that the chiral absorbers have much better performance than non-chiral ones. It is concluded that much less number of layers is needed to achieve a prescribed maximum level of the reflection coefficient over a wide frequency range.

REFERENCES

[1] J. A. Adam, "How to design an invisible aircraft," *IEEE Spectrum*, vol. 25, pp. 26-31, April 1988.

[2] D. S. Weile, E. Michielssen, and D. E. Goldberg, "Genetic algorithm design of Pareto optimal broadband microwave absorbers," *IEEE Trans. EM Compatibility*, vol. 38, no. 3, pp. 518-525, August 1996.

[3] S. F. Mahmoud, "Design of a planar microwave absorber," *ICECS'97, Cairo, Egypt*, pp. 1110-1113, December 1997.

[4] H. M. Musal, J. R. and H. T. Hahn, "Thin-layer electromagnetic absorber design," *IEEE Trans. Mag.* vol. 25, no. 5, pp. 3851-3853, September 1989.

[5] R. L. Fante and M. T. Mc Cromick, "Reflection properties of the Salisbury screen," *IEEE Trans. AP*, vol. 36, no. 10, pp. 1443-1454, October 1988.

[6] E. F. Knott, "The thickness criterion for single-layer radar absorbents," *IEEE AP*, vol. 27, pp. 698-701, 1979.

[7] F. A. Frenandez and A. Q. Valenzuela, "General solution for single-layer electromagnetic wave absorber," *Electronics Letters*, vol. 21, no. 1, pp. 20-21, January 1985.

[8] A. Q. Valenzuela and F. A. Frenandez, "General design theory for single-layer homogeneous absorber," *IEEE Trans. AP.*, vol. 44, no. 7, pp. 822-826, July 1996.

[9] S. F. Mahmoud, "A two-layer planar microwave absorber," *Microwave and Optical Technology Letters*, vol. 15, no. 3, pp. 170-173, June 1997.

[10] S. F. Mahmoud and M. K. Habib, "Design of a two-layer microwave absorber," *Journal of Electromagnetic waves and Applications*, vol. 12, pp. 1005-1014, 1998.

[11] E. A. Hashish, "Design of wideband thin layer planar absorber," *Electromagnetic Waves and Applications*, vol. 16, no. 2, pp. 227-241, 2002.

[12] B. Chambers, "Frequency tuning characteristics of an adaptive Jaumann radar absorber incorporating variable impedance layers," *Electronics Letters*, vol. 30, no. 22, pp. 1892-1893, October 1994.

[13] J. J. Pesque, D. P. Bouche, and R. Mittra, "Optimization of multilayer antireflection coatings using an optimal control method," *IEEE Trans. MTT*, vol. 40, no. 9, pp. 1789-1796, September 1992.

[14] E. Michielssen, J. M. Sajer, S. Ranjithan, and R. Mittra, "Design of lightweight, broad-band microwave absorbers using genetic algorithms," *IEEE Trans. MTT.*, vol. 41, no. 6/7, pp. 1024-1030, June/July 1993.

[15] D. G. Li and A. C. Watson "Optical thin film optimization design using genetic algorithms," *IEEE International Conference on intelligent processing systems, Oct. 28-31 Bejing, China*, pp. 132-136, 1997.

[16] C. N. Chiu and I. T. Chiang, "Transient reflection properties of a dispersive and lossy Bi-isotropic slab with an anisotropic laminated composite packing," *IEEE Trans. On EMC*, vol. 47, no. 4, pp. 845-852, November 2005.

[17] N. Engheta and D. L. Jaggard, "Electromagnetic chirality and its applications," *IEEE Antennas Propagat. Soc. Newsletter*, vol. 30, no. 5, pp. 6-12, 1988.

[18] S. F. Mahmoud, "Mode characteristics in chirowaveguides with constant impedance walls," *Journal of Electromagnetic Waves and Applications, (JEMWA)*, vol. 6, no. 5/6, pp. 625-640, 1992.

[19] J. C. Liu and D. L. Jaggard, "Chiral layers on planar surfaces," *Journal of Electromagnetic Waves and Applications, (JEMWA)*, vol. 6, no. 5/6, pp. 651-667, 1992.

Samir F. Mahmoud graduated from the Electronic Engineering Dept., Cairo university, Egypt in 1964. He received the M.Sc and Ph.D. degrees in the Electrical Engineering Department, Queen's university, Kingston, Ontario, Canada in 1970 and 1973. During the academic year 1973-1974, he was a visiting research fellow at the Cooperative Institute for Research in Environmental Sciences (CIRES). Boulder, CO, doing research on Communication in Tunnels. He spent two sabbatical years, 1980-1982, between Queen Mary College, London and the British Aerospace, Stevenage, where he was involved in design of antennas for satellite communication. Currently Dr. Mahmoud is a full professor at the EE Department, Kuwait University. Recently, he has visited several places including Interuniversity Micro-Electronics Centre (IMEC), Leuven, Belgium and spent a sabbatical leave at Queen's University and the royal Military College, Kingston, Ontario, Canada in 2001-2002. His research activities have been in the areas of antennas, geophysics, tunnel communication, e.m wave interaction with composite materials and microwave integrated circuits. Dr. Mahmoud is a Fellow of IET and one of the recipients of the best IEEE/MTT paper for 2003.

Simulations of a Shaped Dielectric Lens Antenna by FEKO

Y. Tajima and [1]Y. Yamada

Department of Electrical and Electronic Engineering, National Defense Academy
1-10-20 Hashirimizu, Yokosuka-shi, 239-8686 JAPAN
[1] yyamada@nda.ac.jp

Abstract – In the Intelligent Transportation System (ITS), millimeter waves are used and antennas are requested to have beam scanning ability. In the millimeter wave operation, a dielectric lens antenna is one of the prominent candidates. Authors designed a shaped dielectric lens antenna based on the Abbe's sine condition. Wide angle beam scanning characteristics were ensured through the ray tracing calculations and radiation pattern measurement. Recently, owing to the enhancement of electromagnetic simulator abilities, simulations of a dielectric lens antenna become possible. By employing an electromagnetic simulation, it is expected that detailed electrical performances of both the feed horn and the dielectric lens will be made clear. In this paper, electromagnetic simulations of a shaped dielectric lens antenna by FEKO suit 5.3 are conducted. First, the corrugate horn used for the feed horn is electromagnetically simulated. Excellent simulated radiation patterns coinciding with the measured results are achieved. Next, the feed horn radiation patterns are combined with the dielectric lens simulations. And simulation results of beam scanning characteristics are obtained. When comparing the simulated scanned beam shapes with the measured results, very good agreements are obtained. So, accuracies of simulations are ensured. Moreover, unexpected sidelobe increases in the specific wide angle region that were pointed out previously are studied. Simulated and measured results can confirm the sidelobe increases. As an additional study, electrical field distributions in the dielectric lens are simulated. Then, multiple reflections between lens surfaces are visually made clear. The reason of sidelobe increases can be clearly understood. As a result, it is confirmed that the FEKO simulator can rigorously simulate electromagnetic characteristics of a shaped dielectric lens antenna.

Keywords: Dielectric Lens Antenna, Wide Angle Beam Scanning and Wide Angle Radiation Pattern.

I. INTRODUCTION

In the Intelligent Transportation System (ITS), millimeter waves are used and antennas are requested to have beam scanning ability in the collision avoidance system. Here a dielectric lens antenna is one of the prominent candidates which achieves wide angle beam scanning [1]. Authors designed and fabricated the shaped dielectric lens antenna [2]. The wide angle radiation patterns were examined through ray tracing calculations [3] and measurements [4]. Good agreements of calculated and measured results were ensured. However, in the case of the ray tracing method, the electric performance of the feed horn was approximated by a simple mathematical function. For more exact analysis, FDTD method is used for calculation of lens antennas. However it requires huge computer memory and calculation time [5]. In order to reduce calculation memory, axi-symmetrical FDTD is developed [6]. Even though the method can reduce calculation memory, it can not calculate off-focus feed. And Method of Moment (MoM) can be also used for calculation of homogeneous dielectric body [7]. In this method, instead of a volume distribution, calculation can be formulated in terms of a surface distribution and calculation memory can be reduced. And an electromagnetic simulation ability handling a dielectric lens antenna is enhanced in the FEKO suit 5.3 based on MoM. By employing this electromagnetic simulator, both the feed horn and the dielectric lens antenna can be analyzed exactly.

In this paper, FEKO calculation results of detailed electrical characteristics on the corrugate horn used as the feed horn and the shaped dielectric lens antenna are obtained. And radiation patterns are compared with the measured results in order to ensure the calculation accuracies. In section 2, the outline of the shaped dielectric lens antenna is explained. And summaries of simulation parameters and computer loads are explained. In section 3, simulation conditions of the corrugate horn so as to coincide with the measured results are shown. In section 4, simulated and measured results of beam scanning characteristics on the shaped lens antenna are shown. In section 5, as for wide angle radiation patterns, simulated and measured results are shown. Remarkable sidelobe increases in the specific wide angle region are indicated. In order to clarify the reason, electrical fields in the lens are investigated and trials of matching layers attachment on the lens surfaces are conducted.

II. SHAPED DIELECTRIC LENS ANTENNA FOR WIDE ANGLE BEAM SCANNING

A. Configuration of The Lens Antenna

Figure 1 shows the configuration of the shaped dielectric lens antenna in the simulation and the measurement. The lens has axi-symmetrical structure around the Z-axis. A corrugate horn is employed as the feed horn. And the lens and the feed are surrounded by an electromagnetic absorber in order to suppress spill over. The lens material is Teflon and surfaces are designed by introducing Abbe's sine condition [8]. The focal length L_f of 105mm and the lens diameter D of 100mm are employed. The frequency of 60GHz (λ=5mm) are employed. The lens diameter is corresponding to 20λ. The beam scan is achieved by off focus feed shown as a broken line and the off-focus position of 25° scanning beam (θ_s=25°) is indicated. At the time, the length between the horn and the lens center L_f' becomes 81.9mm. The polarizations of the feed horn are also shown. The electrical field component of the horn is parallel to the Y-axis. For the off-focus position, the coordinate system is rotated around the Y-axis. The new axis are denoted by the X' and Z' as shown in the figure. And the plane on which the horn moves (ZX-plane) is called as a scanning plane and the plane which transverse the scanning plane (YZ or YZ'-plane) is called as the transverse plane.

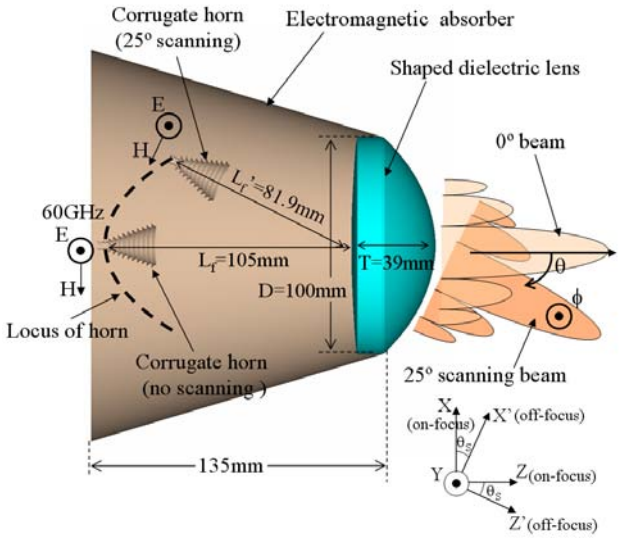

Fig. 1. Lens antenna configuration.

The specification of a personal computer and simulation parameters are shown in Table 1. In calculation, the FEKO simulator that can use the Multilevel Fast Multipole Method (MLFMM) is employed in order to save the computer memory and speed up to calculation time. Surface Equivalence Principle (SEP) and Volume Equivalence Principle (VEP) are employed for the calculation of the dielectric lens and electromagnetic absorber, respectively. So, all antenna parts can be simulated by the Method of Moment. The mesh size of λ/8 is employed for the corrugate horn. For the dielectric lens and electromagnetic absorber, mesh size of λ/3 is employed because these dielectric objects are very large compare to one wave length. The mesh size might look too coarse, there is a little difference in radiation pattern shapes and null depths in mesh size of λ/3 to λ/7. So, the dielectric objects of mesh size of λ/3 can be simulated accurately. As for the dielectric constant of the electromagnetic absorber, the catalog data of ε_r=2 and tanδ=1 is used. The dielectric lens and the electromagnetic absorber require large memory of 2.6GByte and 3.1GByte respectively. The calculation time is 44.4 hours and it corresponds to about 2 days.

Table 1. Simulation parameters.

Computer specification	CPU	Xeon 3.2GHz
	Loaded memory (Byte)	20G
	Software	FEKO (Suit 5.3), MOM with MLFMM
Feed horn (Corrugate horn)	Mesh size	λ/8
	Number of mesh	13,102
	Calculation memory (Byte)	365M
Dielectric lens	ε_r	1.94
	Tanδ	7.5×10^{-4}
	Mesh size	λ/3
	Number of mesh	33,843
	Calculation Memory (Byte)	2.6G
Electromagnetic absorber	ε_r	2
	tanδ	1
	Thickness	10mm
	Mesh size	λ/3
	Number of mesh	75.346
	Calculation Memory (Byte)	3.1G
Calculation time (h)	44.4	

B. Estimation of Beam Scanning by a Ray Tracing Method

Outlines of the beam scanning abilities can be anticipated through the ray tracing results. Rays from the feed horn to the lens outside are calculated by the ray tracing software developed by authors. Rays emitted from the positions of θ_s=0° and 25° are shown in Figs. 2(a) and (b), respectively. In Fig. 2(a), rays in the X-axis and the Y-axis directions become parallel after refraction by the shaped dielectric lens. From results of the rays, an axi-symmetrical pencil beam is expected. In Fig. 2(b), while rays in the X-axis direction become parallel after refraction by the lens, rays in the Y-axis direction do not

become parallel. Moreover, rays do not exist in a flat plane and compose a curved plane. So, phase deterioration in the Y-axis direction is suspected. Also, it is suspected that the beam shape will be distorted in the transverse plane.

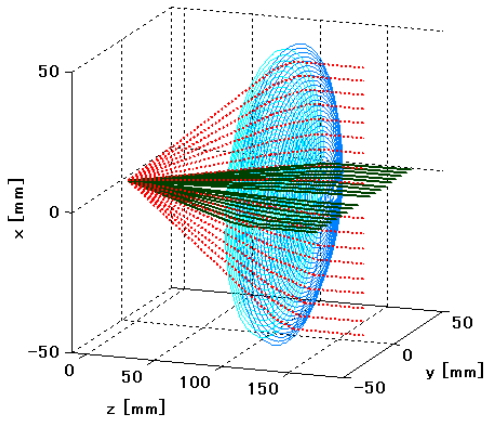

(a) No scanning

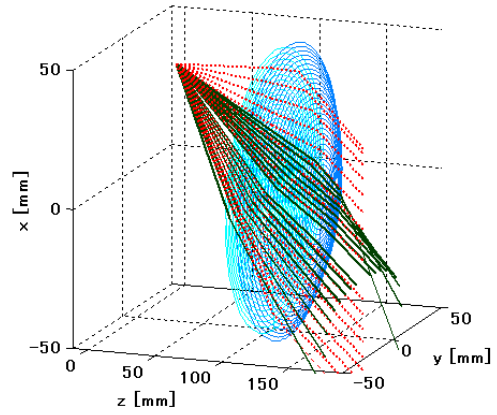

(b) 25° scanning

Fig. 2. Rays on the scanning and transverse directions.

III. SIMULATION CONDITIONS OF THE FEED CORRUGATE HORN

The corrugated horn used in the simulation is designed depending on the measured horn structure shown in Fig. 3. The simulated horn is excited at the feed point by an electric point source, while the actual horn is connected with a wave guide. The depth of the groove is optimized in order to achieve the scalar feed characteristics and to coincide with the measured radiation patterns. At the distant points on the lens surface, the phase center of the corrugate horn becomes 20mm inside from the aperture.

Figure 4 shows simulated and measured radiation patterns. The simulated patterns are shown by dotted lines and the measured patterns are shown by solid lines. As a result of the scalar feed, the patterns of E and H-plane become almost the same. As a result of adequate horn parameters, the radiation patterns of simulated and measured results agree very well. The 3dB beam width of each pattern is 21°. Edge levels of the lens antenna become -15 dB and -18 dB at θ_s = 0° and θ_s = 25°, respectively.

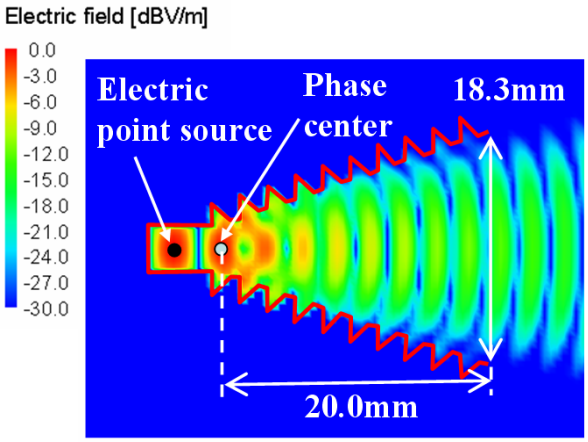

Fig. 3. Corrugate feed horn.

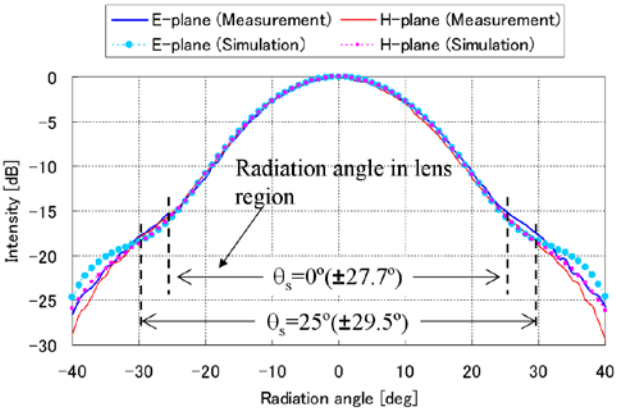

Fig. 4. Radiation patterns of the corrugate feed horn.

IV. BEAM SCANNING CHARACTERISTICS

Figure 5 shows a photograph in measurements of the lens antenna. The lens is supported by a plastic plate covered by an electromagnetic absorber. The feed horn is supported by the positioning mount. The positioning mount can be moved along the X and Z-axis and rotated around the Y-axis. In the measurement setting, the far filed criterion given by $2(d_1+d_2)^2/\lambda$ is 6.2m and the range between the lens antenna and a receiving antenna is 4.4m. So, adequate radiation patterns can be obtained.

A. No Scanning Beam Pattern

Measured and simulated radiation patterns of on focus feed are shown in Fig. 6. The simulated patterns are

shown by broken lines and the measured patterns are shown by solid lines. In Figs. 6(a) and (b), the radiation patterns on the scanning and transverse planes become almost same due to the scalar feed characteristics of the feed horn. Beam widths on the scanning and transverse planes are 3.6° and 3.5°, respectively. As for comparisons of the measured and the simulated patterns, very good agreements are achieved. In the case, the lens material (Teflon) permittivity of 1.96 is employed. So, 1.96 is suitable for the permittivity of Teflon at the frequency of 60GHz. The antenna gains of measurement and simulation are 34.7dBi and 34.2dBi, respectively. These antenna gains agree very well. The simulated gain is 1.8dB lower than the uniformly illuminated aperture gain of 36.0dBi. This gain reduction corresponds to the aperture efficiency of 66%. Loss factors of the lens antenna are summarized in Table 2. Total loss of 2.2dB agrees well to the simulated gain reduction of 1.8dB.

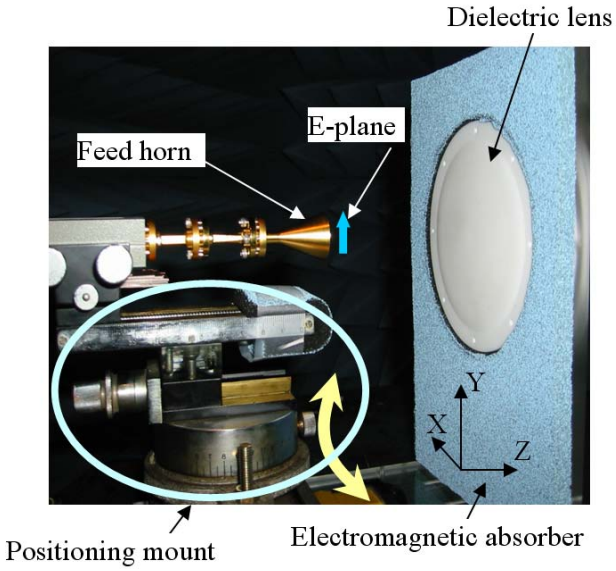

Fig. 5. Measurement setting.

Table 2. Loss factors.

	Gain	Loss
Uniform illumination	36.0dBi	
Intensity taper		0.74dB
Reflection		0.25dB
Dielectric loss		0.13dB
Spill over		1.12dB
Total loss		2.24dB
Calculated gain	33.8dBi	
Simulated gain by FEKO	34.2dBi	1.8dB

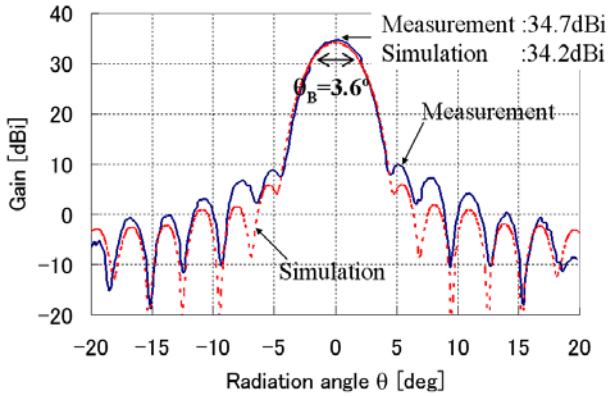

(a) Scanning-plane (H-plane)

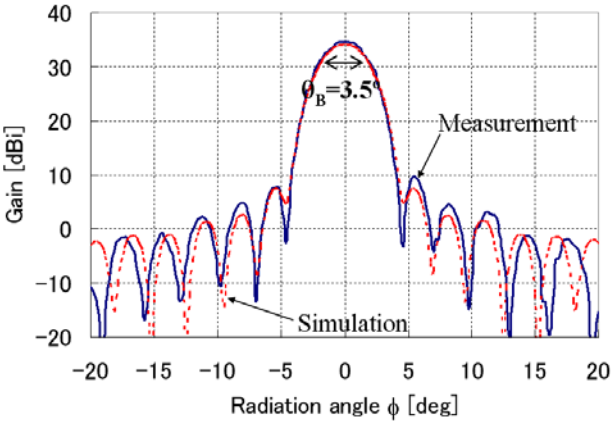

(b) Transverse-plane (E-Plane)

Fig. 6. Radiation patterns of lens antenna (no scanning).

B. 25° Scanning Beam Pattern

Measured and simulated radiation patterns in the case of 25° scanning are shown in Figs. 7(a) and (b). The measured and the simulated patterns agree well. The measured and simulated 3dB beam widths in the scanning-plane are 4.0°. And at radiation angle of 15°<θ<20°, shoulder patterns are observed in both of the measurement and simulation. It indicates that the small phase error is occurred on the plane. In the transverse-plane, 3dB beam widths of measurement and simulation become 5.4°. And the main lobes deteriorate to broaden shapes. Comparing with the no scanning beam, the scanning-plane beam width is broadened only 0.4°. However the transverse-plane beam width is broadened about 1.9°. The reason of this beam broadening is considered that phase deviation is produced in the transverse-plane. The gains of measurement and simulation are 32.1dBi and 31.8dBi, respectively. These gain reductions are corresponding to the beam widths broaden.

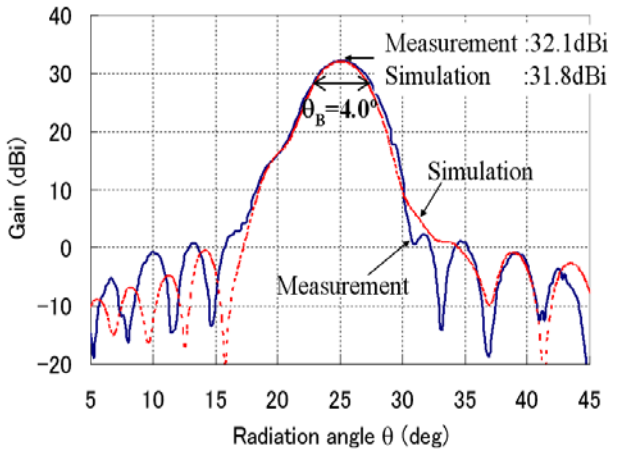

(a) XZ-plane (Scanning)

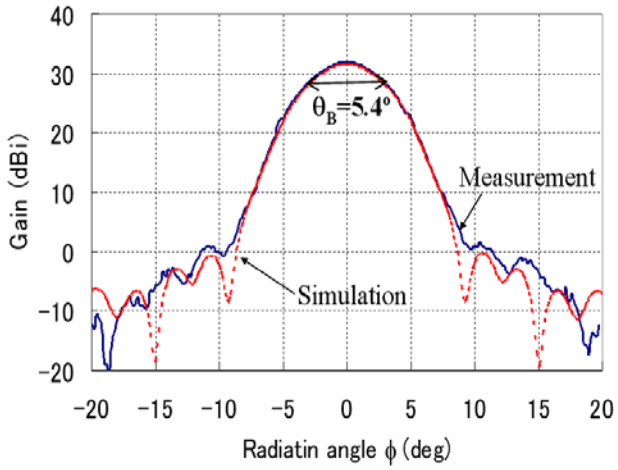

(b) YZ-plane (Transverse)

Fig. 7. Radiation patterns of lens antenna (25° scanning).

In order to understand the reason of beam broadening, the field intensity and phase distributions on the X'Y-plane of the lens aperture are shown in Figs. 8(a) and (b). In the field intensity, almost axi-symmetrical pattern is obtained as shown in Fig. 8(a). This distribution is almost satisfactory. In Fig. 8(b), the phase distribution along the scanning direction is almost constant due to the lens surface shaping. However, the phase distribution along the transverse direction is delayed to the aperture edge and the difference between the center and the edge is more than 150°. This large phase delay is considered the cause of the transverse-plane radiation deterioration. In order to correct the phase delay, array antenna configuration to the feed is effective [9].

As conclusions of beam scanning characteristics, calculation results by the FEKO simulator agree very well with measured results. So, calculation accuracies are ensured.

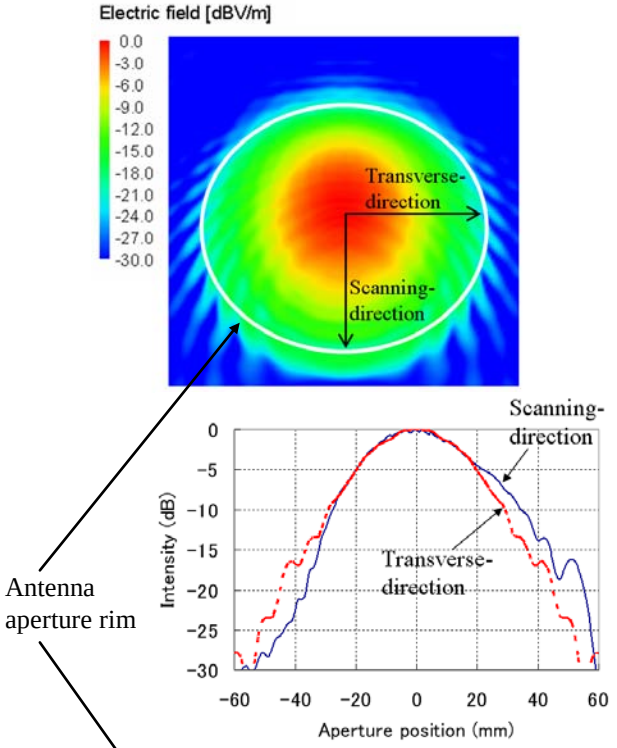

(a) Field intensity (X'Y-plane).

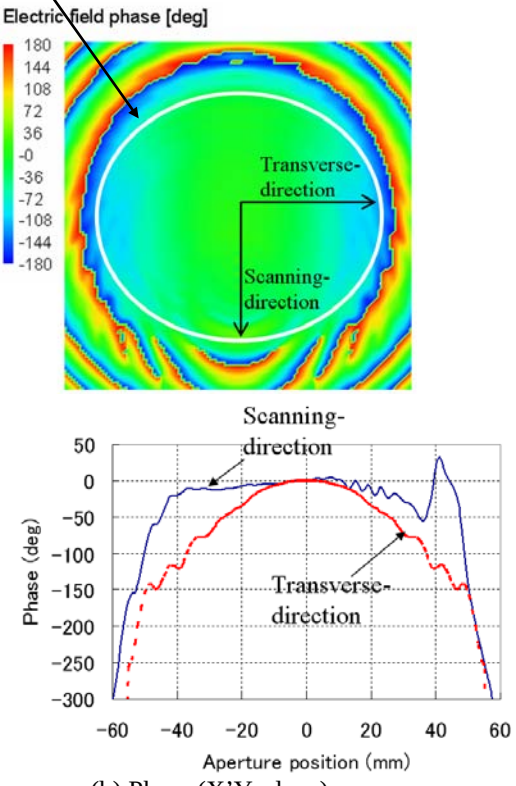

(b) Phase (X'Y-plane).

Fig. 8. Aperture electrical field distributions.

V. WIDE ANGLE RADIATION PATTERN

Previously, it was reported that multi-reflections between lens surfaces increased radiation levels in specific wide angle region [4]. So, we tried to clarify the multiple reflections through electromagnetic simulations. Figure 9 shows measurement setting of wide angle radiation pattern. In the case of measurement, the feed horn and lens edge are covered by the electromagnetic absorber.

Measured and calculated radiation patterns in the wide angle region are shown in Fig. 10. In the measured result, almost symmetrical pattern is obtained. So, the measurement accuracy is ensured. Sidelobe levels are decreasing gradually to 40 degree. However, sidelobe levels suddenly increase at 45°. Sidelobe levels become almost -10dBi in the angle region 45°<|θ|<75°. Measured and simulation patterns agree very well. Both the simulation and measurement results indicate sidelobe increases precisely. So, simulations of this phenomenon are considered accurate.

In order to investigate the reason of sidelobe increase, electric field in the lens is shown in Fig. 11. Inside the dielectric lens, many high intensity lines are observed. Judging from the directions of lines, these lines indicate reflections from the front surface. Outside the front surface, weak radiations to wide angle regions are observed and these radiations are thought the cause of the sidelobe increase. Next in order to investigate surface reflections precisely, ray tracing results are obtained by the ray tracing software developed by authors. Ray tracing results are shown in Fig. 12. The incoming rays to the lens antenna are shown by dotted lines. Reflected rays are shown by solid lines. First, incoming rays are reflected at the front surface. Then, reflected rays are once again reflected at the rear surface. Finally, dually reflected rays are radiated in wide angle regions. Through the electromagnetic simulations and the ray tracing calculations, the reason of sidelobe increases in the wide angle region is clarified.

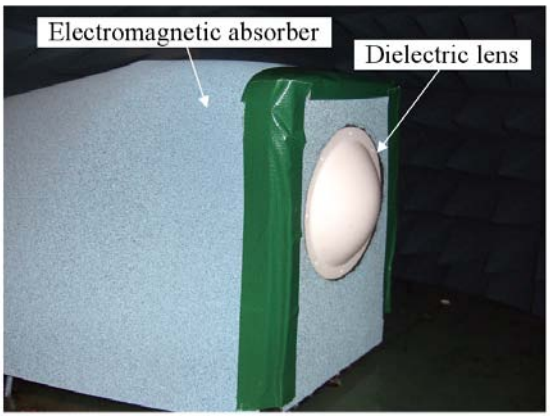

Fig. 9. Measurement setting of wide angle radiation pattern.

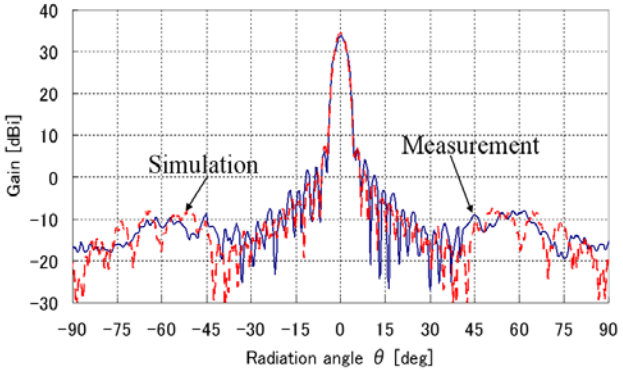

Fig. 10. Wide angle radiation pattern (without matching layer).

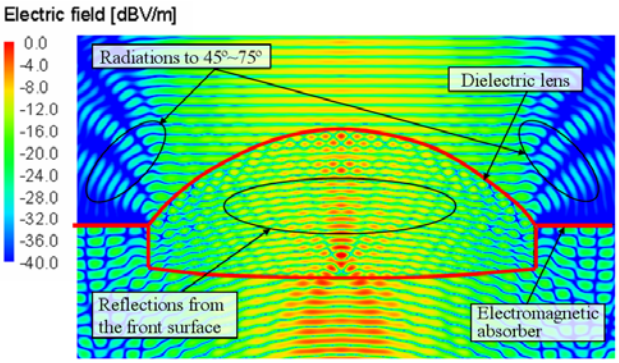

Fig. 11. Electric fields in the lens.

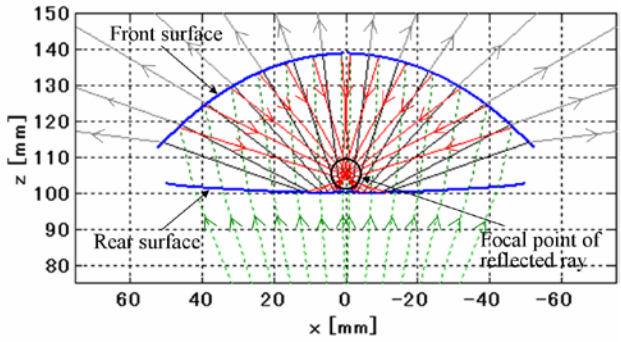

Fig. 12. Ray trace of multiple reflections.

One more trial to ensure multiple reflections is conducted by attaching matching layers on the lens surfaces. Situations of matching layers are shown in Fig. 13. The material of matching layers is foamed Teflon. Its permittivity is assumed as 1.41 and its thickness is 1.0mm ($\approx\lambda_g/4$). The matching layers are attached on the dielectric lens with double-stick tape.

The measured and simulation results are shown in Fig. 14. In the measured and simulated results, increased sidelobes in the angle region 45°<|θ|<75° are sufficiently suppressed. However, because the matching layers are not

completely designed, small sidelobe increases remain in the angular region 60°<|θ|<90° in the simulation and 40°<|θ|<90° in the measurement, respectively. Next in order to understand the effect of matching layers, electrical fields in the lens are obtained. Simulated results are shown in Fig. 15. Reflected waves from the front surface become very weak. The effects of matching layers are ensured. In designing matching layers, the ray tracing results of Fig. 12 provide the very important data. Reflected rays from the front surface concentrate in front of the rear surface. So, the designed matching conditions carefully at the center region of the rear surface seems the most important.

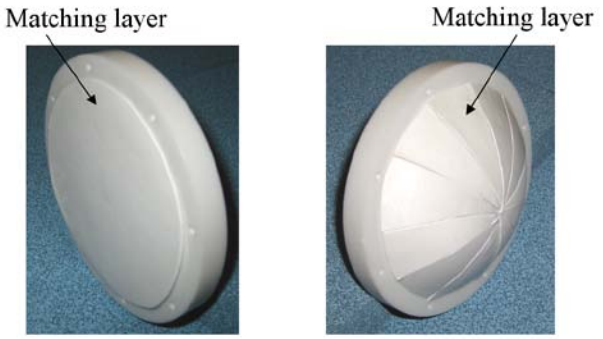

(a) Rear surface (Feed side) (b) Front surface (Aperture side)

Fig. 13. Matching layer.

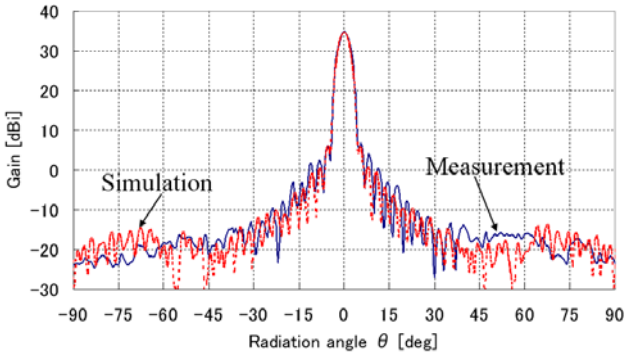

Fig. 14. Wide angle radiation pattern (with matching layer)

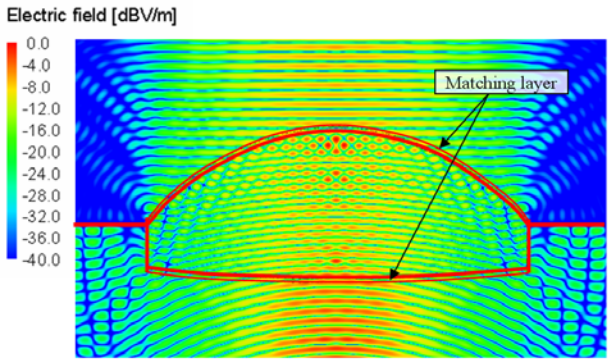

Fig. 15. Electric fields in the lens.

As conclusions of simulations of wide angle radiation characteristics, it is ensured that FEKO simulator can produce exact electromagnetic solutions. Moreover, very interesting phenomena of multiple reflections between lens surfaces are visually clarified.

VI. CONCLUSIONS

In accordance with the improvement of simulation abilities for dielectric objects in FEKO suit 5.3, authors tried to simulate the shaped dielectric lens antenna developed by authors. Accuracies of simulations are ensured through comparing the simulated results with measured results. Moreover, some interesting phenomena happened in the lens are visually clarified.

- Beam scanning characteristics that are the main subject of the shaped dielectric lens antenna could be simulated successfully. Simulation accuracies are ensured through the good agreement with the measured results.
- Amplitude and phase distributions of electrical fields on the antenna aperture plane are visually clarified in the case of beam scanning.
- Affects on radiation patterns of multiple reflections inside the lens are exactly simulated and simulated radiation patterns agree very well with the measured results.
- Electrical field distributions indicating multiple reflections inside the lens are shown and this phenomenon are visually clarified.

ACKNOWLEDGEMENT

Authors express thanks to Dr. Naobumi Michishita of National Defense Academy for his helpful discussions.

REFERENCES

[1] T. Kato et. al., “76 GHz high performance rader sensor featuring fine step scanning mechanism utilizing NRD technology,” *IEEE Intelligent Vehicles Symposium*, pp. 163-170, May 2001.

[2] Y. Tajima and Y. Yamada, “Design of shaped dielectric lens antennas for wide angle beam steering”, *WILEY Periodicals Inc., Electron. and Comm. in Japan*, Part 3, vol. 89, no. 2, pp. 1-12, Feb. 2006.

[3] Y. Tajima, Y. Yamada, S. Sasaki, and A. Kezuka, “Calculation of wide angle radiation patterns and caustics of a dielectric lens antenna by a Ray tracing method”, *IEICE Trans.*, vol. E-87-C, no. 9, pp. 1432-1440, Sep. 2004.

[4] Y. Tajima, Y. Yamada, and A. Kezuka, “Measured results of dielectric lens antenna for wide angle bean scanning”, *IEICE Trans. in Japanese*, vol. J88-B, no. 12, pp. 2394-2397, Dec. 2005.

[5] A. Kezuka, Y. Yamada, and H. Kida, "Radiation pattern syntheseis of a lens horn antenna", *IEICE Trans.*, vol. E87-C, no. 9, pp. 1425-1431, Sep. 2004.
[6] A. Kezuka, Y. Yamada, and Y. Kazama, "Phase correction method for GO designed dielectric lens horn antenna", *IEICE Trans.*, vol. E88-B, no. 6, pp. 2334-2340, June 2005.
[7] R. F. Harrington, *Field Computaion by Moment Methods*, *IEEE PRESS*, pp. 38-40, 1993.
[8] Y. T. Lo and S. W. Lee, *Antenna Handbook*, volume 2, Van Nostrand Reinhold Company, Ch. 16, pp. 16-23, 1988.
[9] Y. Tajima and Y. Yamada, "Improvement of beam scanning characteristics of a dielectric lens antenna by array feeds", *IEICE Trans*., vol. J91-A no. 7, pp. 1616-1624, Jun. 2008.

Tajima was born in Oita, Japan on February 28, 1978. He received the B.S. and M.S. degrees in Electronics Engineering from National Defense Academy, Kanagawa, in 2000 and 2005. He enlisted in Japan-Air-Self-Defense-Force in 2000. He was engaged in tests and developments of radar equipments. Now he is a Capt. He entered the doctor course of Electronics and Information Engineering of National Defense Academy. His current research interests include lens antennas and array antennas.

Yoshihide Yamada graduated from Nagoya Institute of Technology and received the BS and MS degrees of electronics in 1971 and 1973, respectively. And he received the DE degree from Tokyo Institute of Technology in 1989. In 1973 he joined the Electrical Communication Laboratories of Nippon Telegraph and Telephone Corporation (NTT). Till 1984, he was engaged in research and development of reflector antennas for terrestrial and satellite communications. From 1985, he engaged in R&D of base station antennas for mobile radio systems. In 1993, he moved to NTT Mobile Communications Network Inc. (NTT DoCoMo). In 1995, he was temporarily transferred to YRP Mobile Telecommunications Key Technology Research Laboratories Co., Ltd. At the same time, he was a guest professor of the cooperative research center of Niigata University, and a lecturer of Science University of Tokyo, both from 1996. In 1998, he changed his occupation to a professor of National Defense Academy. Now, he is interested in very small RFID antennas, shaped dielectric lens antennas and electromagnetic simulations of large objects. He is a member of the IEICE and JSST of Japan and IEEE society members of AP, VT and COMM.

Cross Slot Antenna with U-Shaped Tuning Stub for Ultra Wideband Applications

D. S. Javan and O. H. Ghouchani

Department of Electrical Engineering, Ferdowsi University, Mashhad, Iran
Email: dawoodjavan@yahoo.com

Abstract – A novel design of an Ultra Wideband (UWB) slot antenna is presented. This antenna operates as a transmitter and receiver antenna. Effects of the antenna dimensional parameters are studied through experimental and simulation results. Design procedures are developed and verified for different frequency bands. The experimental and simulation results exhibit good impedance bandwidth, radiation pattern and relatively stable gain over the entire band of frequency. Antenna gain and directivity at boresight and in their maximum states are close to each other and indicate high radiation efficiency. To use the antenna as a linearly polarized antenna, the radiation pattern in E-plane is better than that in H-plane.

I. INTRODUCTION

The Federal Communication Commission (FCC) issued a ruling for ultra-wideband (UWB) implementation in data communication [1]. A UWB technology promotes communication system, particularly in wireless multimedia system with high data rate. According to FCC, a UWB antenna should provide a gain and impedance bandwidth from 3.1 GHz to 10.6 GHz. A microstrip slot antenna may be a good choice as it is low profile, low cost, lightweight, easy integration with monolithic microwave integrated circuits (MMICs). Feed interactions of wideband slot antennas are analyzed using finite element -optimization methods and effects of feeding mechanisms on dimensions of slots have been discussed in [2]. Several methods have been proposed to increase the bandwidth of microstrip-fed slot or cavity-backed slot antenna, such as printed radial stub [3]. A printed wide-slot antenna is fed by a microstrip line with a fork-like tuning stub for bandwidth enhancement [4]. A design of a microstrip-line-fed printed wide-slot antenna had been studied in [5]. An ultra-wideband coplanar waveguide (CPW) fed slot antenna was excited by a 50-Ω CPW with a U-shaped tuning stub [6]. Experimental investigations on a wideband slot antenna element have been proposed [7] as a building block for designing single- or multi-element wideband or dual-band slot antennas. This element shows bandwidth values up to 37%, if used in the wideband mode.

A circular slot antenna is fed by a circular open-ended microstrip line to provide UWB impedance bandwidth [8]. Also an ultra-wideband square-ring slot antenna (SRSA) has been proposed which is fed by a microstrip line with a U-shaped tuning stub [9]. However, the SRSA is split inside the U-shaped feed, so it is called split square-ring slot antenna (SSRSA). A printed rectangular slot antenna with a U-shaped tuning stub is backed with reflector for improvement in the impedance bandwidth and unidirectional radiation patterns [10].

In this paper, we propose a novel structure that is driven by wide-slot antenna and merged by a cross- slot for improvement in gain and impedance bandwidth. The measurement and simulation results of the impedance bandwidth are in good agreement with each other.

II. ANTENNA STRUCTURE

Figure 1 shows the proposed printed slot antenna. The antenna structure is a split square ring slot in the ground plane of dielectric substrate with a cross slot in center of square ring. This structure is fed by a single microstrip line with a U- shaped tuning stub. The slot antenna is fed near an edge by a microstrip line and a fictitious short circuit that produces more resonant frequencies [7].

The SSRSA can be considered as a combination of numerous of narrow slot radiators which are connected to each other, so it can provide a couple of resonances at different frequencies. The split in one arm actually increases the number of resonances by introducing new resonant lengths. The cross slot is located in center of the square ring. Actually it can resonate more than resonant frequencies of square ring slot and this improves the impedance matching rather than [9]. This structure is fabricated on a 0.5mm RO4003B substrate with a dielectric constant equal to 3.4. Photograph of the proposed antenna is shown in Fig. 2. The antenna includes a microstrip feed line with the U-shaped tuning stub. By splitting the square ring slot antenna (SRSA) and optimization of the feeding network, the required impedance bandwidth is achieved over the UWB frequency range (3.1 to 10.6 GHz).The ground plane size is $Lg \times Wg$ =100mm × 100mm.

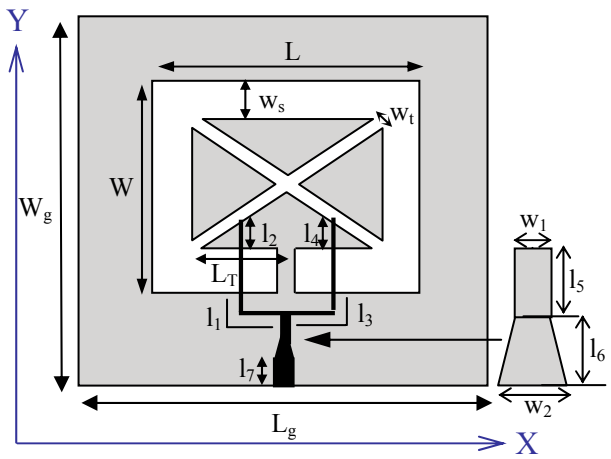

Fig. 1. Configuration of the proposed antenna.

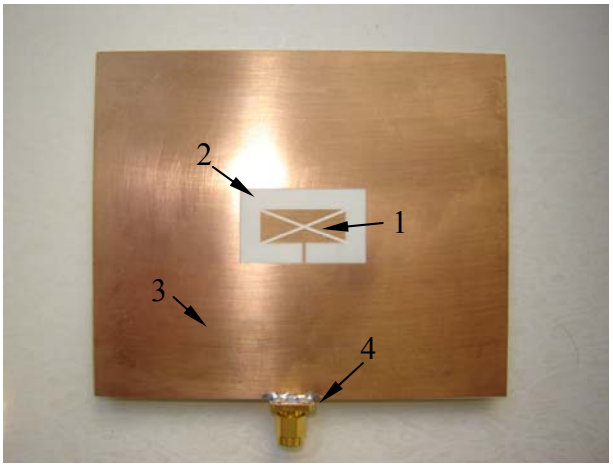

Fig. 2. Photograph of the antenna, (1) Cross slot, (2) square slot, (3) Ground plane, and (4) Input port connected to microstrip line.

III. RESULTS AND DISCUSSIONS

Effect of L_T variations on the return loss of antenna, which has been evaluated by IE3D software [11], is shown in Fig. 3.

The longer the L_T, the better the impedance matching, for the coupling between the square ring and the cross-slot.

It is obvious the upper resonances are created by off-center microstrip feed [7].

The U-shaped tuning stub is employed for wideband performance. The impedance matching of the proposed antenna is unfavorable when the L_T is less than 13mm. The prototype antenna was simulated by IE3D software and fabricated with L_T= 13mm and W_t= 1mm. The simulation and measurement results are shown in Fig. 4.

The resonant frequencies of the simulation and measurement results are in good agreement within the matching frequency band 3 GHz to 12 GHz, which corresponds to the impedance bandwidth (S_{11}<-10 dB). This structure is more compact than [8]. The antenna provides a VSWR lower than 2 (S_{11}<-10dB) from 3 GHz to 12 GHz.

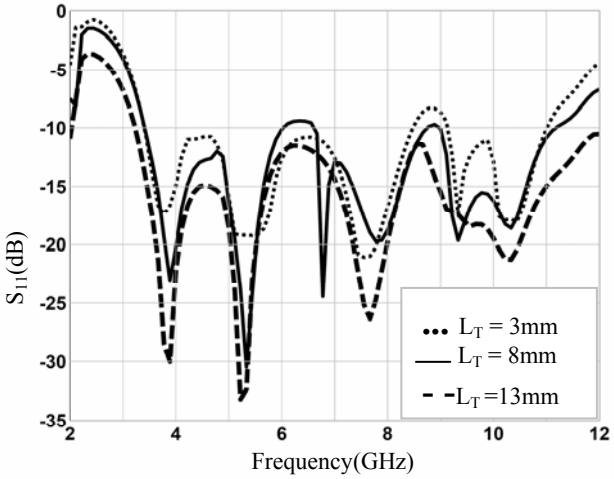

Fig. 3. Effect of L_T changes on return loss. L_T is distance between the center of the cross slot and the square ring .

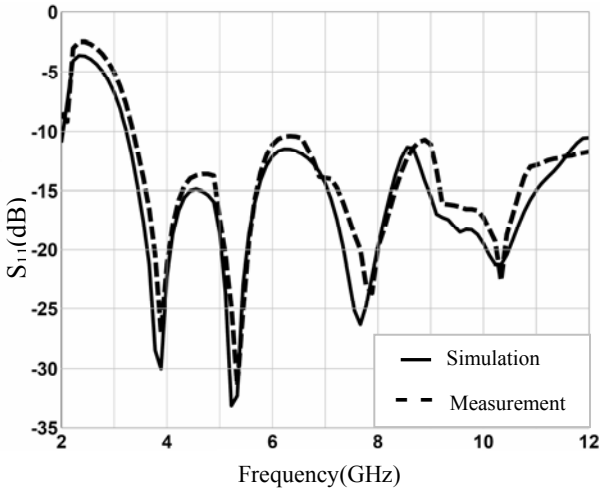

Fig. 4. Measured and simulated return loss of the proposed antenna.

The parameter dimensions are obtained after performing an optimization and identified in Table1. These dimensions were obtained by performing an optimization for improving the impedance bandwidth by ADS software [12]. Figure 5 shows the gain of optimized antenna at broadside (φ=0, θ=0) from 2 GHz to 12GHz. The directivity at the direction of maximum radiation is shown in this figure. The antenna gain and directivity at boresight and in their maximum states are close to each other and indicate high radiation efficiency.

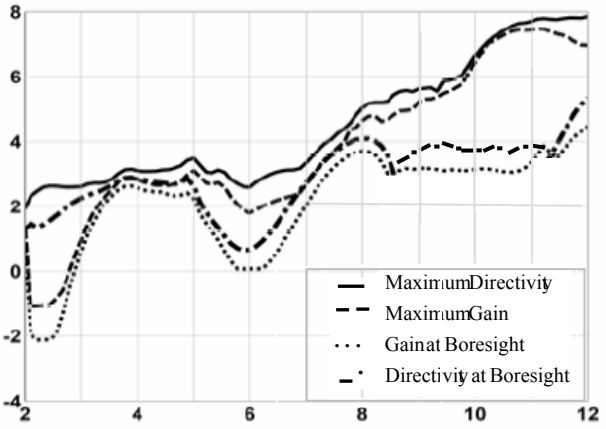

Fig. 5. Simulated values of gain and values of directivity (dBi).

Figure 5 also shows that above 10.5 GHz the directivity and gain at boresight increase and it is a reason for this: each slot of the cross slot is a branch of the square ring. These branches have the W_t= 1mm and this is less than W_S= 6mm. This causes high current distribution flows to the cross-slot rather than square-ring slot and the gain increases at boresight above the 10.5 GHz. So the combination of the cross-slot and square ring slot improves the gain and directivity more than [9]. Figure 6 shows the measured maximum gain and gain at boresight.

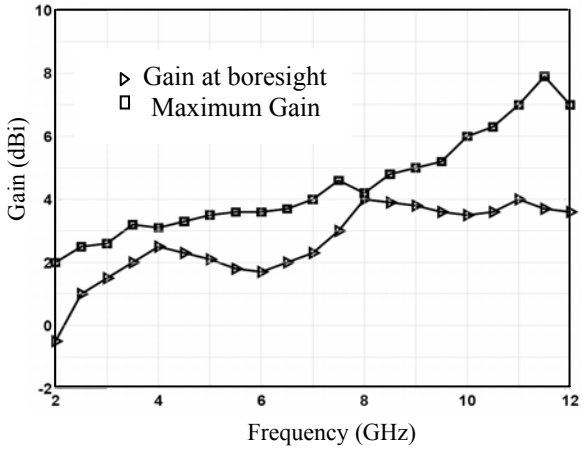

Fig. 6. Measured values of the gain.

This figure shows the gain at boresight is more than 2dBi and is relatively constant from 8 to12 GHz. The electric field distribution on the square-ring and cross-slot for proposed antenna was simulated with the IE3D simulation software. Figure 7 shows the electric field distribution on the slots.

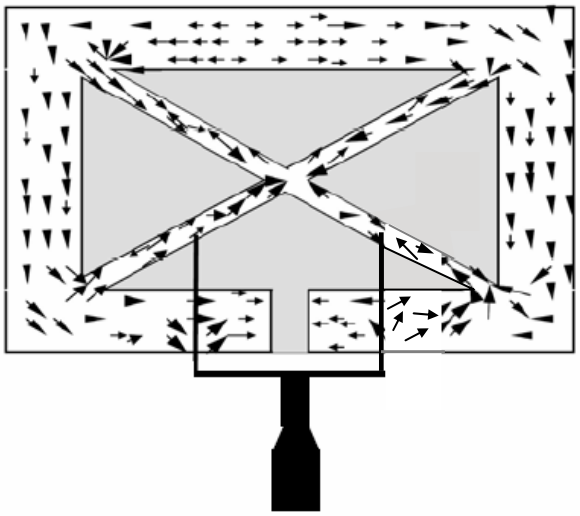

Fig. 7. Simulated electric field distribution on the slots at the frequency of 10 GHz.

Figures 8 and 9 show the measured H-plane (xz plane) and E-plane (yz plane) radiation patterns for both co- and cross-polarizations at f = 3.5, 5.5, 7.5 , 9.5 and 10.5 GHz . From the results, it is concluded that the proposed antenna in operating frequencies provides the same polarization planes and similar radiation patterns.

To use the antenna as a linearly polarized antenna, the radiation pattern in the E-plane is better than H-plane. The E and H plane patterns start to introduce spurious radiation in high frequency (i.e, from 8.5 GHz) because the U-shaped stub length is almost equal to a half wavelength. However, the radiation patterns start to change in high frequencies and show higher directivities in other directions. In the E-plane, the cross-polar radiation is at least -10 dB less than the co-polar radiation.

Table 1. The dimensions of proposed antenna.

Parameter	W	W_s	W_1	W_2	W_t	L	l_1	l_2	l_3	l_4	l_5	l_6	l_7	L_T
Magnitude (mm)	21	6	0.7	13	1	35	14.3	3	14	4.1	0.6	1.8	30	13

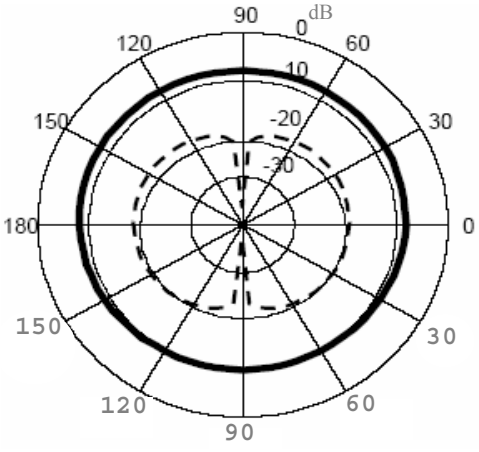

3.5 GHz

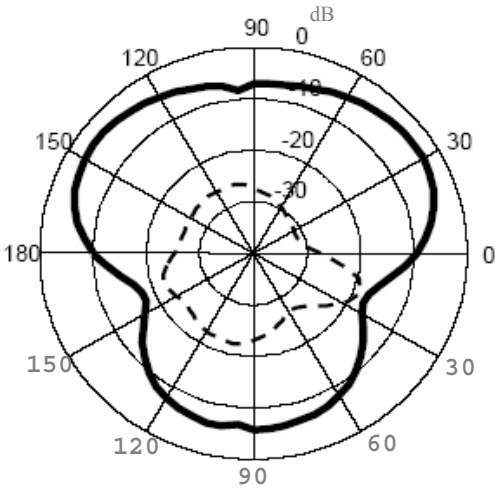

5.5 GHz

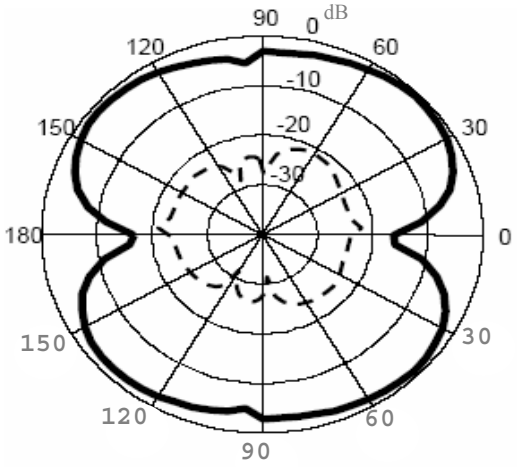

7.5 GHz

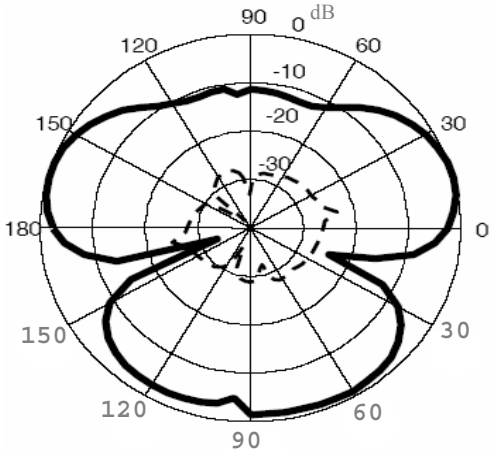

9.5 GHz

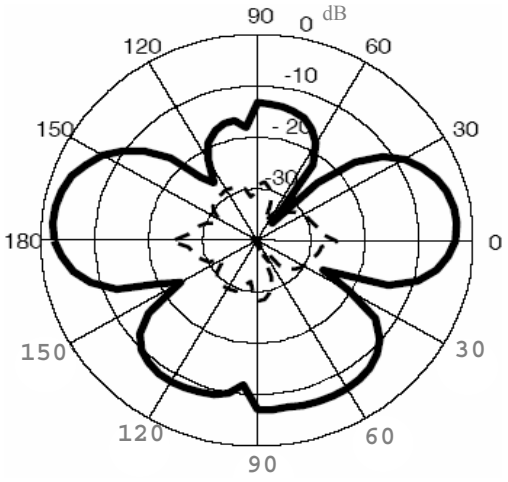

10.5 GHz

Fig. 8. Measured radiation pattern of cross slot antenna in H-plane ($\varphi = 0\circ$). The solid line is co-polar and the dash line is cross-polar component.

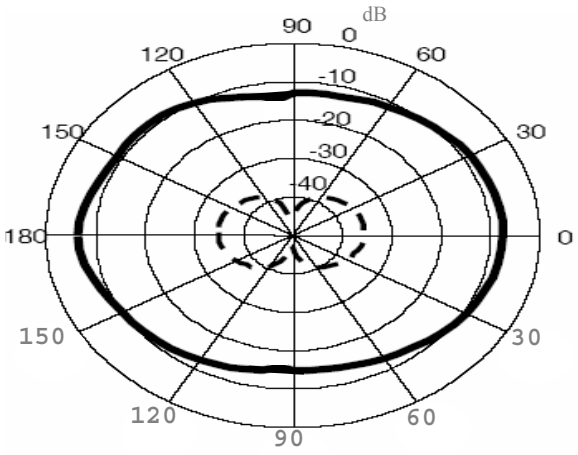

5.5 GHz

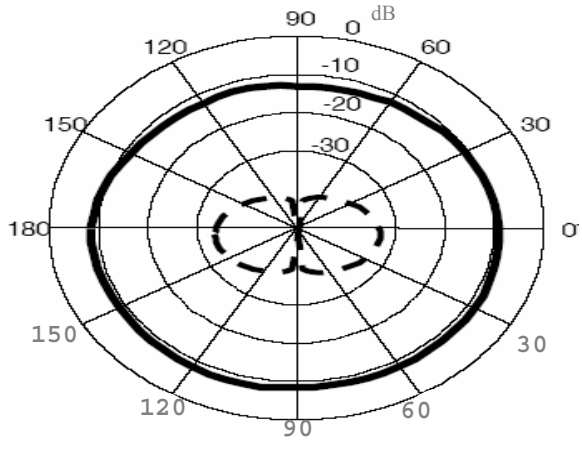

3.5 GHz

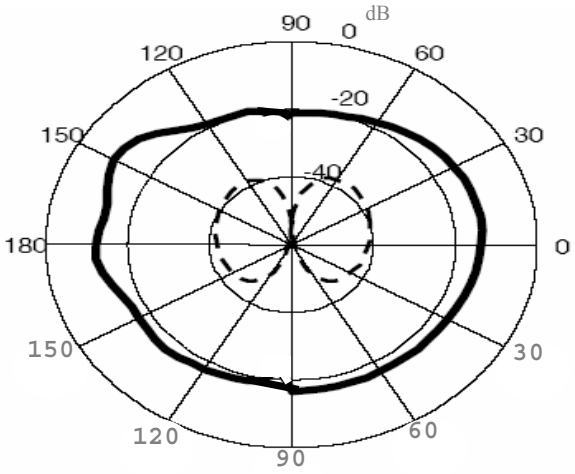

7.5 GHz

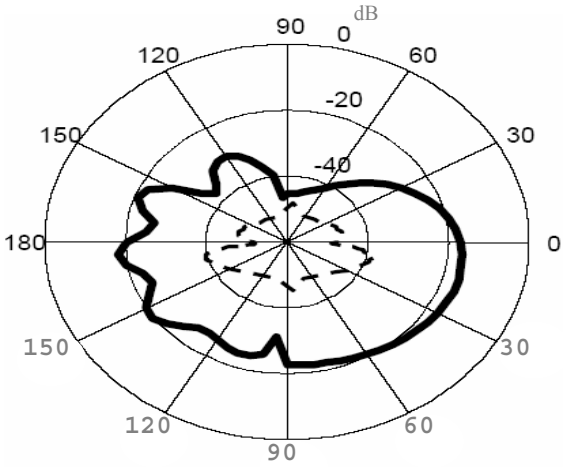

9.5 GHz

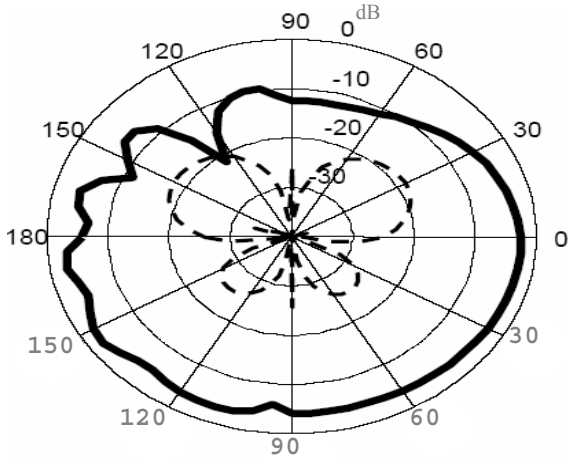

10.5 GHz

Fig. 9. Measured radiation pattern of cross slot antenna in E-plane ($\varphi = 90\circ$). The solid line is co-polar and the dash line is cross-polar component.

IV. CONCLUSIONS

A novel microstrip square ring slot is merged with cross-slot and fed with a U- shaped tuning stub. The proposed antenna has been designed, simulated, optimized and measured for the broadband operation. The novel antenna promotes gain, impedance bandwidth, and radiation pattern. The proposed antenna provides a good impedance matching from 3 GHz to 12 GHz. This antenna has a favorable field gain across the matching band as a desirable feature for UWB applications. The gain and directivity at boresight are close to each other and provide high radiation efficiency.

REFERENCES

[1] FCC report and order for part 15 acceptance of ultra wideband (UWB) System from 3.1 GHz to 10.6 GHz, Washington, DC, 2002.

[2] P. H. Rao, "Feed effects on the dimensions of wide band slot antennas," *Microwave and Opt. Technol. Lett.*, vol. 40, no. 1, January 2004.

[3] P. H. Rao, V. F. Fusco, and R. Cahill, "Linearly polarized radial stub-fed high-performance wideband slot antenna," *Electron Lett.*, vol. 37, pp. 335–337, 2001.

[4] J. Y. Sze and K. L. Wong, "Bandwidth enhancement of a microstrip-line-fed printed wide-slot antenna," *IEEE Trans. Antennas and Propagation*, vol. 49, vo.7, 2001.

[5] Y. W. Jang, "Broadband cross-shaped microstrip-fed slot antenna," *Electron. Lett.*, vol. 36, no. 25, 2000.

[6] R. Chair, A. A. Kishk, and K. F. Lee, "Ultrawide-band coplanar waveguide-fed rectangular slot antenna," *IEEE Antennas and Wireless Propagation*, *Lett.*, vol. 3, 2004.

[7] N. Behdad and K. Sarabandi, "A wide-band slot antenna design employing a fictitious short circuit concept," *IEEE Trans. Antennas and Propagation*, vol. 53, no.1, 2005.

[8] F. G. Kharakhili, M. Fardis, G. Dadashzadeh, A. Ahmadi, and N. Hojjat "Circular slot with a novel circular microstrip open ended microstrip feed for UWB applications," *PIER Journal*, vol. 68, pp. 161-167. 2007.

[9] S. Sadat, M. Fardis, F. Geran, and G. Dadashzadeh "A compact microstrip square-ring slot antenna for UWB applications," *PIER Journal*, vol. 67. pp. 173-179, 2007.

[10] R. Chair, A. A. Kishk, and K. F. Lee, C. E. Smith, and D. Kajfez, "Micro strip line and CPW fed ultra wideband slot antenna with U-shaped tuning stub and reflector," *PIER Journal*, vol. 56, pp. 163–182, 2006.

[11] "IE3D 9.1 Electromagnetic simulation software," *Zeland software*, Inc.

[12] Advanced Design System Agilent Technologies.

Dawood Seyed Javan was born in Mashhad, Iran, in1985. He received the B.S. degree from Department of Electrical Engineering of Islamic Azad University, Mashhad, Iran, in 2007. He is currently pursuing the M.S. degree in the Department of Electrical Engineering of Ferdowsi University, Mash-had, Iran.

Omid Hashemi Ghouchani born in Mashhad, Iran, in1985. He received the B.S. degree from Department of Electrical Engineering of Islamic Azad University, Mashhad, Iran, in 2007. He is currently pursuing the M.S. degree in the Department of Electrical Engineering of Ferdowsi University, Mashhad, Iran.

Analysis of Mutual Coupling in Interconnect Lines using Finite Difference Time Domain Method

[1]N. Farahat, [2]R. Mittra, and [1]J. Carrión

[1] Electrical and Computer Engineering Department, Polytechnic University of Puerto Rico
P.O. box 192017 San Juan, PR 00919
[2] Electromagnetic Communication Laboratory, Pennsylvania State University, 319 EE East
University Park, PA, 16802
nader.farahat@gmail.com

Abstract – In this paper, we present a simple technique for analyzing the mutual coupling effects in interconnects using the Finite Difference Time Domain (FDTD) method. The interconnect lines are divided into a set of uniform segments of parallel lines with short lengths. Next, the mutual capacitances and inductances of each of these segments are extracted by incorporating the FDTD solution into the telegrapher's equations. Two examples of coplanar lines and microstrip lines on different dielectric substrates are studied.

I. INTRODUCTION

The Finite Difference Time Domain (FDTD) [1] has been previously used to analyze interconnect lines and extract their equivalent circuit parameters, *viz.,* the series inductance L and the shunt capacitance C [2, 3]. In this paper we modify the algorithm in [3] in order to model the mutual coupling effects between the interconnect lines.

This modification allows one to consider a system of n coupled lines and compute the self and mutual capacitances and inductances between each 2 lines. By increasing the number of unknowns the number of excitations (simulations) is increased to generate enough equations.

Since this technique is a FDTD based method therefore a single run can provide the frequency response in the frequency band of operation by adjusting the amplitude of the Gaussian pulse spectrum into the band. In addition the staggered location of computing the electric and magnetic fields, and in turn computing voltages and currents along the transmission line, in FDTD mesh allows one to avoid the numerical differentiation in the telegrapher's equations and maintain the simplicity of the method. The numerical results show that this approach is accurate enough to obtain the parameters of several practical circuits.

This method is particularly useful for non-uniform transmission lines and it can readily provide the self and mutual capacitance and inductances along the line. We have shown the usefulness of the technique by considering the microstrip step discontinuity and variation of its main parameters along the line as well as in close proximity of the step discontinuity itself.

Two examples of interconnect lines of practical interest are considered: (i) coplanar striplines on different dielectric substrates interconnecting a 12 channel fiber-optic module to IC driver; (ii) and a uniform microstrip line in parallel with a step discontinuity in its width.

II. THEORY

We start with a 2n-port network comprising of n parallel transmission lines. The lines may be approximated by a number of uniform parallel line sections, each of which may be represented with a combination of L, C, R and G and mutual inductance L^m_{ij} and capacitance $C^m_{ij,}$ as shown in Fig. 1. Next, we write the telegrapher's equations in the matrix form as,

$$\hat{V}_1 - \hat{V}_2 = \hat{R}\hat{I}_1 + j\omega\hat{L}\hat{I}_1 \tag{1-a}$$

$$\hat{I}_1 - \hat{I}_2 = \hat{G}\hat{V}_1 + j\omega\hat{C}\hat{V}_1, \tag{1-b}$$

where,

$$\hat{V}_i = \begin{pmatrix} V_i^1 \\ V_i^2 \\ .... \\ V_i^n \end{pmatrix}, \quad \hat{I}_i = \begin{pmatrix} I_i^1 \\ I_i^2 \\ .... \\ I_i^n \end{pmatrix}, \quad i = 1,2 \tag{2}$$

$$\hat{R} = \begin{pmatrix} R_1 0 0 ..... 0 \\ 0 R_2 0 ..... 0 \\ ..... \\ 0 ..... R_n \end{pmatrix}, \ \hat{G} = \begin{pmatrix} G_1 0 0 ..... 0 \\ 0 G_2 0 ..... 0 \\ ..... \\ 0 ..... G_n \end{pmatrix}, \tag{3}$$

$$\hat{L}=\begin{pmatrix} L_{11}L_{12}.....L_{1n} \\ L_{21}L_{22}.....L_{2n} \\ ..... \\ L_{n1}L_{n2}.....L_{nn} \end{pmatrix},\ \hat{C}=\begin{pmatrix} C_{11}C_{12}.....C_{1n} \\ C_{21}C_{22}.....C_{2n} \\ ..... \\ C_{n1}C_{n2}.....C_{nn} \end{pmatrix}. \quad (4)$$

The relationships between the elements of the C matrix and the physical mutual capacitances in Fig. 1, for example for ports 1 and 2, are given by,

$$C_{11}=C_1+C_{12}^m+C_{13}^m+.....+C_{1n}^m \quad (5)$$

$$C_{12}=C_{21}=-C_{12}^m. \quad (6)$$

To determine the vectors in equation (2) from the FDTD simulations, we discretize the computational domain in a way such that the segmentations coincide with the FDTD meshing, both having rectangular boundaries. After the time-domain simulation is over and the level of the pulse is negligible in the entire computational domain, the time domain signals of the components of electric and magnetic fields in any location in the computational domain can be obtained and analyzed. We particularly compute the vertical component of the electric field underneath the transmission line obtained from the FDTD simulation and add them between all the cells from the ground plate to the conductor (computing the line integral) to derive the voltage V for each cell.

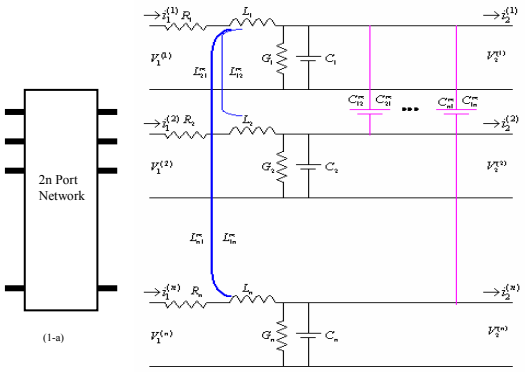

Fig. 1. (a) The schematic and (b) equivalent circuit of a 2n port network comprising of parallel transmission lines.

The same procedure is repeated for the time domain magnetic field signals around the conductor to carry out the closed-path line integral and following the Ampere's law to obtain the current I, which is computed at a half-cell away from the point where V is derived. At the final step we transform the above voltages and currents by using Fast Fourier Transform routine in Matlab in order to derive their frequency domain counterparts.

Next, in order to determine elements of the matrices in equations (3) and (4), we substitute the V and I vectors in equation (2), that are obtained from the excitations of each of the n ports—one part at a time—in equations (1-a) and (1-b). Having n equations for the n unknowns we are able to solve the equations for the R, L, G, C matrices in equations (3) and (4). The above procedure is repeated for each segment of the line and for all frequencies of interest. It should be noted that the staggered sampling of the V and I, which occurs naturally in the FDTD algorithm, enables us to circumvent the need to numerically differentiate the data derived from the FDTD simulation.

III. NUMERICAL EXAMPLES

For the first example we consider the geometry in Fig. 2 comprising of 6 pairs of coplanar striplines (50 microns wide and separated by 125 microns gap) on the dielectric substrate (0.4 mm thickness). This geometry is one half of the actual 12 channel interconnect that is inserted between IC driver and the VCSEL package in a fiber-optic module. Since the differential lines or coplanar striplines provide separate return current path for each signal their use significantly reduces the crosstalk [4-6]. In order to model the matched loads terminating the two ends (the driver IC and the VCSEL package) the lines are truncated by using perfectly matched layers (PML). Furthermore, the coplanar stripline 3 is fed by a voltage source (Gaussian pulse with 25 GHz 3dB cutoff frequency) connected between the traces. Next, the voltages and currents at the reference planes 1 and 2 (rp1, rp2), located in the center of the line 3 (active) and 4 (passive) are observed in the time domain. The same procedure is repeated when the line 4 is excited. The data from the above simulations are transferred into frequency domain and used to calculate self and mutual (per unit length) inductance L and capacitance C of lines 3 and 4 (in the presence of the other lines).The computational domain divided by 40 cells in wavelength inside the dielectric in all three directions. The simulation is carried out until the level of the time signal in the load end of the line is insignificant (20000 time steps). This number of time steps gives a sufficient resolution in the frequency domain.

The self and mutual capacitance and inductance per unit length of line 3 and 4 vs. frequency are shown in Figs. 3 and 4. In addition, the change in mutual capacitance due to different substrates, Du Pont's LTCC (ε_r=7.8), Alumina (ε_r=9.6) and the case of epoxy-added (same thickness as substrate) on top of the traces are shown in Fig. 5.

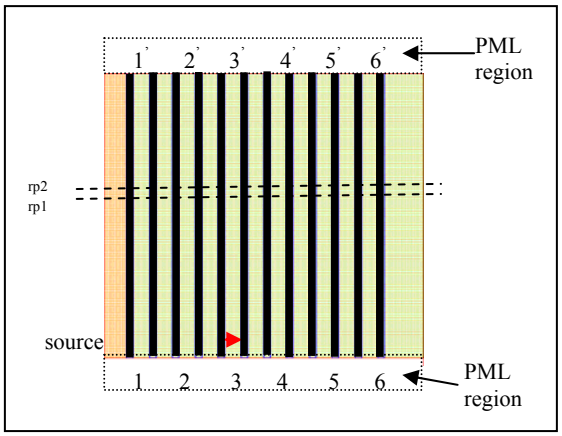

Fig. 2. The top view of the interconnect geometry omprising of 6 pairs coplanar striplines.

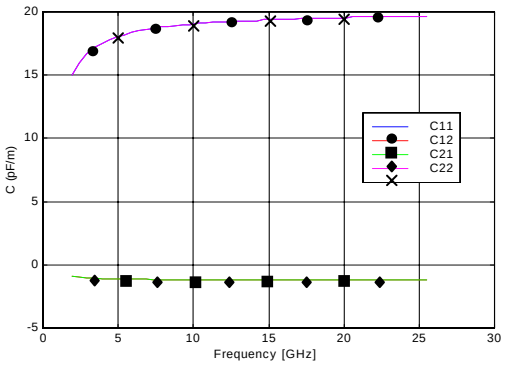

Fig. 3. The self and mutual capacitance C per unit length of two adjacent lines vs. frequency.

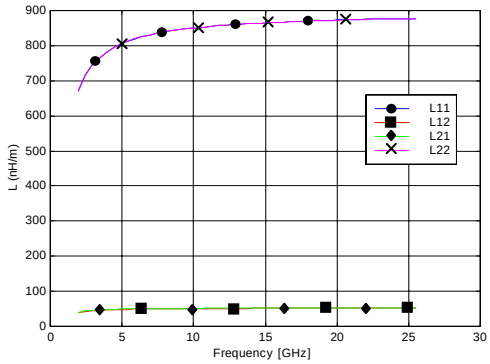

Fig. 4 . The self and mutual inductance L per unit ength of two adjacent lines vs. frequency.

For the second example, we simulate the uniform microstrip line located parallel to a step-in-width sitting on dielectric substrate backed by perfect electric conductor (Fig. 6). The computational domain in this example also is divided by 40 cells in wavelength inside the dielectric in all three directions. The simulation is carried out until the level of the time signal everywhere in the domain is insignificant (10000 time steps). Following the same procedure as in the previous example, and using 20 segments (FDTD cells) in left and right of the step discontinuity, we can derive the self and mutual inductance along the line at a frequency of 10 GHz. The inductance values for the left side of the geometry, comprising of two parallel microstrip lines with the same dimensions as in [2], are in good agreement with the reference data. However, the step discontinuity found to be at the 20th cell causes these values to change, as may be seen in Fig. 7.

It must be noted, however, that the lossless dielectric and perfect conductors have been used in the examples, which lead to zero resistance and conductance in the computations.

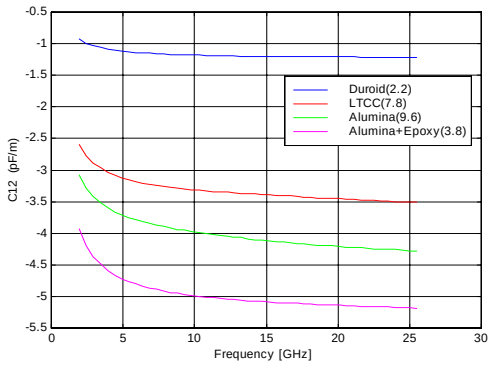

Fig. 5. The mutual capacitance per unit length of two adjacent lines for different substrates vs. frequency.

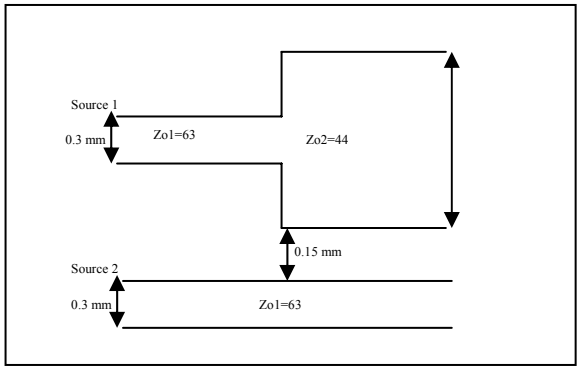

Fig. 6. Top view of an interconnect structure comprising of a uniform microstrip line parallel to a step-in-width.

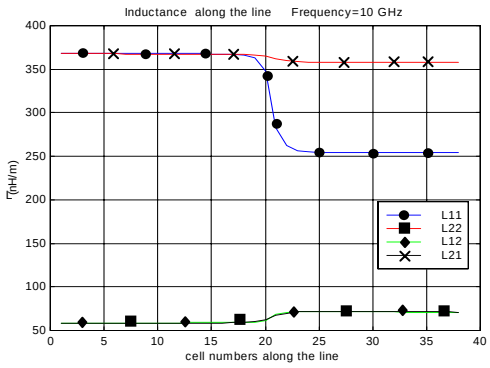

Fig. 7. The self and mutual inductance per unit length of uniform microstrip line in parallel with step-in-width vs. cell numbers along the line for frequency of 10 GHz.

IV. CONCLUSION

A simple technique to analyze the mutual coupling effect in interconnects using the Finite Difference Time Domain (FDTD) method is presented. It was shown that the staggered sampling of the voltage and current, which occurs naturally in the FDTD algorithm, enables us to circumvent the need to numerically differentiate the data derived from the FDTD simulation. The validity of technique is shown through several examples in extraction of self and mutual capacitances of the coupled lines.

REFERENCES

[1] K. S. Yee, "Numerical solution of initial boundary value problems involving Maxwell's equations in isotropic media," *IEEE Trans. Antennas and Propagation*, vol. AP-14, pp. 302-307, May 1966.

[2] J. Zhao and Z. F. Li, "A time-domain full-wave extraction method of frequency-dependent equivalent circuit parameters of multiconductor interconnection lines," *IEEE Trans. On Microwave Theory and Techniques,* vol. 45, no. 1, pp. 23-31, January 1997.

[3] N. Farahat and R. Mittra, "Extraction of equivalent-circuit parameters of interconnection lines using the FDTD method," *Microwave and Optical Technology Letters,* pp. 132-134, 20 April 2002.

[4] T. C. Edwards and M. B. Steer, *Foundations of Interconnect and Microstrip Design*, *John Wiley & Sons, Inc.* 2000.

[5] C. K. Cheng, J. Lillis, S. Lin, and N. Chang, *Interconnect Analysis and Synthesis*, *John Wiley & Sons, Inc.* 2000.

[6] H. Kosaka, M. Kajita, and M. Yamada, "2D alignment free VCSEL-array module with push/pull fibre connector," *Electronics Letters*, vol. 32, no. 21, pp. 1991-1992, October 1996.

Nader Farahat is Associate Professor in the Electrical Engineering department of Polytechnic University of Puerto Rico. He is also adjunct research associate at Pennsylvania State University.

Raj Mittra is Professor in the Electrical Engineering department of the Pennsylvania State University and the Director of the Electromagnetic Communication Laboratory. He is also the President of RM Associates, which is a consulting organization that provides services to industrial and governmental organizations, both in the U. S. and abroad.

José Carrión received a BS in electrical engineering from University of Puerto Rico Mayagüez campus in 2002 and an MS in electrical engineering from Polytechnic University of Puerto Rico in 2007. Currently, he is an electronic engineer with Lockheed Martin.

2009 INSTITUTIONAL MEMBERS

AUSTRALIAN DEFENCE LIBRARY
Northcott Drive
Canberra, A.C.T. 2600 Australia

BAE SYSTEMS
W423A Warton Aerodome
Preston, Lancashire
United Kingdom PR4 1AX

DARTMOUTH COLLEGE
6193 Murdough Center
Hanover, NH 03755-3560

DSTO-DSTORL EDINBURGH
Jets AU/33851-99, PO Box 562
Milsons Point, NSW
Australia 1565

DTIC-OCP/LIBRARY
8725 John J. Kingman Rd. Ste 0944
Ft. Belvoir, VA 22060-6218

ELLEDIEMME
Libri Dal Mondo
PO Box 69/Poste S. Silvestro
Rome, Italy 00187

ELSEVIER
Bibliographic Databases
PO Box 2227
Amsterdam, Netherlands 1000 CE

ENGINEERING INFORMATION, INC
PO Box 543
Amsterdam, Netherlands 1000 Am

ETSE TELECOMUNICACION
Biblioteca, Campus Lagoas
Vigo, 36200 Spain

FGAN-FHR
Neuenahrerstrasse 20
Wachtberg, Germany 53343

FLORIDA INTERNATIONAL UNIV
10555 W. Flagler Street
Miami, FL 33174

GEORGIA TECH LIBRARY
225 North Avenue, NW
Atlanta, GA 30332-0001

HANYANG UNIVERSITY
Paiknam Academic Info. Ctr Library
17 Haengdang-Dong
Seongdong-Ku
Seoul, South Korea 133-791

HRL LABS, RESEARCH LIBRARY
3011 Malibu Canyon
Malibu, CA 90265

IEE INSPEC/Acquisitions Section
Michael Faraday House
6 Hills Way
Stevenage, Herts UK SG1 2AY

IND CANTABRIA
PO Box 830470
Birmingham, AL 35283

INSTITUTE FOR SCIENTIFIC INFO.
Publication Processing Dept.
3501 Market St.
Philadelphia, PA 19104-3302

L-3 IS
1133 Wood Valley Drive
Woodway, TX 76712

LIBRARY – DRDC OTTAWA
3701 Carling Avenue
Ottawa, Ontario, Canada K1A OZ4

LIBRARY of CONGRESS
Reg. Of Copyrights
Attn: 40T Deposits
Washington DC, 20559

LINDA HALL LIBRARY
5109 Cherry Street
Kansas City, MO 64110-2498

LULEA UNIV. OF TECHNOLOGY
Porson
Lulea, Sweden 97187

MISSISSIPPI STATE UNIV LIBRARY
PO Box 9570
Mississippi State, MS 39762

MISSOURI S&T
400 W 14th Street
Rolla, MO 56409

MIT LINCOLN LABORATORY
Periodicals Library
244 Wood Street
Lexington, MA 02420

NATIONAL DEFENSE ACADEMY
1-10-20 Hashirimizu
Yokosuka, Kanagawa
239-8686 Japan

NAVAL POSTGRADUATE SCHOOL
Attn:J. Rozdal/411 Dyer Rd./ Rm 111
Monterey, CA 93943-5101

NDL KAGAKU
C/0 KWE-ACCESS
PO Box 300613 (JFK A/P)
Jamaica, NY 11430-0613

OHIO STATE UNIVERSITY
1320 Kinnear Road
Columbus, OH 43212

OVIEDO LIBRARY
PO BOX 830679
Birmingham, AL 35283

PENN STATE UNIVERSITY
126 Paterno Library
University Park, PA 16802-1808

DAVID J. PINION
1122 E PIKE STREET #1217
SEATTLE, WA 98122

SOUTHWEST RESEARCH INSTITUTE
6220 Culebra Road
San Antonio, TX 78238

SWETS INFORMATION SERVICES
160 Ninth Avenue, Suite A
Runnemede, NJ 08078

TELSTRA
13/242 Exhibition Street
Melbourne, Victoria
3000 Australia

TIB & UNIV. BIB. HANNOVER
DE/5100/G1/0001
Welfengarten 1B
Hannover, Germany 30167

TU DARMSTADT
Schlossgartenstrasse 8
Darmstadt, Hessen
Germany D-64289

UNIV OF CENTRAL FLORIDA LIB.
4000 Central Florida Boulevard
Orlando, FL 32816-8005

UNIVERSITY OF KANSAS – WATSON
1425 Jayhawk Blvd 210S
Lawrence, KS 66045-7594

UNIVERSITY OF MISSISSIPPI
JD Williams Library
University, MS 38677-1848

UNIVERSITY OF PALERMO
PO Box 69- Poste S. Silvestr
Rome, 00187, Italy

VIRTUAL EM INC.
2019 Georgetown Blvd.
Ann Arbor, MI 48105

ACES COPYRIGHT FORM

This form is intended for original, previously unpublished manuscripts submitted to ACES periodicals and conference publications. The signed form, appropriately completed, MUST ACCOMPANY any paper in order to be published by ACES. PLEASE READ REVERSE SIDE OF THIS FORM FOR FURTHER DETAILS.

TITLE OF PAPER:

AUTHORS(S)

PUBLICATION TITLE/DATE:

RETURN FORM TO:

Dr. Atef Z. Elsherbeni
University of Mississippi
Dept. of Electrical Engineering
Anderson Hall Box 13
University, MS 38677 USA

PART A - COPYRIGHT TRANSFER FORM

(NOTE: Company or other forms may not be substituted for this form. U.S. Government employees whose work is not subject to copyright may so certify by signing Part B below. Authors whose work is subject to Crown Copyright may sign Part C overleaf).

The undersigned, desiring to publish the above paper in a publication of ACES, hereby transfer their copyrights in the above paper to The Applied Computational Electromagnetics Society (ACES). The undersigned hereby represents and warrants that the paper is original and that he/she is the author of the paper or otherwise has the power and authority to make and execute this assignment.

Returned Rights: In return for these rights, ACES hereby grants to the above authors, and the employers for whom the work was performed, royalty-free permission to:

1. Retain all proprietary rights other than copyright, such as patent rights.
2. Reuse all or portions of the above paper in other works.
3. Reproduce, or have reproduced, the above paper for the author's personal use or for internal company use provided that (a) the source and ACES copyright are indicated, (b) the copies are not used in a way that implies ACES endorsement of a product or service of an employer, and (c) the copies per se are not offered for sale.
4. Make limited distribution of all or portions of the above paper prior to publication.
5. In the case of work performed under U.S. Government contract, ACES grants the U.S. Government royalty-free permission to reproduce all or portions of the above paper, and to authorize others to do so, for U.S. Government purposes only.

ACES Obligations: In exercising its rights under copyright, ACES will make all reasonable efforts to act in the interests of the authors and employers as well as in its own interest. In particular, ACES REQUIRES that:

1. The consent of the first-named author be sought as a condition in granting re-publication permission to others.
2. The consent of the undersigned employer be obtained as a condition in granting permission to others to reuse all or portions of the paper for promotion or marketing purposes.

In the event the above paper is not accepted and published by ACES or is withdrawn by the author(s) before acceptance by ACES, this agreement becomes null and void.

AUTHORIZED SIGNATURE — TITLE (IF NOT AUTHOR)

EMPLOYER FOR WHOM WORK WAS PERFORMED — DATE FORM SIGNED

Part B - U.S. GOVERNMENT EMPLOYEE CERTIFICATION

(NOTE: if your work was performed under Government contract but you are not a Government employee, sign transfer form above and see item 5 under Returned Rights).

This certifies that all authors of the above paper are employees of the U.S. Government and performed this work as part of their employment and that the paper is therefor not subject to U.S. copyright protection.

AUTHORIZED SIGNATURE — TITLE (IF NOT AUTHOR)

NAME OF GOVERNMENT ORGANIZATION — DATE FORM SIGNED

PART C - CROWN COPYRIGHT

(NOTE: ACES recognizes and will honor Crown Copyright as it does U.S. Copyright. It is understood that, in asserting Crown Copyright, ACES in no way diminishes its rights as publisher. Sign only if *ALL* authors are subject to Crown Copyright).

This certifies that all authors of the above Paper are subject to Crown Copyright. (Appropriate documentation and instructions regarding form of Crown Copyright notice may be attached).

AUTHORIZED SIGNATURE TITLE OF SIGNEE

NAME OF GOVERNMENT BRANCH DATE FORM SIGNED

Information to Authors

ACES POLICY

ACES distributes its technical publications throughout the world, and it may be necessary to translate and abstract its publications, and articles contained therein, for inclusion in various compendiums and similar publications, etc. When an article is submitted for publication by ACES, acceptance of the article implies that ACES has the rights to do all of the things it normally does with such an article.

In connection with its publishing activities, it is the policy of ACES to own the copyrights in its technical publications, and to the contributions contained therein, in order to protect the interests of ACES, its authors and their employers, and at the same time to facilitate the appropriate re-use of this material by others.

The new United States copyright law requires that the transfer of copyrights in each contribution from the author to ACES be confirmed in writing. It is therefore necessary that you execute either Part A-Copyright Transfer Form or Part B-U.S. Government Employee Certification or Part C-Crown Copyright on this sheet and return it to the Managing Editor (or person who supplied this sheet) as promptly as possible.

CLEARANCE OF PAPERS

ACES must of necessity assume that materials presented at its meetings or submitted to its publications is properly available for general dissemination to the audiences these activities are organized to serve. It is the responsibility of the authors, not ACES, to determine whether disclosure of their material requires the prior consent of other parties and if so, to obtain it. Furthermore, ACES must assume that, if an author uses within his/her article previously published and/or copyrighted material that permission has been obtained for such use and that any required credit lines, copyright notices, etc. are duly noted.

AUTHOR/COMPANY RIGHTS

If you are employed and you prepared your paper as a part of your job, the rights to your paper initially rest with your employer. In that case, when you sign the copyright form, we assume you are authorized to do so by your employer and that your employer has consented to all of the terms and conditions of this form. If not, it should be signed by someone so authorized.

NOTE RE RETURNED RIGHTS: Just as ACES now requires a signed copyright transfer form in order to do "business as usual", it is the intent of this form to return rights to the author and employer so that they too may do "business as usual". If further clarification is required, please contact: The Managing Editor, R. W. Adler, Naval Postgraduate School, Code EC/AB, Monterey, CA, 93943, USA (408)656-2352.

Please note that, although authors are permitted to re-use all or portions of their ACES copyrighted material in other works, this does not include granting third party requests for reprinting, republishing, or other types of re-use.

JOINT AUTHORSHIP

For jointly authored papers, only one signature is required, but we assume all authors have been advised and have consented to the terms of this form.

U.S. GOVERNMENT EMPLOYEES

Authors who are U.S. Government employees are not required to sign the Copyright Transfer Form (Part A), but any co-authors outside the Government are.

Part B of the form is to be used instead of Part A only if all authors are U.S. Government employees and prepared the paper as part of their job.

NOTE RE GOVERNMENT CONTRACT WORK: Authors whose work was performed under a U.S. Government contract but who are not Government employees are required so sign Part A-Copyright Transfer Form. However, item 5 of the form returns reproduction rights to the U. S. Government when required, even though ACES copyright policy is in effect with respect to the reuse of material by the general public.

APPLIED COMPUTATIONAL ELECTROMAGNETICS SOCIETY JOURNAL
http://aces.ee.olemiss.edu

INFORMATION FOR AUTHORS

PUBLICATION CRITERIA

Each paper is required to manifest some relation to applied computational electromagnetics. **Papers may address general issues in applied computational electromagnetics, or they may focus on specific applications, techniques, codes, or computational issues.** While the following list is not exhaustive, each paper will generally relate to at least one of these areas:

1. **Code validation.** This is done using internal checks or experimental, analytical or other computational data. Measured data of potential utility to code validation efforts will also be considered for publication.

2. **Code performance analysis.** This usually involves identification of numerical accuracy or other limitations, solution convergence, numerical and physical modeling error, and parameter tradeoffs. However, it is also permissible to address issues such as ease-of-use, set-up time, run time, special outputs, or other special features.

3. **Computational studies of basic physics.** This involves using a code, algorithm, or computational technique to simulate reality in such a way that better, or new physical insight or understanding, is achieved.

4. **New computational techniques** or new applications for existing computational techniques or codes.

5. **"Tricks of the trade"** in selecting and applying codes and techniques.

6. **New codes, algorithms, code enhancement, and code fixes.** This category is self-explanatory, but includes significant changes to existing codes, such as applicability extensions, algorithm optimization, problem correction, limitation removal, or other performance improvement. **Note: Code (or algorithm) capability descriptions are not acceptable, unless they contain sufficient technical material to justify consideration.**

7. **Code input/output issues.** This normally involves innovations in input (such as input geometry standardization, automatic mesh generation, or computer-aided design) or in output (whether it be tabular, graphical, statistical, Fourier-transformed, or otherwise signal-processed). Material dealing with input/output database management, output interpretation, or other input/output issues will also be considered for publication.

8. **Computer hardware issues.** This is the category for analysis of hardware capabilities and limitations of various types of electromagnetics computational requirements. Vector and parallel computational techniques and implementation are of particular interest.

Applications of interest include, but are not limited to, antennas (and their electromagnetic environments), networks, static fields, radar cross section, inverse scattering, shielding, radiation hazards, biological effects, biomedical applications, electromagnetic pulse (EMP), electromagnetic interference (EMI), electromagnetic compatibility (EMC), power transmission, charge transport, dielectric, magnetic and nonlinear materials, microwave components, MEMS, RFID, and MMIC technologies, remote sensing and geometrical and physical optics, radar and communications systems, sensors, fiber optics, plasmas, particle accelerators, generators and motors, electromagnetic wave propagation, non-destructive evaluation, eddy currents, and inverse scattering.

Techniques of interest include but not limited to frequency-domain and time-domain techniques, integral equation and differential equation techniques, diffraction theories, physical and geometrical optics, method of moments, finite differences and finite element techniques, transmission line method, modal expansions, perturbation methods, and hybrid methods.

Where possible and appropriate, authors are required to provide statements of quantitative accuracy for measured and/or computed data. This issue is discussed in "Accuracy & Publication: Requiring, quantitative accuracy statements to accompany data," by E. K. Miller, *ACES Newsletter*, Vol. 9, No. 3, pp. 23-29, 1994, ISBN 1056-9170.

SUBMITTAL PROCEDURE

All submissions should be uploaded to ACES server through ACES web site (http://aces.ee.olemiss.edu) by using the upload button, journal section. Only pdf files are accepted for submission. The file size should not be larger than 5MB, otherwise permission from the Editor-in-Chief should be obtained first. Automated acknowledgment of the electronic submission, after the upload process is successfully completed, will be sent to the corresponding author only. It is the responsibility of the corresponding author to keep the remaining authors, if applicable, informed. Email submission is not accepted and will not be processed.

PAPER FORMAT (INITIAL SUBMISSION)

The preferred format for initial submission manuscripts is 12 point Times Roman font, single line spacing and single column format, with 1 inch for top, bottom, left, and right margins. Manuscripts should be prepared for standard 8.5x11 inch paper.

EDITORIAL REVIEW

In order to ensure an appropriate level of quality control, papers are peer reviewed. They are reviewed both for

technical correctness and for adherence to the listed guidelines regarding information content and format.

PAPER FORMAT (FINAL SUBMISSION)

Only camera-ready electronic files are accepted for publication. The term **"camera-ready" means that the material is neat, legible, reproducible, and in accordance with the final version format listed below.**

The following requirements are in effect for the final version of an ACES Journal paper:

1. The paper title should not be placed on a separate page. The title, author(s), abstract, and (space permitting) beginning of the paper itself should all be on the first page. The title, author(s), and author affiliations should be centered (center-justified) on the first page. The title should be of font size 16 and bolded, the author names should be of font size 12 and bolded, and the author affiliation should be of font size 12 (regular font, neither italic nor bolded).

2. An abstract is required. The abstract should be a brief summary of the work described in the paper. It should state the computer codes, computational techniques, and applications discussed in the paper (as applicable) and should otherwise be usable by technical abstracting and indexing services. The word "Abstract" has to be placed at the left margin of the paper, and should be bolded and italic. It also should be followed by a hyphen (—) with the main text of the abstract starting on the same line.

3. All section titles have to be centered and all the title letters should be written in caps. The section titles need to be numbered using roman numbering (I. II. ….)

4. Either British English or American English spellings may be used, provided that each word is spelled consistently throughout the paper.

5. Internal consistency of references format should be maintained. As a guideline for authors, we recommend that references be given using numerical numbering in the body of the paper (with numerical listing of all references at the end of the paper). The first letter of the authors' first name should be listed followed by a period, which in turn, followed by the authors' complete last name. Use a coma (,) to separate between the authors' names. Titles of papers or articles should be in quotation marks (" "), followed by the title of journal, which should be in italic font. The journal volume (vol.), issue number (no.), page numbering (pp.), month and year of publication should come after the journal title in the sequence listed here.

6. Internal consistency shall also be maintained for other elements of style, such as equation numbering. As a guideline for authors who have no other preference, we suggest that equation numbers be placed in parentheses at the right column margin.

7. The intent and meaning of all text must be clear. For authors who are not masters of the English language, the ACES Editorial Staff will provide assistance with grammar (subject to clarity of intent and meaning). However, this may delay the scheduled publication date.

8. Unused space should be minimized. Sections and subsections should not normally begin on a new page.

ACES reserves the right to edit any uploaded material, however, this is not generally done. It is the author(s) responsibility to provide acceptable camera-ready pdf files. Incompatible or incomplete pdf files will not be processed for publication, and authors will be requested to re-upload a revised acceptable version.

COPYRIGHTS AND RELEASES

Each primary author must sign a copyright form and obtain a release from his/her organization vesting the copyright with ACES. Copyright forms are available at ACES, web site (http://aces.ee.olemiss.edu). To shorten the review process time, the executed copyright form should be forwarded to the Editor-in-Chief immediately after the completion of the upload (electronic submission) process. Both the author and his/her organization are allowed to use the copyrighted material freely for their own private purposes.

Permission is granted to quote short passages and reproduce figures and tables from and ACES Journal issue provided the source is cited. Copies of ACES Journal articles may be made in accordance with usage permitted by Sections 107 or 108 of the U.S. Copyright Law. This consent does not extend to other kinds of copying, such as for general distribution, for advertising or promotional purposes, for creating new collective works, or for resale. The reproduction of multiple copies and the use of articles or extracts for commercial purposes require the consent of the author and specific permission from ACES. Institutional members are allowed to copy any ACES Journal issue for their internal distribution only.

PUBLICATION CHARGES

All authors are allowed for 8 printed pages per paper without charge. Mandatory page charges of $75 a page apply to all pages in excess of 8 printed pages. Authors are entitled to one, free of charge, copy of the journal issue in which their paper was published. Additional reprints are available for a nominal fee by submitting a request to the managing editor or ACES Secretary.

Authors are subject to fill out a one page over-page charge form and submit it online along with the copyright form before publication of their manuscript.

ACES Journal is abstracted in INSPEC, in Engineering Index, DTIC, Science Citation Index Expanded, the Research Alert, and to Current Contents/Engineering, Computing & Technology.